

Solubility of Ore Minerals in Magmatic- Hydrothermal Deposits: Constraints from Natural and Synthetic Fluid Inclusions

Von der Naturwissenschaftlichen Fakultät der
Gottfried Wilhelm Leibniz Universität Hannover

zur Erlangung des Grades
Doktorin der Naturwissenschaften (Dr. rer. nat.)

genehmigte Dissertation

von

Insa Theresa Cassens, geb. Derrey

Diplom-Mineralogin

2021

Referent: Prof. Dr. rer. nat. François Holtz
Korreferent: Prof. Dr. Roman E. Botcharnikov (PhD)
Tag der Promotion: 22.10.2021

“I argue that there is no necessary connection between the size of an object and the value of a fact, and that, though the objects I have described are minute, the conclusions to be derived from the facts are great.”

(H. C. Sorby, the “father” of fluid inclusion studies, in 1858)

Acknowledgements

During my time as a PhD student I came across numerous amazing and supportive people, for which I am extremely grateful.

First and foremost, I would like to thank my adviser François Holtz for his support throughout the years, his open door, lengthy discussions and always constructive criticism, constant honey supply as well as his big heart. It was a pleasure and honor to work with you, also within the FZ:GEO.

My sincere thanks also go to Roman Botcharnikov and Harald Behrens, who introduced me to the wonderful world of experimental petrology and supported me along the way with many fruitful discussions and advise. My second home during this study was the geochemistry group of Stefan Weyer. I want to express my gratitude for their incredible scientific and technical support in the clean-lab and MS-labs. This includes in particular Stefan Weyer, Ingo Horn, Martin Oeser-Rabe, Stephan Schuth and Alexandra Tangen. A big thankyou also goes to Moritz Albrecht. Working with you was a great pleasure and the countless hours together in the LA-ICP-MS lab wouldn't have been half as fun without you.

It's always good to look beyond your own horizon and I am grateful for many discussions with researchers from around the world at conferences or other occasions. I am particularly grateful to Dave Polya, who did not only provide me with his great insights and discussions on Panasqueira, but also with the great specimen, which was the foundation of my natural study. Without a claim to be complete, I would also like to thank Andreas Audétat, Bob Bodner, Bob Linnen, Pilar Lecumberri-Sanchez, Gaëtan Launay and Matthew Steel McInnes.

I have enjoyed my time at the Institute of Mineralogy at University of Hannover a lot, which was mostly due to many wonderful colleagues. For countless discussions, scientific, technical and administrative support, but also welcome distractions like beers at "Klein Kröpcke", after-work climbing at "Klettercampus", parties at "Chez Heinz", Christmas Parties with "Bosseln", "Flunkie Ball" contests in the park, "Tea days", knitting nights or baby showers, I want to thank: Renat Almeev, Marine Boulanger, Bernard Charlier, Max Collinet, Franzi and Lars Crede, Adriana Currin Sala, Otto Dietrich, Ute and Marcel Dietrich, Martin and Svenja Erdmann, Julian Feige, Adrian and Jaayke Fiege, Lennart Fischer, Parveen Fuchs, Anika Husen, Malte Junge, Maria Kirchenbaur, Jürgen Köpke, Kristin Kortlang, Uli Kroll, Sabine Kropp, Nuo Li, Stefan Linsler, Marize Muniz da Silva, Julie Michaud, Olivier Namur, David Neave, Annika Neddermeyer, Peter Nowaczyk, Yvonne Röbbert, Sebastian Ross, Dongmei Qi, Lena Stark, André and Kristina Stechern, Lena Steinmann, Anna-Maria Welsch-Kirby, Tobi Wengorsch, Eric Wolf and Teresa Zahoransky. And I am very sorry, as I surely forgot to mention some of you.

I consider myself extremely lucky to have wonderful friends and some of them have been already mentioned above. In addition, I want to thank Ann Bernhardt, Beccy Döring, Erika Dotzler and Babsi Ratschbacher for their long-lasting friendship, which is invaluable to me.

Last but not least, I want to thank my family: My parents for their never-ending support, not only as extensive babysitters during the Corona pandemic. My brother Helge for threatening me that he would buy himself a PhD degree from the internet, if I were not to finish my PhD. My daughters Skadi and Edda for being the greatest joy of my life, and my beloved husband for always being there for me and still loving me even though he must have felt like a single parent quite often recently.

Abstract

Magmatic-hydrothermal ore deposits are among the most important resources of many elements that are crucial for our technologically oriented civilization. Fluids expelled from crystallizing and cooling plutons are the subject of this study, as they are responsible for the transport and selective concentration of many economically important elements, such as, e.g., Cu, Mo, Sn, W and Au. To understand the potential of such magmatic-hydrothermal fluids to transport elements of interest, the trace element concentrations in fluid inclusions in minerals need to be analyzed quantitatively, and in addition synthetic inclusions need to be prepared and analyzed at relevant geological conditions. To reach these goals a new analytical LA-ICP-MS setup was developed based on the combination of a femtosecond-laser with a fast scanning sector field ICP-MS. An experimental protocol for the formation of synthetic fluid inclusions, trapped from fluids at high temperatures and pressures, was tested and refined to ensure the achievement of equilibrium during syntheses. Concentrations of Mo, W and Au in synthetic fluid inclusions in equilibrium with various ore minerals were determined at different T, P, salinity, fO_2 and fS_2 conditions and compared to existing natural and experimental data as well as results from thermodynamic modelling. With W being of tremendous economic importance, a particular attention was given to the determination of the solubility of the two most abundant W minerals, i.e., wolframite and scheelite. According to our experiments, T is the most important parameter controlling W transport and deposition, followed by the salinity of the fluid, fO_2 and fS_2 . Pressure has no significant effect in the investigated range of 100-300 MPa. The temperature dependence of wolframite and scheelite solubility is different, which may explain natural observations indicating a decreasing wolframite/scheelite ratio with depth in some W-deposits, or the dominance of ferberite over scheelite in many W-deposits. In addition, geochemical interaction with country-rocks plays an important role in the formation of magmatic-hydrothermal W-deposits, which is supported by our study of natural fluid inclusions from the Panasqueira W-Sn-(Cu-)deposit in Portugal. Fluids from the Main Sulfide Stage at Panasqueira further show a sharp decrease of Cu and As concentrations concomitant to the precipitation of chalcopyrite and arsenopyrite and were likely derived from a single pulse of a rather homogenous magmatic-hydrothermal fluid. The combination of our experimental data with measured W concentrations in natural fluid inclusions from Panasqueira indicate that W concentrations during the mineralization stages ($\sim 1-70$ ppm W) are ca. one to two orders of magnitude higher than previously estimated (~ 0.2 ppm W). This results in a reduction of the required amount of hydrothermal fluid to ca. 10-100 km³ to explain the amount of W precipitated in the Main Oxide Silicate Stage. This finding diminishes, but does not preclude, the necessity of the involvement of meteoric fluids in the formation of the Panasqueira W-Sn-(Cu-)deposit.

Keywords: magmatic-hydrothermal fluids, fluid inclusions, high-P/high-T experiments, solubility of ore-minerals, LA-ICP-MS, Panasqueira W-Sn-(Cu-)deposit

Zusammenfassung

Magmatisch-hydrothermale Erzvorkommen gehören zu den wichtigsten Ressourcen für viele Elemente, die für unsere technologie-orientierte Gesellschaft von großer Bedeutung sind. Im Rahmen der vorliegenden Arbeit wurden Fluide untersucht, die von auskristallisierenden und abkühlenden Plutonen freigesetzt werden, da diese für den Transport und die selektive Anreicherung vieler dieser wirtschaftlich bedeutsamen Elemente (z. B. Cu, Mo, Sn, W und Au) verantwortlich sind. Um das Potenzial dieser magmatisch-hydrothermalen Fluide zu verstehen bestimmte Elemente zu transportieren, müssen einerseits die Spurenelementkonzentrationen in Flüssigkeitseinschlüssen in Mineralen quantitativ analysiert und andererseits synthetische Einschlüsse unter relevanten geologischen Bedingungen präpariert und analysiert werden. Hierfür wurde ein neuer analytischer LA-ICP-MS-Aufbau entwickelt, der auf der Kombination eines Femtosekundenlasers mit einem schnell scannenden Sektorfeld-ICP-MS basiert. Zur Bildung von synthetischen Flüssigkeitseinschlüssen aus Fluiden unter hohen Temperaturen und Drucken, wurde ein experimentelles Verfahren getestet und weiterentwickelt, um das Erreichen von Gleichgewichtsbedingungen während der Synthesen sicherzustellen. Bei verschiedenen T-, P-, Salinitäts-, fO_2 - und fS_2 -Bedingungen wurden Konzentrationen von Mo, W und Au in synthetischen Flüssigkeitseinschlüssen im Gleichgewicht mit verschiedenen Erzmineralen bestimmt und mit vorhandenen natürlichen und experimentellen Daten sowie den Ergebnissen thermodynamischer Modellierungen verglichen. Aufgrund der großen wirtschaftlichen Bedeutung von W wurde der Bestimmung der Löslichkeit der beiden am häufigsten vorkommenden W-Mineralen (Wolframit und Scheelit) besondere Aufmerksamkeit gewidmet. Die Ergebnisse zeigen, dass die Temperatur der wichtigste Parameter ist, der den W-Transport und die Ablagerung beeinflusst, gefolgt von der Salinität des Fluids, fO_2 und fS_2 . Der Druck hat im untersuchten Bereich von 100-300 MPa keinen signifikanten Effekt. Die unterschiedliche T-Abhängigkeit der Löslichkeiten von Wolframit und Scheelit könnte die natürlichen Beobachtungen erklären, dass in einigen W-Lagerstätten das Wolframit/Scheelit-Verhältnis mit der Tiefe zunimmt und in vielen W-Lagerstätten Ferberit gegenüber Scheelit dominiert. Darüber hinaus spielt die geochemische Interaktion mit dem Nebengestein eine wichtige Rolle bei der Bildung von magmatisch-hydrothermalen W-Lagerstätten, was durch unsere Untersuchungen an natürlichen Flüssigkeitseinschlüssen der Panasqueira W-Sn-(Cu-)Lagerstätte in Portugal untermauert wird. Fluide aus der „Main Sulfide Stage“ in Panasqueira zeigen zudem eine starke Abnahme der Cu- und As-Konzentrationen, die mit der Ausfällung von Chalkopyrit und Arsenopyrit einhergeht, und stammen wahrscheinlich von einem einzelnen relativ homogenen magmatisch-hydrothermalen Fluid ab. Der Vergleich unserer experimentellen Daten mit gemessenen W-Konzentrationen in natürlichen Flüssigkeitseinschlüssen aus Panasqueira zeigt, dass die W-Konzentrationen während der Mineralisation ($\sim 1-70$ ppm W) ein bis zwei Größenordnungen höher sind als bisher berechnet ($\sim 0,2$ ppm W). Dies hat eine Reduktion der benötigten Fluidmenge auf ca. $10-100$ km³ zur Folge, die benötigt wird, um die während der „Main Oxide Silicate Stage“ ausgeschiedene Wolframmenge zu erklären. Diese Erkenntnis vermindert die Notwendigkeit der Beteiligung meteorischer Fluide an der Bildung der Panasqueira W-Sn-(Cu-)Lagerstätte, schließt sie jedoch nicht aus.

Schlagwörter: Magmatisch-Hydrothermale Fluide, Flüssigkeitseinschlüsse, Hochdruck-/Hochtemperatur-Experimente, Löslichkeit von Erzmineralien, LA-ICP-MS, Panasqueira

TABLE OF CONTENTS

ACKNOWLEDGEMENTS	V
ABSTRACT	VII
ZUSAMMENFASSUNG	IX
TABLE OF CONTENTS	XI
1 IMPORTANCE OF FLUIDS IN MAGMATIC-HYDROTHERMAL ORE DEPOSITS	1
2 OBJECTIVES AND STATE OF THE ART	5
2.1 LASER ABLATION INDUCTIVELY COUPLED PLASMA MASS SPECTROMETRY OF FLUID INCLUSIONS	5
2.2 SYNTHETIC FLUID INCLUSIONS	8
2.2.1 EQUILIBRIUM IN SYNTHETIC FLUID INCLUSIONS	8
2.2.2 MINERAL SOLUBILITIES FROM ANALYSES OF SYNTHETIC FLUID INCLUSIONS WITH A FOCUS ON TUNGSTEN (W) ORE MINERALS	11
2.3 NATURAL FLUID INCLUSIONS IN MAGMATIC-HYDROTHERMAL ORE DEPOSITS	12
3 THE ANALYTICAL METHOD - QUANTIFICATION OF TRACE ELEMENT CONTENTS IN FROZEN FLUID INCLUSIONS BY UV-FS-LA-ICP-MS ANALYSIS	15
3.1 INSTRUMENTATION	15
3.2 CALIBRATION	19
3.3 SAMPLES/SYNTHETIC FLUID INCLUSIONS	20
3.4 ABLATION PROCEDURE	21
3.5 DATA PROCESSING	22
3.6 ACCURACY AND PRECISION	22
3.7 LIMITS OF DETECTION	25
3.8 CONCLUSIONS REGARDING THE ANALYTICAL METHOD	26
4 THE EXPERIMENTAL METHOD - EXPERIMENTAL TESTS ON ACHIEVING EQUILIBRIUM IN SYNTHETIC FLUID INCLUSIONS	29
4.1 EXPERIMENTAL PROCEDURE	29
4.1.1 GENERAL EXPERIMENTAL PROCEDURE	29
4.1.2 SETUP 1: EXPERIMENTAL APPROACH FOR EQUILIBRATION TESTS AT 800 °C	31
4.1.3 SETUP 2: EXPERIMENTAL APPROACH TO TEST THE EFFICIENCY OF AN INTERMEDIATE QUENCH FOR RE-OPENING OF FLUID INCLUSIONS FORMED AT 600 °C	32
	XI

4.1.4	SETUP 3: DISSOLUTION KINETICS AND TIME-DEPENDENT EXPERIMENTS	32
4.2	RESULTS	33
4.2.1	SETUP 1: EQUILIBRATIONS TESTS	33
4.2.2	SETUP 2: ROLE OF THE INTERMEDIATE QUENCH	36
4.2.3	SETUP 3: TIME-DEPENDENT EXPERIMENTS	37
4.3	DISCUSSION	39
4.3.1	SIZE AND NUMBER OF FLUID INCLUSIONS	39
4.3.2	DISSOLUTION KINETICS	39
4.3.3	IMPORTANCE OF INTERMEDIATE QUENCH	41
4.3.4	LIMITATIONS OF PRESSURE CYCLING	42
4.3.5	DISCUSSION OF AU, MO AND W CONCENTRATIONS IN FLUIDS IN EQUILIBRIUM WITH AU METAL, MOLYBDENITE AND SCHEELITE	43
4.4	CONCLUSIONS REGARDING THE EXPERIMENTAL METHOD	45
5	<u>APPLICATION #1: SYNTHETIC FLUID INCLUSIONS - SOLUBILITY OF SCHEELITE (CaWO₄), FERBERITE (FeWO₄) AND GOLD (Au) IN HYDROTHERMAL FLUIDS</u>	47
5.1	EXPERIMENTAL PROCEDURE	48
5.2	ANALYTICS	50
5.3	RESULTS	51
5.4	DISCUSSION	56
5.4.1	MOLYBDENITE AND POWELLITE SOLUBILITY	56
5.4.2	GOLD SOLUBILITY	57
5.4.3	SCHEELITE AND FERBERITE SOLUBILITY	59
5.4.4	IMPLICATIONS FOR W-COMPLEXATION	62
5.4.5	TEMPERATURE DEPENDENCE OF SCHEELITE, MOLYBDENITE AND GOLD SOLUBILITIES AND THERMODYNAMIC CONSIDERATIONS	65
5.4.6	COMPARISON WITH TUNGSTEN CONCENTRATIONS IN NATURAL FLUID INCLUSIONS	67
6	<u>APPLICATION #2: NATURAL FLUID INCLUSIONS - TUNGSTEN (W) AND OTHER ELEMENT CONCENTRATIONS IN FLUID INCLUSIONS OF THE PANASQUEIRA W-Sn-(Cu-)DEPOSIT</u>	69
6.1	GEOLOGICAL SETTING	69
6.2	THE MINERALIZED VEINS	70
6.3	PREVIOUS WORK ON FLUID INCLUSIONS OF THE PANASQUEIRA VEIN SYSTEM	74
6.4	SAMPLE DESCRIPTION	77
6.5	ANALYTICAL METHODS	79
6.6	RESULTS	80
6.6.1	MICROTHERMOMETRY	84

6.6.2	ESTIMATION OF THE SALINITY OF THE FLUID PHASE	89
6.6.3	RESULTS FROM LA-ICP-MS ANALYSES	92
6.7	DISCUSSION	96
6.7.1	GENERAL FLUID CHARACTERISTICS	96
6.7.2	CHEMICAL EVOLUTION OF THE FLUID	100
6.7.3	IMPLICATIONS FOR ORE DEPOSITION AND REQUIRED FLUID-ROCK RATIOS	103
7	CONCLUSIONS	107
8	REFERENCES	111
	APPENDIX I	123
	APPENDIX II	125
	APPENDIX III	129
	APPENDIX IV	145
	CURRICULUM VITAE	163
	LIST OF PUBLICATIONS (PEER-REVIEWED)	165

1 Importance of Fluids in Magmatic-Hydrothermal Ore Deposits

Ore deposits are natural sources of elements of economic interest. Therefore, they play a fundamental role in the origin and evolution of our technologically oriented civilization. According to the popular textbook on ore-forming processes of Robb (2005) “ore deposits form when a useful commodity is sufficiently concentrated in an accessible part of the Earth’s crust so that it can be profitably extracted”. Consequently, knowledge of the basic processes that are responsible for ore-deposit formation is of significant importance not only for geoscientists but also for human society in general. Formation of ore deposits can occur in a variety of geological settings, reaching from near-surface systems (e.g., supergene deposits), sedimentary basins, metamorphic sequences, to hydrothermal and magmatic systems (e.g., Robb, 2005).

Independent of the depositional environment, it is widely acknowledged that magmatic and hydrothermal fluids play a crucial role in the formation of the majority of ore deposits, as they are the main transporting agents controlling mobilization and selective concentration of elements in the Earth’s crust (e.g., Heinrich and Candela, 2014; Kesler, 2005). Among these elements are many metals of economic interest, which are most commonly found as oxide or sulfide phases, that precipitated from fluids at shallow crustal levels as a result of one or several of the following factors: change in temperature, change in pressure, phase separation, fluid mixing, fluid/rock reaction, adsorption as well as biologically enhanced mineralization (Robb, 2005).

Hydrothermal ore deposits in a broad sense are an enrichment of metals by the selective dissolution of mineral compounds in an aqueous fluid, followed by transport and physical focusing of the fluid and subsequent precipitation of metal-rich minerals (Barnes, 1997; Heinrich and Candela, 2014). Among the diverse and widespread class of hydrothermal ore deposits, the so-called magmatic-hydrothermal ore deposits are considered to have formed from the most primitive or “juvenile” hydrothermal fluids, which were directly expelled from magmas upon decompression (first boiling) and crystallization (second boiling) (e.g., Kesler, 2005; Robb, 2005). When an aqueous fluid is expelled from a crystallizing hydrous magma this results in an increase of the total volume ($V_{\text{Fluid}} +$

$V_{\text{IgneousRock}} > V_{\text{HydrousMelt}}$; Burnham and Ohmoto, 1980), which leads to lithostatic overpressure. Therefore, boiling of hydrous magmas upon emplacement and crystallization in the upper crust is thought to be the main driving force for hydraulic fracturing and rapid fluid flow through the roof of an intrusion. As a consequence, magmatic-hydrothermal ore deposits usually occur around cupolas or other felsic intrusions, which are considered to be the primary source of not only the magmatic fluids, but also the heat, which fuels convection in the hydrothermal system as well as the source of metals and transporting ligands themselves (e.g., Audétat, 2019; Audétat et al., 2008; Barnes, 1997; Bodnar et al., 2014; Heinrich and Candela, 2014).

Magmatic-hydrothermal ore deposits are of great economic importance, as they are the world's main source of Cu, Mo, Sn, and W as well as a major source of Au, Ag, Pb, and Zn (Kesler and Simon, 2015). Several specific types of ore-deposits are universally classified as magmatic-hydrothermal ore deposits in the literature, i.e., porphyry deposits, Sn-W-vein and replacement (greisen) deposits as well as skarn deposits (e.g., Audétat, 2019; Heinrich and Candela, 2014; Robb, 2005). Depending on the model of ore formation (and the extent of contribution of a magmatic fluid) some authors also consider pegmatite deposits (c.f., discussion in Robb, 2005 and references therein) and high-sulphidation epithermal deposits (e.g., Robb, 2005; Williams-Jones and Heinrich, 2005) to belong to the class of magmatic-hydrothermal deposits.

When studying the development of magmatic-hydrothermal (and other) ore-deposits, one is faced with the problem that the bulk of the fluids, which percolated within the paleo-hydrothermal system and which was responsible for the deposition of ore minerals, is long gone and cannot be sampled directly, let alone under the pressure (P) and temperature (T) conditions during its formation and ascent. To elude this problem, scientists have used little fluid archives called fluid inclusions for more than 150 years.

It was as early as 1858, when Henry C. Sorby recorded and described microscopic images of fluid inclusions in minerals for the first time and postulated that they were portions of the fluid, from which the respective mineral had grown and which had been trapped upon crystal growth (Sorby, 1858). He was also the first to realize the opportunity to use fluid inclusions to reconstruct the conditions under which the host mineral had grown. Although Sorby faced many critics at his time, who did not acknowledge the use of something as small as fluid inclusions to understand something as large as a mountain

range or an ore deposit, their great value for the understanding of many geological processes is undisputed today (Shepherd et al., 1985).

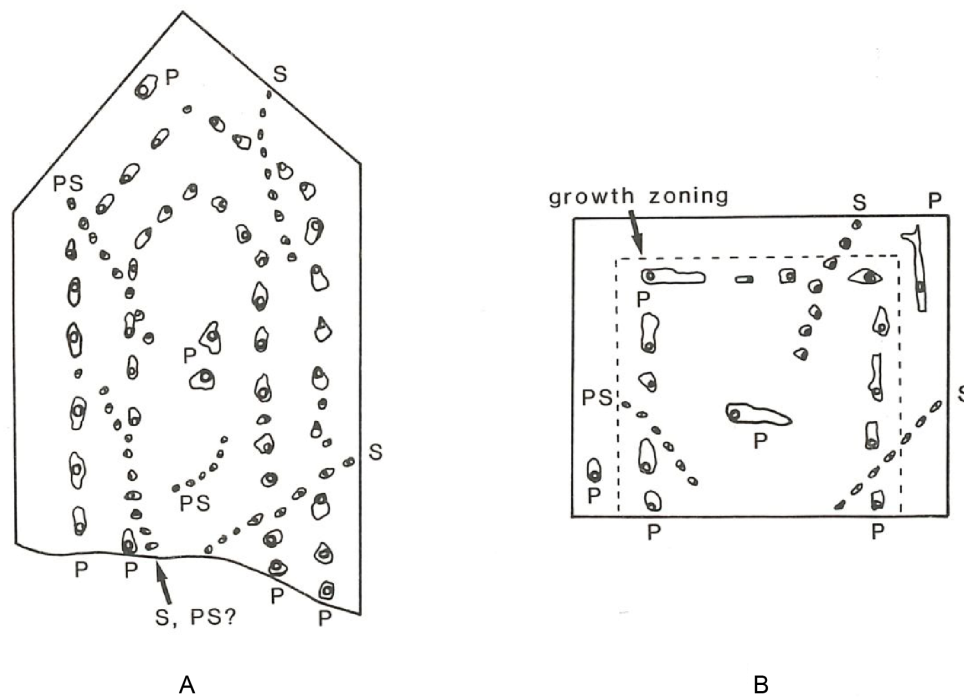


Fig. 1.1: Idealized distribution of different types of fluid inclusions (P: primary; PS: pseudosecondary; S: secondary) in A) quartz, parallel to c-axis and B) fluorite, parallel to cube face (from Shepherd et al., 1985).

Today's general understanding is that fluid inclusions can be trapped during either mineral growth or recrystallization, when a small portion of an aqueous fluid is trapped along irregularities inside a crystal. It is distinguished between primary fluid inclusions (PFI), which form along crystal faces of a growing mineral, pseudosecondary fluid inclusions (PSFI), which are trapped in healing fractures in the host mineral during its growth and secondary fluid inclusions (SFI), which form by healing of fractures at a later point in time, when the crystal is no longer growing (Fig. 1.1). Whereas PFI and PSFI are thought to represent the fluids present during the growth of the crystal and concomitant geological events, SFI represent later fluids, which can be completely unrelated to the early fluids. (Roedder, 1984; Shepherd et al., 1985). The study of PFI and PSFI (as well as SFI, if they can be correlated to a geological event of interest) is of great use for ore-deposit research and much of what we know about the temperatures, pressures and compositions of ore-forming fluids in hydrothermal systems comes from fluid inclusion studies (e.g., Bodnar et al., 2014; Kesler and Simon, 2015). Regarding the transport and

deposition of metals by fluids in magmatic-hydrothermal deposits, fluid inclusions provide the most direct record of the hydrothermal solutions, which were present around the time of formation (Audétat, 2019; Kesler, 2005; Roedder, 1984; Shepherd et al., 1985). Quantitative fluid inclusion research was established in the 1950s and 1960s and up to the day a multitude of information has been collected on fluid inclusions. In the early decades of fluid inclusion research, most information on hydrothermal fluids was obtained from microthermometry and Raman spectroscopy, including temperatures and pressures of formation as well as compositional information on major components, i.e., bulk salinity, major salts and volatiles (cf., Roedder, 1984). Before 1998 there was only few data on minor and trace element concentrations in fluid inclusions, which were obtained by crush-leach analysis (e.g., Banks and Yardley, 1992; Campbell et al., 1995), proton-induced X-ray emission (e.g., Anderson et al., 1989; Heinrich et al., 1992), or synchrotron X-ray fluorescence (e.g., Frantz et al., 1988; Mavrogenes et al., 1995). In the late 1990s a new era of fluid inclusion research started with crucial improvements of laser ablation inductively coupled plasma mass spectrometry (LA-ICP-MS), which allow for the fast and routine analysis of major and trace elements in individual fluid inclusions down to the ppm level (Audétat et al., 1998; Günther et al., 1998).

2 Objectives and State of the Art

This chapter contains quotes of the author's papers Derrey et al. 2017 and Albrecht et al. 2014. All other citations are highlighted accordingly.

The present study aims to reconstruct the conditions during magmatic-hydrothermal ore formation. To do so, the LA-ICP-MS technique for analysis of fluid inclusions is refined and applied to both natural and synthetic fluid inclusions. Synthetic fluid inclusions provide the opportunity to systematically quantify the evolution of the fluid's composition as a function of major parameters that control the properties of magmatic-hydrothermal systems. The prerequisite for this approach is that equilibrium between fluid and solid phases in the experiment was reached prior to the formation of fluid inclusions. Within the scope of this study the protocol to synthesize inclusions from an equilibrated fluid is tested thoroughly and refined before it will be applied to study solubilities of different ore minerals in hydrothermal fluids under varying conditions.

Whereas synthetic fluid inclusions can provide information on maximum concentrations of elements resulting from solubility of the respective ore minerals, natural fluids are often undersaturated so that concentrations even in high temperature fluid inclusions are usually low. During this study, element concentrations in natural fluid inclusions will be compared to maximum solubilities derived from experiments to get a better understanding of metal transport and deposition in magmatic-hydrothermal systems.

2.1 Laser Ablation Inductively Coupled Plasma Mass Spectrometry of Fluid Inclusions

Laser ablation inductively coupled plasma mass spectrometry is regarded as the most reliable technique for the determination of concentrations of solutes in fluid inclusions for a large number of elements (e.g., Pettke et al., 2012). This technique provides a high dynamic range, which allows determination of elemental concentrations from the $\mu\text{g/g}$ to the wt% level. LA-ICP-MS measurements can provide trace element concentrations (e.g. Cu, Zn, Au, Sn, Sr, Rb, Cs, Mo, W, Pb) as well as major element concentrations (e.g. Na, K,

Ca, Mg) from small sample volumes of fluid inclusions from short transient signals acquired by ICP-MS (Heinrich et al., 2003). Even isotope ratio determinations have been carried out on fluid inclusions using this highly versatile technique (Pettke et al., 2011). Besides the common determination of cation contents, it is also possible to quantify elements that exist as anions in the fluid inclusions, such as Cl, Br, and S (Guillong et al., 2008a; Seo et al., 2011). The basic principles for LA-ICP-MS analysis of fluid inclusions have been pioneered by Günther et al. (1998) using a nanosecond ultraviolet laser ablation system (UV-ns-LA, 193 nm, ArF excimer) in combination with a quadrupole ICP-MS (QMS). The method was refined by Günther et al. (2001), Halter et al. (2002), Heinrich et al. (2003) and Allan et al. (2005) but did not change in general.

High control over the laser ablation process is required to achieve representative fluid inclusion analysis. Problems can occur when fragments of the host mineral (most commonly quartz) quarry out during ablation and the fluid is lost through cracks before the ablation process reaches the inclusion. Other problems arise from incomplete mobilization of the inclusion, or the lack in mass spectrometric acquisition speed leading to an underestimation of the elemental concentrations. In order to achieve representative analysis, the complete volume of the inclusion, which may be composed of gas, liquid, and crystals, needs to be mobilized and transported to the ICP-MS.

Opening the inclusions is considered one of the most critical steps in fluid inclusion analysis (Günther et al., 1998). Especially the analysis of shallow inclusions (< 10 μm depth) is often accompanied by uncontrolled release of the fluid inclusion content due to overpressure in the inclusions and splashing of the material out of the ablation pit (Fig. 2.1a). Allan et al. (2005) estimated that the sampling process frequently controls the precision achieved for fluid inclusion analysis. Depending on their extent, most elemental concentrations can be determined with a precision in the order of 20–30 % RSD. Better precision values have been reported for elements with high concentration levels (e.g. up to the wt%-range) in relatively large fluid inclusions (Pettke et al., 2012).

Quadrupole MS systems have been favored over magnetic sector field mass spectrometers as they are capable of fast peak scanning, which is essential for the sequential analysis of the transient signal that is typically generated during laser ablation analyses of fluid inclusions. Sweep times as short as 260 ms have been used for QMS analyses of a set of 20 isotopes (Pettke et al., 2012). However, more recently fast scanning sector field mass spectrometers with a high transmission and a large dynamic detection

range such as the Element XR™ from ThermoScientific™ have been developed. These are particularly suitable for short laser ablation analyses of low concentration levels.

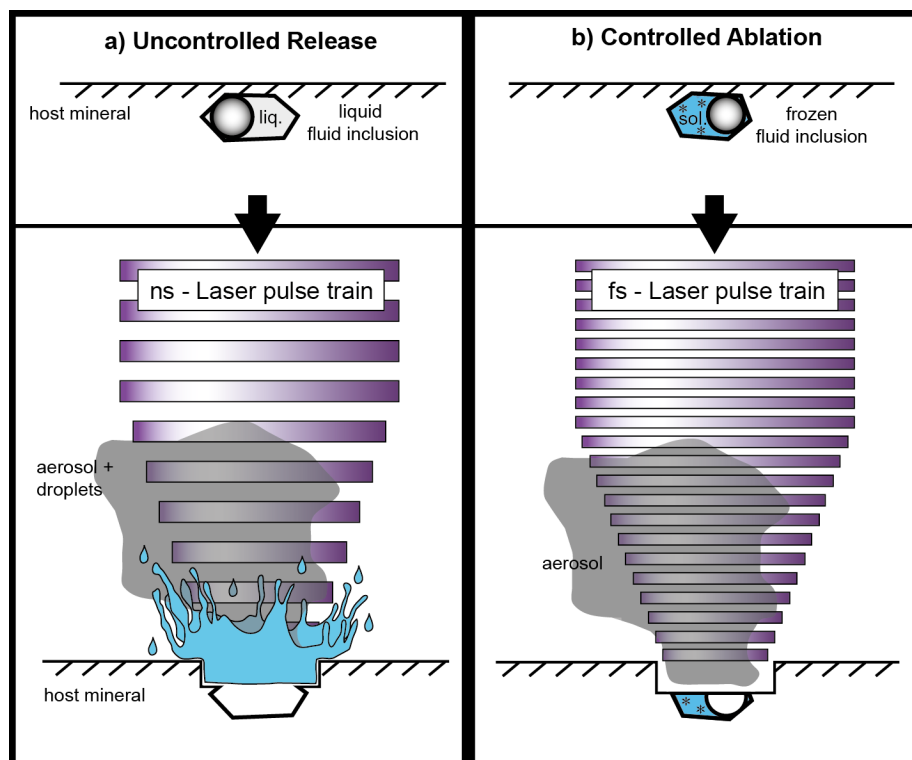


Fig. 2.1: Comparative drawing of (a) UV-ns-LA of shallow fluid inclusions at room temperature and (b) UV-fs-LA of fluid inclusions with freezing technique of this study. The ablation of shallow fluid inclusions tends to lead to uncontrolled release of the fluid with UV-ns-LA, which results in unstable ICP-MS signals. UV-fs-LA with frozen fluid inclusions ensures very high control on the opening of inclusions, which results in a higher success rate and very reliable data production from single fluid inclusion analysis. Illustration is not to scale.

Advantages of 196 nm femtosecond UV laser ablation systems (UV-fs-LA) over UV-ns-LA systems have been reported for the determination of isotopic ratios of heavy stable isotope systems (Horn et al., 2006; Steinhoefel et al., 2009a; Steinhoefel et al., 2009b; Steinhoefel et al., 2010) as well as Pb-U mineral dating (Horn and von Blanckenburg, 2007), but only preliminary experience has been documented for trace element analyses with single collector ICP-MS applications (Pettke et al., 2012). To the best of our knowledge, only one study had been published prior to 2014 (i.e. the publication of Albrecht et al. (2014)) using femtosecond laser ablation (fs-LA) for the analysis of fluid inclusions with respect to solute quantification. Borisova et al. (2012) used a NIR-fs-LA-QMS system in their study. Pettke et al. (2012) speculated that, particularly for fluid inclusion analysis with fs-LA, problems such as cracking at the crater bottom and associated material loss or phase explosions and an uncontrolled opening of the inclusion

may arise. Nevertheless, the greatest advantage of fs-LA is the minimal heat transfer from the laser spot into the sample during ablation (Pronko et al., 1995) resulting in minimized elemental fractionation effects (Horn and von Blanckenburg, 2007).

In Chapter 3, a new analytical setup for the determination of major, minor and trace element concentrations in fluid inclusions is presented, where a 194 nm UV-fs laser is coupled with a fast scanning sector field ICP-MS. To make use of the low heat transfer of the fs-laser to its full capacity, we adapted a heating–freezing stage as the ablation cell and performed the ablations at low temperatures (e.g., $-40\text{ }^{\circ}\text{C}$, c.f., Fig. 2.1b). This new approach was tested by the analysis of different types of synthetic fluid inclusions with known concentrations. During the development of the LA-ICP-MS method, we focused on smaller inclusions ($\leq 30\text{ }\mu\text{m}$) with an elemental load of $\leq 53\text{ }\mu\text{g/g}$, which is of high significance for the chemical characterization of natural fluid inclusions, but analytically challenging.

2.2 Synthetic Fluid Inclusions

The correct reconstruction of natural conditions, e.g., during magmatic-hydrothermal ore formation, requires accurate and systematic quantification of the evolution of the fluid composition as a function of major parameters that control the properties of magmatic-hydrothermal systems. The main approach applied for such quantifications at high pressure and temperature is the experimental synthesis of fluid inclusions, which was described in the pioneering studies of Roedder and Kopp (1975), Shelton and Orville (1980) and Sterner and Bodnar (1984). In recent years, synthesis of fluid inclusions and subsequent LA-ICP-MS analysis has become the method of choice in collecting thermodynamic data constraining metal transport in aqueous fluids and partitioning of metals between coexisting phases (e.g., Berry et al., 2006; Duc-Tin et al., 2007; Frank et al., 2011; Hack and Mavrogenes, 2006; Hanley et al., 2005; Heinrich et al., 1999a; Lerchbaumer and Audétat, 2009; Loucks and Mavrogenes, 1999; Simon et al., 2006; Ulrich and Mavrogenes, 2008; Zajacz et al., 2010; Zhang et al., 2012).

2.2.1 Equilibrium in Synthetic Fluid Inclusions

One of the main challenges in such studies on synthetic fluid inclusions is to ensure that equilibrium conditions between liquid and solid phases were reached prior to the

formation of fluid inclusions in the host mineral. For example, Hanley et al. (2005) stated that it was “impossible to demonstrate that brine-metal equilibrium was reached before fluid entrapment” in their experiments. There are two major kinetic factors influencing the entrapment of equilibrated fluid inclusions in experimental studies: a) the time necessary for the system to reach equilibrium with respect to all phases and buffer mineral assemblages (t_{equil}) and b) the time needed to heal cavities in the respective host minerals (quartz in most studies) (t_{heal}). Obviously, t_{heal} must be longer than t_{equil} to synthesize fluid inclusions representing equilibrium fluids.

Since healing of cracks and mineral growth can occur quite fast, various methods have been suggested to ensure achievement of equilibrium before fluid entrapment: by delaying healing of the host mineral, by reopening previously healed cracks or by opening new cracks after a defined period of time. For instance, in their solubility study of NaCl and KCl in aqueous fluid, Sterner et al. (1988) delayed crack healing of quartz by cycling pressure between 200 and 600 MPa in the first two hours of the experiment. With this technique, the compression and decompression of the fluid would lead to a continuous in- and out-flux of the fluid through the cracks due to changes in fluid density, keeping the fluid in the cracks of the host mineral connected with the surrounding fluid. Using this approach, Sterner et al. (1988) were able to trap fluid inclusions with homogenous salt concentrations even at very high salinities. Subsequently it was proven that pressure cycling of about 100 MPa in total is sufficient to prevent fast healing of the cracks (P. Lecumberri-Sanchez, personal communication).

More recently, Li and Audétat (2009) developed a method to synthesize larger fluid inclusions under unfavorable growth conditions (e.g., low temperatures), which also provides a different method to constrain the time of system equilibration before onset of fluid entrapment using a rapid heat/rapid quench cold seal pressure vessel (RH/RQ-CSPV; design described in Matthews et al. (2003)). This method was used and tested by Zhang et al. (2012), when investigating the solubility of molybdenite in hydrothermal fluids. In a first step, they produced primary fluid inclusions by growing a new layer of quartz over an etched quartz piece. In a second step, some of the primary inclusions were reopened applying an intermediate quench using a rapid quench system (drop from 800 °C to \pm room temperature), which leads to in-situ fracturing of the quartz cylinder. Subsequently, the sample was replaced into the hot zone to trap secondary inclusions in the reopened cavities. Zhang et al. (2012) claimed that refilled inclusions trapped after

the intermediate quench can be distinguished optically from primary inclusions by the intersection of cracks. Consequently, they could focus subsequent analysis of fluid inclusions via LA-ICP-MS on inclusions that formed after quenching and reheating. They noted that these fluid inclusions showed compositions considerably more constant than fluid inclusions from experiments without an intermediate quench.

A similar approach was used by Zajacz et al. (2010), who trapped two generations of synthetic fluid inclusions in a) a pre-fractured and b) a non pre-treated quartz chip in the same capsule, whereas the latter was only fractured in-situ by the intermediate quench (drop from 1000 °C to ± room temperature after 24 h). They observed that the compositions of fluid inclusions in the pre-fractured and in the in-situ fractured quartz chips were usually identical within uncertainty, which supports their conclusion that equilibrium had been achieved before healing of the fractures in the pre-fractured chip.

Up to this point our knowledge on the best approach (among those described above) to synthesize equilibrated fluid inclusions remains poor. It is also not clear, which method is most suitable for certain P, T and X conditions. The pioneering studies applying an intermediate quench by Zhang et al. (2012) and Zajacz et al. (2010) were performed at 600-800 °C and 1000 °C respectively and they differ in their outcomes concerning the ubiquitous need for an intermediate quench. Little is known about the efficiency of in-situ quenching at lower temperatures prevailing in the hydrothermal regime of ore deposits. In addition, kinetic studies to constrain the actual time necessary to equilibrate the fluid (t_{equil}) and trap it in the host mineral (t_{heal}) are required.

In Chapter 4, a series of experiments is described, which were conducted at 800 °C, 200 MPa and constant oxygen fugacity (f_{O_2}) and sulfur fugacity (f_{S_2} ; buffered with the assemblage pyrite + pyrrhotite + magnetite: PPM). In those experiments, we tested the effects of quartz pretreatment, pressure cycling and intermediate quenching on the formation and composition of metal-bearing fluid inclusions, which were trapped from aqueous fluids coexisting with molybdenite (MoS_2), scheelite (CaWO_4) and gold at 800 °C and 200 MPa (setup 1). We further applied an experimental protocol to test the efficiency of an intermediate quench and to distinguish fluid inclusions formed before and after an intermediate quench (setup 2). To obtain a better understanding of the relationship between t_{heal} and t_{equil} , we further conducted a series of time-dependent experiments (1 to 100 hours, setup 3).

2.2.2 Mineral Solubilities from Analyses of Synthetic Fluid Inclusions with a Focus on Tungsten (W) Ore Minerals

Due to its special physical properties, such as extreme robustness, corrosion resistance and the highest melting point of all elements, W is essential for many industrial applications. For example W is used in large amounts for the manufacturing of tungsten carbides (67 % of W consumed in the EU in 2019), which are used in mill and cutting tools, as well as in mining and construction tools and others (Latunussa et al., 2020). Consequentially, in the four existing lists of critical raw materials from the European Commission (list of CRMs 2011, 2014, 2017, 2020), W was continuously classified as a critical raw material, which is defined by the combination of economic importance and supply risk (Fig. 2.2). In the last three lists of CRM, W was rated as the (non-energy, non-agricultural) raw material with the greatest economic importance. Therefore, understanding the transport and deposition of W is highly desirable, which requires data on the solubility of W-minerals.

Scheelite (CaWO_4) and wolframite ($(\text{Fe,Mn})\text{WO}_4$) are the dominant W-bearing minerals in tungsten deposits, such as porphyry W-deposits, W-greisen, and W-skarn and vein deposits (e.g., Bodnar et al., 2014) and there have been several attempts to determine the solubility of these phases experimentally or based on solubility calculation (e.g., Gibert et al., 1992; Liu and Xiao, 2020; Malinin and Kurovskaya, 1993; Polyá, 1990; Schröcke et al., 1984; Wang et al., 2021; Wood, 1992; Wood and Samson, 2000; Yastrebova et al., 1963). But previous experiments were mostly performed at either ambient conditions or high T, but ambient P and are not representative of the conditions in natural W-deposits. Studies, which were performed at high T and P, either used the direct fluid sampling or weight loss technique, which are prone to large errors due to the formation of quench precipitates. Especially in low-salinity fluids, such as they mostly prevail in natural W-deposits, tungsten tends to form colloids, so that determined solubilities from direct fluid sampling are usually too high. The synthetic fluid inclusion approach avoids this problem, as it allows the complete separation of the fluid from the solid phases. In experiments described in Chapter 5, we synthesized fluid inclusions, which were subsequently analyzed with LA-ICP-MS to sample aqueous fluids at high pressures and temperatures. The principal objective was to obtain solubility data for scheelite and wolframite to provide key data for the quantification of transport properties of fluids as well as for modeling of ore forming processes.

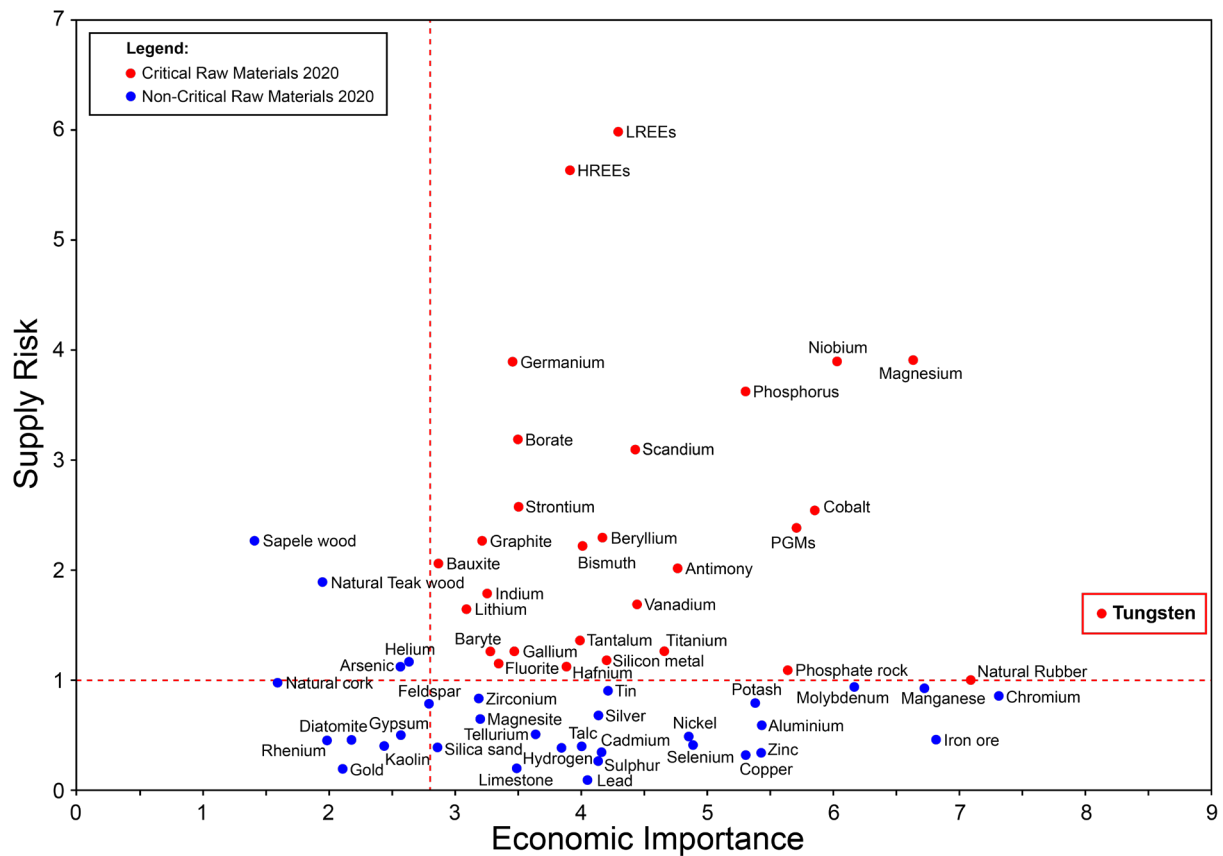


Fig. 2.2: Criticality assessment results according to the 4th list of Critical Raw Materials. Modified after publication from the European Commission (<https://rmis.jrc.ec.europa.eu/?page=crm-list-2020-e294f6>, accessed on 30.03.2021).

2.3 Natural Fluid Inclusions in Magmatic-Hydrothermal Ore Deposits

As previously mentioned, much of what we know about ore-forming fluids in magmatic-hydrothermal systems comes from studies of natural fluid inclusions (Bodnar et al., 2014; Kesler and Simon, 2015). They consist predominantly of H₂O with usually subordinate but locally abundant CO₂ and smaller portions of H₂S, CH₄, and N₂. Dissolved species mostly include the cations Na, K, Ca, Mg, Fe, and Si, whereas Cl is the dominant anion with smaller amounts of HCO₃⁻ and SO₄²⁻ (Kesler, 2005; Roedder and Bodnar, 1997).

Thanks to LA-ICP-MS of fluid inclusions a lot of information has been collected on minor and trace elements in fluid inclusions in recent years. In most cases the elements of concern are ore-forming elements from magmatic-hydrothermal deposits (e.g., Albrecht, 2017; Audétat et al., 1998; Audétat et al., 2008; Chang et al., 2018; Chen et al., 2019;

Lecumberri-Sanchez et al., 2017; Ulrich et al., 2002; Williams-Jones and Heinrich, 2005; Zajacz et al., 2008).

In his review of LA-ICP-MS data of high temperature fluid inclusions (temperature of homogenization (T_{hom}) > 450 °C) from magmatic-hydrothermal deposits, Audétat (2019) aims at answering the question, whether the mineralization potential of magmatic-hydrothermal ore deposits was already predetermined by the metal content of the exsolving fluids or if other conditions have to coincide or are more decisive for the formation of an economic deposit. In his comparison, Audétat (2019) shows that fluids from Sn- and Cu-deposits contained significantly more Sn and Cu, respectively, than fluids from barren intrusions or other ore deposits. Whereas no such trend could be shown for Mo, the evaluated data indicates that a similar correlation might exist for W and REE and their respective mineralized intrusions. This justifies the need of further trace element studies on fluid inclusions from magmatic-hydrothermal deposits, as data availability is still insufficient to assess all aspects of ore metal transport and deposition. In Chapter 6, we present trace element data from fluid inclusions in a vug quartz crystal from the world-class Panasqueira W-Sn-(Cu-)vein deposits in Portugal, which has been mined for more than 100 years and is one of the leading tungsten producers in Europe. Exploration at the Panasqueira mine is still ongoing and its geology was described in detail by numerous studies (Bussink, 1984; Foxford et al., 1991; Foxford et al., 2000; Kelly and Rye, 1979; Launay et al., 2018; Marignac, 1982; Noronha et al., 1992; Polyá, 1989; Polyá et al., 2000; Polyá, 1988).

With our results we do not only intend to add data to the collection of fluid inclusion trace element data on ore-deposits, but also to get a better understanding of W-transport and deposition in W-mineralizing systems and to compare our experimental data from Chapter 5 on the maximum solubilities of scheelite and wolframite with actual concentrations of W in natural fluid inclusions. High temperature natural fluids are rarely saturated with respect to ore-forming minerals (e.g., Gibert et al., 1992; Pokrovski et al., 2014). But nevertheless, saturation must be reached to precipitate the respective ore-mineral. The combination of experimental and natural fluid inclusions studies bears the potential to unravel the interplay of availability (from the primary source, i.e, the melt) and saturation of the ore mineral (cf., Heinrich and Candela, 2014).

3 The Analytical Method - Quantification of Trace Element Contents in Frozen Fluid Inclusions by UV-fs-LA-ICP-MS Analysis

The following chapter is based on Albrecht et al. (2014). The author's contributions as a coauthor are approximately as follows:

- *Preparation and analyses of standard fluids – 50 %*
- *Experiments to produce synthetic standard fluid inclusions – 100 %*
- *Discussion, development and refinement of the analytical method – 20 %*
- *Writing of the manuscript and figure design – 20 %*

3.1 Instrumentation

Analyses have been carried out with an Element XR™ fast scanning sector field inductively coupled plasma mass spectrometer (ThermoScientific™, Bremen, Germany) in combination with an in-house build laser ablation system, which is based on a Spectra-Physics™ femtosecond (Ti:Sapphire) laser (Solstice™) operating in the deep UV at 194 nm. The laser system produces a pulse energy of 70–90 µJ in the fourth harmonic. This ultra-short-pulsed laser generates a soft ablation with high control and avoids elemental fractionation at the sample site. The ablations of the standard reference materials (NIST610) were carried out with a repetition rate of 10 Hz. For fluid inclusion analysis, the repetition rate was adjusted depending on the depth of the inclusions. For shallow inclusions, between near surface and 30 µm depth, a repetition rate of 2–5 Hz was used, resulting in signal intensities significantly above the respective detection limits (Tab. 3.1). Inclusions deeper than 30 µm were analyzed with 10 Hz for faster drilling. The laser repetition rate controls the signal shape, intensity and finally the limits of detection (LOD) for the measured elements. A higher repetition rate results in shorter and higher signals and subsequently in better, i.e. lower, LODs (Pettke et al., 2012).

The selected spot size on the sample surface is chosen to be bigger than the analyzed fluid inclusion in order to guarantee that the whole fluid inclusion is ablated and subsequently

transported to the ICP-MS. An adjustable aperture in the beam path controls the spot size. It is possible to use spot sizes of up to 30 μm for the ablation of quartz. Ablations of quartz with bigger spot diameters would result in insufficient ablation rates, because of reduced laser energy density. The spot size was held constant during the analysis which differs from the ablation procedure described by (Günther et al., 1998).

Tab. 3.1: Intensities of background and fluid inclusion signal from analysis 19nov22; $3SD_{\text{Background}}$ defines the LODs; $\text{Signal}_{\text{Flinc}}$ shows background corrected count rates of fluid inclusion; all values in counts per second (cps)

Isotope	Background	$3SD_{\text{Background}}$	$\text{Signal}_{\text{Flinc}}$
^{23}Na	1 258 057	63 932	4 375 165
^{88}Sr	1327	1306	7089
^{197}Au	113	205	728

With our technique there is no need for stepwise opening of the inclusions, because an explosion of the inclusion or splashing of the material out of the ablation pit can be excluded when the inclusions are frozen. Especially the analysis of CO_2 bearing inclusions are expected to be simplified since the pressure is strongly decreased upon phase transformation of $\text{CO}_{2(\text{gas})}$ to $\text{CO}_{2(\text{solid})}$. We expected that this approach works especially with femtosecond laser pulses due to their low thermal energy transfer, keeping even fluid inclusions with low ice melting temperatures (e.g., $-65\text{ }^\circ\text{C}$) in their frozen state. The heat-affected zone during fs-LA has been investigated in earlier studies. Hirayama and Obara (2005) showed that the layer affected by heating with a femtosecond laser is only a few nm thick. In contrast, nanosecond laser ablation results in significant conductive heat transfer within a layer of several μm (Hergenröder, 2006).

For analyses, the Element XR™ is operated in “speed mode” which provides an optimized data acquisition for short transient signals as produced during LA of fluid inclusions. Due to faster magnetic scanning and faster scanning of the electrical field in the electrostatic analyzer unit, the sweep time is much shorter than that commonly used for analyses with sector field instruments. For 20 isotopes ranging between ^9Be and ^{209}Bi , one sweep takes 477 ms. A short sweep time is essential for fluid inclusion measurements, because the signal peak commonly occurs subsequent to the opening of the fluid inclusion (Fig. 3.1) and slow data acquisition may result in a preliminary signal cut-off and artificially fractionated element concentrations.

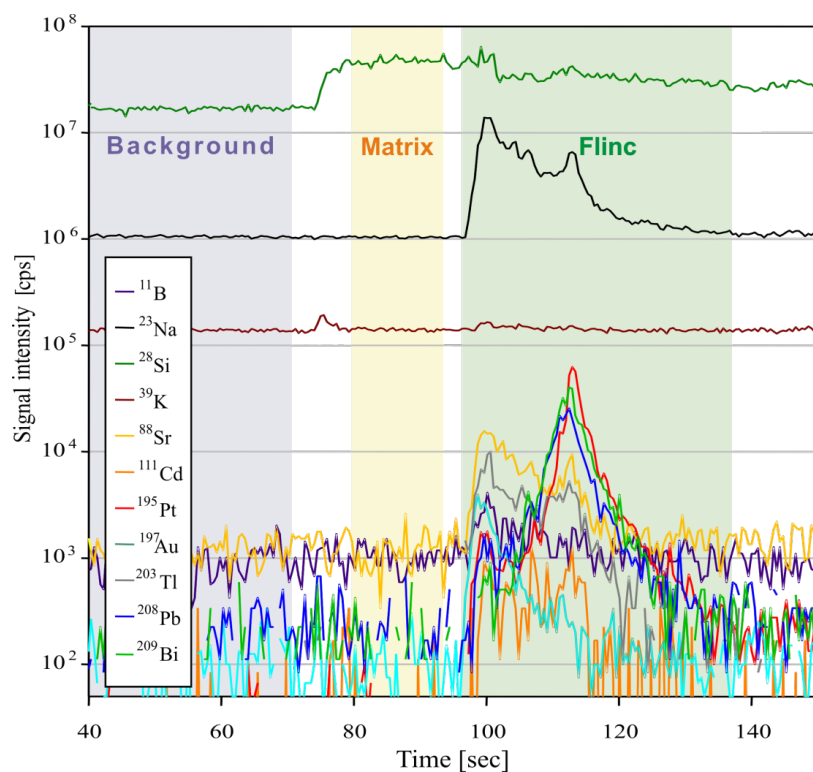


Fig. 3.1: Fluid inclusion (“Flinc”) signal from analysis 19nov37 on sample ID189-Pt. Filled areas show the integration windows for background, matrix and inclusion signal chosen for data evaluation. The size of the inclusion was 21 μm in diameter, located at 20 μm depth. The laser repetition rate was 2 Hz.

Further ICPMS operational settings are shown in Tab. 3.2. For this study, we used a modified heating-freezing cell for laser ablation in order to overcome some fundamental limitations of LA-ICP-MS analysis of fluid inclusions. One of the aims was to improve the fluid inclusion opening procedure and thereby avoid the explosive ejection of the material during opening. With frozen inclusions and the small ablation rate of the UV-fs laser, we aimed to enhance the control during the opening process and as a result to improve the success rate of fluid inclusion analyses.

While frozen, cracking at the bottom of the fluid inclusion would only result in the loss of gases, which are not frozen and cannot be detected with the instrumentation used. Furthermore, we expected that the transient signal could be stretched in time using low repetition rates and frozen solid fluid inclusion. Additionally, we aimed to improve the standardization process by using frozen matrix matched calibration standards prepared from standard solution in addition to the NIST610 and NIST612 glass standards. The matrix-matched standards enabled precise quantifications even at low counting rates. Independent of the external standard used, the precision of the analyses still depends on the size, shape and position of the inclusions, as well as on the laser repetition rate.

Tab. 3.2: ICP-MS settings for fluid inclusion analyses

Spectrometer	ElementXR™
RF Power	950 W
Carrier gas flow (He)	0.27 – 0.3 L/min
Auxiliary gas flow	0.65 L/min
Cool gas flow	14.5 L/min
Cones	Ni “Jet” sampler, Ni “H” skimmer
Sample time	0.003 s (0.01 s for Au and Pt)
Samples per peak	100
Mass window	4 %

The analytical setup was realized with a modified ‘HCS622V’ cell from INSTEC™, Colorado, USA. The cell is vacuum tight and provides an appropriate cell window to sample distance suiting the use of an objective with a focal length of 20 mm. It provides precise temperature control over the range from -190 °C to $+600\text{ °C}$. To optimize the cell volume, the main cell was modified to carry a removable 3 cm^3 small cell made from Teflon, which is sealed to the main cell by means of O-rings. The small cell connects to the gas inlet and outlet with Teflon tubes. With this modification the washout time is reduced dramatically. Helium, a gas with much higher thermal conductivity compared to Argon, can be used with flow rates of up to 0.8 L/min limiting the lowest reachable temperature to -100 °C . Without the small Teflon cell, we observed a strong signal loss between room temperature and -40 °C which exceeded 70 % for all measured isotopes due to the rising viscosity of helium at lower temperatures. This deficiency was reduced to a signal loss of $< 5\%$ when the modified Teflon cell was inserted. Furthermore, the transient signal shape from raster analysis, e.g. on NIST glasses, does not differ from those obtained at ambient temperature. The cooled sample area is large enough to provide space for a standard reference material (SRM) and several sample chips. Hence it is not necessary to open the cell during the data acquisition for calibration.

3.2 Calibration

To prove that LA analysis at low temperatures results in adequate values, we measured the NIST612 glass against the NIST610 glass at $-40\text{ }^{\circ}\text{C}$. Results indicate that the preferred concentration values of most elements (taken from the GeoRem database: <http://georem.mpch-mainz.gwdg.de>) can be measured with an accuracy of $\pm 5\%$.

To test the performance of our method for analysis of frozen liquids, we analyzed a self-prepared standard solution against the NIST610 glass (Fig. 3.2). As low partition coefficients of most elements between aqueous solution and ice results in the formation of micro-nuggets on grain boundaries, it was necessary to freeze the solution with a high cooling rate to hamper the growth of ice crystals and generate small grain sizes resulting in a more homogeneous element distribution. Raster ablations (2 Hz, $30\text{ }\mu\text{m}$ spot size) on larger areas were carried out to contribute to homogeneous sampling. The calculated results agree within analytical uncertainties (1RSD) with a specific value of $108\text{ }\mu\text{g/g}$ (Fig. 3.2).

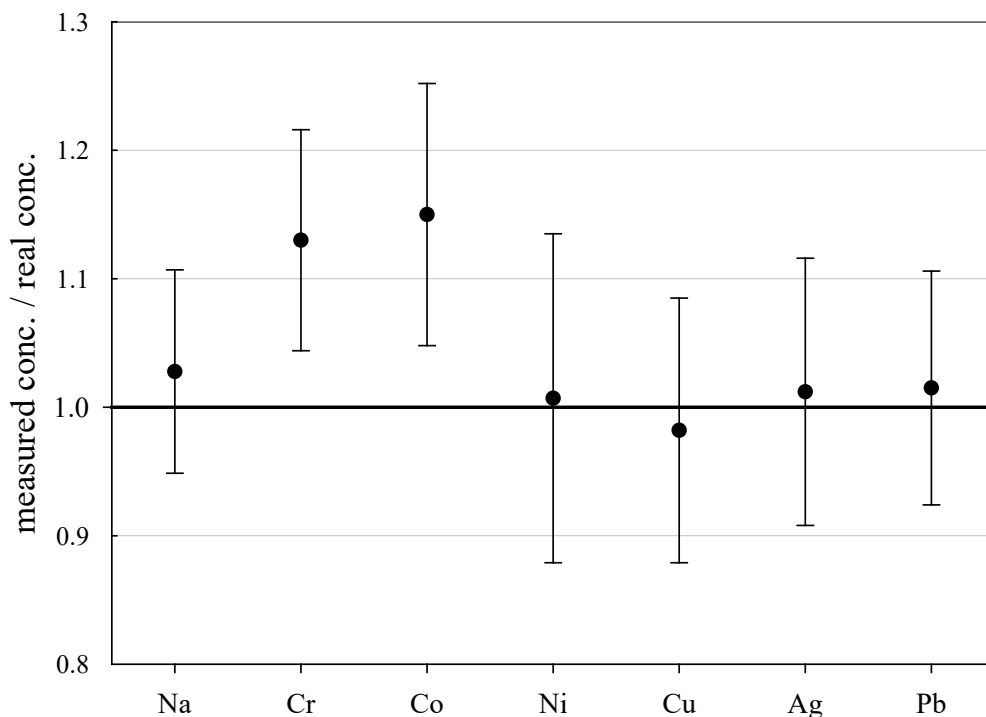


Fig. 3.2: Analysis of a self-prepared frozen standard solution against NIST610 glass. The real concentration of all elements is $108\text{ }\mu\text{g/g}$. Error bars show 1RSD values of 11 analyses.

Because of easier handling, for fluid inclusion analysis the NIST610 glass rather than frozen standard solutions was used for external calibration of element. The analyses were performed using the standard-bracketing method, with a standard ablation after every fourth sample. Final ice melting temperatures were determined by microthermometry and provided the sodium chloride equivalent ($\text{NaCl}_{\text{eq.}}$) values, which were used as internal standard for the calculation of elemental concentrations (Günther et al., 1998) using the SILLS software.

3.3 Samples/Synthetic Fluid Inclusions

To test our analytical setup, we used synthetic fluid inclusions in quartz, which were generated from a standard solution of known concentration. The solution was prepared as a 1:1 mixture from the MERCK™ VIII ICPMS-multi-element-standard and a 20 % NaCl solution; its composition is given in Tab. 3.3.

Tab. 3.3: Composition of the stock solution for HP/HT experiments; all values in $\mu\text{g/g}$; * Na in wt%.

Al	B	Ba	Be	Bi	Ca	Cd	Co	Cr	Cu	Fe	Ga
52.3	52.8	52.8	53.3	53.3	52.8	52.8	52.8	52.3	53.3	52.8	53.9
K	Li	Mg	Mn	Na*	Ni	Pb	Se	Sr	Te	Tl	Zn
52.8	52.8	54.4	52.8	9.7*	52.8	52.8	53.9	53.3	53.9	52.8	53.3

Preparation for fluid inclusion synthesis generally followed the workflow described by Bodnar et al. (1985) with minor modifications. Cores of 2.5 mm diameter and ca. 2 mm length were drilled from inclusion free alpine quartz, heated to 350 °C and subsequently immersed in concentrated hydrofluoric acid for 10 minutes to widen the cracks.

Two experiments were performed, one in a gold (ID188-Au) and one in a platinum (ID189-Pt) capsule, respectively, with dimensions of 20 mm length, 3.2 mm outer diameter and a wall thickness of 0.2 mm. In each capsule one pre-fractured quartz cylinder was placed together with 5 μg silica gel (to accelerate crack healing) and 30 μl of the standard solution. The capsules were pressurized to 200 MPa and heated isobarically to 800 °C in a rapid-heat/rapid-quench hydrothermal autoclave of the design described

by Matthews et al. (2003) using argon as pressure medium. After a runtime of 5 days the autoclave was slowly cooled to room temperature. The recovered capsules were weighed to check for potential leaks during the run. The quartz cylinders were cleaned, dried and embedded in Araldite to be cut and polished to chips of 300 μm thickness. The experimental method will be described in greater detail in Chapter 4.

The quartz chips from both capsules contained abundant synthetic fluid inclusions and 55 inclusions were selected for microthermometric and LA-ICP-MS analyses. Microthermometric measurements of final ice melting temperatures ($T_{\text{m-ice}}$) of -6.2 ± 0.1 $^{\circ}\text{C}$ correspond to a salinity of 9.47 ± 0.13 wt% NaCl_{eq} , calculated after Bodnar (1993) which is in full agreement with the standard solution composition.

3.4 Ablation Procedure

In this study, we followed the workflow of fluid inclusion analysis reported by Heinrich et al. (2003). Since the inclusions are analyzed in the frozen state, problems such as explosive opening and sputtering of the inclusion content during ablation can be excluded, and we were able to use so-called ‘straight ablation’ for the measurements. In contrast to the stepwise opening procedure which is used especially for polyphase inclusions, the “straight ablation” procedure holds some advantages, as reported by Pettke et al. (2012). These are (1) lower amount of surface contamination, (2) higher signal/background ratios and (3) lower limits of detection (LOD).

Prior to ablation the samples and reference materials were cleaned with deionized water and acetone, and the heating–freezing cell was wiped out carefully with dilute nitric acid. The positions of the inclusions were mapped off-line prior to the analyses using a standard petrographic microscope, which simplifies the search with the video imaging system of the LA stage.

In a first step, fluid inclusions are frozen quickly by lowering the sample temperature to ca. -100 $^{\circ}\text{C}$. Depending on the fluid inclusion chemistry, the temperature is subsequently raised to a temperature sufficiently below the solution's eutectic point, so that the inclusions remain entirely frozen. Reference materials were analyzed at the same temperatures since the tuning of the mass spectrometer is also performed under these conditions. For the synthetic fluid inclusions, the heating–freezing cell was set to -40 $^{\circ}\text{C}$, since they were generated from a simple binary $\text{NaCl-H}_2\text{O}$ fluid.

A gas blank of at least 40 seconds was recorded prior to each single analysis before the start of ablation. The scan speed for the raster pattern performed on the used SRM was set to 20 $\mu\text{m/s}$.

3.5 Data Processing

For calculation of trace element concentrations in fluid inclusions, it is necessary to separate the inclusion signal from the chemically distinct signal of the host mineral. We used the data reduction software SILLS (Guillong et al., 2008b), which is able to separate the short transient signal of the inclusion by a matrix correction. The software follows the procedures and equations from Allan et al. (2005), Halter et al. (2002), Heinrich et al. (2003) and Longerich et al. (1996). As silicon concentration in the inclusion is negligible compared to silicon in quartz, it was used as the matrix-only tracer. Three integration windows for background, matrix and inclusion signal were defined for each single analysis (Fig. 3.1). The length of the integrated inclusion signal was adjusted to that of Na, because Na was used as the internal standard for the quantification of the elemental concentrations. Sample compositions were calculated using the mass balance approach of SILLS.

As reported by Pettke et al. (2012) the best way to determine concentration values and analytical uncertainties for LA-ICP-MS analyses of fluid inclusions is to calculate the mean value and the external error from a batch of analysis of individual inclusions belonging to the same assemblage. The analytical error is based on the external precision (1SD) and is defined as the relative standard deviation (RSD) in %. Since all inclusions in our samples are considered to be chemically identical, we calculated the mean concentration and the RSD from all single analyses of one sample.

3.6 Accuracy and Precision

Synthetic inclusions were used to check the analytical precision and accuracy of the method. By dividing the measured concentration with the theoretical value of the starting solution used for the high pressure/high temperature (HP/HT) experiment, the relative accuracy of these measurements can be estimated. The experimental solution contains 24 elements from the MERCK™ VIII ICPMS-standard-solution with known concentrations (Tab. 3.3). However, only 10 of them could be recovered in the synthesized fluid

inclusions. The missing elements probably either reacted with the capsule material (e.g., the transition metals with Au or Pt) or have been enriched at the surface of the quartz host phase due to diffusive processes, like Li, Mg, Al and K. Consequently, the original concentration of $\sim 53 \mu\text{g/g}$ in the experimentally synthesized fluid inclusions was found for only a few elements (Fig. 3.3). The two samples *ID188-Au* and *ID189-Pt* were analyzed in separate sessions. In total 53 of 55 measured inclusions could be analyzed successfully. Only two inclusions that were located directly under the sample surface could not be used for quantification, as a matrix correction could not be performed due to the missing separation of the host mineral signal from the inclusion signal. Single values, which lie beyond the 2SD threshold, were considered as outliers and have not been used for the calculation of mean values and standard deviations (Suppl. Tab. 1 and Suppl. Tab. 2). Note that ^{195}Au and ^{197}Pt are not contained in the MERCK™ VIII standard solution and were likely leached out from the capsule material. The results for ^{11}B , ^{111}Cd , ^{125}Te , ^{203}Tl , ^{208}Pb , and ^{209}Bi (Fig. 3.3, Suppl. Tab. 1 and Suppl. Tab. 2) indicate that these elements have been nearly completely recovered in the synthetic fluid inclusions and were measured with an accuracy relative to the starting composition of the fluid of $> 90 \%$.

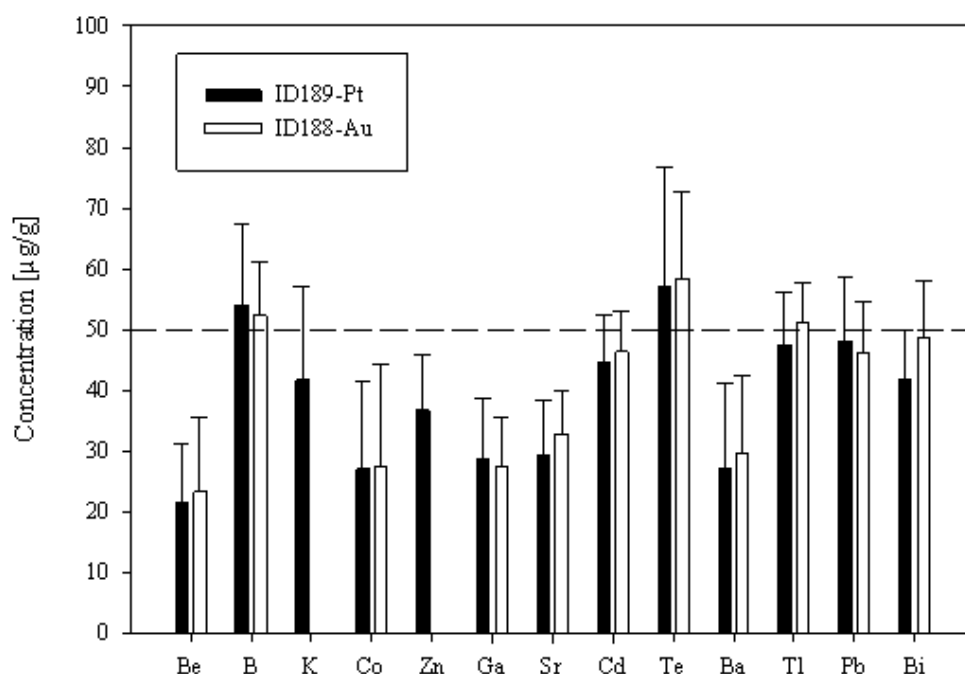


Fig. 3.3: Results of the analysis of synthetic fluid inclusions from experiment *ID188-Au* (white columns) and *ID189-Pt* (black columns). The dashed line represents the starting composition of the experimental fluid, which was identical for both experiments. Only B, K, Cd, Te, Tl, Pb and Bi (for *ID188-Au*) could be fully recovered in the inclusions. Error bars show 1SD of the mean values from all analyzed inclusions from the specific sample.

The calculated mean value for these elements is in accordance with the original fluid compositions and is within analytical uncertainties (1RSD), i.e., between 13 % (^{203}Tl) and 25 % (^{125}Te) for sample *ID188-Au* and 17 % (^{111}Cd) to 25 % (^{11}B) for sample *ID189-Pt* (Fig. 3.4). ^{39}K was only measured for sample *ID189-Pt* and could also be detected in the host mineral (quartz). After matrix correction, the determined K concentration of 42 $\mu\text{g/g}$ (RSD = 37 %) is in accordance with the original fluid. ^{64}Zn was only analyzed in some inclusions of sample *ID189-Pt*, with a mean value of 37 $\mu\text{g/g}$ (25 % RSD). The concentrations determined for ^9Be , ^{59}Co , ^{69}Ga , ^{88}Sr and ^{137}Ba in the synthesized fluid inclusions of both samples are significantly below the concentration of the original standard solution. Furthermore, the reproducibility of these elements was lower than that of the other elements in most cases. Beryllium, Co, and Ba show the highest variability with RSDs between 40 % and 60 %.

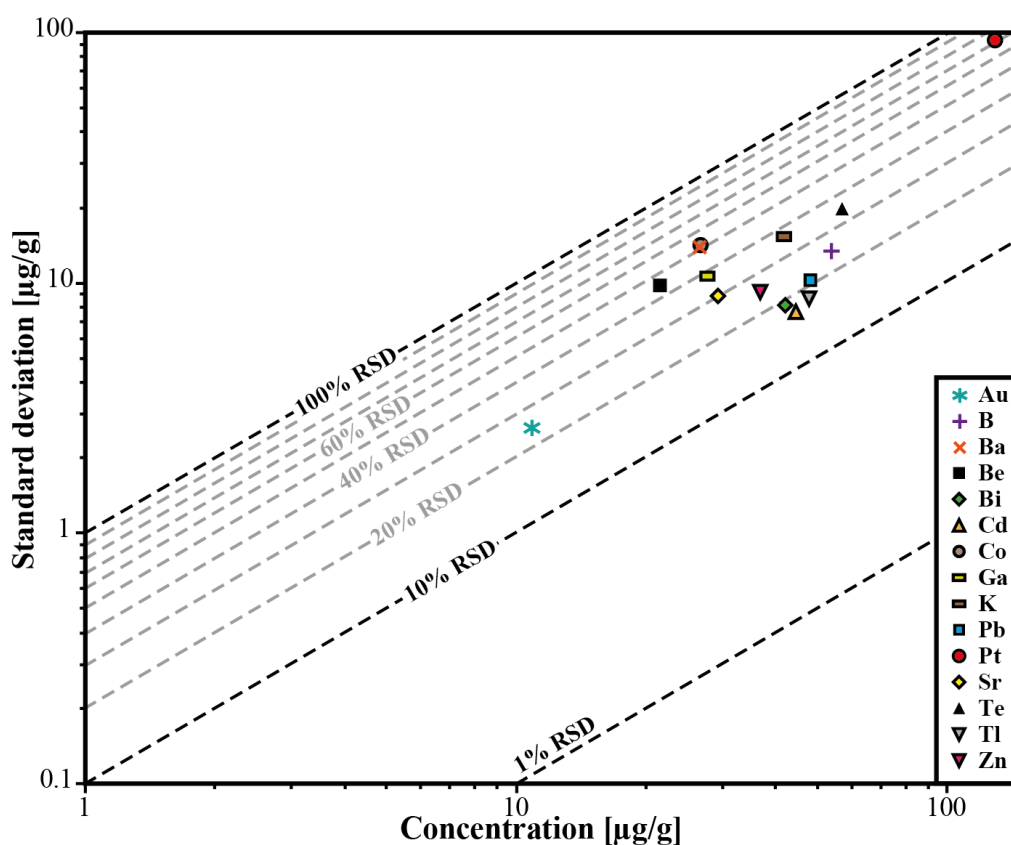


Fig. 3.4: Relative standard deviation for the determined concentrations in sample *ID189-Pt*. Pt and Au were not part of the stock solution and were leached out of the capsule material.

Gold and Pt have also been analyzed, because they were expected to be leached out of the capsule walls during the experiments. The inclusions in sample *ID188-Au*, which were

synthesized in gold capsules, contain 1.6 wt% Au (RSD = 29 %), which seems to be an extraordinary high value compared to Au concentrations in natural fluid inclusions that do not exceed the lower $\mu\text{g/g}$ range (Heinrich et al., 1999b; Ulrich et al., 2002). The mixture between the MERCK™ VIII solution, which is 1 M HNO_3 , and the NaCl-fluid may support the leaching of the capsule material during the experiments by formation of nitrohydrochloric acid, also known as “aqua regia”. Likewise, the inclusions in sample *ID189-Pt*, which were synthesized in platinum capsules, contain higher concentrations of Pt (124 $\mu\text{g/g}$), which is heterogeneously distributed (with 73 % RSD) and 11 $\mu\text{g/g}$ Au (RSD = 26 %). The inclusions can be separated into two groups with ~ 200 $\mu\text{g/g}$ and ~ 50 $\mu\text{g/g}$ Pt, respectively. Both groups show relatively homogeneous Pt concentrations with an RSD of 38 % and 34 %, respectively. This may indicate formation of two generations of fluid inclusions in experiment *ID189-Pt*, which can only be identified due to their Pt concentration since all other elements show similar values in both groups. None of the other analyzed elements, except Pt and Au, could be identified to originate from the capsule material.

3.7 Limits of Detection

The lower limits of detection vary for the measured isotopes over a range of three orders of magnitude (0.1 to 100 $\mu\text{g/g}$). They were calculated using the method reported by Pettke et al. (2012) for integration windows, based on the total signal length of Na.

The LODs are controlled by the laser repetition rate, the total integration time and the volume of the inclusions. Even though the differences in size of the analyzed inclusions are not large (8–26 μm), a significant correlation between LODs and inclusion size can still be observed (Fig. 3.5), which is the same for all analyzed elements. For lighter isotopes like ^{11}B or ^{39}K , the LODs vary between 4 $\mu\text{g/g}$ and 16 $\mu\text{g/g}$. Isotopes in the medium mass range like ^{59}Co , ^{69}Ga , or ^{88}Sr have LODs between 0.3 $\mu\text{g/g}$ and 1.8 $\mu\text{g/g}$. Heavy isotopes like ^{195}Pt and ^{209}Bi show the lowest LODs (0.09–0.6 $\mu\text{g/g}$). Furthermore, ^{195}Pt and ^{197}Au have been analyzed with a longer dwell time of 10 ms, resulting in a longer total integration time, which improved the lower limit of detection.

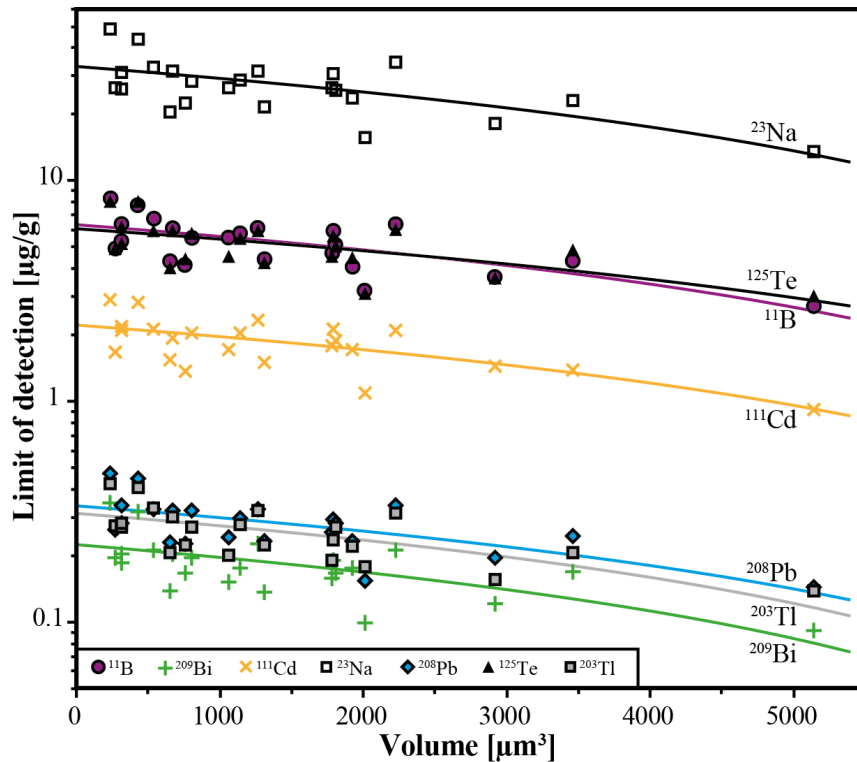


Fig. 3.5: Limits of detection as a function of the inclusion volume for the 6 completely transferred elements (B, Cd, Te, Tl, Pb, Bi) and Na from all individual analyses from sample *ID188-Au*.

3.8 Conclusions Regarding the Analytical Method

We have tested a new analytical setup for the determination of trace element concentrations in fluid inclusion with fs-LA-ICP-MS. Ablation with femtosecond laser pulses allows to analyze fluid inclusions in their frozen state. With this technique, 53 of 55 synthetic fluid inclusions in quartz, covering a size range between 8 μm and 25 μm and down to a depth of 50 μm , could be analyzed successfully. The 194 nm UV-fs-laser allows excellent control over the opening procedure of fluid inclusions. Due to the low thermal heat transfer onto the sample surface the inclusions do not melt while the sample material is mobilized. It is even possible to measure very shallow inclusions that frequently explode under room temperature conditions with a nanosecond laser, resulting in material loss during analysis.

The use of a fast scanning magnetic sector field ICP-MS with a SEM (Secondary Electron Multiplier) and a Faraday detector allows the detection of elements across the concentration range from $\mu\text{g/g}$ to wt%. The lower limits of detection for fluid inclusion analysis vary between 0.1 $\mu\text{g/g}$ (for ^{209}Bi) and 10 $\mu\text{g/g}$ (for ^{39}K). The detection of 20

isotopes over the whole mass range takes 477 ms. The typical analytical uncertainty ranges between 15 % and 30 % (1RSD). This is a significant improvement in precision compared to earlier studies for samples with such low concentration levels. Elements from the stock solution, which did not react with the capsule material or host mineral during the HP/HT experiments, could be fully recovered in the synthetic fluid inclusions at their original concentrations. The results illustrate that our method is able to produce adequate data from natural fluid inclusions.

With respect to the time-consuming work for preparation and characterization of fluid inclusion studies, especially microthermometry, our method offers a highly efficient tool for solute quantification in fluid inclusions with a success rate of > 90 %. First tests with natural inclusions in quartz have shown that the success rate can be expected to be similar to our results. Given that most natural samples often host only very few inclusions of sufficient size to be analyzed ($\geq 10 \mu\text{m}$), this method provides new possibilities for fluid inclusion studies. The applicability of our approach to the widespread UV-ns-LA systems needs to be tested. If successful, it may become a useful tool for the opening of fluid inclusions by LA-ICP-MS analysis.

4 The Experimental Method – Experimental Tests on Achieving Equilibrium in Synthetic Fluid Inclusions

The following chapter is based mostly on the author's publication Derrey et al. (2017).

4.1 Experimental Procedure

4.1.1 General Experimental Procedure

All experiments were conducted in the Institute of Mineralogy at Leibniz University Hannover, Germany, in two RH/RQ-CSPVs of the design described in Matthews et al. (2003). Argon was used as pressure medium and the experimental temperature and pressure conditions were $T = 400\text{-}800\text{ }^{\circ}\text{C}$ and $P = 100\text{-}300\text{ MPa}$, with uncertainties of $\pm 5\text{ }^{\circ}\text{C}$ and $\pm 5\text{ MPa}$, respectively. The external oxygen fugacity ($f\text{O}_2$) of the system was determined to be ca. $\text{NNO}+2.3$ (i.e., 2.3 log units above the Ni-NiO buffer; Berndt et al., 2001). Solid buffer assemblages were used to buffer oxygen (and in some cases sulfur) fugacity and were analyzed after the run at the Federal Institute for Geosciences and Natural Resources (BGR) by X-ray diffraction (XRD) to check if all buffer phases were still present at the end of the experiment. Capsule preparation for fluid inclusion synthesis generally followed the workflow described by Bodnar et al. (1985) with some modifications, which will be described below. Cylinders of 2.5 mm in diameter and ca. 2 mm in length were drilled out of inclusion-free alpine quartz. The cylinders were cleaned in concentrated HCl for 30 minutes and in an ultrasonic bath with distilled water for 5 minutes. After specific pre-treatments, described below and in Fig. 4.1, quartz cylinders were placed in Au capsules of ca. 25 mm length, 3.2 mm outer diameter and a wall thickness of 0.2 mm together with NaCl-solutions of different salinities, different mineral powders, and silica gel to accelerate crack healing (for details see setup descriptions). The NaCl-solutions were spiked with ca. 400 ppm Rb and 400 ppm Cs (exact concentrations were calculated by gravimetry and confirmed by ICP-MS) and were used as internal standard during LA-ICP-MS analysis (also see method in Duc-Tin et al. (2007)).

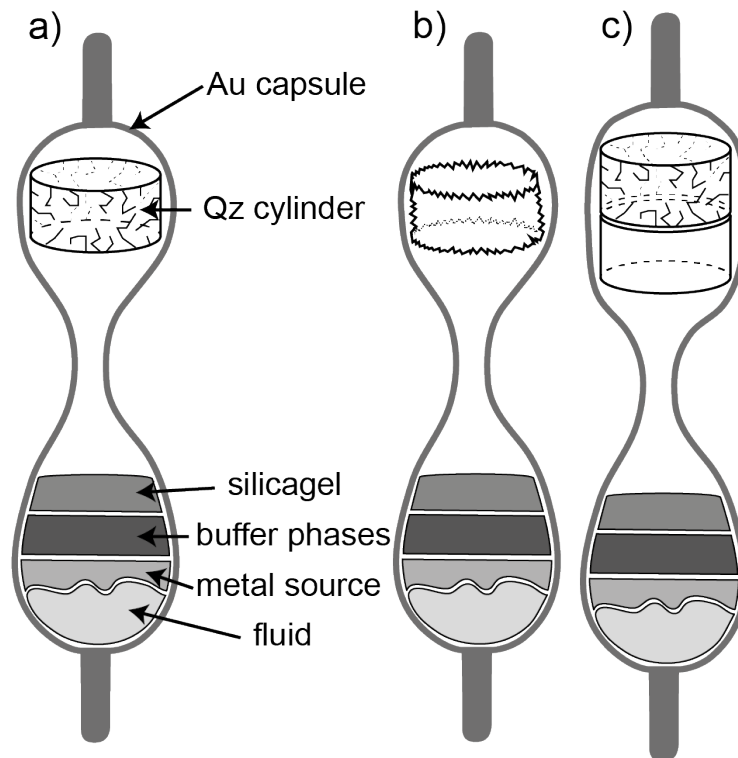


Fig. 4.1: Different capsule designs: a) with quartz cylinder, which was pre-fractured at 350 °C and put into concentrated HF for 10 min, b) with quartz cylinder etched in concentrated HF for 30 min, c) with two quartz cylinders, one of which was pre-treated as in a) and the other was cleaned in HCl only; note that all capsules were crimped in the center, so that the quartz cylinder(s) were not in direct contact with the other phases of the experimental charge prior to the experiment. All capsules contained aqueous fluid with different NaCl concentrations, one or several ore minerals as metal source, silica gel to enhance quartz healing as well as a solid mineral buffer assemblage to buffer fO_2 and in some cases fS_2 . Gold capsules served as a source for Au in the experiments.

Capsules were pressurized to the desired experimental pressure at room temperature and then rapidly moved to the preheated hot zone of the autoclave using the rapid heat device of the CSPV. The heating of the capsules to the target T occurred rapidly, within a few minutes, at isobaric conditions. In some experiments, the Au capsule was quenched quickly during the experiment by pulling the capsule from the hot end of the vertical autoclave to the water-cooled end to cause cracks within the quartz cylinder as a result of thermal stress (Li and Audétat, 2009). After this “intermediate quench” step of a few seconds, the capsule was moved back to the hot zone of the furnace. After a desired runtime, the autoclave was pulled out of the furnace and slowly cooled to room temperature (ca. 30 °C/min in the temperature range 800 – 300 °C) to avoid unnecessary cracking of the quartz chip. The capsules were weighed to check for potential leaks during the run. The recovered quartz cylinders were cleaned, dried and embedded in araldite to be cut and polished to chips of ca. 300 µm thickness.

4.1.2 Setup 1: Experimental Approach for Equilibration Tests at 800 °C

To identify the most reliable technique to synthesize fluid inclusions equilibrated with metal-bearing phases, we compared the methods of Sterner et al. (1988), Zhang et al. (2012) and Zajacz et al. (2010) that were described above. Each test was conducted in a Au capsule containing molybdenite (MoS_2) and scheelite (CaWO_4) as metal sources, an 8 wt% NaCl solution and silica gel powder.

Experiment A: For pressure-cycling experiments, we used quartz cylinders that were previously heated to 350 °C in a muffle type furnace, quenched in distilled water, dried and immersed in concentrated (40 wt%) hydrofluoric acid (HF) for 10 minutes to widen the cracks. According to the design in Fig. 4.1a, one quartz cylinder was placed in a Au capsule together with 25 μl of NaCl solution, 5-15 mg of each mineral powder, ca. 50 mg PPM buffer (mixed in weight ratio 1 pyrite : 3 pyrrotite : 1 magnetite) and 3-5 mg of silica gel powder.

Experiment B: Capsules for experiments of the design of Zhang et al. (2012) were prepared in the same way, but quartz cylinders were not cracked thermally and only immersed in concentrated HF for 30 minutes to produce cavities along the surface of the quartz cylinder (Fig. 4.1b).

Experiment C: Capsules that were designed according to Zajacz et al. (2010) contained two quartz cylinders on top of each other (Fig. 4.1c), one was pre-treated in the same way as in *Experiment A* (*C_1*) and one was not pre-treated, except for HCl cleaning in an ultrasonic bath (*C_2*).

Experiment A was started as described above. Once the sample was moved into the hot zone, which was pre-heated to 800 °C, pressure (which was previously set to 200 MPa) was cycled from 150 MPa to 250 MPa for five times every 10 minutes for a total time span of 8 hours. After pressure cycling, pressure was held constant at 200 MPa for three days before the capsule was quenched slowly.

For *experiments B and C*, the capsules were moved into the hot zone of the pre-heated (800 °C) and pre-pressurized (200 MPa) autoclave. After two days at constant P and T, an intermediate quench was conducted for approximately 10 seconds. The capsules were then moved back and left in the hot zone for another three days before quenching slowly.

4.1.3 Setup 2: Experimental Approach to Test the Efficiency of an Intermediate Quench for Re-opening of Fluid Inclusions Formed at 600 °C

In this approach, we tested to which extent the application of an intermediate quench is successful for re-opening fluid inclusions. In the first phase of the experiment, the temperature was fixed to 600 °C (200 MPa). After the intermediate quench, temperature was set to 400 °C before the capsule was reentered into the hot zone. In this way, we were able to distinguish easily between fluid inclusions formed before (600 °C) and after the intermediate quench (400 °C) via microthermometry. To investigate the possible influence of different quartz pre-treatment, each experiment was performed with two capsules: one containing a quartz cylinder pre-treated as in *experiment A* (cracked at 350 °C plus 10 min in HF) and one containing quartz pre-treated in the traditional way described by Sterner and Bodnar (1984), who only cracked the quartz thermally at 350 °C. With the two different types of pre-treated quartz cylinders, a series of 2 x 3 Au-capsules were prepared containing 2.5, 5 and 10 wt% NaCl solution and 2-6 mg silica gel powder. After 7 days at 600 °C, the samples were quenched rapidly and left in the cold zone of the autoclave until the furnace had cooled nearly isobarically to 400 °C. The samples were then placed back into the hot end of the autoclave, where they were left for 13 days at 400 °C before the experiment was terminated with a slow quench.

4.1.4 Setup 3: Dissolution Kinetics and Time-Dependent Experiments

To assess the time necessary to form inclusions in pre-cracked quartz and to equilibrate molybdenite, scheelite and gold with fluids at 800 °C, we designed a series of experiments at 200 MPa with runtimes ranging from 1.8 to 100 hours. For each investigated run duration two gold capsules were prepared, one containing molybdenite and the other one containing scheelite as mineral powder. The capsule design was such that one quartz cylinder (pre-treated as in *experiment A*: thermally cracked at 350 °C plus 10 min in concentrated HF) was placed in a Au capsule together with 25 µl of an 8 wt% NaCl solution, 5-15 mg of the respective mineral powder, ca. 50 mg PPM buffer and 3-5 mg of silica gel powder. Experiments were run as described above without an intermediate quench and the results compared to experiments from setup 1. Accounting for the exponential character of dissolution processes, the different runtimes were chosen to be evenly distributed when plotted logarithmically (c.f., Fig. 4.6).

4.2 Results

Fluid inclusions recovered from equilibration test and time-dependent runs (setup 1 and 3) were analyzed for their major and trace element contents by LA-ICP-MS, as described in Chapter 3. The method was slightly adjusted by mixing the helium carrier gas with 2 vol% hydrogen to adjust the hydrogen flow rate to ca. 5-6 ml/min as suggested by Guillong and Heinrich (2007) to increase the sensitivity of the method. Analyses were performed at a temperature of -60 °C, which guarantees completely frozen fluid inclusions prior to the ablation. NIST610 glass was used as external standard (using reference values of the GeoReM database (Jochum et al., 2005)) and measured with a repetition rate of 10Hz after every fourth inclusion. To evaluate the acquired data, the SILLS data reduction software (Guillong et al., 2008b) was used, which is particularly suitable for the interpretation of fluid inclusion signals. The known Cs concentration of the starting fluid was used for internal standardization and compared to Rb and Na concentrations, which were also known. Fluid inclusion analyses in which the Rb/Cs-ratio deviated by more than 10 % and/or the Na/Cs-ratio by more than 20 % were discarded as they are considered to represent analyses of poor quality (Zhang et al., 2012).

Fluid inclusions from experiments testing the efficiency of an intermediate quench (setup 2) were examined by microthermometry using a Linkam FTIR600 heating-freezing stage. About 30 fluid inclusions were analyzed from each quartz chip. Final ice melting temperatures (T_{m-ice}) were determined to check, if the resulting salinities corresponded to the weight salinities of the different starting fluids. Homogenization temperatures (T_{hom}) were determined to distinguish between fluid inclusions that formed prior to (600 °C, 200 MPa) and after the intermediate quench (400 °C, 200 MPa). The expected T_{hom} were calculated using the SoWat code, which comprises the data of Driesner (2007) and Driesner and Heinrich (2007).

4.2.1 Setup 1: Equilibrations Tests

All experimental run products from setup 1 contain abundant synthetic fluid inclusions varying in size from a few μm to more than 100 μm (for examples see Fig. 4.2). Whereas the experimental designs *B* and *C_1* produced a large amount of fluid inclusions with

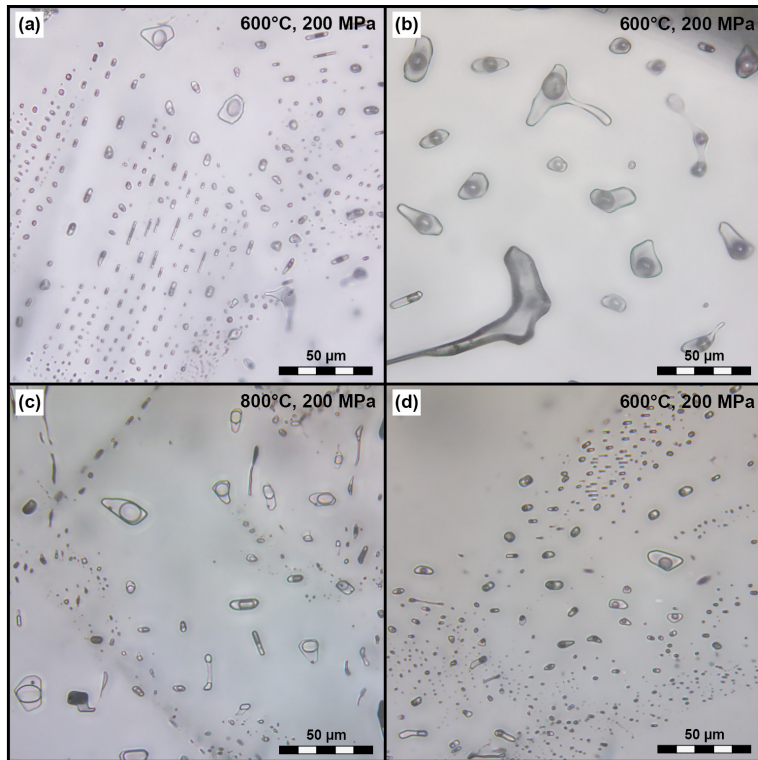


Fig. 4.2: Typical appearance of synthetic fluid inclusions formed (a) at 600 °C and 200 MPa in quartz that was only pre-cracked at 350 °C, (b) at 600 °C and 200 MPa in quartz that was pre-cracked at 350 °C and immersed in concentrated HF for 10 minutes, (c, d) in-situ by an intermediate quench in a previously not fractured quartz at (c) 800 °C and (d) 600 °C and 200 MPa.

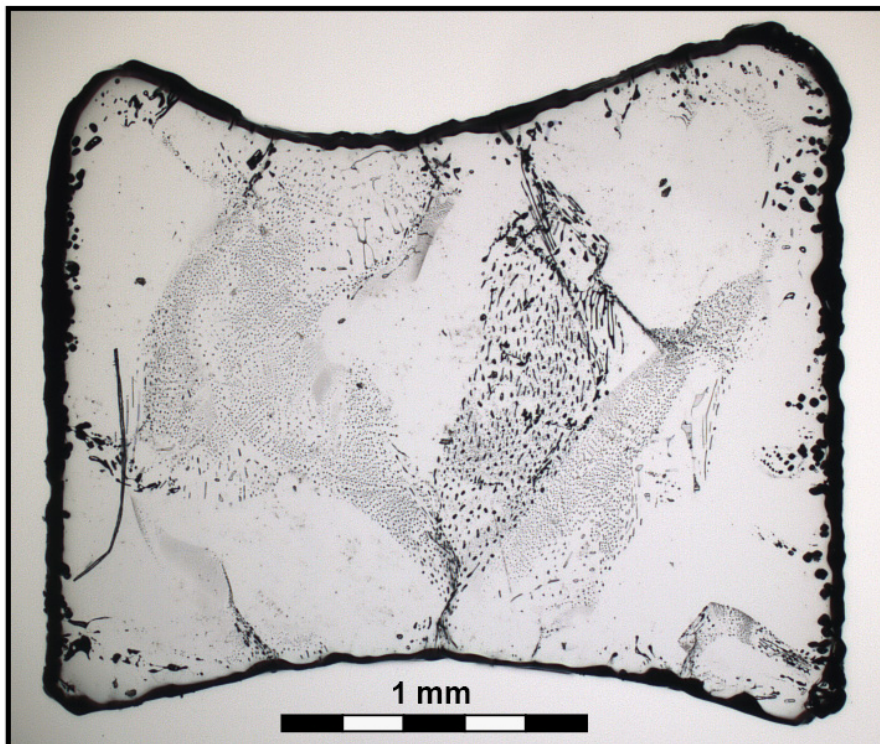


Fig. 4.3: Polished section of quartz chip from pressure cycling experiment A. Note the concave top and bottom faces of the cylinder, which were roughly parallel to each other prior to the experiment.

many of them in the preferable range for LA-ICP-MS analysis ($> 10\mu\text{m}$), designs *A* and *C*₂ contain on average smaller and fewer fluid inclusions, but still abundant and large enough for analysis. Quartz chips made from cylinders from design *A* (pressure cycling) appeared to be slightly deformed after the experiments (Fig. 4.3).

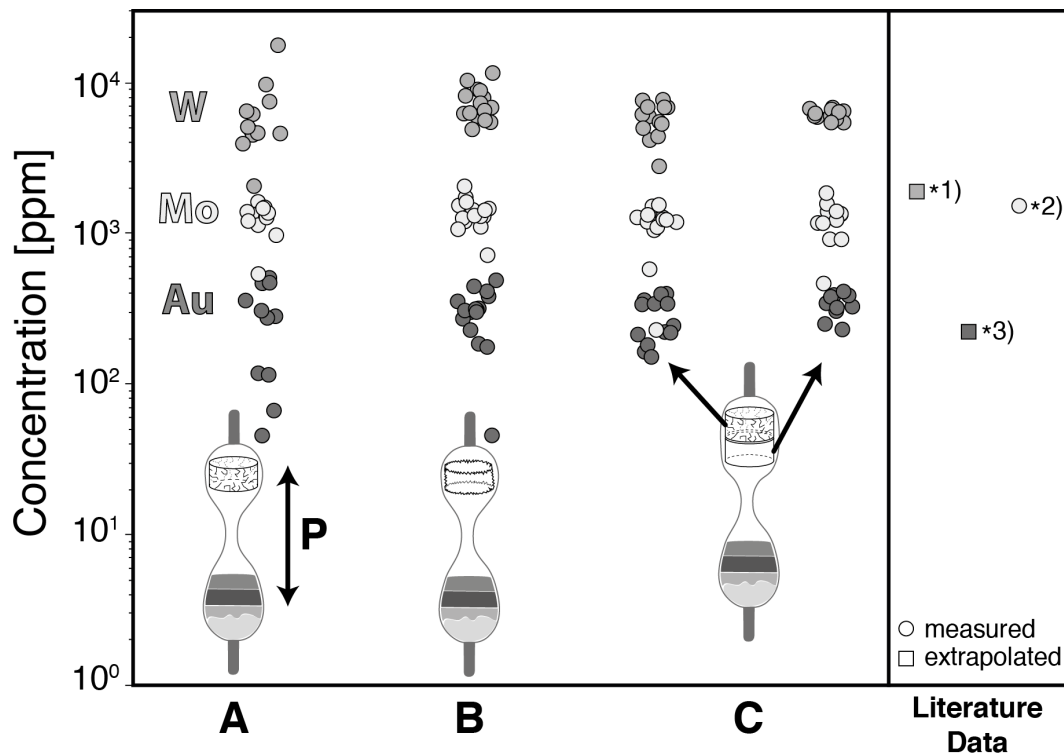


Fig. 4.4: Results from setup 1 (equilibrations tests) using different approaches: Fluid concentrations of W from scheelite dissolution, Mo from molybdenite dissolution and Au from metallic gold dissolution at 800 °C, 200 MPa, 8 wt% NaCl and f_{O_2} and f_{S_2} conditions buffered with Pyrite - Pyrrhotite - Magnetite (PPM). *Experiment A:* results from pressure cycling experiment (150 MPa to 250 MPa for five times every 10 minutes for 8 hours, followed by 3 days at 200 MPa) with pre-cracked (350 °C to room temperature) and pre-etched (10 min in concentrated HF) quartz cylinder, *Experiment B:* results from experiment with pre-etched (30 min in concentrated HF) quartz cylinder and intermediate quench (2 + 3 days), *Experiment C:* results from experiment with two quartz cylinders (left/top: pre-cracked and pre-etched (350 °C to room temperature followed by 10 min in concentrated HF), right/bottom: not pre-treated) and intermediate quench (2 + 3 days), Literature Data: *1) W concentration extrapolated to 800 °C using data from Foster (1977, 252-529°C, 100-200 MPa, muscovite - K-feldspar - quartz buffer + 1 M KCl, metal source was also scheelite), *2) measured Mo concentration from Zhang et al. (2012, 800°C, 200 MPa, PPM buffer, 8 wt% NaCl, metal source: molybdenite), *3) Au concentration extrapolated to 800 °C using data from Loucks and Mavrogenes (1999, 625-725°C, 110 MPa, PPM buffer, 1 m HCl, metal source: metallic gold).

The outcome of the different experimental designs to achieve equilibrium between solid phases and fluid are shown in Fig. 4.4 and mean values including standard deviations are summarized in Tab. 4.1. Metal concentrations in fluids from all experimental designs are in the same range within error and correspond to approximately 6000 ppm W for scheelite-bearing samples, 1300 ppm Mo for molybdenite-bearing samples and 300 ppm

Au, clustering within a standard deviation range of ca. 10 – 25 % (cf., Tab. 4.1). The pressure cycling experiment (design A), however, resulted in fluid inclusions with a larger range in the analyzed concentrations (at least for W and Au).

Tab. 4.1: Summary of experiments from setup 1 and respective results. W, Mo and Au concentrations are given in ppm by weight.

#	Type	T [°C]	P [MPa]	Composition	logfO ₂ [bar]	logfS ₂ [bar]	n	W [ppm] in fluid		Mo [ppm] in fluid		Au [ppm] in fluid	
								Mean	Stdev	Mean	Stdev	Mean	Stdev
A	P-cycling	800	200	8 wt% NaCl, Mol, Sch, PPM	-11.2	0.4	11	6370	4000	1320	180	270	160
B	HF pretreatment	800	200	8 wt% NaCl, Mol, Sch, PPM	-11.2	0.4	15	7370	1740	1400	250	330	80
C_1	350 °C + HF	800	200	8 wt% NaCl, Mol, Sch, PPM	-11.2	0.4	13	5900	1280	1260	140	280	90
C_2	not pre-treated	800	200	8 wt% NaCl, Mol, Sch, PPM	-11.2	0.4	12	6100	470	1290	270	330	60

4.2.2 Setup 2: Role of the Intermediate Quench

Fluid inclusions in quartz cylinders, which were not only cracked at 350 °C but additionally etched in concentrated HF are considerably larger (many inclusions > 20 µm; Fig. 4.2b) than those from cracked cylinders without etching (usually < 20 µm, mostly < 10 µm; Fig. 4.2a). Furthermore, no fluid inclusions that formed at 400 °C were measurable in the latter cylinders. Inclusions that formed in cracked and etched quartz cylinders show clearly two distinct groups with different T_{hom}, which can be related (after pressure correction according to Driesner and Heinrich (2007)) to the two different formation temperatures of 600 °C and 400 °C (Fig. 4.5, Suppl. Tab. 3 in the Appendix). Both generations can be distinguished easily by their different T_{hom} via microthermometry, but it was not possible to distinguish the two generations optically, which is in contrast to the observation of Zhang et al. (2012), who used an identical temperature of 800 °C prior and after the intermediate quench. Fluid inclusions that formed at 600 °C and 400 °C could not be distinguished according to their distribution in the quartz chip, as they occur

adjacent to each other in all parts of the quartz (from center to rim) with no obvious relation to certain areas or surfaces.

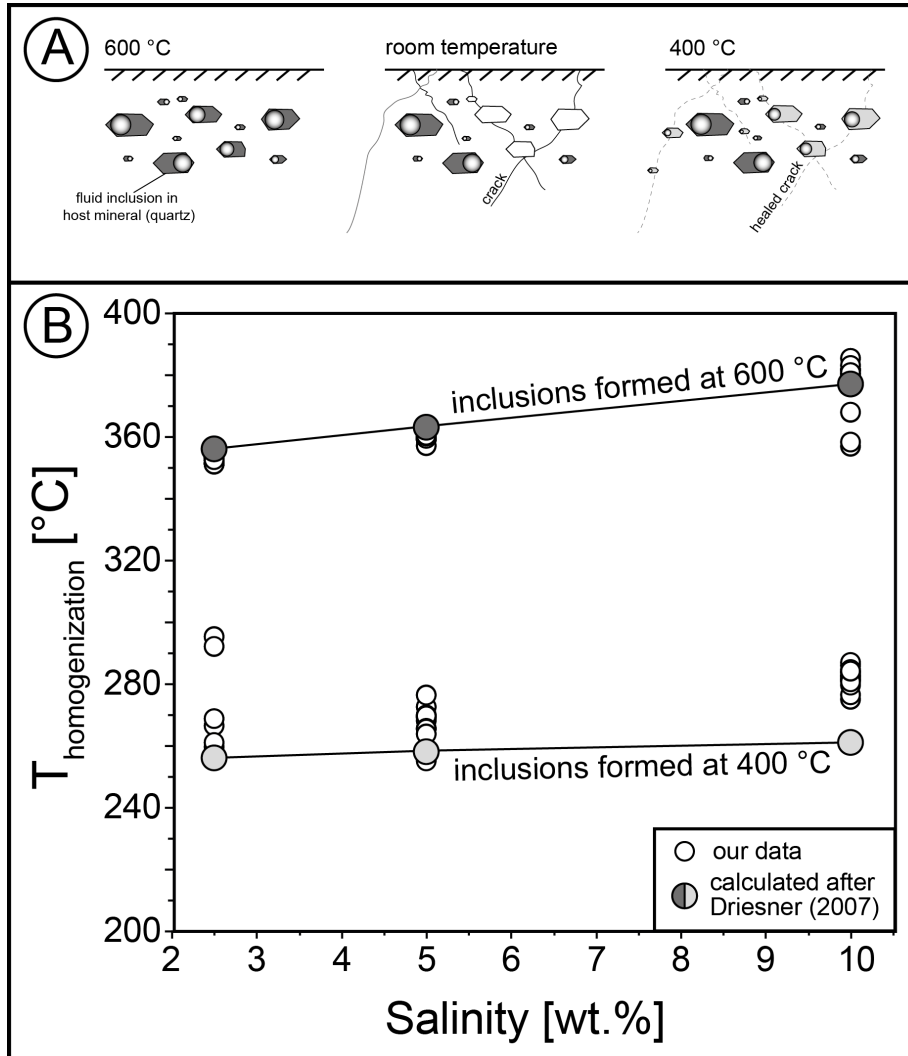


Fig. 4.5: A) Strategy applied to test the role of intermediate quench on fluid inclusion formation (setup 2). From left to right: 1. Formation of fluid inclusions in pre-treated (pre-cracked at 350 °C and immersed in concentrated HF for 10 minutes) quartz cylinder at 600 °C (200 MPa) – 2. Intermediate quench of the sample from 600 °C to room temperature, leading to the formation of new cracks and opening of some of the early formed fluid inclusions – 3. Formation of new and refilled fluid inclusions at 400 °C by healing of the newly formed cracks. B) Results from setup 2: Measured homogenization temperatures (T_{hom}) of fluid inclusions in our three samples versus fluid salinity (white circles). Grey circles depict calculated T_{hom} for 400 °C (light grey) and 600 °C (dark grey) and 200 MPa for the different fluid salinities after Driesner (2007).

4.2.3 Setup 3: Time-dependent Experiments

Fig. 4.6 depicts the results of the time-dependent experiments (summarized in Suppl. Tab. 4 in the Appendix). Even in the two shortest runs (1.8 h and 3.2 h) abundant fluid inclusions were trapped in the quartz crystals, but they are considerably smaller (mostly

< 10 μm , few inclusions between 10 – 20 μm) than those from longer runs, resulting in larger analytical errors due to insufficient counting statistics. In this experimental series, no intermediate quench was performed, so that the large range in concentrations of one element in fluid inclusions within one sample is primarily interpreted to represent true variations due to different times of entrapment rather than analytical error. Fluid inclusions which formed early in the experiment are expected to show non-equilibrated metal concentrations.

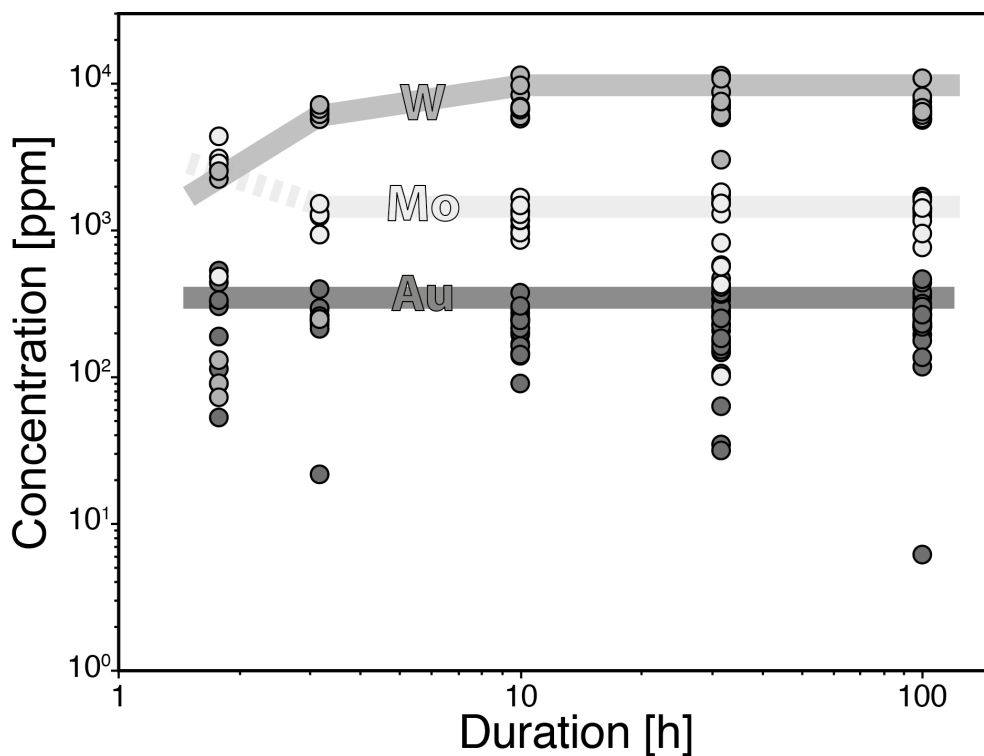


Fig. 4.6: Results from setup 3 (time-dependent experiments): concentrations of W from scheelite dissolution (medium grey circles), Mo from molybdenite dissolution (light grey circles) and Au (dark grey circles) from native gold dissolution after different runtimes (1.8 to 100 h) at 800 °C, 200 MPa, 8 wt% NaCl and f_{O_2} and f_{S_2} conditions buffered with the PPM buffer. Transparent lines roughly trace the development of maximum metal concentrations with time. See text for discussion of initially higher Mo values (indicated by dashed line).

Fig. 4.6 demonstrates that the highest Mo and Au concentrations are in the same range in all experiments (except for the shortest run where Mo concentrations are higher), independent on the run duration. This indicates that equilibration of fluids with respect to molybdenite and gold is reached fast within the first few hours of the experiment. On the other hand, the maximum W concentrations increase within the first hours and remain constant after approximately 10 hours.

4.3 Discussion

In the following the outcomes of the experiments are used to discuss the best approach for the synthesis of equilibrated fluid inclusions.

4.3.1 Size and Number of Fluid Inclusions

When preparing mineral cylinders to trap hydrothermal fluids during an experiment, we suggest a pre-treatment of cylinders by both thermal cracking (10 min. at 350 °C followed by quench in room temperature distilled water) and immersion in concentrated HF for 10 minutes. If quartz is pre-treated in this way, the formation of the highest number of fluid inclusions (compared to pre-treatment with HF only) is observed and fluid inclusions have a considerably larger size (compared to quartz that was only thermally-cracked). This becomes especially important in experiments at lower temperatures because fluid inclusions are usually too small for LA-ICP-MS (ca. < 10 µm) or even microthermometry (ca. < 5 µm) under these conditions. Furthermore, our experiments from setup 1 showed that fluid inclusions in both thermally cracked and HF-etched quartz are more prone to in-situ fracturing by an intermediate quench, which becomes especially important in experiments with long equilibration times.

4.3.2 Dissolution Kinetics

From the time-dependent experimental series (setup 3) for the dissolution of molybdenite, scheelite and gold we gained two main insights, which are: 1) that fluid inclusions start to form almost instantaneously (< 1.8h) under the applied conditions and 2) that dissolution of the investigated metal-bearing phases at 800 °C is fast. As the metal concentrations from setup 3 are very similar to those from setup 1 (equilibration tests; cf. Fig. 4.4 and Fig. 4.6), it can be concluded that equilibrium of the fluid was reached in the time scale of a few hours (< 1.8 h to ca. 10 h). Thus, although the fast formation of inclusions at 800 °C has a negative influence on the formation of equilibrated fluid inclusions, this effect is reduced by the fact that metal dissolution is comparably fast. The fast entrapment of fluid inclusions in quartz emphasizes the importance of a rapid heating autoclave, which keeps the time until the experimental temperature in the capsule is reached at a minimum.

It is known that quartz solubility depends on the salinity of the fluid (e.g., Akinfiyev and Diamond, 2009; Newton and Manning, 2000), which possibly influences the velocity of crack healing. Our time dependent series was conducted with an 8 wt% NaCl fluid. According to Newton and Manning (2000) at this salinity and our experimental P-T-conditions (800 °C, 200 MPa) quartz solubility is close to its maximum. Thus, any deviation in the salinity of the fluid would lead to a decrease in quartz solubility. So, if there were an effect, it would likely be a delay of crack healing, which would be advantageous for reaching equilibrium prior to entrapment of the fluid.

Whereas molybdenite and gold appear to dissolve and equilibrate very fast (faster than our shortest experimental run, with an apparent oversaturation of molybdenite in the shortest run), maximum W concentrations from scheelite dissolution rise from ca. 2400 ppm after 1.8 h to ca. 7300 ppm within the first 10 hours, before they remain constant (Fig. 4.6). This might be due to the more covalent bonding of W in the tungstate molecule and concomitant slower dissolution kinetics compared to Mo from molybdenite and Au from native gold. Additionally, different crystal structure and chemical composition of scheelite, including Ca as an additional cation, likely influences dissolution kinetics. Fast equilibration of Au concentration was also shown by Benning and Seward (1996), who determined Au equilibration times of roughly 3 days at 150 °C, 1.5 days at 200 °C, 1 day at 300 °C and “a few hours” at 500 °C. Exponential extrapolation of this dataset results in an equilibration time of < 1h at 800 °C, which is in perfect agreement with our findings.

Our results indicate that time dependent series similar to ours are useful to get an estimate of optimal run durations needed to equilibrate the system of interest with respect to all phases including buffers. Findings of Zajacz et al. (2010) showed that there are cases where equilibration might take longer, e.g. due to a slowly adjusting buffer. In their experiments, this occurred in a case study where a large amount of H₂ had to diffuse out of the gold capsule to achieve redox equilibrium and crack healing was apparently faster than the time needed to equilibrate the system. As a result, the compositions of fluid inclusions were different in a pre-treated and in a previously not fractured and in-situ quenched quartz chip. However, in most systems metal concentrations seem to equilibrate fast enough to be studied by the synthetic fluid inclusion technique, which is also supported by the findings of Simon et al. (2007). According to them, quartz crack healing is slow enough to allow the entrapment of fully equilibrated fluids at 800 °C and 100 MPa in the haplogranite – magnetite – gold – NaCl – KCl – HCl – H₂O system, but no

estimate of crack healing time is given. Simon et al. (2007) further highlighted the importance of a low thermal gradient ($\leq \pm 5$ °C) across the experimental charge to prevent the formation of a rapidly precipitating primary quartz overgrowth. We determined a temperature gradient of $\leq \pm 2$ °C over the length of 3 cm for our experimental charges.

4.3.3 Importance of Intermediate Quench

As shown by Zhang et al. (2012), Zajacz et al. (2010) and this study, an intermediate quench (i.e., in-situ quartz cracking) after a sufficient equilibration time will lead to the smallest scatter in metal concentrations in the resultant fluid inclusions. In our equilibration tests at 800 °C, the best results were achieved with fluid inclusions formed after an intermediate quench in quartz cylinders which were not pre-treated (Fig. 4.4, design C_2). This could be expected, as this approach is the only design in which inclusions cannot form before the intermediate quench (we did not observe formation of quartz overgrowth which could have led to entrapment of primary fluid inclusions). The drawback of this method is that it gets increasingly less effective at lower temperatures. Thus, the design C_2 is appropriate and recommended for experiments at rather high temperatures (1000 °C, Zajacz et al. (2010); 800 °C, this study).

From our experience, it was only possible to induce enough cracks in quartz and to produce fluid inclusions sufficiently large for LA-ICP-MS analysis by an intermediate quench down to a temperature of ca. 600 °C. Below 600 °C only few and very small inclusions form in the un-fractured quartz and such inclusions were not suitable for LA-ICP-MS analyses. Fig. 4.2c) and d) show the different appearance of fluid inclusions formed in an un-fractured quartz chip by an intermediate quench at 800 °C and 600 °C, respectively. Both, the abundance and size of synthetic fluid inclusions decrease rapidly with decreasing temperature. Thermal cracking is further hindered by the use of double capsules (Eugster, 1957 and publications thereafter), which makes in-situ cracking less effective than in single capsules. Therefore, in-situ cracking of initially un-fractured quartz by an intermediate quench should be the method of choice for synthesis of fluid inclusions at high temperatures, but it is less useful at temperatures below 600 °C. In any case, it is recommended to add a pre-treated quartz (of design B or C_1) to the capsule to ensure the formation of sufficient fluid inclusions of optimal size, which can then be compared to inclusions from initially un-fractured quartz. In our experiments, the results from design B and C_1 show only minor deviation from results of design C_2 with not pre-

treated, in-situ cracked quartz, but a larger range in the individual analyses (Fig. 4.4). However, both designs are recommended for experiments below 600 °C, as they will ensure the formation of adequate fluid inclusions down to at least 400 °C. Our experiments testing the re-opening of fluid inclusions after an intermediate quench showed that in-situ quenching and subsequent formation of new fluid inclusions works down to at least 600 °C (Fig. 4.5B). The replacement of fluid inclusions, however, only occurs partly and we were not able to distinguish optically between fluid inclusions that formed prior to and after the intermediate quench. Thus, the interpretation of LA-ICP-MS analyses of fluid inclusions that formed after the intermediate quench may be difficult. The yield of equilibrated fluid inclusions might be increased by quenching the sample in-situ several times in short succession (R. Linnen, personal communication).

4.3.4 Limitations of Pressure Cycling

Equilibration design *A* (pressure cycling) does not seem suitable for our conditions, as the metal concentrations in fluid inclusions show the largest range (but comparable mean values, Fig. 4.4). This is interpreted to be due to several factors: One possible reason could be that the duration of pressure cycling (8 hours) was too short for the metal concentrations to equilibrate. But this interpretation is not confirmed by the results from the time-dependent experiments, at least for Mo and Au (Fig. 4.6). A second possible explanation is that some inclusions with low metal concentrations formed in the very early stages of the experiment and were not re-opened despite of pressure cycling. Possibly, a higher total pressure difference is needed (as applied by Sterner et al. (1988)) to change the fluid density enough to prevent the cracks from healing. Yet another explanation would be that some inclusions decrepitated as a result of pressure variation, which may explain anomalous high and low metal concentrations. The observed change in shape of the quartz cylinders after the experiment (Fig. 4.3) might be due to deformation of the quartz during the experiment, which may indicate that partial decrepitation occurred during pressure cycling. This would imply that a temperature of 800 °C is too high for pressure cycling experiments, as the quartz crystal becomes ductile and deforms in response to the oscillating pressure. However, no decrepitation of fluid inclusions was observed under the microscope and the observed change in shape could also be the result of quartz overgrowth along preferred crystallographic orientations. Fluctuations in quartz solubility during pressure cycling may have resulted in enhanced

dissolution and reprecipitation of quartz. At lower T this effect should also be minimized so that, with an appropriate cycling period and pressure difference, this method might be the method of choice for some applications at low temperatures, as for example described by Sterner et al. (1988). The use of a different host mineral, which is less soluble than quartz at high temperatures, could possibly expand the applicability of this method to higher temperatures.

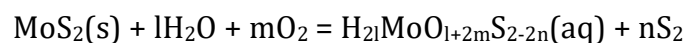
4.3.5 Discussion of Au, Mo and W Concentrations in Fluids in Equilibrium with Au Metal, Molybdenite and Scheelite

As Au and Mo concentrations in fluid inclusions from all experimental designs are identical within error (except for the shortest run from setup 3, where Mo concentrations are higher) and are in the same range as the maximum concentrations determined in the time-dependent experiments, they are interpreted to represent concentrations in 8 wt% NaCl fluids in equilibrium with Au metal and molybdenite at 800 °C, 200 MPa and PPM buffered conditions. Comparing maximum W concentrations from the equilibration tests and time-dependent experiments, it is noticeable that W concentrations are slightly lower in the former (ca. 6100 ppm versus ca. 7300 ppm). This might be a result of the relatively large scatter of W concentrations (standard deviation ca. 2000 ppm) in the time-dependent experiments, which were performed without an intermediate quench. However, the difference in the capsule design between the two setups is that in the equilibration tests scheelite and molybdenite were placed together in the same capsule, whereas capsules with either scheelite or molybdenite were prepared for the time dependent experiments. Therefore, W solubility could be dependent on Mo in the system, whereas Mo concentrations do not change notably between both experimental designs and are in the order of 1300 ppm. This is also in good agreement with the data from Zhang et al. (2012) (see *2 in Fig. 4.4), who performed experiments with molybdenite only and who reported mean Mo concentrations for experiments of the same design of 1200 to 1510 ppm. This may indicate that W and Mo, both of which are hard Lewis acids, compete for the same ligands (e.g., OH⁻, O²⁻, Cl⁻) but that Mo forms the more stable complexes and is thus complexed preferentially, possibly due to the slightly higher difference in electronegativity with respect to oxygen.

Fig. 4.4 (*1) also shows W concentration extrapolated from scheelite solubility data from Foster (1977) obtained between 252 and 529 °C in the pressure range of 100-200 MPa.

Assuming a linear correlation of $\log W$ (ppm) vs. $1000/(T \text{ in K})$, a least square extrapolation resulted in a value of ca. 1200 ppm (or 1900 ppm if two obvious outliers are discarded). This is lower by a factor of ca. 3-5 when compared to our data (fluids in equilibrium with scheelite only) and the possible variation may be due to the use of a different buffer (Msk-Kfs-Qz) and salt in the solution (1 M KCl, which corresponds to 7.17 wt% KCl), but likely also due to quenching problems and the formation of precipitates, as Foster (1977) sampled the fluid directly from the capsule. Loucks and Mavrogenes (1999), who applied the synthetic fluid inclusion approach, investigated the solubility of gold. Extrapolation of their Au concentrations from experiments in the range of 625 to 725 °C led to a value of roughly 220 ppm Au (Fig. 4.4, *3), which is slightly lower than our results of ca. 300 ppm. Even though their experiments were performed under the same buffer conditions (PPM), other experimental conditions differed, which may explain the small discrepancy. In particular, the experiments were conducted at 110 MPa and they used a 1 m HCl solution. Extrapolation of Au concentrations determined via direct fluid sampling from the capsule by Gibert et al. (1998) in the range of 350 to 450 °C leads to a value of roughly 40 ppm Au, which is considerably lower than our results. The experiments of Gibert et al. (1998) were performed under the same buffer conditions (PPM), but were conducted at 50 MPa and the authors additionally used the Msk-Kfs-Qz buffer and a 0.5 M KCl solution. The lower concentration might also stem from quenching problems and the formation of quench precipitates. In general, extrapolation to higher temperatures and pressures must be considered with caution, as metal complexation at low P-T conditions may be different from that at higher P-T (Pokrovski et al., 2015).

It was previously mentioned that analyses from the shortest time-dependent experiment are subject to a large analytical error due to the small size of produced fluid inclusions. Therefore, the slightly higher Mo concentrations in the experiment compared to the longer durations might be solely explained by bad counting statistics. It cannot be ruled out though that Mo experiences a true early oversaturation, which might be due to a lower fS_2 in the fluid before the Pyrite-Pyrrhotite-Magnetite buffer has equilibrated. Following Chatelier's principle, a lower fS_2 would lead to a distortion of the dissolution equilibrium as proposed by Zhang et al. (2012) in favor of the side with the dissolved species:



4.4 Conclusions Regarding the Experimental Method

The experimental tests confirm that synthetic fluid inclusions are a successful tool to probe fluids in experiments at high temperatures and pressures without the problem of fluid quenching. Solubilities of solid phases in different fluids can be determined under various conditions, including the possibility to access partitioning data of elements between various phases. However, the implication of the discussion is that there is currently no universal and perfect experimental design for the synthesis of equilibrated fluid inclusions. Depending on the investigated temperature, pressure, equilibrating phases and host mineral in the experiments, different designs need to be applied to obtain reliable results.

For experiments with $T \geq 600$ °C, we recommend the use of experimental design *C*, as from our experience this design produces results of the best quality. In particular, applying an intermediate quench (or possibly several) after a well-defined equilibration time is strongly recommended. Time-dependent experiments showed that mineral dissolution is considerably faster than usually assumed (e.g. Hanley et al., 2005; Simon et al., 2007; Zhang et al., 2012). The dissolution of scheelite takes slightly longer than that of molybdenite and gold, but is still in the order of hours rather than days at 800 °C. As a consequence, experimental durations can be designed much shorter than previously done, which is a great advantage when using fast consuming solid mineral buffers. Nevertheless, equilibration times of the used buffer also need to be taken into account when deciding on the length of the experiment prior to the intermediate quench.

For experiments distinctly below 600 °C, the use of an un-fractured additional mineral cylinder can be discarded, as it does not yield fluid inclusions that are large enough for LA-ICP-MS analysis. It is, however, possible to produce adequate fluid inclusions down to at least a temperature of 400 °C in doubly pre-treated quartz cylinders. But care must be taken in estimating t_{heal} and t_{equil} , which will be longer compared to higher temperatures. Below 400 °C we were not able to produce fluid inclusions which were suitable for LA-ICP-MS analysis, so that different experimental approaches (e.g., direct sampling of the fluid in a reaction cell autoclave such as the design of Seyfried et al. (1979)) need to be applied.

5 Application #1: Synthetic Fluid Inclusions - Solubility of Scheelite (CaWO_4), Ferberite (FeWO_4) and Gold (Au) in Hydrothermal Fluids

We investigated the solubility of molybdenite (MoS_2), powellite (CaMoO_4), scheelite, ferberite and gold under selected conditions using the synthetic fluid inclusion technique with subsequent LA-ICP-MS analysis. We chose molybdenite to compare our results to those of Zhang et al. (2012), who thoroughly investigated molybdenite solubility under various conditions. We were interested in the solubility of powellite as it contains Mo, too, but as a molybdate, such as W prevails as tungstate in scheelite. Investigating gold was primarily only a byproduct as we were using gold capsules, but we covered a range, which was previously not investigated for gold and the results complement previous data well and provide some interesting findings. The focus of this study lies on the solubility of the W-phases scheelite and ferberite, as despite of the economic importance of tungsten, no reliable data existed so far.

According to a summary of Wood and Samson (2000), the deposition of scheelite and wolframite (solid solution of ferberite and hübnerite, MnWO_4) mostly takes place between 200 and 500 °C and 20 and 150 MPa. Fluid salinities determined via microthermometry lie mostly below 15 wt% NaCl_{eq} and oxygen fugacity is estimated to vary between FMQ (fayalite-magnetite-quartz) and HM (haematite-magnetite) buffers. We selected our experimental parameters accordingly. As we are focusing on the transport of W prior to its deposition, we selected temperatures from 450 °C to 800 °C and pressures of 100 to 300 MPa, which should cover the conditions between the exsolution of a magmatic fluid from a granitoid magma and the final deposition of ore minerals in the upper crust. Under all investigated conditions the fluid was in the one phase fluid field (according to Driesner (2007) and Driesner and Heinrich (2007), c.f., Fig. 5.1). Salinity was varied between 1 and 20 wt% NaCl and oxygen fugacity (f_{O_2}) was fixed by either the FMQ, NNO (nickel-nickel oxide) or PPM (pyrite-pyrrhotite-magnetite) buffer, the latter introducing sulfur to the system and fixing sulfur fugacity (f_{S_2}).

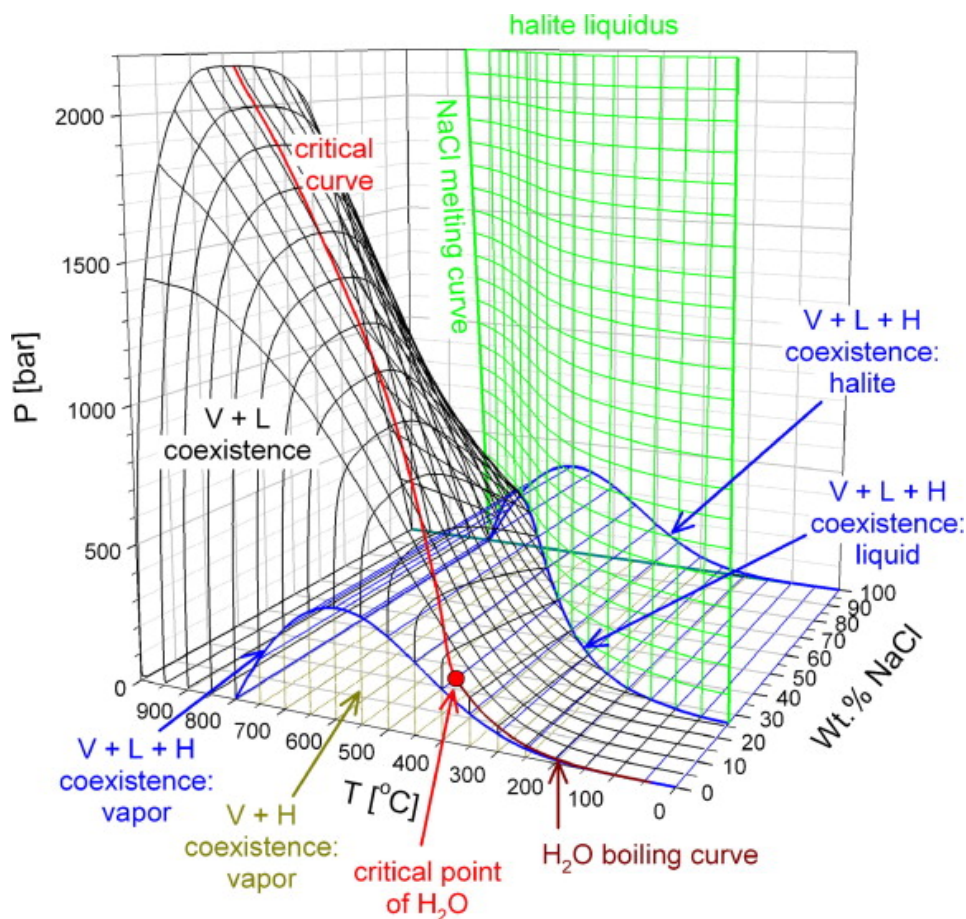


Fig. 5.1: Phase diagram of the H₂O–NaCl system in pressure-temperature-composition (P-T-X) space (Driesner and Heinrich, 2007). At the investigated conditions (T = 450–800 °C, P = 1000–3000 bar, salinity = 1–20 wt% NaCl), the fluid composition is located above the black envelope delimiting the V+L field. Therefore, only one fluid is expected.

5.1 Experimental Procedure

Solubility experiments were conducted in the Institute of Mineralogy at Leibniz Universität Hannover, Germany, as described in Chapter 294 and Derrey et al. (2017). In early experiments one quartz cylinder (as described in Chapter 4, experiment A and C_1) was placed in a Au capsule of ca. 25 mm length together with NaCl-solution (1, 8 or 20 wt% NaCl), the respective mineral powders, and silica gel. In the course of the proceeding experimental series, it proved useful to add a second quartz cylinder to Au capsules of ca. 30 mm length, which was previously only cleaned with HCl and distilled water (cf., Derrey et al. (2017) experiment C_2, and Zajacz et al. (2010)). Capsules were pressurized at room T and then moved to the preheated hot zone of the autoclave using the rapid heat device (external Nd-magnet) of the CSPV. Heating of the capsules to the target T occurred rapidly,

within a few minutes, at approximately isobaric conditions. During the experiment, the gold capsule was quenched quickly by pulling it from the hot end of the vertical autoclave to the water-cooled central part to cause cracks within the quartz cylinder(s) as a result of thermal stress. This method proved to be capable of both reopening previously formed inclusions to refill them with the fluid that equilibrated for a defined time with the surrounding phases in the capsule, as well as forming new cracks (Derrey et al., 2017; Li and Audétat, 2009; Zajacz et al., 2010; Zhang et al., 2012). Fig. 5.2 shows synthetic fluid inclusions in quartz chips from (a) previously fractured and (b) previously un-fractured quartz cylinders formed at 600 °C and 200 MPa.

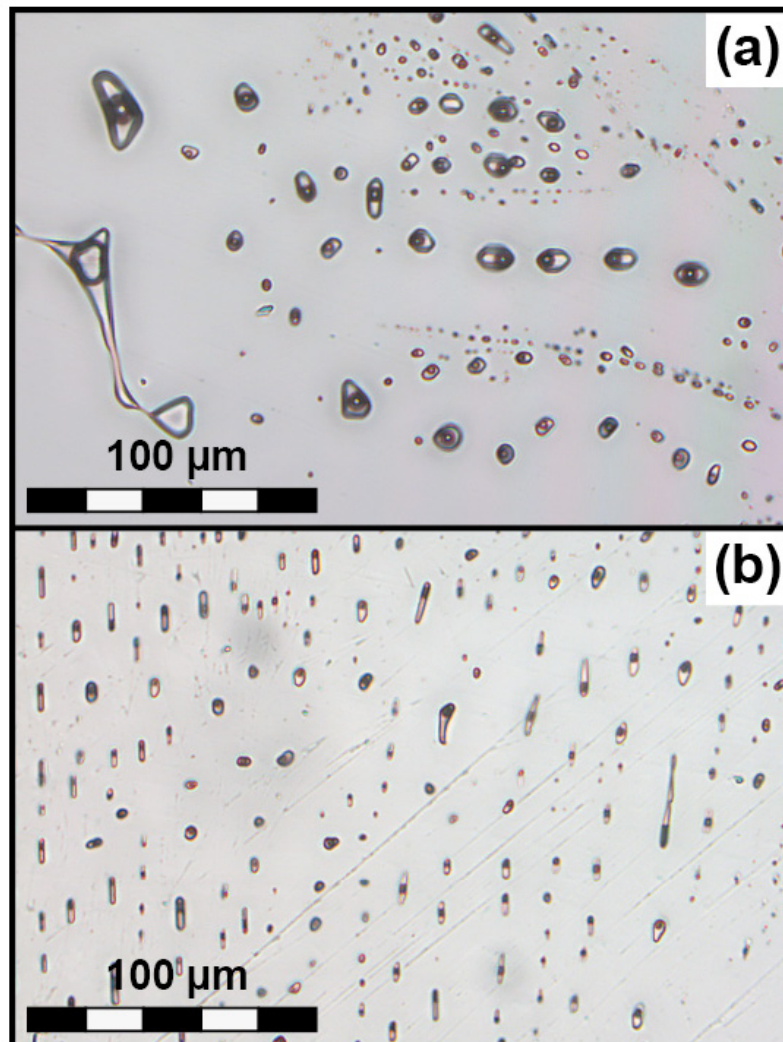


Fig. 5.2: Synthetic fluid inclusions in quartz formed at 600 °C and 200 MPa in a quartz cylinder, which was (a) fractured prior to the experiment and in-situ and (b) only fractured in-situ by an intermediate quench.

5.2 Analytics

Fluid inclusions produced in this way were analyzed by LA-ICP-MS for their major and trace element contents at the Institute of Mineralogy at Leibniz Universität Hannover. The general technique was described in detail in Chapter 3 as well as Albrecht et al. (2014). A description specifically for the application on synthetic fluid inclusions is provided in Chapter 4.2. Analyses were performed at temperatures of either $-40\text{ }^{\circ}\text{C}$ or $-60\text{ }^{\circ}\text{C}$ (depending on the eutectic point of the system; the latter for inclusions from Ca-bearing experiments), guaranteeing completely frozen fluid inclusions prior to the ablation. The SILLS data reduction software of Guillong et al. (2008b) was used to evaluate the acquired data. As internal standard the known Cs concentration of the starting fluid was used and compared to the also known Rb and Na concentrations. Fluid inclusion analyses in which the Rb/Cs-ratio and/or the Na/Cs-ratio deviated by more than 20 % were discarded as they are considered to represent analyses of poor quality (Zhang et al., 2012). Fig. 5.3 shows a representative spectrum of an analysis of a synthetic fluid inclusion from an experiment at $600\text{ }^{\circ}\text{C}$ and 200 MPa with scheelite as W source.

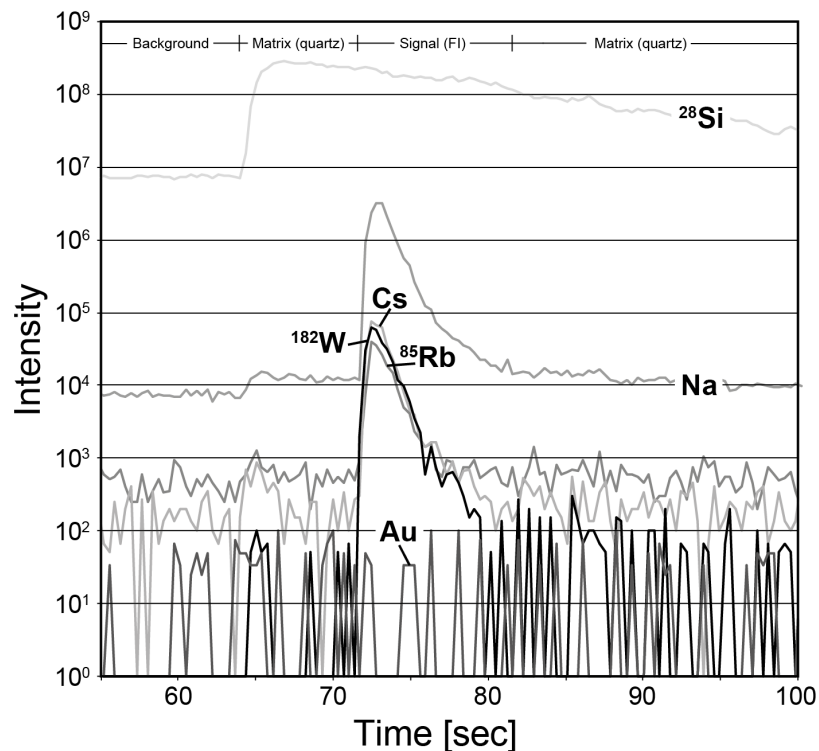


Fig. 5.3: Typical LA-ICP-MS signal from a frozen fluid inclusion (metal source: scheelite + gold, formed at $600\text{ }^{\circ}\text{C}$, 2 kbar, 20 wt% NaCl, PPM buffer) using a UV-fs-laser, heating-freezing cell and *Element XR* ICP-MS.

5.3 Results

Individual experiments and analytical results are given in Suppl. Tab. 5. In Fig. 5.4 to Fig. 5.10, the mean and standard deviation ($\pm 1\sigma$) of each experiment are given. Black symbols represent analyses from fluid inclusions, which formed in the not pre-treated quartz chip, i.e., after the intermediate quench. Grey symbols represent analyses from all fluid inclusions (not pre-treated, and pre-cracked and etched quartz chip) and formed before as well as after the intermediate quench. Where possible, mean values were calculated using only analyses from not pre-treated quartz chips, otherwise we reverted to values from pre-treated quartz chips for better statistics.

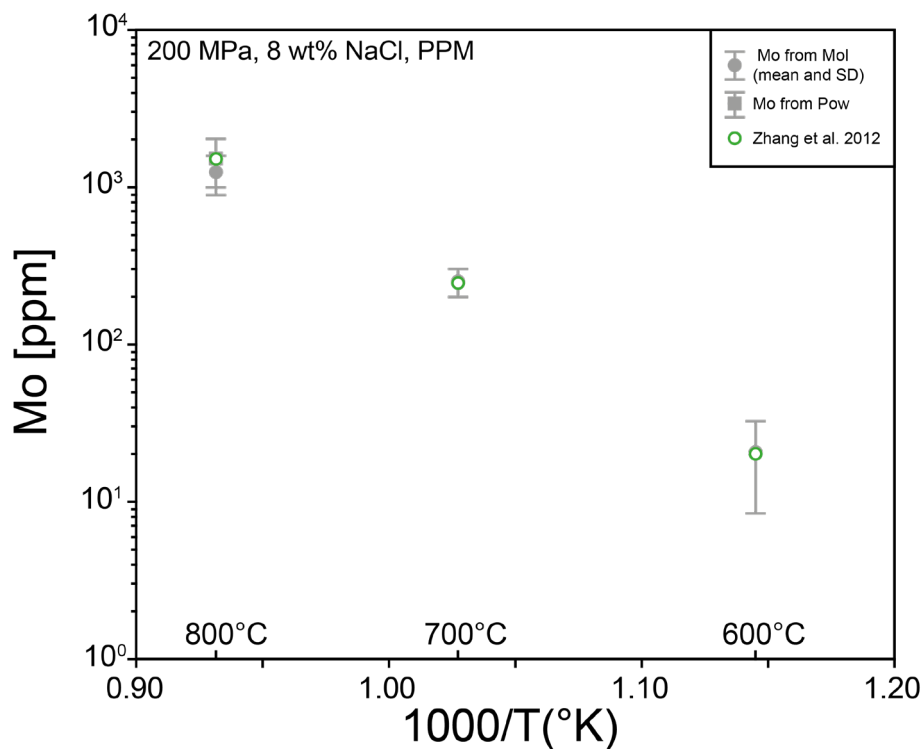


Fig. 5.4: Mo concentrations from solubility of molybdenite (full circles: this study; empty green circles: Zhang et al. (2012)) at 600, 700 and 800 °C and 200 MPa, and from powellite solubility (full square) at 800 °C and 200 MPa. The aqueous fluid contained 8 wt% NaCl and was buffered using the PPM mineral buffer. Note that results of Zhang et al. (2012) coincide very well with our results so that the data points overlap each other.

A series of runs at 600, 700 and 800 °C and 200 MPa was conducted with molybdenite in an 8 wt% NaCl fluid buffered with the PPM buffer to compare the results with those of Zhang et al. (2012), who performed experiments under the same conditions. Fig. 5.4 shows the linear relationship between $\log Mo$ [ppm] in the fluid from dissolution of

molybdenite with $1000/(T [K])$. The results from this study agree well with data from Zhang et al. (2012). Solubility of powellite (CaMoO_4), which contains Mo in the molybdate oxoanion rather than coupled with sulfur, appears to be slightly higher than that of molybdenite (Fig. 5.4, 1630 ± 300 ppm vs. 1300 ± 260 ppm) at the investigated conditions of 800 °C, 200 MPa, 8 wt% NaCl fluid and PPM buffer. However, Mo concentrations overlap within one standard deviation and XRD measurements revealed that in the powellite-bearing experiments molybdenite formed in addition to powellite.

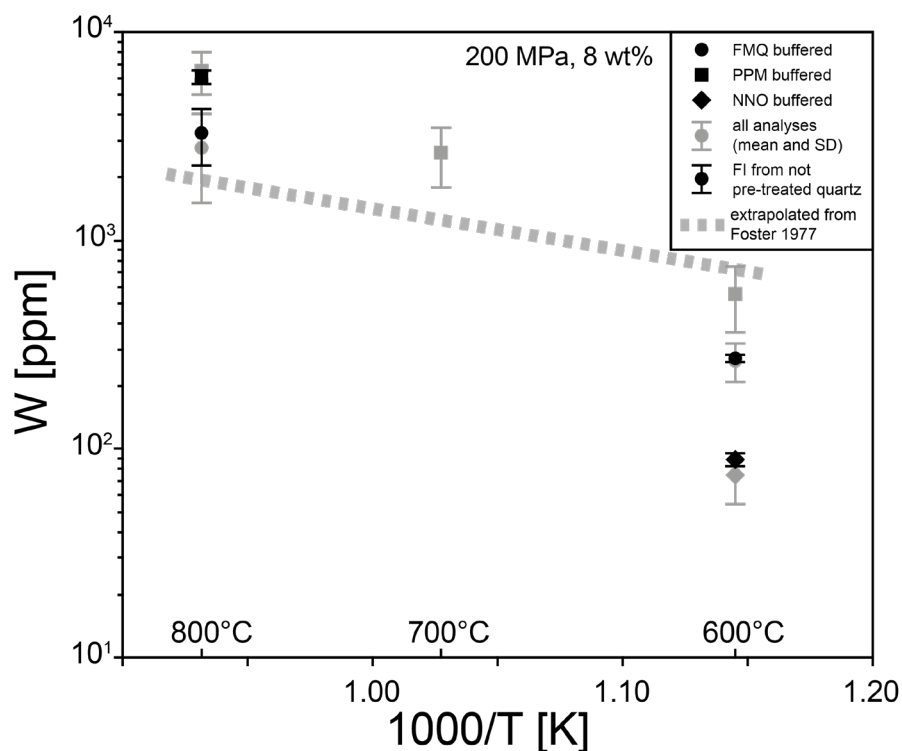


Fig. 5.5: W concentrations from solubility of scheelite at 600, 700 and 800 °C, 200 MPa with an aqueous fluid containing 8 wt% NaCl. Three different mineral buffers were used: black circles - FMQ buffer, squares - PPM buffer, diamonds - NNO buffer). Extrapolated W concentration using data from Foster (1977, 252-529°C, 100-200 MPa, muscovite - K-feldspar - quartz buffer + 1 M KCl, metal source was also scheelite) are depicted as open circles for comparison.

Linear relationships of $\log[\text{ppm}]$ vs. $1000/(T[K])$ were also found for the concentration of W from scheelite and ferberite solubility as well as Au from solubility of metallic gold (Fig. 5.5, Fig. 5.6 and Fig. 5.7). Scheelite is less soluble in experiments buffered with FMQ than with PPM buffer (ca. 0.3 log units, Fig. 5.5). Comparing W concentrations from experiments with ferberite and scheelite, it appears that ferberite is more soluble than scheelite under most investigated conditions (Fig. 5.7). At 600 °C and varying pressures

(100, 200, 300 MPa, Fig. 5.8) or salinities (1, 8, 20 wt% NaCl, Fig. 5.9) W concentrations from dissolution of ferberite are always higher than W concentrations from dissolution of scheelite. However, W concentrations from dissolution of both phases are the same within error (ca. 40 ppm) at 450 °C, 200 MPa and 8 wt% NaCl (Fig. 5.7). The temperature trends suggest a reverse in solubility below ca. 450 °C.

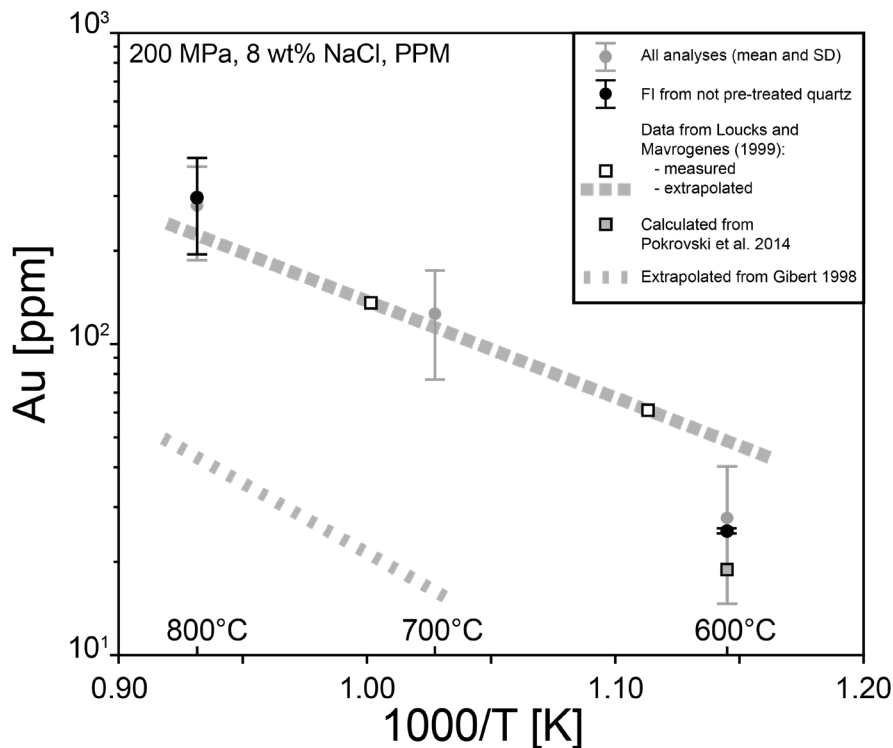


Fig. 5.6: Au concentrations from solubility of native gold at 600, 700 and 800 °C and 200 MPa. The aqueous fluid contained 8 wt% NaCl and was buffered using the PPM mineral buffer. Circles: this study; empty squares: data of Loucks and Mavrogenes (1999); grey square: calculated from Pokrovski et al. (2014); dashed lines: extrapolated from data of Loucks and Mavrogenes (1999) and Gibert et al. (1998).

Pressure does not show a pronounced influence on scheelite solubility, and only a small positive effect on the solubility of ferberite under the investigated conditions in the range from 100 to 300 MPa (Fig. 5.8). No effect of pressure on the solubility of gold can be observed, which straddles the detection limit (ca. a few ppm to tens of ppm depending on the volume of the fluid inclusion) at 600 °C under sulfur free FMQ buffered conditions. In contrast to pressure, NaCl content of the fluid considerably influences the solubility of scheelite and ferberite in that W concentration increases with increasing salinity. Whereas logW from dissolution of scheelite appears to increase linearly with increasing log NaCl, this correlation could not be found for ferberite (Fig. 5.9). For gold solubility no

clear correlation can be seen with salinity of the fluid at 800 °C, 200 MPa and PPM buffered conditions. Gold solubility is similar in an 8 wt% and 20 wt% NaCl fluid (ca. 200-300 ppm), but slightly lower in a 1 wt% fluid (ca. 90 ppm, Fig. 5.10). Nevertheless, the relative effect is much smaller than that found for scheelite and ferberite solubility (this study) or molybdenite solubility (Zhang et al., 2012).

It is important to note that for using the FMQ buffer at 800 °C, the experimental runtime had to be reduced to 12 hours before and 12 hours after the intermediate quench (cf., Chapter 4.3.2 and Fig. 4.6 for equilibration time estimates) to make sure that fayalite from the buffer was not fully consumed during the experiment. We were not able to successfully buffer an experiment at 600 °C with the cobalt-cobalt oxide (CCO) buffer, which lies ca. one log unit below the FMQ buffer, as Co was consumed too fast during the experiment. An experiment on scheelite solubility at 600 °C, 200 MPa and with an 8 wt% NaCl fluid buffered with the NNO buffer, which lies ca. 0.7 log units above FMQ, resulted in a W concentration of ca. 90 ppm compared to ca. 270 ppm at FMQ (Fig. 5.5). Both CCO and NNO buffers were applied using the double capsule technique (Eugster, 1957 and following).

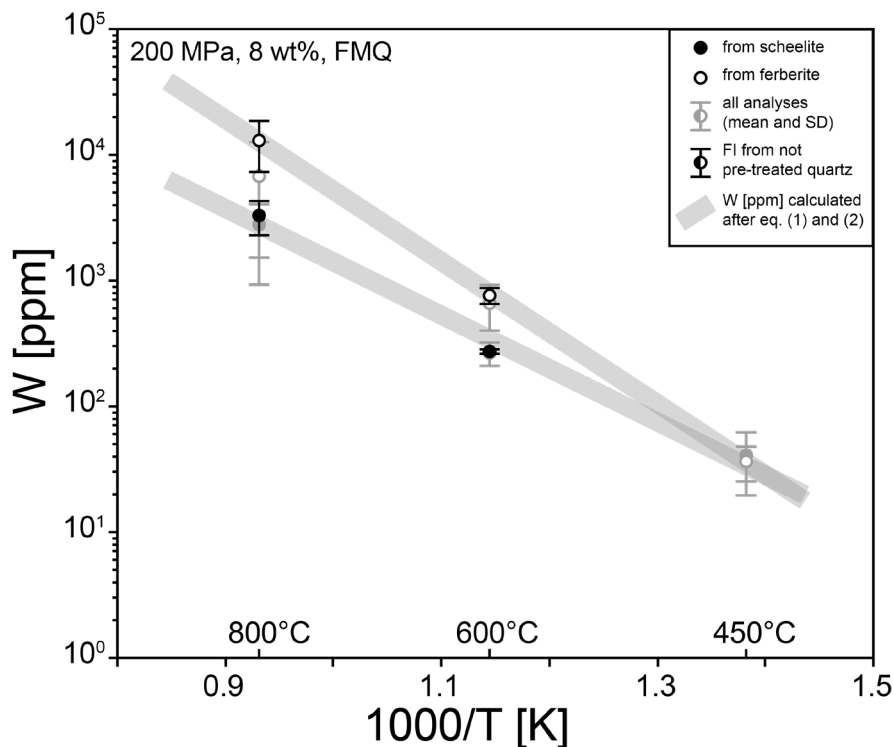


Fig. 5.7: W concentrations from solubility of scheelite and ferberite at 450, 600 and 800 °C, 200 MPa in an aqueous fluid containing 8 wt% NaCl at oxygen fugacities buffered with the FMQ mineral buffer. Positions of the grey lines were calculated after Equation 1 and 2 in Chapter 5.4.3 of the discussion.

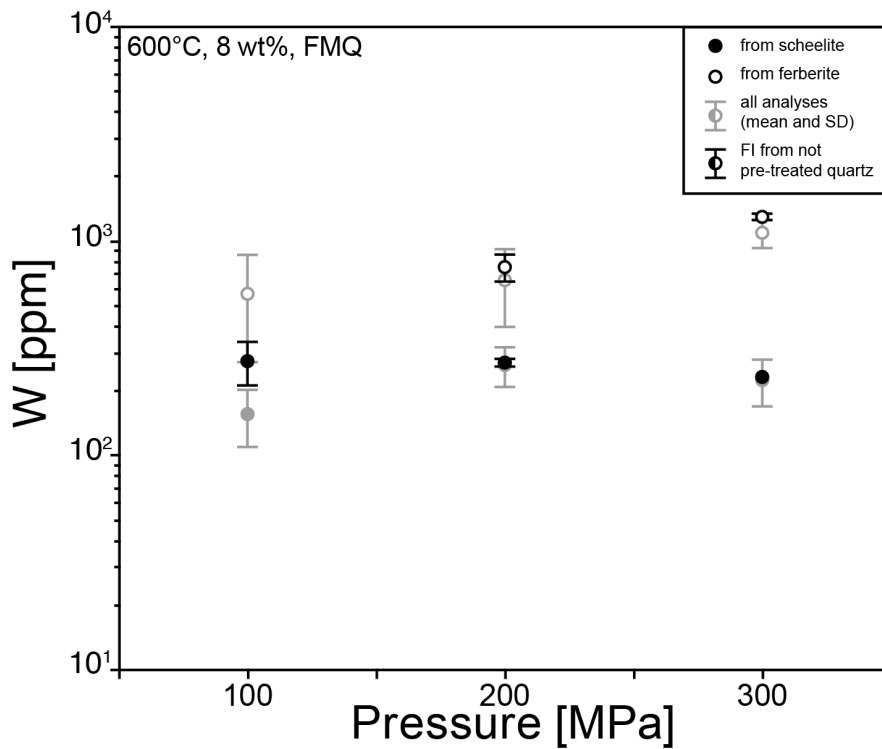


Fig. 5.8: W concentrations from solubility of scheelite and ferberite at 600 °C, 100, 200 or 300 MPa in an aqueous fluid containing 8 wt% NaCl at oxygen fugacities buffered with the FMQ mineral buffer.

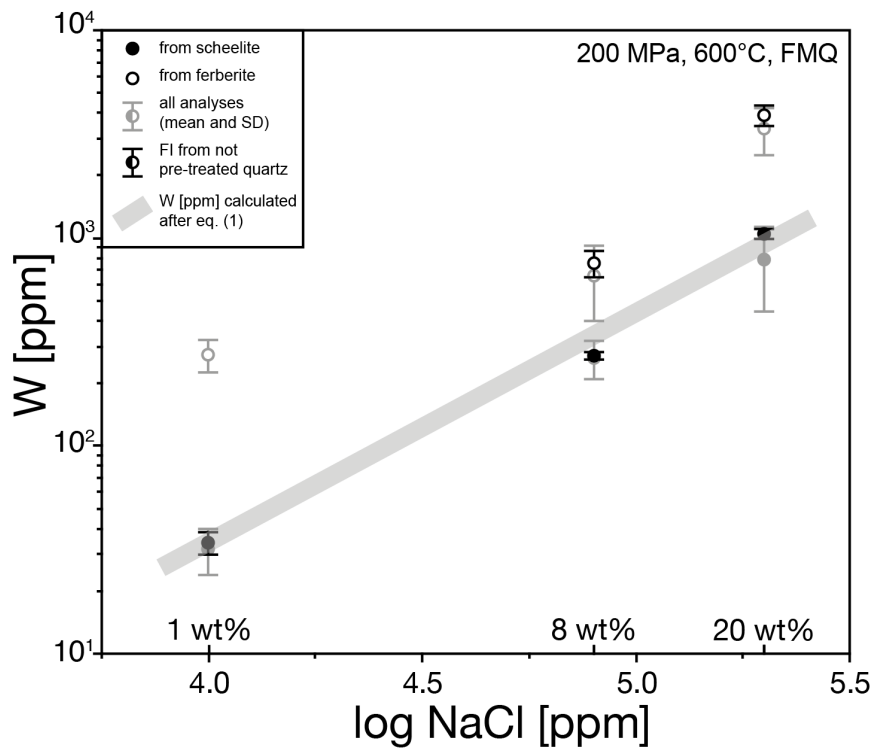


Fig. 5.9: W concentrations from solubility of scheelite and ferberite at 600 °C, 200 MPa in an aqueous fluid containing 1, 8 or 20 wt% NaCl at oxygen fugacity buffered with the FMQ mineral buffer. Position of the grey line was calculated after Eq. 1 in the discussion.

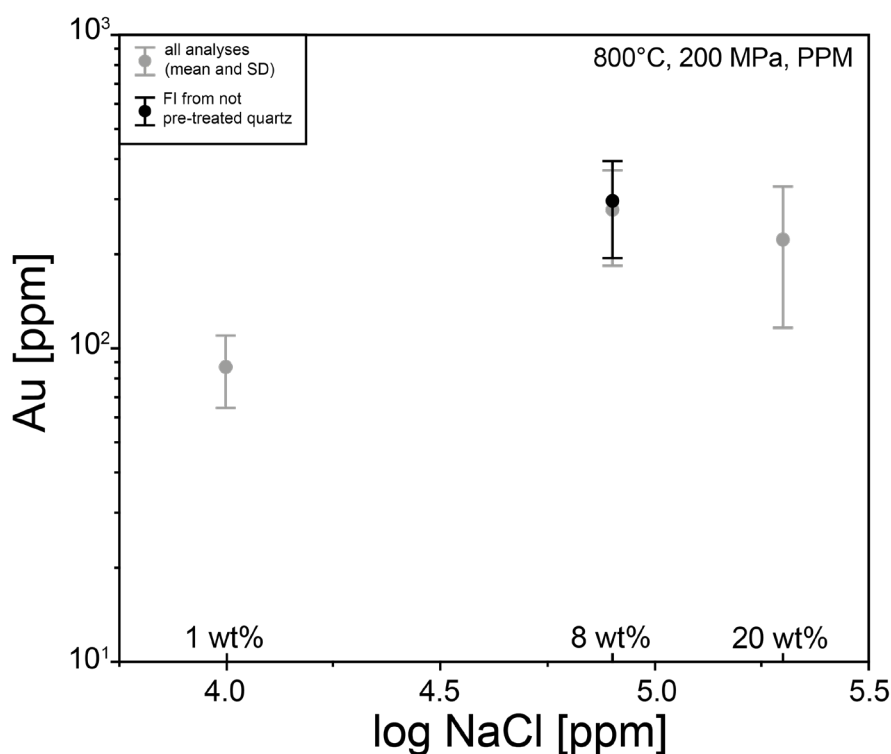


Fig. 5.10: Au concentrations from solubility of gold at 800 °C, 200 MPa in an aqueous fluid containing 1, 8 or 20 wt% NaCl at oxygen fugacity buffered with the PPM mineral buffer.

5.4 Discussion

5.4.1 Molybdenite and Powellite Solubility

As discussed in Chapter 4, we are confident about the achievement of equilibrium in our experiments as well as the accuracy of the analytical method. This is supported by the perfect agreement of our results for molybdenite solubility with results from Zhang et al. (2012) (Fig. 5.4), who used the experimental design described in Chapter 4.1.2 setup 1 (experiment B).

Under the investigated conditions (800 °C, 200 MPa, PPM buffer) molybdenite precipitated next to powellite in the powellite-bearing runs. Therefore, this experiment does not report true powellite solubility. Nevertheless, Mo concentration is slightly higher than in runs with molybdenite only, suggesting that powellite is more soluble than molybdenite, which would explain its scarcity in nature where it mostly occurs in the oxidation zones of hydrothermal Mo-deposits. According to Hsu (1977) stabilizing powellite at the expense of molybdenite requires very oxidized conditions, whereas the

chemical W counterpart scheelite is stable over a wide range of common geological conditions. As the investigated conditions were rather oxidized (ca. NNO +2.6), it can be expected that the solubility difference between molybdenite and powellite will increase at more reducing conditions, which would need to be confirmed by future experiments.

5.4.2 Gold Solubility

When assessing the pressure dependence of gold, it has to be noted that gold concentrations straddle the detection limit under the investigated conditions (100 – 300 MPa, 600 °C, 8 wt% NaCl, FMQ buffer) and are subject to large analytical errors. The apparent independence of Au solubility on pressure in the investigated range (100 to 300 MPa) is in accordance with the model of Pokrovski et al. (2015), who calculated that Au is hardly effected by pressure above ca. 100 MPa. According to their model this changes drastically at lower pressures, which implies that whereas pressure has supposedly no effect on the mobilization and transport of gold at depth, its role for the precipitation of gold and the formation of economic gold deposits may be significant in near-surface systems (low P).

Gold solubility is significantly enhanced by the presence of sulfur in the fluid, and gold concentrations from experiments including sulfur (PPM buffer) are one to two orders of magnitude higher than in experiments without sulfur (FMQ buffer). This is in agreement with the general notion of Au-complexation by reduced sulfur (e.g, Krauskopf, 1951; Pokrovski et al., 2014), which forms soft ligands and will, according to Pearson's Principle, preferentially bond with soft metals such as the Au⁺-cation (Pearson, 1963). But as water changes its structure at high temperatures, metal-ligand interaction also changes and other ligands such as Cl⁻ might gain importance. This hypothesis is strongly supported by a study of Guo et al. (2018), who investigated the solubility of gold in highly oxidized and sulfur-bearing fluids at 500-850 °C. In their experiments, they found Au concentrations of up to a few wt% at highly oxidizing conditions (three log units above the hematite-magnetite buffer) and with considerable amounts of HCl, NaCl and H₂SO₄ added to the fluids. In experiments under geologically more realistic conditions comparable to those prevalent in porphyry Cu-Au system, Guo et al. (2018) reported maximum Au concentrations of ca. 750 and 880 ppm at 750 °C and 850 °C, respectively (230 MPa, MnO-Mn₃O₄ buffer (MMO), 7 wt% NaCl, 1 wt% S, 1.1 wt% HCl). This concentration is in the same order of magnitude than the Au concentrations determined in our experiments at

800 °C, 200 MPa, 8wt% and PPM buffer (Au concentrations of ca. 300 ppm, c.f., Fig. 5.6). The slightly higher values are likely explained by the higher fO_2 of the MMO buffer (ca. one log unit higher than FMQ) and the addition of HCl, which are both parameters favoring the solubility of gold according to Guo et al. (2018). Salinity of the fluid and run temperature showed only a subordinate influence on Au solubility in their study. Pokrovski et al. (2014) also argued that in magmatic brines above 500 °C, chloride complexes were expected to play a major role in gold transport, provided that Au species with other sulphur-bearing ligands (e.g., SO_2 and S_3^-) turn out to be insignificant at these conditions. Nevertheless, Fig. 5.10 shows that in our experiments a varying NaCl concentration in the fluid has only minimal effect, if at all, on the solubility of gold at 800 °C, 200 MPa and PPM buffered conditions. Subsequently, Pokrovski et al. (2015) showed that traditionally invoked gold complexes such as $AuHS$, $Au(HS)_2^-$ or $AuCl_2^-$ are incapable of mobilizing sufficient gold to explain observed gold concentrations, neither in natural fluid inclusions (e.g., Pokrovski et al., 2014; Ulrich et al., 1999) nor in laboratory experiments on gold solubility (e.g., Loucks and Mavrogenes, 1999; Zajacz et al., 2010). They suggest that sulfur radical ions, such as S_3^- , are responsible for the formation of the majority of Au deposits on Earth and proved that gold-trisulfur ion complexes ($Au(S_3^-)$) are capable of carrying Au concentrations of tens to hundreds of ppm, which is in accordance with the range observed in our experiments. The existence of the trisulfur radical ion and other sulfur polymers in natural fluid inclusions is also strongly supported by a Raman spectroscopic study of fluid inclusions at elevated temperatures by Barré et al. (2017).

Next to sulfur, temperature has a pronounced effect on the solubility of gold in our study (Fig. 5.6) and is believed to be one of the dominant factors that influence both its transport and precipitation. For example, Helgeson and Garrels (1968) suggested that cooling of a saline fluid alone is sufficient to deposit gold in veins together with quartz and pyrite. Pokrovski et al. (2014) acknowledge the importance of cooling as a precipitation mechanism for gold, but highlight that the effect is less straightforward than for other metals, as it is constrained by the ratio of ferrous iron over reduced sulfur. In the case of excess ferrous iron (and copper) cooling will result in the precipitation of pyrite (and chalcopyrite), removing sulfur from the fluid and thus triggering Au precipitation. Whereas in the case of excess sulfur, e.g., in vapor-like fluids produced by phase unmixing, considerable amounts of gold can stay in solution down to much lower temperatures.

In Fig. 5.6 we plotted gold concentrations from Loucks and Mavrogenes (1999), who also applied the synthetic fluid inclusion approach to investigate the solubility of gold. Their experimental data at 625 and 725 °C using the PPM buffer are in the same order of magnitude as our data, even though they were conducted at 110 MPa and a 1 M HCl solution was used. Extrapolation of Au concentrations determined via direct fluid sampling from the capsule by Gibert et al. (1998) in the range of 350 to 450 °C leads to gold concentrations considerably lower than our results, but the slope in $\log[\text{ppm}]$ vs. $1000/(T [\text{K}])$ space is very similar (Fig. 5.6). Gibert et al. (1998) also used the PPM buffer, but conducted their experiments at a lower pressure (50 MPa) and additionally added a pH buffer (Msk-Kfs-Qz) and a 0.5 M KCl solution. In addition to the different experimental conditions, the method of direct fluid sampling from the capsule is thought to cause quenching problems such as the formation of quench precipitates, so that the measured concentrations might be lower than true equilibrium values.

5.4.3 Scheelite and Ferberite Solubility

Among the proposed factors that govern the deposition of W-minerals in W-deposits the most popular are (1) cooling (e.g., Chen et al., 2018; Heinrich, 1990; O'Reilly et al., 1997; Seal et al., 1987; Wood and Samson, 2000); (2) an increase in pH associated with wallrock alteration reactions (e.g., Cattalani and Williams-Jones, 1991; Polya, 1989; Seal et al., 1987; Wood and Samson, 2000), (3) fluid mixing, including dilution (e.g., Giuliani, 1984; Landis and Rye, 1974; Pan et al., 2019; Samson, 1990); and (4) boiling and/or CO₂ effervescence (e.g., Higgins and Kerrich, 1982; Korges et al., 2018; Pan et al., 2019; Seal et al., 1987; So and Yun, 1994).

General findings from thermodynamic modeling of ferberite and scheelite solubilities by Wood and Samson (2000) support our result that W concentrations from dissolution experiments of both scheelite and ferberite decrease strongly with decreasing temperature and NaCl concentration in the fluid, but that they are only weakly dependent on pressure (Fig. 5.5 and Fig. 5.7 - Fig. 5.9). For a constant pressure of 200 MPa and FMQ buffered conditions, we derived a simple equation (eq.) for the solubility of scheelite, which is applicable at least within the investigated T-X conditions:

$$\log C_w (\text{scheelite}) = -4.222 \times (1000/T) + 1.106 \times \log C_{\text{NaCl}} + 1.941 \quad (1)$$

where C_W and C_{NaCl} are the concentrations of W and NaCl in ppm by weight and T is temperature in Kelvin.

As ferberite solubility does not to behave linearly with changes in salinity, an empirical model was formulated to calculate the W concentration from dissolution of ferberite as a function of temperature for a fixed pressure of 200 MPa and a fluid salinity of 8 wt% NaCl:

$$\log C_W (\text{ferberite}) = -5.657 \times (1000/T) + 9.371 \quad (2)$$

As can be seen in Fig. 5.5 scheelite is more stable (i.e., less soluble) in experiments with FMQ buffer compared to experiments using the PPM buffer at 600 °C and 200 MPa, which following Hsu (1977) is due to the imposed fS_2 from the PPM buffer destabilizing scheelite. More oxidized condition without S on the other hand stabilize scheelite, which could be shown in the experiment using the NNO buffer. Together with the observation that W mineralizations usually occur within the “oxide stage” of ore deposits (e.g., Wood and Samson, 2000), this supports the idea that oxidizing conditions favor the stabilization and deposition of W-minerals, such as scheelite and wolframite.

Calculations of Wood and Samson (2000) suggest that scheelite becomes more stable relative to ferberite with increasing temperature. This is strongly supported by the data from our temperature-dependent series (Fig. 5.7), which show that, whereas solubilities of ferberite and scheelite under the investigated condition (200 MPa, 8 wt% NaCl, FMQ buffer) are the same within error at 450 °C (ca. 40 ppm), W concentration from dissolution of ferberite increases more rapidly with temperature than from dissolution of scheelite. The thermodynamic implications of these trends will be discussed at the end of this section. At 800 °C, W concentration from dissolution of ferberite is roughly four times higher than from dissolution of scheelite. This is also in agreement with natural studies. E.g., Shelton et al. (1986) described the Sannae deposit in Korea, where both scheelite and wolframite occur. According to their study, the wolframite/scheelite ratio decreases with increasing depth in the mine, which can be related to increasing temperature of formation, supporting the idea that scheelite becomes more stable relative to wolframite with increasing temperature. In addition, the availability and ratio of Ca and Fe (+ Mn) will influence the deposition of both minerals, i.e. the trend might be reverse if there is more Fe (and/or Mn) available at high temperatures and/or more Ca at low temperatures, e.g., due to assimilation of host rocks (also cf., Lecumberri-Sanchez et al., 2017 and discussion below). In fact, in many W deposits late-stage replacement of ferberite by

scheelite is observed, which requires an increase in the Ca/Fe ratio, e.g., by an external addition of Ca to the fluid (Wood and Samson, 2000).

There are some inconsistencies in the literature concerning the effect of pressure on the solubility of W-minerals. In contrast to our data, calculated wolframite solubility by Polya (1990) and scheelite solubility by Gibert et al. (1992) predicted a strong pressure dependence. Our finding that pressure has only a weak influence on the solubilities of both ferberite and scheelite is in better agreement with calculations of Wood and Samson (2000) as well as measurements of Malinin and Kurovskaya (1996). According to Wood and Samson (2000) the effect of pressure appears to be minimal between 50 and 100 MPa; an observation, which can be expanded up to a pressure of 300 MPa according to our data. This implies that pressure changes, at least in the one-phase fluid field, do not play a major role in the transport and deposition of W and in the formation of W deposits in general. Concerning the effect of pressure on boiling and concomitant CO₂ effervescence, no conclusion can be drawn from our data, but the abundant occurrence of CO₂-rich fluid inclusion in W-deposits around the world (e.g., in the Panasqueira deposit, Portugal; cf., Chapter 6) hints at a possible influence on the transport and deposition of W and needs to be investigated further.

On the other hand, our data clearly demonstrates that both decreasing temperature and/or salinity are efficient mechanisms to precipitate W in the form of W-minerals (Fig. 5.5, Fig. 5.7 and Fig. 5.9). This could be achieved by simple cooling of the metal-bearing hydrothermal fluid upon rising into shallower levels of the crust, infiltration of colder country rocks, or by mixing with a colder and lower saline meteoric fluid. Dilution with an external fluid with a low salinity and low W-concentration at isothermal conditions would have a minimal effect on scheelite precipitation though, as maximum W-concentration varies approximately by the same magnitude as the corresponding NaCl-concentration (c.f., Eq. 1). Therefore, we suggest that simultaneous cooling is required to explain W-ore precipitation by dilution of the ore-forming fluid.

Obviously, a Ca or Fe (and Mn) source is required next to W to precipitate scheelite or wolframite from a hydrothermal fluid. According to Lecumberri-Sanchez et al. (2017) the Ca and Fe concentrations in magmatic fluids with high W contents, which exsolve from evolved granites, would be too low to explain the precipitation of these two ore minerals. Thus, they point out the importance of wall rock chemistry on the formation of a scheelite

or wolframite dominated W-deposit, i.e., the importance of Ca-rich or Fe(/Mn)-rich host-rocks such as, e.g., limestones or shales, respectively.

5.4.4 Implications for W-complexation

In natural fluids aqueous W-bearing species commonly contain W in a hexavalent valence state (W^{6+}), whereas its pentavalent form W^{5+} is thought to occur only under rather reducing conditions (e.g., Wood and Samson, 2000; Wood and Vlassopoulos, 1989). The W^{6+} ion is an extremely hard metal according to Pearson's Principle and therefore likely to form strong complexes with hard bases such as O^{2-} , OH^- , F^- , and CO_3^{2-} in low temperature aqueous solutions (Pearson, 1963).

There is ample discussion in the literature if the borderline ligand Cl^- could form complexes with W^{6+} as well. As all ions generally become harder at increasing temperatures (e.g., Crerar et al., 1985; Seward, 1981) and as there is some evidence of aqueous W-complexes with Cl^- from Raman spectroscopy (Griffith and Lesniak, 1969), complexing of tungsten by Cl^- seems to be a possible hypothesis. This is further supported by Manning and Henderson (1984), who found that the fluid/melt partition coefficients (K_D) for W show a clear positive correlation with chloride concentration, and therefore suggested that W-Cl complexes are responsible for the phenomenon. At a first glance, it appears self-evident that the increase in solubility of ferberite and scheelite as a function of salinity observed in this study (Fig. 5.9) and in others (e.g., Foster, 1977; Manning and Henderson, 1984; Wood and Samson, 2000) should be interpreted as proof for the formation of tungsten complexes with Cl^- as well. But as pointed out by, e.g., Wood and Vlassopoulos (1989) and Wood and Samson (2000) the increase in solubility could also result from formation of either iron and calcium chloride complexes and/or alkali metal-tungstate ion pairs (e.g., $NaWO_4^-$, $Na_2WO_4^0$ or $NaHWO_4^0$).

To avoid these superimposed effects on W solubility, Wood and Vlassopoulos (1989) and Wood (1992) conducted experiments with solids containing W as the only metal (e.g., WO_3 as compared to $CaWO_4$ or $FeWO_4$) and Cl added as HCl instead of NaCl. They found no dependence of WO_3 solubility on HCl concentration, which strongly argues against the formation of pure W chloride complexes in natural hydrothermal fluids.

To investigate possible dissolution reactions of scheelite and ferberite and mechanisms of W-complexation, we used our data from Fig. 5.9 to plot them in $\log X_W$ versus $\log X_{NaCl}$

space (X_n = molar fraction of species n ; Fig. 5.11). In this diagram $\log X_W$ from ferberite dissolution does not show a linear relation with $\log X_{NaCl}$. Assuming a linear relationship between the sample with the lowest salinity of 1 wt% NaCl and an intermediate salinity of 8 wt%, results in a slope of $\frac{1}{2}$. Possible dissolution reactions could be the following:

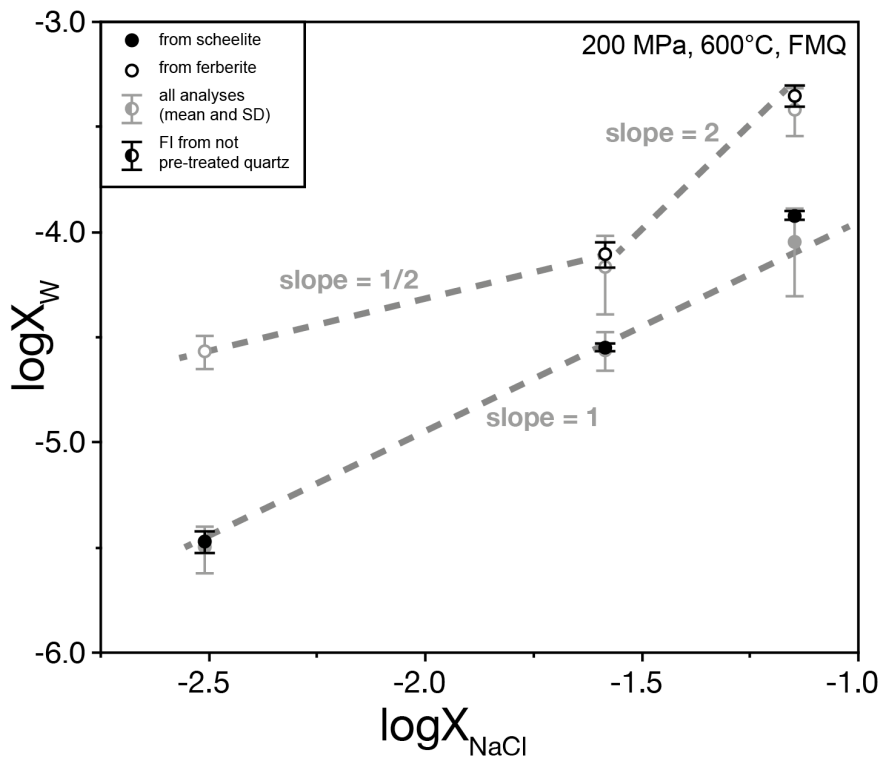
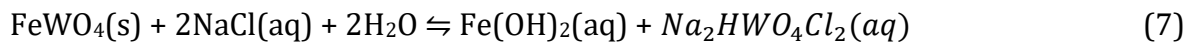
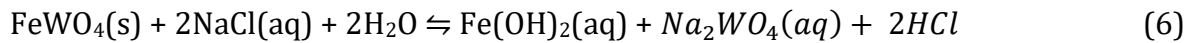
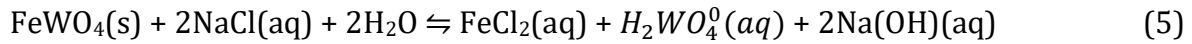
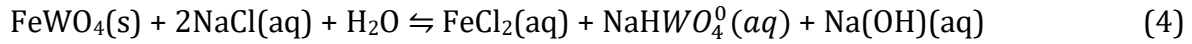
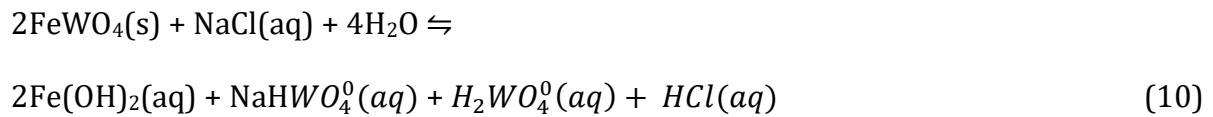
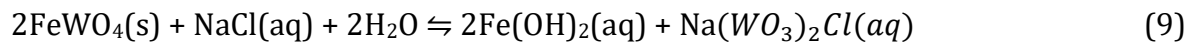
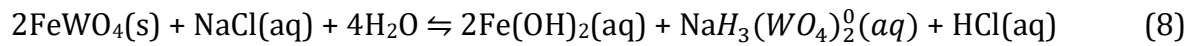


Fig. 5.11: $\log X_W$ vs. $\log X_{NaCl}$ calculated from W concentrations from solubility of scheelite and ferberite at 600 °C, 200 MPa in an aqueous fluid containing 1, 8 or 20 wt% NaCl at oxygen fugacity buffered with the FMQ buffer.

The quench pH of the residual fluid in the capsules was measured with pH-indicator papers. The measured pH was ca. 7-8 for all ferberite- or scheelite-bearing experiments. The seemingly neutral solution supports the dissolution reaction (3) or (7), where no acid or base is produced. But back-reaction and re-precipitation of the W-minerals could have

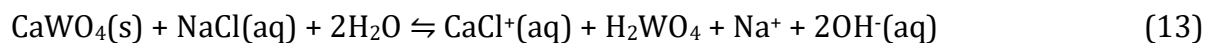
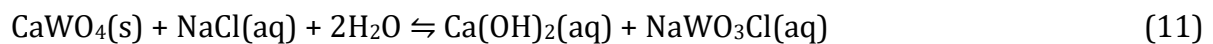
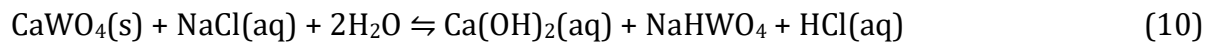
occurred upon cooling, which would influence the pH values determined after the experiment. According to thermodynamic modeling of Wood and Samson (2000) NaHWO_4^0 is the predominant species at 600 °C and 100 MPa, which would argue for reaction (4). They further inferred that dissolved Fe(II) prevails in the form of FeCl_2^0 at the conditions relevant to W-mineralizing fluids, which is the case in reactions (3) to (5).

The trend for $\log X_W$ from ferberite dissolution in Fig. 5.11 steepens considerably at higher salinities to a slope of at least 2. Explaining this trend with a dissolution reaction is less straightforward. The following reactions include species, which have not been proposed for tungsten transport previously ((8) and (9)) or the formation of two different W complexes (10):



According to Wood and Samson (2000), H_2WO_4^0 is never the predominant W species over the inferred range of conditions of W ore formation, but its relative contribution increases with increasing temperature and should therefore be considered regarding the mobilization and transport of W.

In contrast to $\log X_W$ from ferberite dissolution, $\log X_W$ from dissolution of scheelite appears to show a linear relation with $\log X_{\text{NaCl}}$ with a slope of one (Fig. 5.11) in the investigated salinity range. Possible dissolution reactions could be the following:



At high temperatures, neutral complexes are thought to prevail, due to the low density and low dielectric constant of the solvent (Pitzer, 1983), which supports reactions (10) and (11). On the other hand, Wood and Samson (2000) inferred that hydroxide complexes of Ca play an insignificant role compared to complexes of Ca with Cl, which would argue against reaction (10) and (11).

Altogether, we cannot fully unravel the underlying cause of the clear positive influence of salinity on W solubility, based on our experimental data. According to the model of Wood and Samson (2000), the existence of Cl complexes of W is not required to explain the formation of W deposits, as their model predicts W concentrations of several 100s to 1000s of ppm W without taking Cl complexes into account. Nevertheless, their model consistently underestimates W concentrations by a factor of 2 to 10, when comparing it to the available experimental data. This might hint to the necessity to invoke other W species, as e.g., Cl-bearing ones such as NaWO_3Cl or $\text{Na}_2\text{HWO}_4\text{Cl}_2$.

5.4.5 Temperature Dependence of Scheelite, Molybdenite and Gold Solubilities and Thermodynamic Considerations

Temperature is thought to be the most direct factor that influences mineral solubility and accordingly metal transport and precipitation (e.g., Pokrovski et al., 2014). Even though the stability of many metal-ligand complexes increases with increasing temperature this effect is not necessarily the same for different species. For instance, according to Robb (2005) stabilization of metal-chloride complexes is much more temperature-dependent than stabilization of equivalent sulfide complexes. The different effects of temperature on the stability of scheelite, molybdenite and gold can be observed in Fig. 5.12, where we plotted the normal logarithm of the concentrations of W, Mo and Au from dissolution the respective phases versus the inverse absolute temperature at otherwise constant conditions (200 MPa, 8 wt% NaCl and PPM buffer).

For all three metals the trends appear to be linear and concentrations decrease with decreasing temperature in the observed interval. But whereas the dependence of W concentration from dissolution of scheelite, and Au concentration from dissolution of gold is quite similar regardless of their different absolute values, the dependence of Mo concentration from dissolution of molybdenite on temperature is much more pronounced. The qualitative implication of this observation is that the enthalpy change of solution (ΔH_{sol}) is larger for molybdenite than for scheelite and gold. Thus, a decrease in temperature of a saturated solution, will lead to faster, i.e., more efficient precipitation of molybdenite in a narrower temperature interval compared to scheelite and gold.

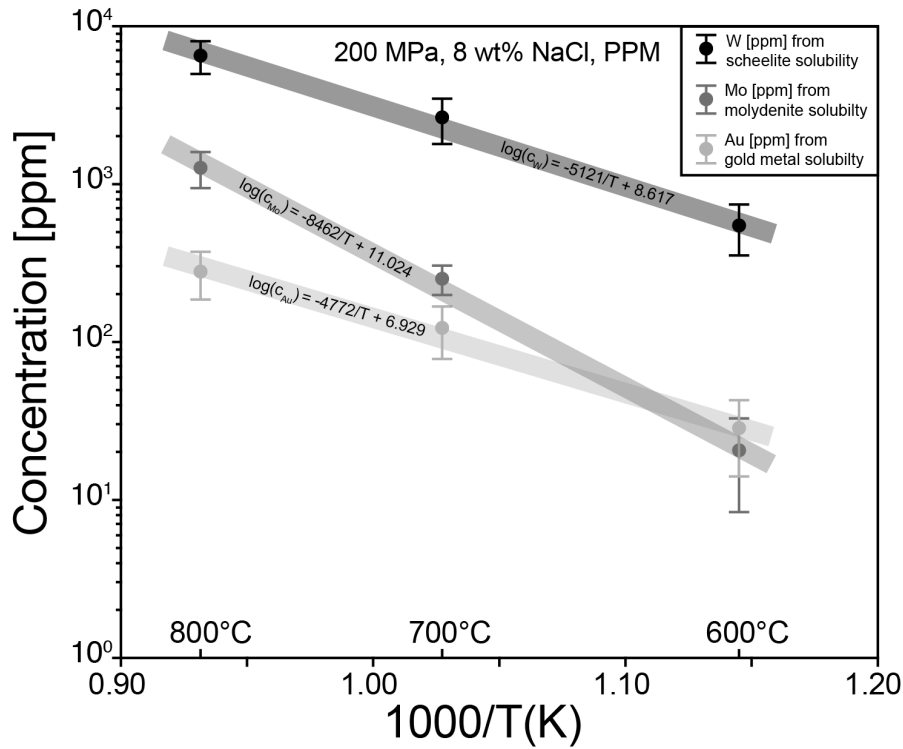


Fig. 5.12: Concentrations of W, Mo and Au from dissolution of scheelite, molybdenite and native gold versus the inverse absolute temperature at otherwise constant conditions (200 MPa, 8 wt% NaCl and PPM buffer). Grey lines were calculated using a logarithmic least square regression.

Without the knowledge of the exact dissolution reaction as well as activity models for the involved phases, it is impossible to calculate the exact ΔH_{sol} from slopes in Fig. 5.12, but simplified reactions can yield a qualitative estimate, as shown for the following example applied to the dissolution reaction involving scheelite:



For this simplified dissolution reaction of scheelite the equilibrium constant K can be written, as: $K = \frac{[\text{Ca}^{2+}] \cdot [\text{WO}_4^{2-}]}{[\text{CaWO}_4]}$ (15)

Assuming an activity of unity for pure scheelite, as well as $[\text{Ca}^{2+}] = [\text{WO}_4^{2-}]$ this gives:

$$K = [\text{WO}_4^{2-}]^2 \quad (16)$$

Rearranging the expression $\Delta G^\circ = \Delta H^\circ - T\Delta S^\circ = -RT \ln K$ and inserting into Eq. 16 leads to:

$$[\text{WO}_4^{2-}]^2 = e^{-\left(\frac{\Delta H^\circ - T\Delta S^\circ}{RT}\right)} \quad (17)$$

And to the following linear expression (with $y = \ln[\text{WO}_4^{2-}]$):

$$\ln[WO_4^{2-}] = -\frac{\Delta H^\circ}{2RT} + \frac{\Delta S^\circ}{2R} \quad (18)$$

With this equation ΔH° can be calculated from the slope of the regression line in Fig. 5.12, after transformation from the common logarithm to the natural logarithm:

$$\log[W] = -\frac{5121}{T} + 8.62 \Rightarrow \ln[W] = -\frac{11791}{T} + 19.84 \quad (19)$$

This leads to a value of ΔH° :

$$-\frac{\Delta H^\circ}{2R} = -11791 \Rightarrow \Delta H^\circ \approx 197 \text{ kJ}$$

As mentioned above, it is emphasized that this value is only a rough estimate of the enthalpy change of solution, taking into account the above assumptions including the highly simplified dissolution reaction of Eq. 14.

5.4.6 Comparison with Tungsten Concentrations in Natural Fluid Inclusions

In contrast to synthetic fluid inclusions with maximum concentrations of an element based on solubility of the respective mineral are determined, natural fluids are often undersaturated with respect to ore metals. Especially at high temperatures concentrations in natural fluid inclusions are usually not comparable to maximum concentrations from experiments (e.g., Heinrich and Candela, 2014; Pokrovski et al., 2014). Reported concentration of W in natural fluids from granite-related Sn-W deposits vary from usually a few ppm to several 100s of ppm, e.g., at Ehrenfriedersdorf, Germany; Grummetstock, Germany; Maoping, China; Mole Granite, Australia; Piaotang, China or Zinnwald, Germany (Albrecht, 2017; Audétat et al., 2000; Graupner et al., 2005; Heinrich et al., 1999a; Korges et al., 2018; Legros et al., 2019), but can reach up to a few 1000s of ppm in some localities, e.g., at the Beauvoir Rare-Metal Granite, France or Schellerhau, Germany (Albrecht, 2017; Harlaux et al., 2017). These concentration ranges are similar to the W-capacities determined within this study for fluids at intermediate to high temperatures (450 – 800 °C) and low salinities (8 wt% NaCl), or intermediate temperatures (600 °C) and low to intermediate salinities (1 – 20 wt%) (c.f., Fig. 5.5 and Fig. 5.9). It has to be noted though, that particularly at high temperatures and/or high salinities, maximum W-capacities from dissolution of ferberite or scheelite exceed common W-concentrations from natural fluid inclusions from W-deposits by far.

Among the different magmatic-hydrothermal W-deposits documented so far, higher W concentrations are often correlated with higher temperatures of formation and higher salinities of the fluid (e.g., Albrecht, 2017; Harlaux et al., 2017; Legros et al., 2019), which is in accordance with the observed trends of maximum W-concentrations in experiments from solubility of wolframite and scheelite. However, this correlation is not ubiquitous in all W-deposits and in some deposits only a clear correlation of W-concentration with either temperature (Audétat et al., 2000) or salinity (Graupner et al., 2005) was shown or no significant correlation was found at all (Korges et al., 2018). This might indicate different dominating transport and precipitation mechanisms in different W-ore deposits, as discussed in Chapter 5.4.3.

In Chapter 6, we determined element concentration from fluids of the Panasqueira W-Sn-(Cu-)deposit in Portugal. Previous studies calculated and determined W-concentrations for the fluids at Panasqueira at the very low end of the reported range, i.e. ca. 0.2 ppm and 1-70 ppm, by Polyá (1989) and Lecumberri-Sanchez et al. (2017), respectively. This is striking, as Panasqueira was historically one of the most important W deposits of the world and the main W producer in Europe.

6 Application #2: Natural Fluid Inclusions - Tungsten (W) and other Element Concentrations in Fluid Inclusions of the Panasqueira W-Sn-(Cu-)deposit

6.1 Geological Setting

The Panasqueira mining district is located in central Portugal ca. 34 km west of the city of Fundão. Geologically it is located within the Central Iberian Zone (CIZ) of the Iberian Massif (Fig. 6.1a), which formed as part of the European Variscan Belt due to the collision of Laurussia and Gondwana. This ultimately led to the closure of the Rheic Ocean (ca. 300 Ma) (e.g., Martínez Catalán et al., 2007; Ribeiro et al., 1990). The Iberian Massif contains numerous and voluminous plutons of granitoid composition, which were emplaced along the CIZ during the latest phases of the Variscan orogeny (synonymous with Hercynian orogeny).

One of these plutons was found by drilling below the Panasqueira district and was therefore called the Panasqueira granite (Fig. 6.1b). It is a peraluminous two-mica granite with porphyritic K-feldspar crystals and a chemical composition typical of S-type granites (Kelly and Rye, 1979; Polya, 1989), with an age of ca. 290 ± 10 Ma, determined by K-Ar dating (Clark, 1970) and ca. 296 ± 4 Ma by U-Pb dating (Launay et al., 2021). The granite intruded into country rocks of a sequence of tightly folded, pelitic schists and psammities of Cambrian or late Precambrian age, regionally called the Beira Schists (Fig. 6.1b) (Kelly and Rye, 1979; Polya, 1989; Thadeau, 1951). During the Variscan orogeny the Beira Schists were tightly folded and metamorphosed to greenschist-facies conditions. The intrusion of the Panasqueira granite occurred post-kinematic and caused intensive contact metamorphism and recrystallization of the Beira Schists in an area of ca. 20 km² around the deposit (spotted schists in Fig. 6.1b)(Kelly and Rye, 1979; Polya, 1989). Whereas the (nearly) fresh two-mica Panasqueira granite is only known from drill cores, the quartz–muscovite greisen cupola of the granite, which is topped by a ca. 15 m massive silicate cap, is exposed in the deeper levels of the underground mine workings (e.g., Noronha et al., 1992). Compared to the fresh granite the greisen shows depletion in Mg,

Ti, Ca, Na, Ba, Sr and REE as well as enrichment in Fe, Li, Rb, Cs, Sn and W, which is interpreted as the result of the interaction of W-Sn-bearing fluids with the granite during greisenization (Launay et al., 2021).

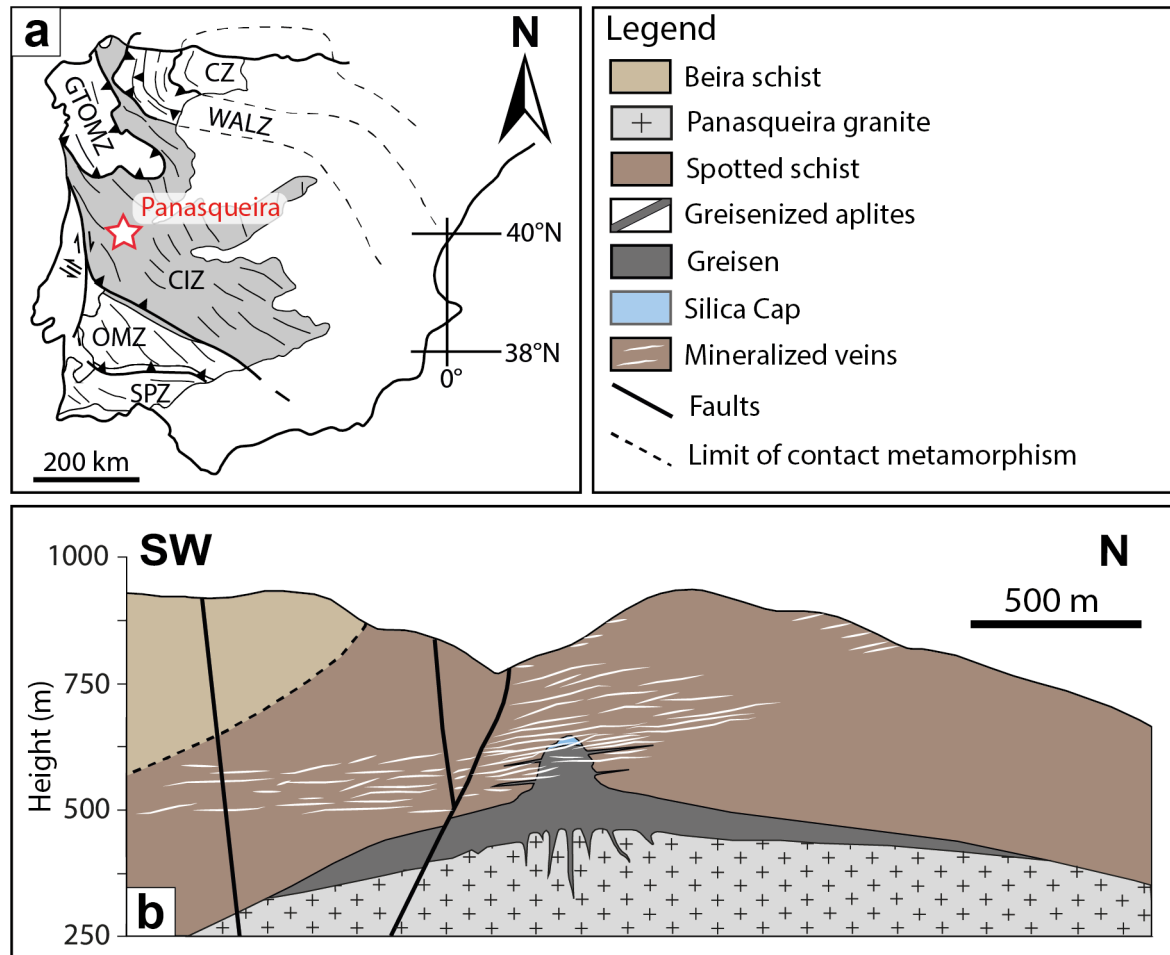



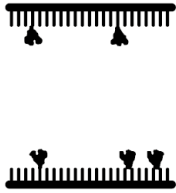


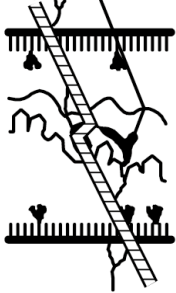
Fig. 6.1: (a) Simplified map of the Iberian Peninsula depicting the main tectonostratigraphic domains of the Variscan Iberian Massif defined by Julivert et al. (1972). CZ: Cantabrian Zone; WALZ: West Asturian-Leonese Zone; GTMZ: Galicia Tràs-os-Montes Zone; CIZ: Central Iberian Zone; OMZ: Ossa-Morena Zone and SPZ: South Portuguese Zone. The red star marks the location of the Panasqueira deposit. (b) Schematic cross section of the Panasqueira deposit depicting the spatial relationship between mineralized veins and the Panasqueira granite, including the greisen cupola and silica cap (data source: Beralt Tin and Wolfram S.A.). Modified after Launay et al. (2018).

6.2 The Mineralized Veins

The economic W-Sn-(Cu) mineralization of Panasqueira consists of a dense network of sub-horizontal quartz veins mostly hosted by the Beira Schists. The ore zone is centered on the greisen cupola, which is also cut by the mineralized veins (e.g., Foxford et al., 1991; Kelly and Rye, 1979; Polya, 1989). The economically important minerals in the veins are

wolframite ((Fe,Mn)WO₄), cassiterite (SnO₂), and chalcopyrite (CuFeS₂) in that order of importance (Kelly and Rye, 1979). The ore zone, i.e., the volume of rock in which the mineralized veins occur, extends over a lateral area of ca. 6 km² and to a depth of several hundred meters (Polya et al., 2000). The paragenetic sequence of the veins was described by Kelly and Rye (1979) and complemented by Foxford et al. (2000), Polya et al. (2000) and Launay (2018). All authors distinguish between four to six mineralization stages, but the classification of Foxford et al. (2000) is used most frequently. In chronological order Foxford et al. (2000) distinguish between the early Quartz-Tourmaline stage (QTS), the Main Oxide Silicate Stage (MOSS), the Main Sulfide Stage (MSS), the Pyrrhotite Alteration Stage (PAS) and the Late Carbonate Stage (LCS). The QTS and MOSS are thought to be a continuous sequence, which was overgrown or crosscut by the MSS mineralization and

Tab. 6.1: Brief characteristics of the paragenetic stages at Panasqueira based on Kelly and Rye (1979), Polya et al. (2000) and Foxford et al. (2000).

	QTS	MOSS	MSS	PAS	LCS
Schematic Appearance					
Primary Minerals	Quartz Tourmaline	Quartz Tourmaline Muscovite Arsenopyrite Topaz Cassiterite Apatite Wolframite	Quartz Tourmaline Muscovite Arsenopyrite Phosphates Apatite Sphalerite Pyrrhotite Pyrite Chalcopyrite Cassiterite	Siderite Pyrite Marcasite Chalcopyrite Stannite Galena As-Bi-Sulphosalts	Dolomite Calcite Ni-As-Sulphides
Approximate Volume	< 1 %	65 %	16 %	3 %	< 1 %
Summary	Quartz and tourmaline were precipitated at propagating vein tips in newly formed fractures.	Growth of muscovite (muscovite selvage formation stage of Polya (1989)), topaz, wolframite, quartz and arsenopyrite into rapidly opening veins.	During the climactic phase of vein opening polymetallic sulphides, quartz and apatite were deposited	Alteration of MSS pyrrhotite and resulting growth of pyrite, marcasite and siderite.	Late precipitation of dolomite, calcite and chlorite from a fluid presumably unrelated to the hydrothermal system.

later crosscut by the PAS and LCS. During the two latest stages the permeable structures changed from horizontal to sub-vertical fractures, which implies a change in the tectonic stresses and lead to the interpretation that these stages postdate the main hydrothermal ore-forming event (Foxford et al., 2000). An overview of the paragenetic sequence is given in Tab. 6.1.

Most of the opening and sealing of the veins occurred during the first three stages, with the maximum opening being related to the MOSS and MSS, which host the economic W-Sn and Cu mineralization, respectively, and which probably formed during one single tectonic event (Foxford et al., 2000; Polya et al., 2000). According to $^{40}\text{Ar}/^{39}\text{Ar}$ dating of muscovites of the MOSS and MSS a timespan from ca. 296 to 292 Ma was derived, which is coeval with the greisenization of the granite, whose youngest muscovites yield an age of ca. 292 Ma (Snee et al., 1988). Similar ages were determined by Launay et al. (2021) with U-Pb dating on apatites from the greisen and mineralized veins, which yielded U-Pb ages of $292 \pm 10\text{Ma}$ and $295 \pm 5\text{Ma}$, respectively, providing strong evidence for the hypothesis of contemporaneous greisenization and formation of the mineralized veins. The additional overlap with the cooling age of the Panasqueira granite itself ($296 \pm 4\text{Ma}$) is interpreted as proof for a close temporal and genetic link between greisenization, W-Sn mineralization and crystallization of the granite (Launay et al., 2021). A statistical multivariate approach using major and trace element data by Launay et al. (2021) demonstrated strong similarities in compositions between quartz and muscovite from greisen and the same minerals in the ore-bearing veins. This further supports the idea that greisenization and the formation of mineralized veins resulted from the same hydrothermal event. In addition Launay et al. (2021) used Ti-in quartz thermometry to determine the thermal development of the magmatic-hydrothermal system from quartz in the granite (700–600 °C), to hydrothermal quartz in the greisen (500–400 °C) and in the mineralized veins (450–350 °C). Launay et al. (2021) interpret their data in accordance with the classical idea of formation of a magmatic-hydrothermal deposit, i.e. the granitic magma is the primary source of heat, fluids as well as metals and transporting ligands (e.g., Audétat, 2019; Audétat et al., 2008; Barnes, 1997; Bodnar et al., 2014; Heinrich and Candela, 2014). Therefore, the greisenization and the formation of W-Sn bearing quartz veins are thought to have developed during the final stage of solidification of the Panasqueira two-mica granite at the magmatic hydrothermal transition, during which metal (W and Sn)-rich orthomagmatic fluids were released.

However, this model is debated in the literature and the actual source of the mineralizing fluids at Panasqueira has been the topic of a controversy for several decades. Based on isotopic and trace element analyses, the fluids at Panasqueira appear to have several different origins, but there is a rather widespread consensus that at least in the first three stages of vein mineralization these fluids were dominated by a magmatic component (Bussink, 1984; Codeço et al., 2017; Kelly and Rye, 1979; Launay et al., 2018; Lecumberri-Sanchez et al., 2017; Neiva, 2008; Polyá et al., 2000; Snee et al., 1988). In contrast, many authors advocate a strong influence of a sedimentary and/or meteoric fluid during the later stages of mineralization and some also argue for the involvement of additional fluids with respect to metal deposition or even transport. Based on an estimation of 0.2 ppm W in the main stage fluids, Polyá (1989) inferred that a total volume of ca. 1000 km³ of hydrothermal fluids must have passed through the vein system solely during the MOSS. Such a large amount of fluid as well as the supposed shallow depth of ore formation (Kelly and Rye, 1979), seems to make the dominance of a meteoric fluid during metal transport and deposition indispensable. Furthermore, high ³He/⁴He ratios from arsenopyrite and wolframite from the mineralized veins also indicate a mantle derived component in the ore fluids (Burnard and Polyá, 2004), whereas other authors have recently advocated for the dominance of metamorphic fluids from the surrounding country rocks as well as a deep feeder zone at a depth of ca. 15-20 km as the result of biotite dehydration reactions (Carocci et al., 2021; Cathelineau et al., 2020).

Even though our study is not designed to unravel the origin of the ore forming fluids at Panasqueira, it provides further constraints based on trace element compositions of the fluids and might narrow down possible sources. As stated in the objectives of this work (Chapter 2), our primary motivation to study fluid inclusions from mineralized veins is to constrain natural metal concentrations in general and W concentrations in particular to get an idea about the ore-forming capacities of the fluids involved, i.e., the fluid volume that is required to form a deposit such as the Panasqueira W-Sn-(Cu-)deposit. Based on our experimental data (Chapter 5), we want to estimate the degree of undersaturation of the natural fluids with respect to W, which will have direct implications on the conditions and possible processes during ore-mineral precipitation.

6.3 Previous Work on Fluid Inclusions of the Panasqueira Vein System

There have been several studies on fluid inclusions of the Panasqueira vein minerals, with the first systematic study being that of Kelly and Rye (1979), who did a microthermometric investigation on different vein minerals from the MOSS, MSS, PAS and LCS. They found homogenization temperatures of 230-360 °C for the first three stages and consistent salinities of ca. 5-10 wt% NaCl_{eq.}. Only in the LCS homogenization temperatures dropped to 70-120 °C and salinities to < 5 wt% NaCl_{eq.}. Similar results were obtained by Bussink (1984), who determined homogenization temperatures of 250-325 °C and salinities between 5-10wt% NaCl_{eq.} for the early stages and ca. 100 °C and ≤ 3wt% NaCl_{eq.} for the LCS, respectively. The reported values from Polya et al. (2000) from a hydrothermal quartz crystal from the MSS also fall within the same homogenization temperature range of 241-260 °C, and salinities of 7.1-8.7 wt% NaCl_{eq.}.

Next to abundant liquid-rich fluid inclusions, Kelly and Rye (1979) and Bussink (1984) reported the occurrence of vapor-rich fluid inclusions in minerals from the MOSS. This led them to the assumption of a boiling fluid during ore deposition and entrapment, so that they directly inferred the temperature and pressure of formation from the point of homogenization of the fluid inclusions. The derived pressures were in a range of 10-150 MPa with the majority at the low pressure end, which led the authors to infer a shallow depth of emplacement for the Panasqueira granite and ore-veins as well as the necessity of the participation of a meteoric fluid during ore formation (Bussink, 1984; Kelly and Rye, 1979). In contrast, Jaques and Pascal (2017) interpret fluid inclusions from Panasqueira vein-quartz with a low degree of fill (vapor-rich) as the result of stretching and necking-down due to post-entrapment changes and rule out boiling as a dominant process. Based on fluid isochores combined with different mineral geothermo- and geobarometers, they derived pressures of ca. 300 MPa, which are in good agreement with the geologic evolution of the region. This is also supported by Cathelineau et al. (2020), who report ample evidence of decrepitation and deformation of fluid inclusions particularly in the early generation of vein quartz. They report similar trapping conditions of ca. 500 ±20 °C and 250 ±20 MPa for undeformed fluid inclusions from topaz, which they interpret to belong to the early MSS, rather than MOSS (c.f., Tab. 6.1).

Kelly and Rye (1979) and Bussink (1984) report the presence of CO₂ and subordinate CH₄ and N₂ in fluid inclusions of the vein minerals. Based on gas chromatography they

determined 0.5-2 mol% CO₂ in the abundant liquid-rich inclusions, and 6-10 mol% in subordinate vapor-rich inclusions. On a H₂O free basis Bussink (1984) further reports a main gas composition of fluid inclusions from quartz, topaz and wolframite of 65-80 mol% CO₂, 10-20 mol% CH₄ and 10-17 mol% N₂. Nevertheless, Kelly and Rye (1979) and Bussink (1984) do not account for the effect of C-species on final ice melting temperatures. This effect occurs due to the formation of gas hydrates (clathrates) in the presence of C-species at low temperatures, which incorporate abundant H₂O in their structure. As a result of the formation of clathrates, the salinity of the residual aqueous solution increases and the observed temperatures of final ice melting (T_{m-ice}) decrease (e.g., Collins, 1979; Darling, 1991; Diamond, 2001; Fall et al., 2011). Mole fractions of non-aqueous gas species were also determined by Noronha et al. (1992) using Raman spectroscopy on fluid inclusions from vein quartz. Their results differ slightly from those of Bussink (1984) with lower CO₂ and CH₄ contents of 60-73 mol% and 6-16 mol%, respectively, and higher N₂ contents of 20-31 mol%. Jaques and Pascal (2017) and Cathelineau et al. (2020) also report CO₂, CH₄ and N₂ as detectable volatile components in fluid inclusions from quartz and topaz from the MSS based on microthermometric observations and Raman spectroscopy. Both studies distinguish between fluid inclusions with visible melting and homogenization of CO₂ (Lc-w) and fluid inclusions in which only clathrates were detected as optical evidence for C-species (Lw-c). Cathelineau et al. (2020) further distinguish fluid inclusions with very low contents of an aqueous liquid (< 10 vol%, Lc-(w)) and Jaques and Pascal (2017) discriminate between fluid inclusions from early, milky quartz (Qz I) and later, clear quartz (Qz II). Except for the CO₂-dominated Lc-(w) inclusions in Topaz from Cathelineau et al. (2020), all fluid inclusions contain an aqueous-rich fluid with low to moderate salinity and variable amounts of CO₂, CH₄ and N₂ in the gaseous phase, whereas CO₂ always has a clear predominance over the other volatiles. Tab. 6.2 summarizes the results obtained from fluid inclusion analyses of the studies mentioned in this chapter. Data from the recent studies of Jaques and Pascal (2017) and Cathelineau et al. (2020) are roughly of the same order as from previous studies, but imply a slightly higher volatile component in the fluids with a stronger predominance of CO₂ than determined in older studies. The mean NaCl_{eq.} content is lower for the two recent studies, because Jaques and Pascal (2017) and Cathelineau et al. (2020) accounted for the effect of clathrates and their impact on final ice melting temperatures.

Resulting mean NaCl_{eq} contents in the different types of aqueous fluid inclusions recalculated to weight percentages are in the range of 3.6 to 5.8 wt%.

Tab. 6.2: Compilation of fluid inclusion data from the mineralized veins at Panasqueira, including microthermometric parameters, volatile phase compositions as determined by Raman spectroscopy and calculated or analyzed bulk compositions.

Study	Host	Type	Stage	Microthermometry (°C)					Volatile phase (mole%)			Bulk composition (mole%)				
				T _{m-ice}	T _{m-clath}	T _{m-co2}	T _{h-co2}	T _{hom}	CO ₂	CH ₄	N ₂	H ₂ O	CO ₂	CH ₄	N ₂	NaCl
K&R 1979	Qz	Type I	MOSS/MSS /PAS	-7.2/ -3.2	-5.4/ 11.0			230/ 360				96	1/2			2
B 1984	Qz	Type I	MOSS/MSS /PAS	-6.5/ -2.0	6.0/ 13.5	-64.0/ -59.0		250/ 325	65/ 80	10/ 20	10/ 17		0.5/ 2.0			
N al. 1992	Qz (I)	Lc-w	MOSS	-6.9	8.3	-60.8	-2.2	288	65	9	26	90/ 93	3.0/ 4.0	0.1/ 0.2	0.1/ 0.9	2.5/ 3.0
J&P 2017	Qz I	Lw-c	MSS	-6.9	8.0			251	62.0	23.6	14.3	94.3	2.4			1.5
J&P 2017	Qz II	Lw-c	MSS	-6.3	7.9			254	65.9	25.8	8.3	94.0	2.7			1.4
J&P 2017	Qz I	Lc-w	MSS	-7.9	8.1	-61.2		231	87.4	5.4	7.2	93.8	3.3			1.4
J&P 2017	Qz II	Lc-w	MSS	-7.5	7.9	-61.2	6.4	236	90.2	7.4	2.3	92.7	4.7			1.2
Cal. 2020	Qz I	Lw-c	MSS	-6.5	8.6	-59.5		204	84.1	10.7	5.2	92.9	4.9	0.3	0.3	1.6
Cal. 2020	Tpz	Lw-c	MSS	-5.7	6.9	-60.0		250	85.2	6.2	8.6	94.6	3.4	0.1	0.1	1.7
Cal. 2020	Tpz	Lc-w	MSS	-5.3	8.6	-59.0	17.1	263	89.5	3.4	7.1	92.2	5.4	0.1	0.3	2.0
Cal. 2020	Tpz	Lc(-w)	MSS	-5.6	9.5	-59.2	11.1	300	85.5	3.2	11.3	14.8	72.9	2.7	9.6	0.1

K&R 1979 – Kelly & Rye (1979), B 1984 – Bussink (1984), N al. 1992 – Noronha et al. (1992), J&P 2017 – Jaques & Pascale (2017), Cal. 2020 – Cathelineau et al. (2020), host – host mineral, stage – paragenetic stage, see text for other abbreviations.

Salinity in natural fluids is mostly dominated by NaCl and so are the fluids at the Panasqueira deposit. Kelly and Rye (1979) did electron microscopy on evaporites from opened inclusions and showed that the salts were predominantly NaCl with small amounts of KCl. Bussink (1984) also detected Na and subordinate K using mass-spectrometry on opened fluid inclusions, as well as trace amounts of Rb and Cs. Polya (1989) analyzed relative concentrations of Na, K, Ca, Mg, and Fe from bulk fluid inclusion leachates and determined the following mean atomic ratios: $\text{K/Na} \approx 0.2$, $\text{Ca/Na} \approx 0.02$, $\text{Mg/Na} \approx 0.02$, and $\text{Fe/Na} \approx 0.0005$. Cation ratios from Noronha et al. (1992) determined by atomic absorption from leachates of crushed quartz also reveal a NaCl-rich fluid with subordinate amounts of K, Ca and Mg, but their atomic ratios differ from those of Polya (1989) in particular for the potassium-sodium ratio, i.e., $\text{K/Na} \approx 0.02$, $\text{Ca/Na} \approx 0.02$, $\text{Mg/Na} \approx 0.03$. To our knowledge, Lecumberri-Sanchez et al. (2017) were the first to perform LA-ICP-MS on individual fluid inclusions of the Panasqueira deposit. Calcium, Mg and (in all but one case) Fe are below the detection limit of the method. But they were able to determine, among other elements, concentrations of the alkali metals Li, Na, K, Rb

and Cs. Recalculated mean atomic ratios from Lecumberri-Sanchez et al. (2017) are $\text{Li/Na} \approx 0.2$, $\text{K/Na} \approx 0.09$, $\text{Rb/Na} \approx 0.001$ and $\text{Cs/Na} \approx 0.002$. Tungsten concentrations determined by Lecumberri-Sanchez et al. (2017) range from 1-70 ppm.

6.4 Sample Description

In this study we analyzed natural fluid inclusions from a ca. 13 cm long euhedral quartz crystal from a mineralized vein, which was collected by Andy Foxford (Dave Polya team, University of Manchester) and has been described in Foxford (1992) as sample Pa150, a “vug quartz crystal coated with muscovite”, sampled in situ from mine grid coordinates “31183[/]53595, Level 2 (576m)”. The sampling location of Pa150 is shown in Fig. 6.2.

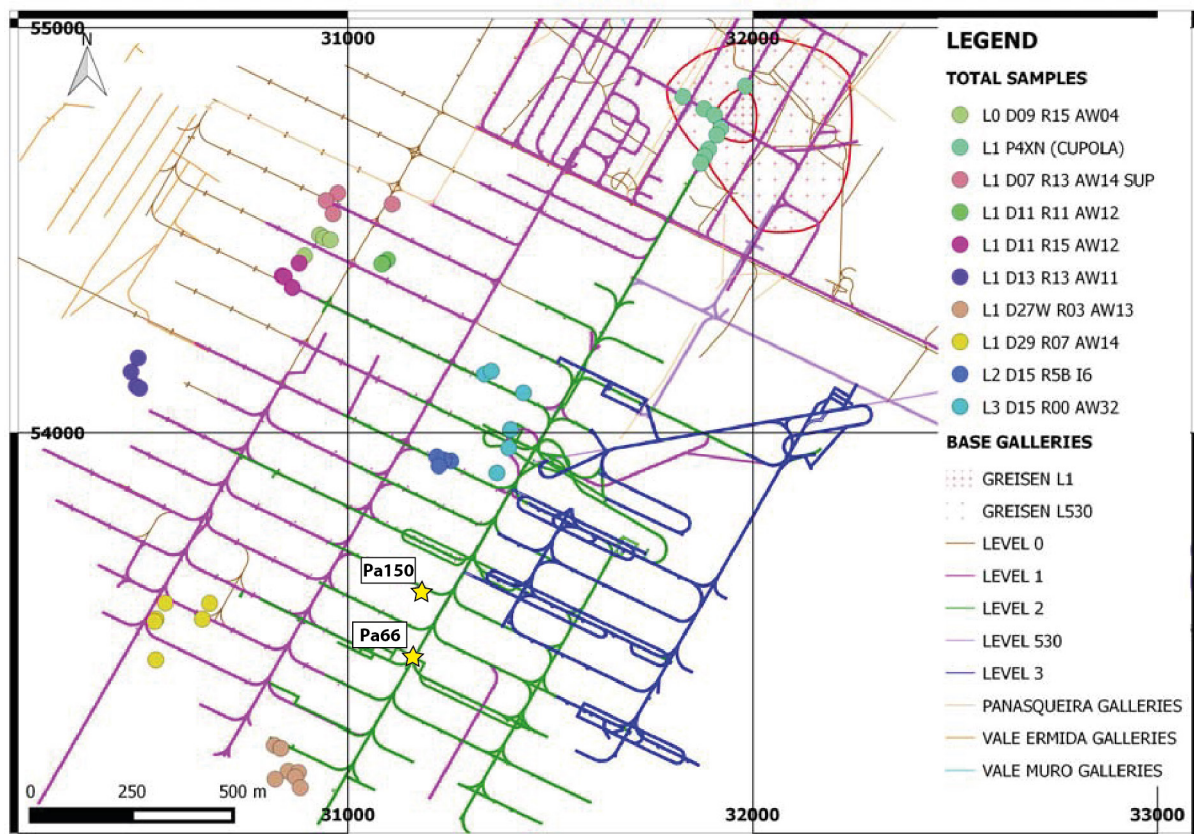


Fig. 6.2: Map projection of the Panasqueira mine with sampling localities from Lecumberri-Sanchez et al. (2017) (circles). Yellow stars mark the sampling localities of two vug quartz crystals Pa66 (studied in Foxford (1992) and Polya et. al (2000)) and Pa150 (studied in Foxford (1992) and this study).

Euhedral crystals in vuggy parts of the veins are common in the Panasqueira mine and are thought to expose the same generations of minerals as the majority of massive vein

fillings. Therefore, vug minerals, such as the investigated quartz Pa150, do not represent late precipitates, but can be regarded as minerals that formed contemporaneously with the main vein stages (Foxford, 1992; Kelly and Rye, 1979). Sample Pa150 comes from such a vuggy part of a mineralized vein, comprising the early paragenetic stages from QTS to MSS. It is partially over- and intergrown with muscovite and sulfides from the MSS (Fig. 6.3a and b) and contains a vast number of fluid inclusions, which are to some extent macroscopically visible. Several growth zones in the quartz crystal are outlined by primary fluid inclusions, and two of these zones are also outlined by sulfides (pyrite and chalcopyrite) of the MSS. Numerous trails of secondary fluid inclusions occur parallel to the basal fracture of the quartz. Isolated trails close to the top of the crystal are interpreted to be of secondary or pseudosecondary nature (Fig. 6.3c).

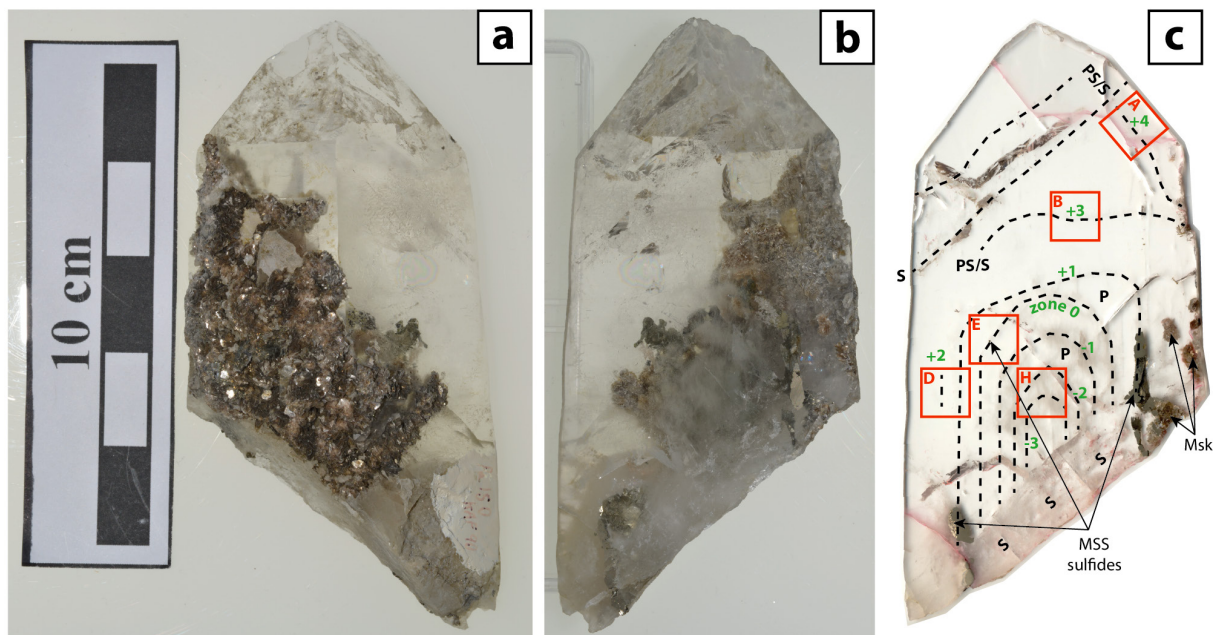


Fig. 6.3: Vug quartz sample Pa 150; a) exterior view of the euhedral quartz crystal, which is partially over- and intergrown with muscovite and sulfides of the MSS; b) cut surface along the c-axis of the crystal; the sulfides of the MSS (mostly pyrite and subordinate chalcopyrite) are intergrown with the quartz crystal along growth zones; c) thick section through the center of the quartz crystal; dashed lines retrace fluid inclusion trails (P: primary fluid inclusions, S: secondary fluid inclusions, PS: pseudosecondary fluid inclusions), which are numbered (in green) with respect to “zone 0”, along which the MSS sulfides occur for the first time; red squares mark the localities, from which sections were prepared for analyses with microthermometry and LA-ICP-MS.

As described by Foxford (1992) the core of the quartz crystal appears milky, due to the large amount of fluid inclusions concentrated in this part of the crystal (Fig. 6.3b and c). Within this “core cloud” no further zones can be distinguished, but the outer boundaries clearly follow the crystallographic faces of the quartz crystal and fluid inclusions from

later stages are mostly aligned along these rhombohedral growth faces and can therefore be regarded as primary fluid inclusions trapped from the fluid that precipitated the quartz upon growth. In a similar quartz crystal from the Panasqueira mine (Pa66, c.f., Fig. 6.2), Polya et al. (2000) interpreted quartz from the milky core to represent either late MOSS or early MSS. Quartz from the distinct growth zones is unequivocally contributed to the MSS stage. We numbered the growth zones with respect to a “zone 0”, which is the face, along which sulfides of the MSS occur next to primary fluid inclusions for the first time, i.e., zones -3, -2 and -1 predate zone 0, and zones +1, +2, +3 and +4 postdate it in successive order.

6.5 Analytical Methods

Fluid inclusions from five 1 cm x 1 cm x 300 μm doubly polished chips from Pa150 (chips A, B, D, E and H from Fig. 6.3c) were examined petrographically and a relative chronological sequence was defined (zones -3 to +4, c.f., Fig. 6.3c). For the determination of NaCl_{eq} values for internal standardization during LA-ICP-MS analyses, more than 500 fluid inclusions were analyzed by microthermometry using a Linkam FTIR600 heating-freezing stage. The microthermometry system was calibrated daily with two self-made synthetic standards with $\text{CO}_2\text{-H}_2\text{O}$ and pure H_2O fluid inclusions, respectively. For the three-point calibration curve in the Linkam Software Linksys32 the melting point of CO_2 , the melting point of H_2O and the homogenization temperature of pure H_2O were determined. For the natural fluid inclusions in Pa150, final ice melting temperatures ($T_{\text{m-ice}}$) were determined and where possible eutectic melting (T_{eutec}), too, to get a first idea about other salts in the system, e.g. CaCl_2 or KCl . In many of the fluid inclusions the formation of clathrates was observed and for those inclusions the melting temperature of clathrate ($T_{\text{m-clath}}$) was determined as well. Unfortunately, precision for clathrate melting temperatures was low and is only given as full $^\circ\text{C}$ values, as the exact melting point was not easy to observe and often varied with each reheating phase by 1-2 $^\circ\text{C}$, which suggests metastable behavior. No homogenization temperatures of fluid inclusions were determined for Pa150 as they are not required for the internal standardization of LA-ICP-MS analyses and there is a considerable risk of decrepitation of fluid inclusions upon heating to several hundred degrees, which would make subsequent LA-ICP-MS analyses impossible. In addition, homogenization temperatures of fluid inclusions from the different mineralizing stages at Panasqueira have been obtained by several authors

before (refer to Chapter 6.2.1; e.g., Bussink, 1984; Cathelineau et al., 2020; Jaques and Pascal, 2017; Kelly and Rye, 1979). Fluid inclusions from the „milky“ core and adjacent growth zones were analyzed for their major and trace element compositions from chips B, D, E and H using the LA-ICP-MS method described in Chapter 3. Samples and external standard (NIST610) were kept at a temperature of -60 °C during analyses and spot ablation was carried out with a repetition rate of 10 Hz. The external standard was measured twice at the beginning and at the end of a sample sequence and once after every fifth fluid inclusion (standard bracketing) to correct for potential machine drift. Fluid inclusions > 25µm were analyzed and ablated completely via a fast-spiral movement of a Linux CNC controlled laser stage with a laser repetition rate of 125 to 250 Hz depending on the depth and size of the inclusion as described in Albrecht (2017). As described in Chapter 4.2, the analytical method was adjusted by mixing He carrier gas with 2 vol% H₂ to increase the sensitivity of the method (Guillong and Heinrich, 2007). However, this leads to a strong polyatomic interference of ³⁸Ar and ¹H from the auxiliary gas and carrier gas, respectively, with ³⁹K, so that potassium could only be detected above the detection limit in very large fluid inclusions. To get a better estimate of K concentrations in the fluids, additional fluid inclusions from sample chips D and H were analyzed with He only as carrier gas. The acquired data was evaluated using the SILLIS data reduction software (Guillong et al., 2008b), where the calculated NaCl_{eq.} values were used for internal standardization.

6.6 Results

Sample chip H represents the “milky” core and contains segments of zones -3 and -2. The fluid inclusions in those two zones are not distributed along narrow trails, but cover broad areas following roughly the crystallographic growth zones. They are densely packed with innumerable fluid inclusions (Fig. 6.4a-c) and the transition from zone -3 to -2 is not sharp but marked by an area with considerably less fluid inclusions in-between the two zones (Fig. 6.4d). Most fluid inclusions show a negative crystal shape with sizes up to 50 µm, but fluid inclusions up to 100 µm are not uncommon. Fluid inclusions are roughly isometric and contain two phases, namely an aqueous liquid and a vapor bubble, with the liquid taking up ca. 70-80 % of the inclusion. Very few fluid inclusions with a higher degree of fill (i.e., a smaller vapor bubble) were observed. They are interpreted to be either of (pseudo-)secondary origin or the result of necking down and were avoided during

analyses. There is evidence for both theories: In Fig. 6.4a and b fluid inclusions that show evidence of stretching and necking-down are marked with red arrows. Fig. 6.4b shows one of two supposedly (pseudo-) secondary trails, which crosscut zone -3 perpendicular to it.

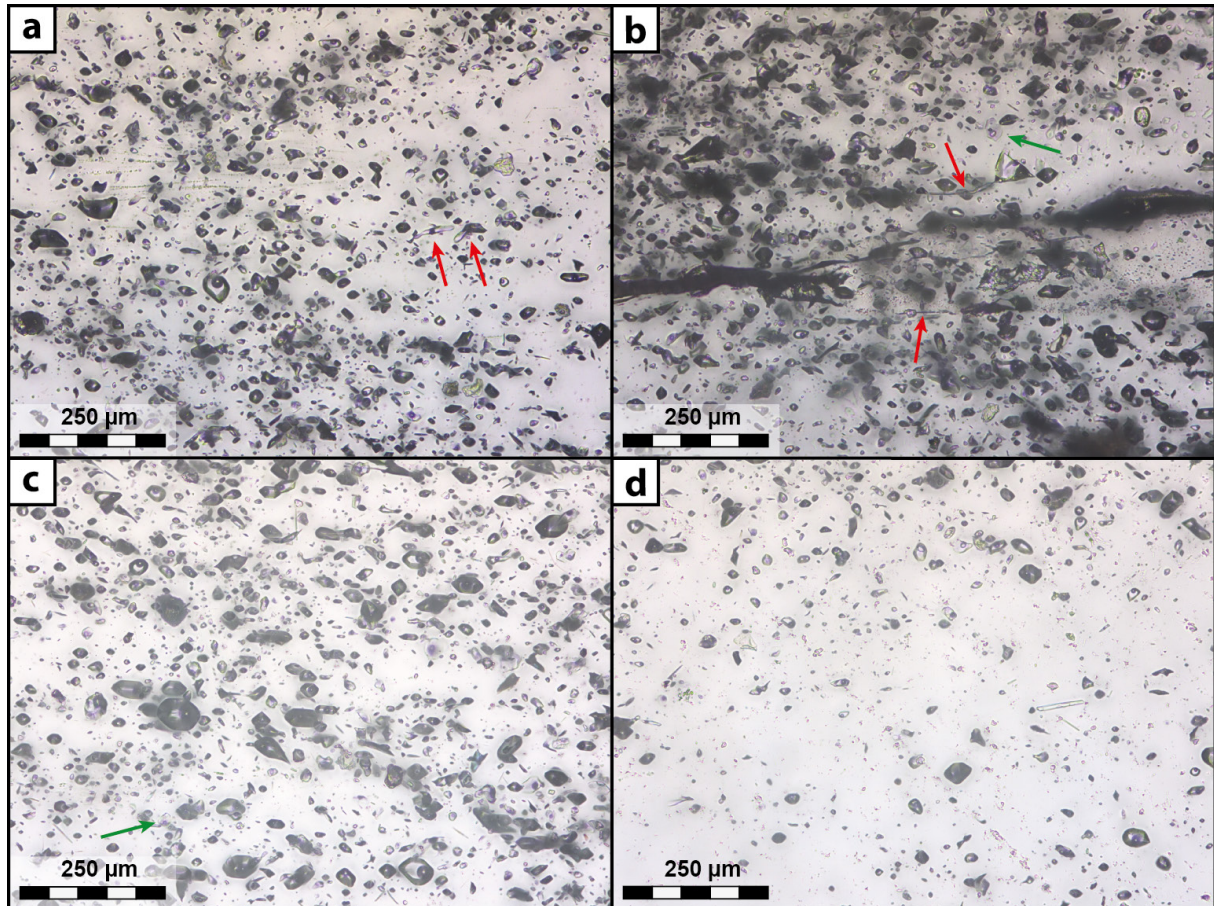


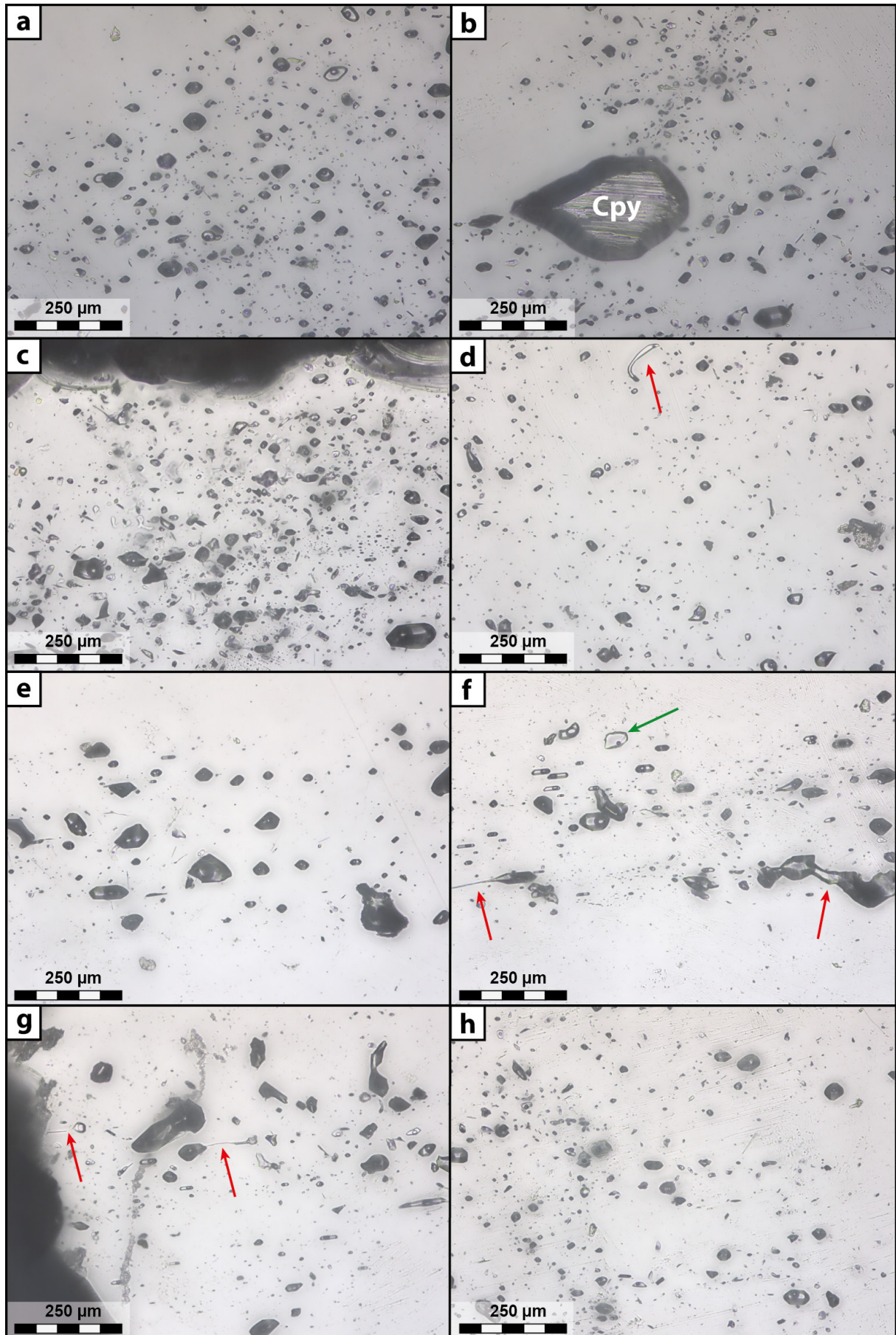
Fig. 6.4: Photomicrographs of two-phase fluid inclusions from the “milky” core of sample chip H. (a and b) Fluid inclusions in zone -3; (b) (pseudo-)secondary trail, crosscutting zone -3 (black sub-horizontal zone); (c) fluid inclusions in zone -2 resemble those in zone -3; (d) area with less fluid inclusions in-between zones -3 and -2. Images were taken in transmitted light and were enhanced by focus stacking. Red arrows point at possible examples of stretching and necking down, i.e., post-entrapment modification, of fluid inclusions; green arrows point at fluid inclusions with a supposedly higher degree of fill.

Sample chips D and E contain three distinct growth zones, which mark former crystal faces that are outlined by trails of fluid inclusions and in the case of zones 0 and +1 additionally with grains of sulfides from the MSS (Fig. 6.3c, Fig. 6.5b). Zone +2 in chip D is marked by three isolated occurrences of fluid inclusion “clouds” with a diameter of ca. 1-2 mm, which are located parallel to zone +1 and cannot be interpreted as primary fluid inclusions unequivocally. In addition, fluid inclusions from the top left corner of chip E

might be from a similar isolated occurrence and cannot be correlated with zone +1 from chip D for sure. Fluid inclusions from zones -1 to +1 are very abundant but less densely crowded than inclusions from the “milky” core and more confined to narrow trails with almost no fluid inclusions in-between different zones. They are similar to inclusions from the core though, in that they mostly show negative crystal shapes and have a similar range in sizes and degrees of fill. In zone +1 larger fluid inclusions of $> 50 \mu\text{m}$ seem to be more common than in the previous zones. Sporadically, inclusions with a higher degree of fill occur throughout chips D and E (e.g., Fig. 6.5f). Similar to the core zones there is only subordinate evidence for post-entrapment modifications of fluid inclusions in the form of stretching and necking-down (red arrows in Fig. 6.5d, f and g).

Fluid inclusions in a supposedly pseudosecondary or secondary trail (zone +3) in chip B are considerably larger on average than inclusions in the previous zones, with quite a few inclusions exceeding $100 \mu\text{m}$ (Fig. 6.6a and b). The inclusions almost always show a negative crystal shape and a constant degree of fill of ca. 70-80 %. No signs of necking-down were observed and all inclusions are close to isometric. Even though fluid inclusions in a trail in chip A (zone +4) are also interpreted as secondary or possibly pseudosecondary inclusions and show similar or even larger sizes than fluid inclusions from zone +3, their appearance is considerably different from inclusions in that zone and all previous zones. Most inclusions in zone +4 show irregular shapes with often serrated surfaces (Fig. 6.6e). Isometric fluid inclusions occur, but many inclusions are elongated. In addition, there is ample evidence of necking-down (red arrows in Fig. 6.6c, d and f), such as “necking tails” and various degrees of fill, which in some areas resemble a boiling assemblage (Fig. 6.6c), but are likely due to heterogeneous necking-down. Therefore, sample chip A was discarded from all further examinations.

Fig. 6.5 (next page): Photomicrographs of two-phase fluid inclusions from sample chips E and D. (a and b) Fluid inclusions in zone 0 from chip E; (b) Chalcopyrite grain (Cpy) along fluid inclusion trail from zone 0 in chip E; (c) fluid inclusions in zone -1 from chip E; (d) fluid inclusions in zone +1 from a possibly isolated occurrence in chip E; (e - g) fluid inclusions in zone +1 from chip D; (h) fluid inclusions in zone +2 from an isolated “cloud” in chip D. Images were taken in transmitted light and were enhanced by focus stacking. Red arrows point at possible examples of stretching and necking down, i.e., post-entrapment modification, of fluid inclusions; green arrow points at a fluid inclusion with a supposedly higher degree of fill.



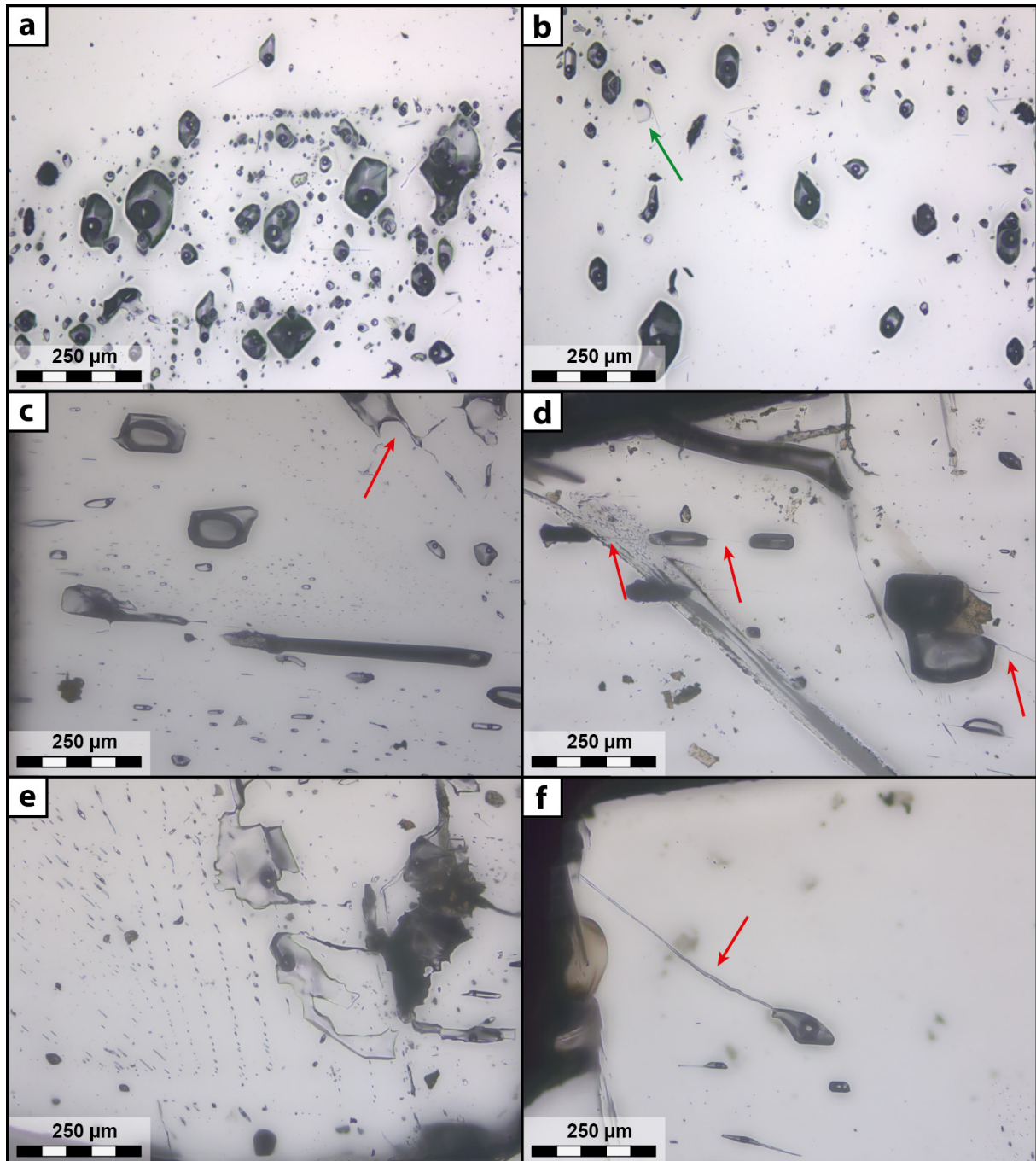


Fig. 6.6: Photomicrographs of two-phase fluid inclusions from sample chips B and A. (a and b) Large fluid inclusions with negative crystal shapes in zone +3 from chip B; (c - f) fluid inclusions in zone +4 from chip A show various degrees of fill and ample evidence of necking down. Images were taken in transmitted light and were enhanced by focus stacking. Red arrows point at examples of necking down of fluid inclusions; green arrow points at a fluid inclusion with a supposedly higher degree of fill in zone +3; due to maybe boiling of the fluid, but rather necking-down various degree of fill occur in zone +4.

6.6.1 Microthermometry

Results from microthermometry are illustrated in Fig. 6.7 to Fig. 6.9 and compiled in Tab. 6.3 (mean values for standardization of LA-ICP-MS) and Suppl. Tab. 6 in the Appendix.

Final ice melting temperatures (T_{m-ice}) of zones -3 and -2 are very similar with mean values of -4.5 ± 0.2 °C ($n=206$) and -4.5 ± 0.3 °C ($n=108$), respectively. The similarity is also evident from (only rough) results of eutectic melting temperatures (T_{eutec}) and final clathrate melting temperatures ($T_{m-clath}$). The mean T_{eutec} are -20 ± 1 °C and -21 ± 2 °C and the mean $T_{m-clath}$ 7 ± 2 °C and 7 ± 2 for zone -3 and zone -2, respectively. Only few $T_{m-clath}$ values in zone -3 and -2 exceed 10 °C. Ice melting temperatures in zone -1 do not cluster around a mean, but range almost evenly from -4.5 to -6.4 °C, with a possible accumulation at the high and low end of the range. Due to a rather small number of analyses ($n=26$) in the small section of zone -1 in chip E, the results may not be representative, though. Only for three fluid inclusions T_{eutec} could be determined (-30 to -23 °C) and T_{clath} values from 20 inclusions range from 2 to 12 °C, with the majority of analyses at the high end. Results from zone 0, i.e., the first zone along which sulfides of the MSS occur, are again statistically more normally distributed than from zone -1. The mean of T_{m-ice} is 4.7 ± 0.6 °C, the mean T_{eutec} -22 ± 2 °C and the mean $T_{m-clath}$ 6 ± 2 °C. No sulfides occur in the section of zone +1, which is sampled in chips D and supposedly E, but abundant sulfide precipitates occur along the continuation of the fluid inclusion trail (c.f., Fig. 6.3b and c). Similar to zone -1, values of T_{m-ice} , T_{eutec} and $T_{m-clath}$ span a rather large range and are far from being normally distributed. It is noteworthy that results from zone +1 in chip D and in chip E are considerably different. Regarded separately the values are much closer to a normal distribution than values from both chips together. Mean values for 25 fluid inclusions from zone +1 in chip D only are -5.5 ± 0.6 °C, -26 ± 6 °C and 12 ± 2 °C for T_{m-ice} , T_{eutec} and $T_{m-clath}$, respectively. For 26 inclusions from zone +1 in chip E the mean values are -4.7 ± 0.4 °C, -22 ± 2 °C and 6 ± 2 °C, respectively. Zone +2 corresponds to three “clouds” of fluid inclusions in chip D, which are not part of a continuous trail. Mean values of the results from 15 fluid inclusions are -4.9 ± 0.1 °C, -22 ± 1 °C and 10 ± 2 °C for T_{m-ice} , T_{eutec} and $T_{m-clath}$, respectively. In zone +3 from chip B, fluid inclusions from a supposedly secondary or pseudosecondary trail are sampled, as this trail is not continuous along a growth zone, but originates at the outer rim of Pa150 and terminates abruptly within the crystal (c.f., Fig. 6.3c). Mean final ice melting temperatures of 45 fluid inclusions are considerably lower than in the previous zones, i.e., -5.8 ± 0.1 °C. Observed T_{eutec} average at -25 ± 2 °C and $T_{m-clath}$ at 9 ± 2 °C.

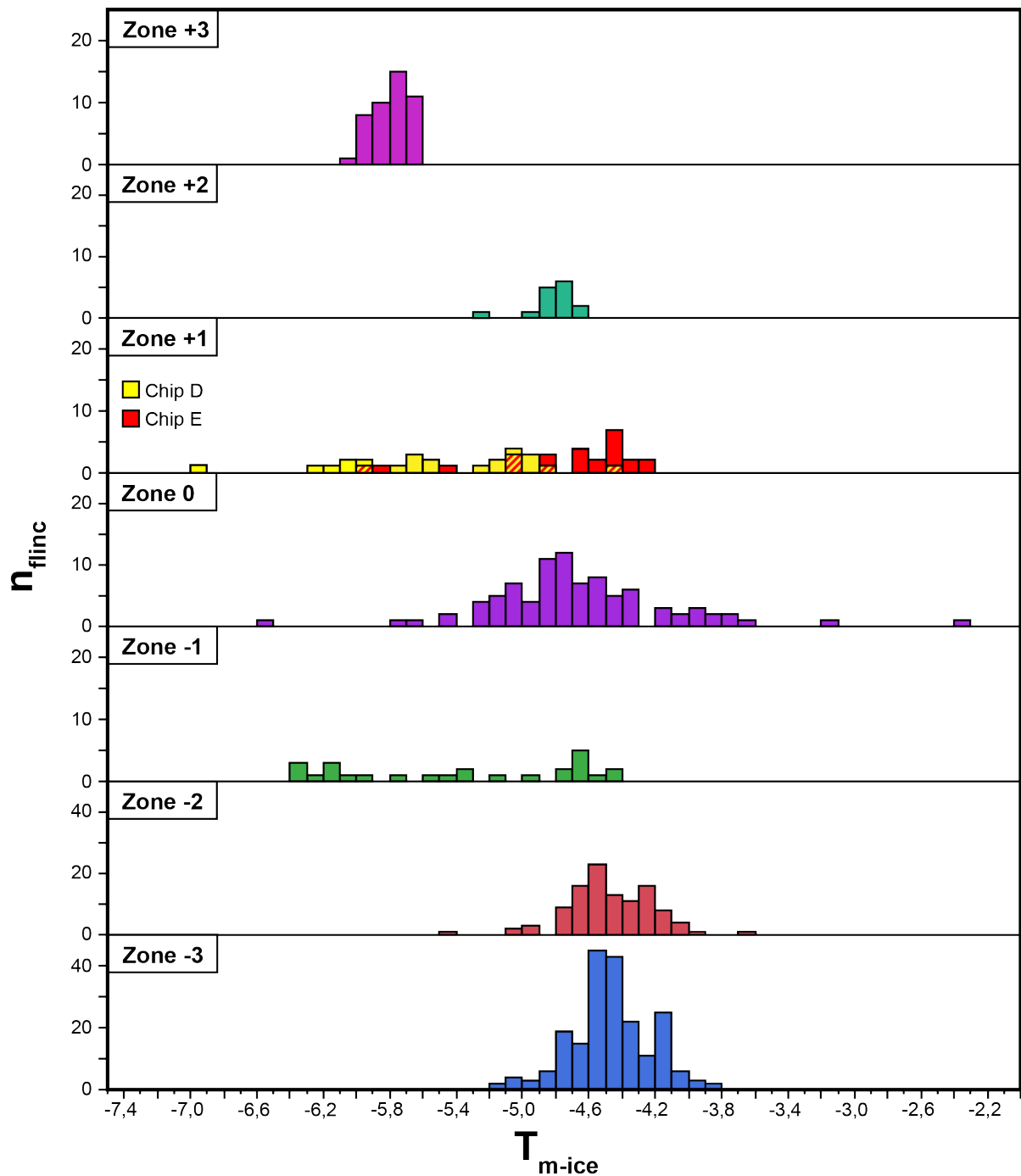


Fig. 6.7: Frequency histograms depicting the final ice melting temperatures in °C (T_{m-ice}) obtained from microthermometry of the different fluid inclusion zones in Pa150. A yellow-red hachure was used where bars of Chip D and E from zone +1 overlap. Note the different scales of the vertical axes.

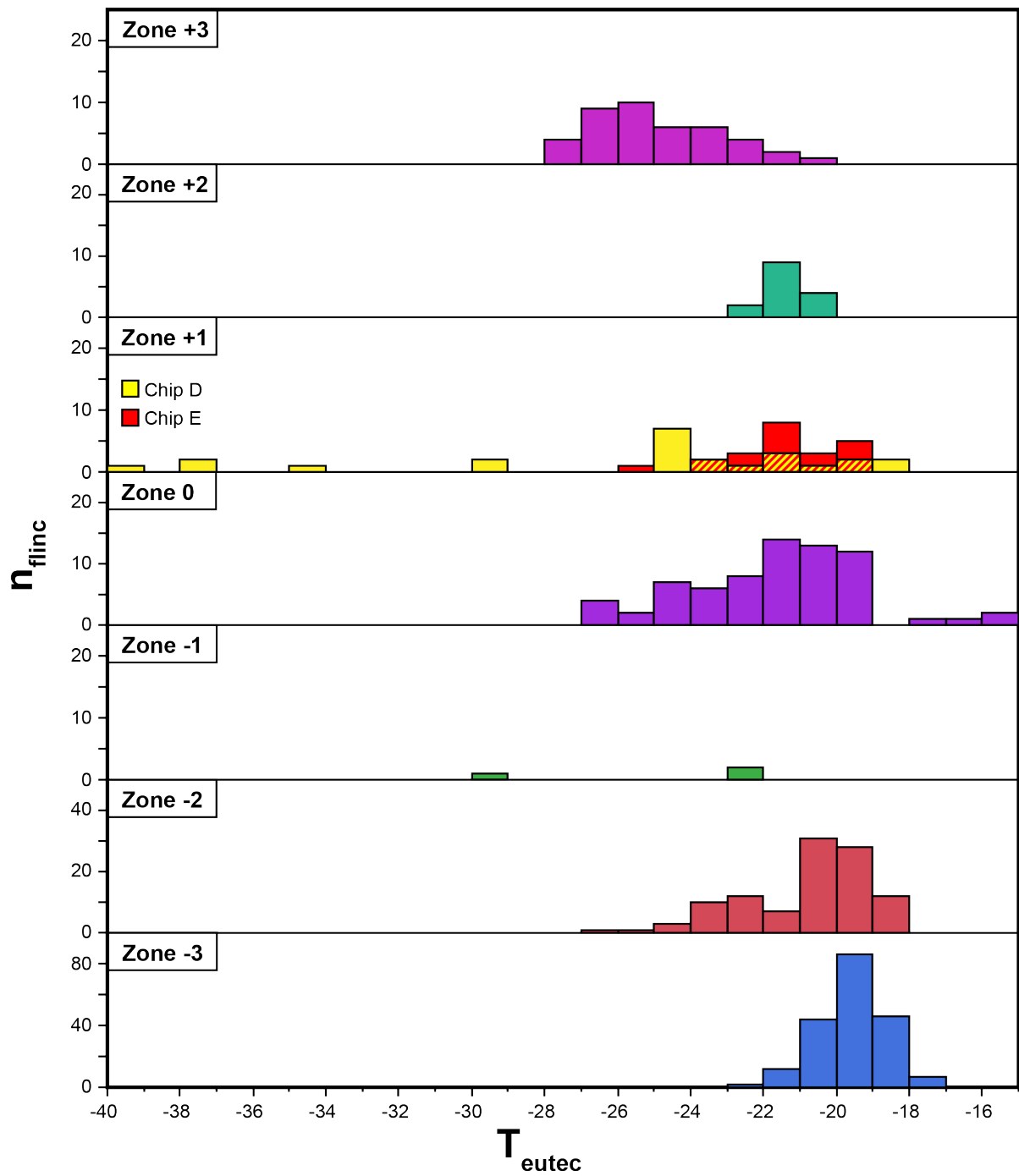


Fig. 6.8: Frequency histograms depicting the roughly determined temperatures of first (eutectic) ice melting in °C (T_{eutec}) obtained from microthermometry of the different fluid inclusion zones in Pa150. A yellow-red hachure was used where bars of Chip D and E from zone +1 overlap. Note the different scales of the vertical axes.

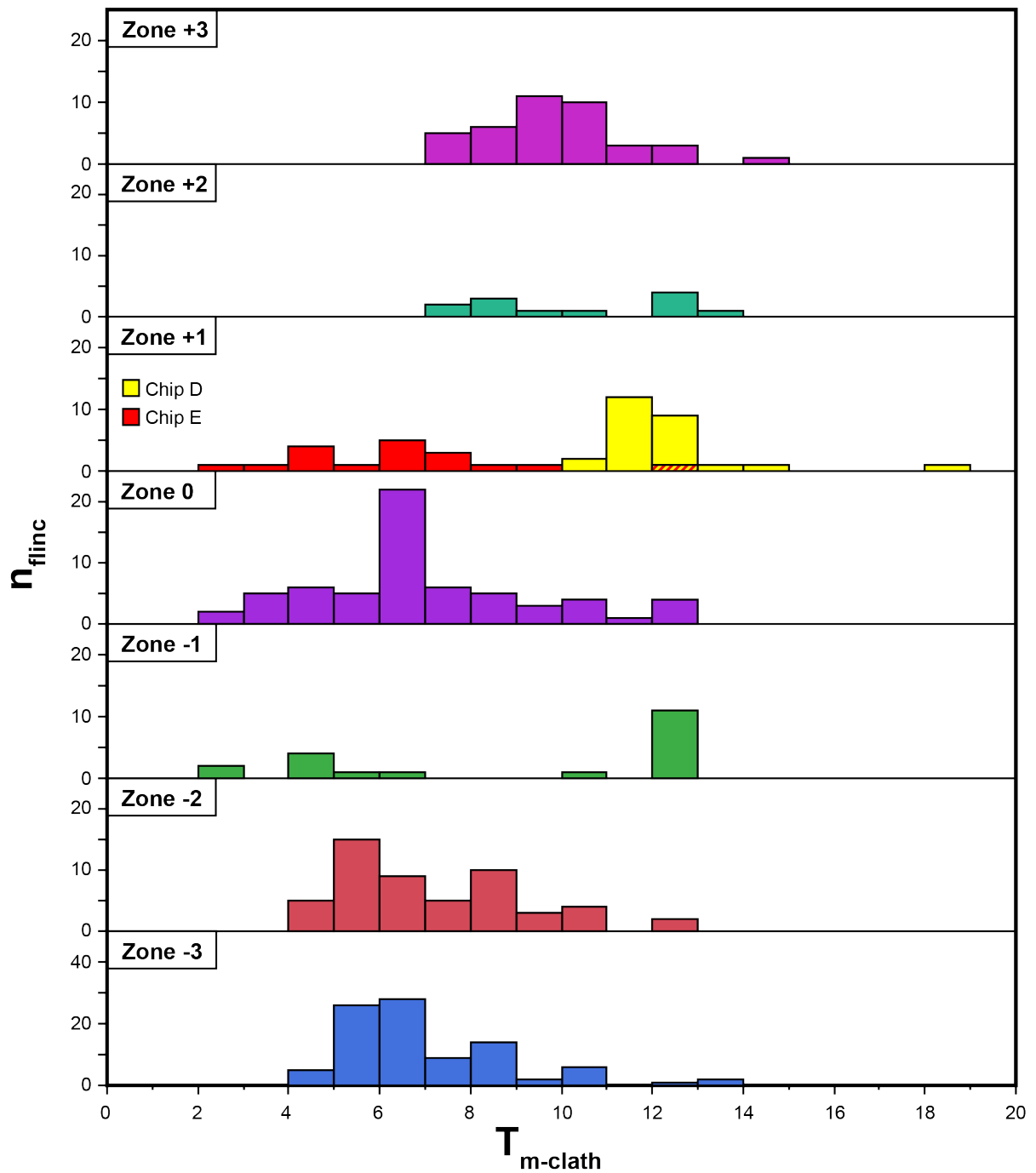


Fig. 6.9: Frequency histograms depicting the roughly determined temperatures of clathrate melting in °C ($T_{m-clath}$) obtained from microthermometry of the different fluid inclusion zones in Pa150. A yellow-red hachure was used where bars of Chip D and E from zone +1 overlap. Note the different scales of the vertical axes.

6.6.2 Estimation of the Salinity of the Fluid Phase

Quantification of LA-ICP-MS signals requires an internal standard of at least one element of a known concentration. For LA-ICP-MS of fluid inclusions, the Na concentration derived from microthermometric determination of the salinity ($\text{NaCl}_{\text{eq.}}$) is commonly used as internal standard. As mentioned in chapter 5.2.1, the presence of C-species in fluid inclusions complicates the determination of $\text{NaCl}_{\text{eq.}}$ from microthermometry due to the formation of clathrates. In the system $\text{H}_2\text{O}-\text{NaCl}-\text{CO}_2$ the true value of $\text{NaCl}_{\text{eq.}}$ can be obtained from final melting of the clathrate ($T_{\text{m-clath}}$) with, e.g., the formula of Darling (1991), if aqueous liquid, CO_2 liquid and CO_2 gas are present during clathrate decomposition (Q_2 in Fig. 6.10). Similar to the final ice melting temperature ($T_{\text{m-ice}}$), $T_{\text{m-clath}}$ shifts from 10°C in the pure $\text{H}_2\text{O}-\text{CO}_2$ (i.e., for 0 wt% NaCl) to successively lower values with increasing salinity.

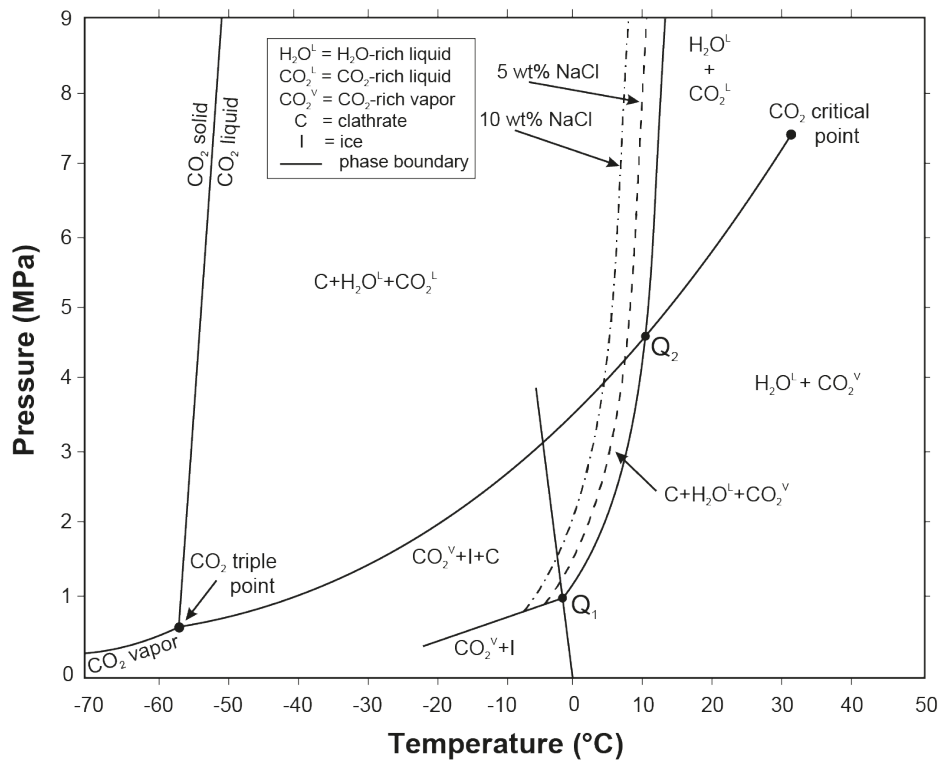


Fig. 6.10: Diagram from Fall et al. (2011) depicting phase relations in the $\text{H}_2\text{O}-\text{CO}_2\pm\text{NaCl}$ system at low temperatures. Phase boundaries in the pure $\text{H}_2\text{O}-\text{CO}_2$ system based on data of Larson (1955) are depicted in solid lines. Dashed lines are based on data from Chen (1972) and represent the CO_2 clathrate stability curves in equilibrium with an aqueous fluid containing 5 and 10 wt% NaCl. At the invariant points Q_1 and Q_2 four phases coexist.

The correction is complicated by several factors. First and foremost, the visual detection during microthermometry is difficult due to the optical properties of the CO₂ clathrate, which is isotropic and shows a very similar reflective index to most aqueous solutions (Roedder, 1972). In addition, either CO₂ liquid or CO₂ gas can be absent during clathrate melting, so that the phase transition will not occur at a univariant point in P-T-space, which is constant for a fixed salinity, but along a bivariate line (c.f., Fig. 6.10) (e.g., Collins, 1979). In this case, temperature and pressure at clathrate decomposition need to be determined, which can be done, e.g., by a combination of microthermometry and Raman spectroscopy (Fall et al., 2011). Whereas the addition of salts drives $T_{m-clath}$ to lower temperatures, the presence of additional C-species, such as CH₄, counteracts the depression of $T_{m-clath}$ and drives the values to higher temperatures, which can exceed the maximum of 10 °C in the pure H₂O-CO₂ system (Collins, 1979; Diamond, 2001). As an additional complication, metastable equilibria and disequilibria in fluid inclusions at low temperatures may further complicate the evaluation of NaCl_{eq.} derived from $T_{m-clath}$ (Diamond, 2001).

As discussed in Chapter 6.2.1, even though CO₂ is the dominant volatile phase in fluid inclusions from the mineralized veins at Panasqueira, there is abundant evidence from various authors for the presence of CH₄ and N₂ and possibly other volatile phases, which influence the thermodynamic behavior of the fluids. Microthermometric analyses during this study support at least the additional presence of CH₄ in fluid inclusions from Pa150. The first observation is that for those fluid inclusions, where final melting of CO₂ (T_{m-CO_2}) could be observed, the values are consistently lower than the melting point of pure CO₂ of -56.6 °C, i.e., -60.1 ± 1.1 °C for zone -1 in chip E (n=10), -60.9 ± 0.3 °C for zone 0 in chip E (n=4) and -59.7 ± 0.7 °C for zone +1 in chip D (n=26). Those values are in good agreement with previous studies (c.f., Tab. 6.2). The second observation in favor of additional volatile phases is a considerable amount of fluid inclusions with $T_{m-clath} > 10$ °C (c.f., Fig. 6.9), which is the highest possible value in the pure H₂O-CO₂-±NaCl system, in particular in zone -1 (chip E) and zone +1 (chip D). This observation is also in agreement with previously published data. The unfortunate consequence is that absolute values of element concentrations from LA-ICP-MS analyses of fluid inclusions in Pa150 can only be determined semi-quantitatively, i.e., with considerable uncertainties. Nevertheless, estimating an upper and lower limit, based on data from this study and studies cited in this chapter, is well possible. In addition, external standardization and determination of

element ratios from LA-ICP-MS intensities are unaffected by microthermometric challenges, which is why the data is also presented as element ratios relative to Na compared to Cs/Na ratios (c.f., Audétat, 2019).

In Tab. 6.3 mean T_{m-ice} and $T_{m-clath}$ in °C from the different zones are summarized together with salinities in wt% NaCl_{eq.} derived from equations of Bodnar (1993) for the system H₂O-NaCl based on T_{m-ice} , and Darling (1991) for the system H₂O-NaCl-CO₂ based on $T_{m-clath}$. Mean salinity for zones -3 and -2 based on T_{m-ice} is 7.2 wt% NaCl_{eq.}, which is reduced to 5.8 wt% NaCl_{eq.} based on $T_{m-clath}$. This value coincides with the highest volatile corrected NaCl_{eq.} value of the combined results from Jaques and Pascal (2017) and Cathelineau et al. (2020) for fluid inclusions from the MSS (c.f., Chapter 6.2.1 and Tab. 6.2) and is used as upper limit for internal standardization of LA-ICP-MS signals. The lowest reported value from these studies is 3.6 wt% NaCl_{eq.} and is used as lower limit. As zones 0, +1(E) and +2 have similar T_{m-ice} , as well as $T_{m-clath}$ (except for +2 where $T_{m-clath}$ is considerably higher), the same upper and lower limit are used for these zones. Zones -1 and +1(D) show a rather large range in microthermometric values and comparably lower mean T_{m-ice} (-5.4 ± 0.7 °C and -5.5 ± 0.6 °C) and higher $T_{m-clath}$ (9 ± 4 °C and 12 ± 2 °C). This would imply a range of 0-8.5 wt% NaCl_{eq.} (or mathematically even negative values), but as there is ample evidence for other volatile species than CO₂, particularly in those two zones, we are confident in using the same lower and upper limits of 3.6-5.8 NaCl_{eq.} as for the other zones. Fluid inclusions in zone +3 show quite homogenous values for T_{m-ice} (-5.8 ± 0.1 °C) and $T_{m-clath}$ (9 ± 2 °C).

Tab. 6.3: Mean T_{m-ice} and $T_{m-clath}$ in °C from zones -3 to +3 and derived salinities in wt% NaCl_{eq.} from equations of Bodnar (1993) for the system H₂O-NaCl based on T_{m-ice} , and Darling (1991) for the system H₂O-NaCl-CO₂ based on $T_{m-clath}$. The choice of lower and upper limits for internal standardization of LA-ICP-MS data is discussed in the text.

Chip	Zone	T_{m-ice} [°C]	$T_{m-clath}$ [°C]	Salinity based on T_{m-ice} [wt% NaCl _{eq.}]	Salinity based on $T_{m-clath}$ [wt% NaCl _{eq.}]	Lower and upper limits for internal standardization [wt% NaCl _{eq.}]
H	-3	-4.5 ± 0.2	7 ± 2	7.2 ± 0.3	5.8 ± 3.5	3.6-5.8
H	-2	-4.5 ± 0.3	7 ± 2	7.2 ± 0.4	5.8 ± 3.7	3.6-5.8
E	-1	-5.4 ± 0.7	9 ± 4	8.4 ± 0.9	2.0 ± 7.6	3.6-5.8
E	0	-4.7 ± 0.6	6 ± 2	7.5 ± 0.6	7.5 ± 4.4	3.6-5.8
E	+1	-4.8 ± 0.4	6 ± 2	7.6 ± 0.6	7.5 ± 4.1	3.6-5.8
D	+1	-5.5 ± 0.6	12 ± 2	8.5 ± 0.8	≤ 0	3.6-5.8
D	+2	-4.9 ± 0.1	10 ± 2	7.7 ± 0.2	$0.0 (+5)$	3.6-5.8
B	+3	-5.8 ± 0.1	9 ± 2	8.9 ± 0.1	1.9 ± 3.3	1.9-8.9

The combination of comparably low T_{m-ice} with high $T_{m-clath}$, suggest a considerable contribution of additional volatile species as well. But as for zone +3 no direct evidence for the presence of CH_4 or N_2 was observed and the zone is interpreted to be of pseudosecondary or even secondary rather than primary origin, i.e., possibly unrelated to the previous primary zones, the lower and upper values for internal standardization of LA-ICP-MS data were chosen more broadly based on T_{m-ice} and $T_{m-clath}$, i.e., 1.9-8.9 wt% $NaCl_{eq.}$. In doing so, we bear in mind that especially the upper value is very likely considerably higher than the true salinity.

6.6.3 Results from LA-ICP-MS analyses

Based on the defined lower and upper limits of $NaCl_{eq.}$, ranges of absolute concentrations were calculated using the SILLIS data reduction software (Guillong et al., 2008b). In addition, results of analyses with He + H_2 as carrier gas were corrected based on mean K/Na ratios, determined from analyses with He only as carrier gas and analyses of large fluid inclusions with K above the detection limit despite the interference of ^{38}Ar and 1H with ^{39}K . The molar K/Na ratios used for the correction are 0.01 for zone -3 and -2 and 0.05 for zones -1 to +2 and the corrections are based on the following formula (Heinrich et al., 2003; Heinrich et al., 1992):

$$NaCl_{eq.}(wt\%) = NaCl(wt\%) + 0.5 \sum XCl(wt\%)$$

Where X stands for cations from other salts present in the solution, e.g., K, Ca, Mg or Fe. The effect of the correction is minimal (usually $\leq 2\%$) and well below the analytical uncertainty of the method of 10 to 30 % (Albrecht et al., 2014). Therefore, we refrain from correction of results from zone +3, as the zone is presumably (pseudo-)secondary and unrelated to the previous zones. As K was not determined for this zone and in addition other important salt cations (Ca, Mg, Fe) are mostly below the detection limit and eutectic temperatures for fluid inclusions from zone +3 are markedly lower than from the previous zones, it is well possible that the fluid has a considerable different salt composition.

In Tab. 6.4 results from LA-ICP-MS analyses of fluid inclusions from different zones in Pa150 are summarized.

Tab. 6.4: Results from LA-ICP-MS of fluid inclusions from different zones in Pa150. Mean concentrations of measured elements are given in ppm with $\pm 1\sigma$ standard deviation; for each element and zone two values are given, which were determined using the estimated upper and lower NaCl_{eq} limit for internal standardization; n is the number of analyses above the detection limit and of good quality based on optical inspection of the ICP-MS signal.

Element	Limit	Zone -3	Zone -2	Zone -1	Zone 0	Zone +1	Zone +2	Zone +3
Li	Lower	130 \pm 60	120 \pm 40	140 \pm 50	200 \pm 100	110 \pm 50	100 \pm 40	80 \pm 40
	Upper	200 \pm 100	200 \pm 70	230 \pm 80	300 \pm 200	180 \pm 80	170 \pm 60	400 \pm 200
	n	48	28	11	6	17	18	19
B	Lower	2200 \pm 300	2200 \pm 500	2100 \pm 600	1800 \pm 300	1300 \pm 700	1800 \pm 300	700 \pm 200
	Upper	3500 \pm 500	3500 \pm 800	3000 \pm 1000	3800 \pm 500	2000 \pm 1000	2800 \pm 400	3300 \pm 900
	n	56	33	16	16	21	18	24
Na	Lower	14000 \pm 200	13800 \pm 500	13000 \pm 2000	13000 \pm 2000	12000 \pm 2000	13000 \pm 1000	7000 \pm 2000
	Upper	22600 \pm 300	22300 \pm 700	21000 \pm 3000	22000 \pm 3000	20000 \pm 3000	21000 \pm 2000	33000 \pm 5000
	n	56	33	16	16	21	18	24
K	Lower	170 \pm 60	600 \pm 900	700 \pm 500	2000 \pm 1000	1200 \pm 500	n.d.	n.d.
	Upper	270 \pm 90	1000 \pm 1000	1200 \pm 800	3000 \pm 2000	1900 \pm 900	n.d.	n.d.
	n	13	9	6	5	12		
Ca	Lower	700 \pm 300	2000 \pm 500	3000 \pm 4000	7000 \pm 3000	5000 \pm 3000	4000 \pm 2000	4000 \pm 5000
	Upper	1100 \pm 500	3300 \pm 900	5000 \pm 7000	11000 \pm 5000	8000 \pm 5000	7000 \pm 3000	20000 \pm 20000
	n	6	4	6	2	10	5	3
Mn	Lower	30 \pm 30	70 \pm 80	17 \pm 5	1000 \pm 1000	70 \pm 20	200 \pm 400	40 \pm 10
	Upper	50 \pm 40	100 \pm 100	27 \pm 8	1000 \pm 2000	100 \pm 30	400 \pm 700	200 \pm 400
	n	12	16	5	3	5	9	10
Fe	Lower	600 \pm 300	500 \pm 200	200 \pm 200	200	800 \pm 500	1000 \pm 300	800 \pm 500
	Upper	1000 \pm 500	800 \pm 400	300 \pm 300	300	1300 \pm 900	1700 \pm 500	4000 \pm 2000
	n	3	5	2	1	3	4	8
Cu	Lower	10 \pm 20	30 \pm 40	70 \pm 90	200 \pm 500	7 \pm 5	400	9 \pm 8
	Upper	20 \pm 30	50 \pm 60	100 \pm 100	300 \pm 800	12 \pm 9	600	40 \pm 40
	n	10	7	7	12	3	1	2
As	Lower	320 \pm 60	310 \pm 80	140 \pm 80	200 \pm 200	7 \pm 2	100 \pm 100	13 \pm 6
	Upper	510 \pm 90	500 \pm 100	200 \pm 100	300 \pm 300	11 \pm 3	200 \pm 200	60 \pm 30
	n	56	33	16	16	12	16	23
Rb	Lower	34 \pm 9	40 \pm 20	40 \pm 20	50 \pm 30	50 \pm 10	40 \pm 30	70 \pm 90
	Upper	60 \pm 20	70 \pm 30	60 \pm 40	80 \pm 40	70 \pm 20	60 \pm 50	300 \pm 400
	n	55	33	16	16	21	16	34
Sr	Lower	3	all < DL	n.d.	n.d.	3,6 \pm 0,3	all < DL	4 \pm 5
	Upper	4	all < DL	n.d.	n.d.	5,8 \pm 0,4	all < DL	20 \pm 20
	n	1				3		
Sn	Lower	10 \pm 9	7 \pm 4	1 \pm 1	30 \pm 60	all < DL	all < DL	all < DL
	Upper	20 \pm 10	12 \pm 6	2 \pm 2	260 \pm 50	all < DL	all < DL	all < DL
	n	2	2	2	6			
Sb	Lower	6 \pm 3	4 \pm 3	20 \pm 20	10 \pm 10	9 \pm 5	5 \pm 4	5 \pm 2
	Upper	10 \pm 5	7 \pm 4	30 \pm 30	20 \pm 20	14 \pm 7	8 \pm 6	20 \pm 10
	n	32	20	6	7	12	5	11
Cs	Lower	180 \pm 20	190 \pm 30	190 \pm 50	180 \pm 40	180 \pm 40	130 \pm 40	70 \pm 20
	Upper	300 \pm 40	300 \pm 50	310 \pm 80	300 \pm 60	280 \pm 60	210 \pm 70	320 \pm 80
	n	56	33	16	16	21	18	24
W	Lower	10 \pm 10	5 \pm 4	10 \pm 10	10 \pm 10	3 \pm 2	3 \pm 3	2 \pm 3
	Upper	10 \pm 20	9 \pm 7	10 \pm 20	10 \pm 20	5 \pm 3	4 \pm 4	10 \pm 10
	n	35	28	13	15	15	8	12
W* ¹	Lower	4 \pm 2	5 \pm 4	1 \pm 2	10 \pm 10	3 \pm 1	3 \pm 3	1 \pm 1
	Upper	6 \pm 4	8 \pm 6	2 \pm 2	10 \pm 20	4 \pm 2	4 \pm 4	6 \pm 5
	n	32	27	11	15	14	8	11
Au	Lower	all < DL	all < DL	all < DL	all < DL	1,4 \pm 0,1	all < DL	all < DL
	Upper	all < DL	all < DL	all < DL	all < DL	2,3 \pm 0,1	all < DL	all < DL
	n					3* ²		
Pb	Lower	4 \pm 7	4 \pm 4	3 \pm 4	10 \pm 10	10 \pm 10	2 \pm 2	20 \pm 40
	Upper	10 \pm 10	7 \pm 7	6 \pm 5	20 \pm 20	10 \pm 20	4 \pm 3	100 \pm 200
	n	11	8	5	9	8	3	4

all < DL: concentrations of all analyses were below the detection limit

n.d.: element was not determined in the respective zone

*1: mean W concentrations, when statistical outliers are eliminated; a point was considered an outlier if it exceeds the upper outlier limit ($Q3+1.5 \times IQR$) or is less than the lower outlier limit ($Q1-1.5 \times IQR$), where $Q1$ and $Q3$ are first and third quartiles and IQR is the inter quartile range ($Q3-Q1$).

*2: including two values of mediocre quality, from analyses, which were precluded for the other elements' mean values.

In Fig. 6.11 and Fig. 6.12 mean element concentrations of selected elements are depicted. Analyses were quantified based on the discussed upper estimates (red circles) and lower estimates of NaCl_{eq} (green circles) and sorted from rim to core (zone -3 to +3). Analyses below the detection limit ($< \text{DL}$) were discarded and so were analyses of bad quality based on visual inspection during the measurement, i.e., analyses with obvious spikes on the count signal of one or more elements, which could not be corrected with the SILLIS software, as well as analyses with evidence of incomplete ablation of the fluid inclusion. Few analyses in zone -1, 0 and +3 show Mg concentrations above the detection limit. All of those analyses correlate with outliers of unrealistically high concentrations of Li and Mn, which is interpreted to result from partial ablation of Li-mica attached to the fluid inclusion. Those analyses (2 in zone -1, 9 in zone 0 and 1 in zone +3) were discarded from the evaluation as well for the respective elements.

For many elements no considerable changes in concentrations from zone -3 to +3 could be detected. Zone +3 has to be treated with caution, as the upper and lower limit of NaCl_{eq} , used for internal standardization, differs from those of the other zones and is higher and lower, respectively. Concentrations of Li, B, Rb and Cs are above the detection limit in most analyses and seem to undergo no significant changes throughout the investigated sequence. K and Ca concentrations seem to show an increase from zone -3 to 0 and remain more or less constant in subsequent zones. It has to be noted though that many analyses of K and Ca are below the detection limit and means were calculated from only a few data points and exhibit large standard deviations. Another element that straddles the detection limit is Fe, which shows roughly constant concentrations in the early zones -3 to 0 and possibly a slight increase in the subsequent zones. Similar to K and Ca, Cu concentrations seem to increase from zone -3 to 0, but drop sharply to considerably lower concentrations in zone +1. For Cu, as well, many concentrations are below the detection limit and calculated standard deviations are even higher relative to the mean values. Concentrations of As are mostly above the detection limit and are fairly constant in zones -3 and -2 of the “milky” core. They vary more strongly in the subsequent zones -1 and 0, where the mean concentrations are slightly lower and drop to considerably lower values in zone +1 before they increase again in the outermost zones, but remain below the concentrations of the core. Tungsten could be detected in the majority of analyzed fluid inclusions. Mean W concentrations are in the order of a few ppm to ca. 10 ppm and do not vary systematically throughout the sequence.

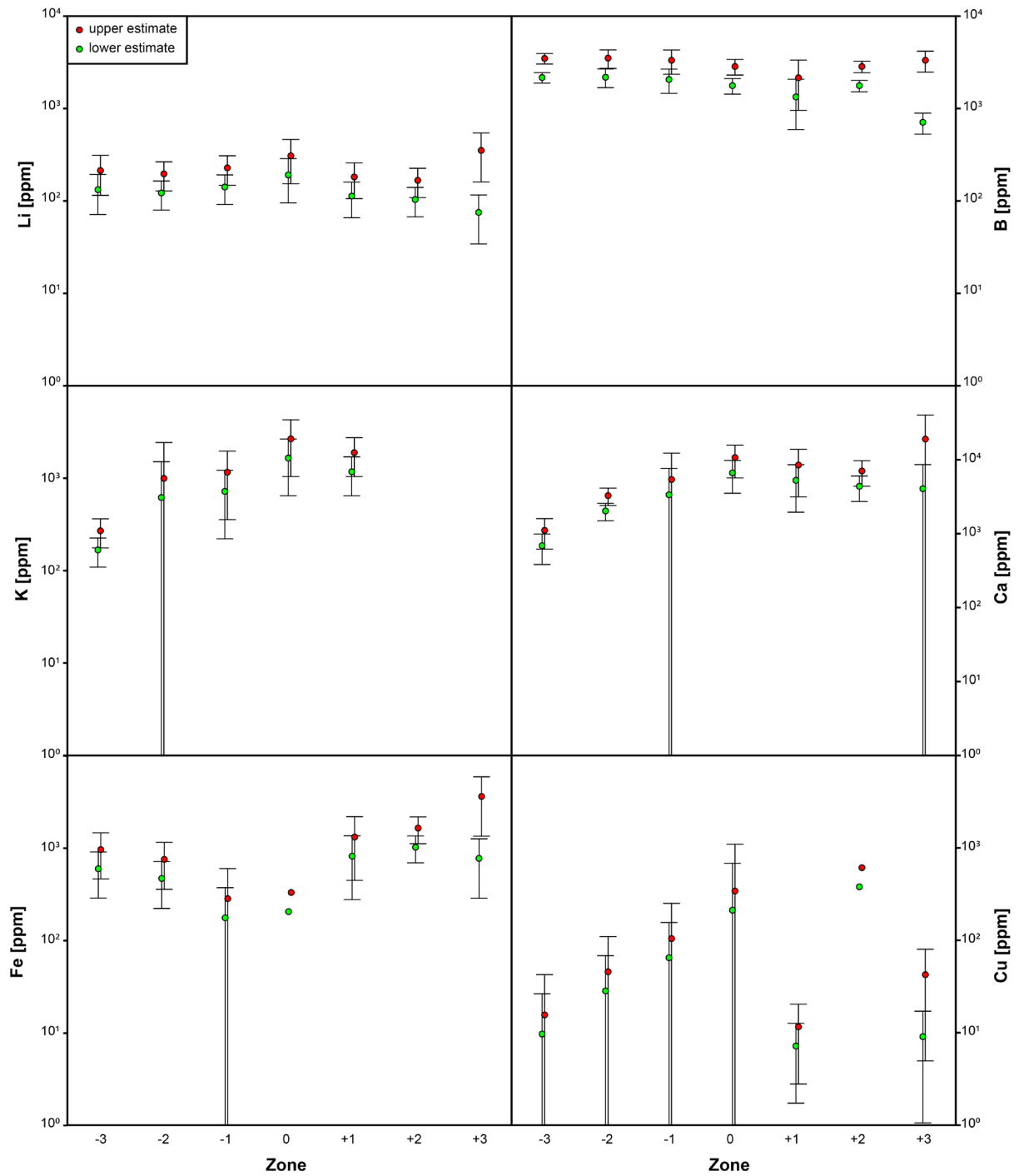


Fig. 6.11: Mean element concentrations determined with LA-ICP-MS of fluid inclusions from different zones (sorted from core to rim) in Pa150. Red circles depict mean values using the upper NaCl_{eq} estimate for internal standardization, green circles using the lower estimate, respectively. Error bars depict 1σ standard deviation. Where concentrations show a large scatter or statistical outliers to high concentration, error bars reach to negative values. Note: NaCl_{eq} values for the upper and lower limit of internal standardization differ for zone +3 compared to the other zones.

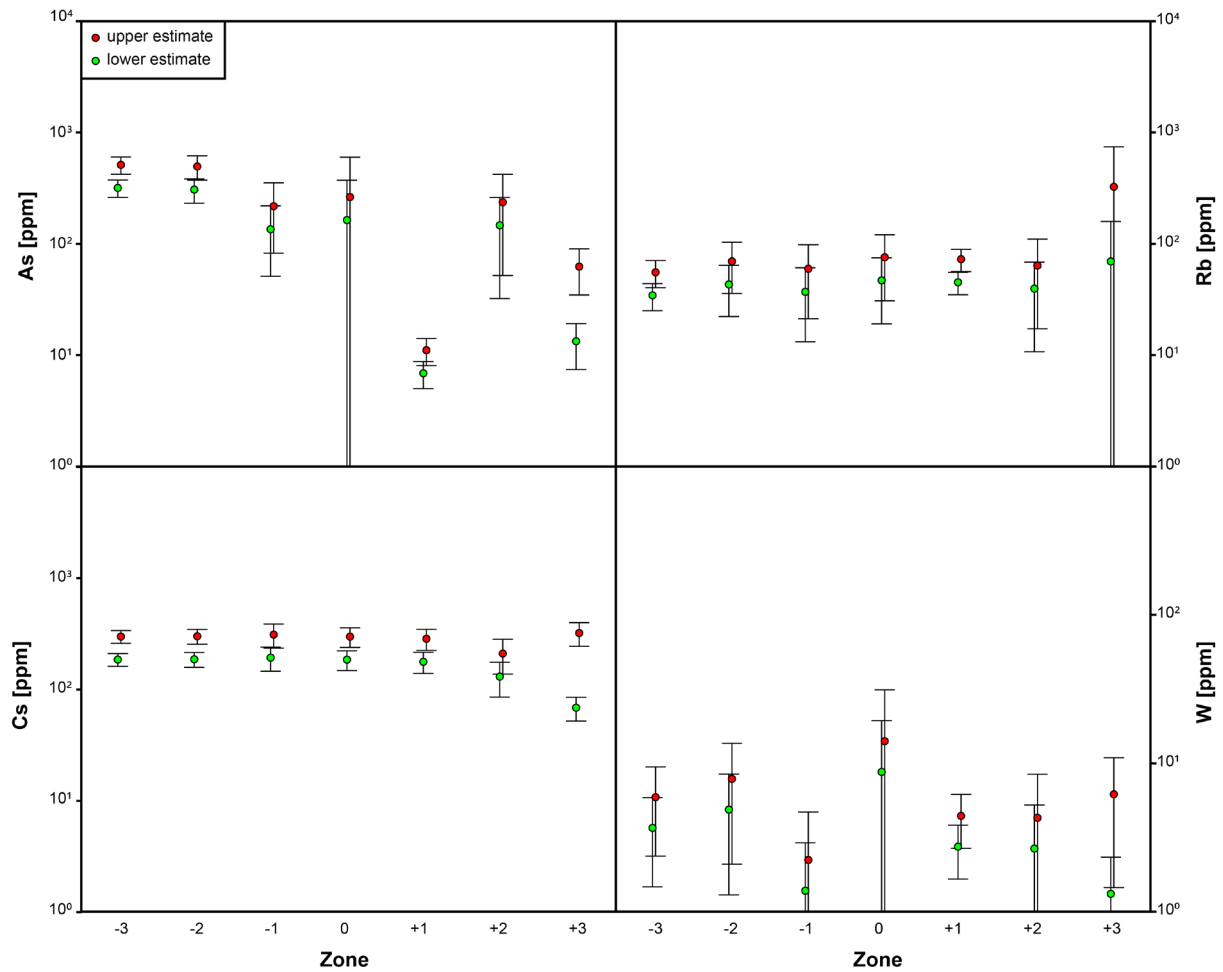


Fig. 6.12: (continued from Fig. 6.11) Mean element concentrations determined with LA-ICP-MS of fluid inclusions from different zones (sorted from core to rim) in Pa150. Red circles depict mean values using the upper NaCl_{eq} estimate for internal standardization, green circles using the lower estimate, respectively. Error bars depict 1σ standard deviation. Where concentrations show a large scatter or statistical outliers to high concentration, error bars reach to negative values. Note: NaCl_{eq} values for the upper and lower limit of internal standardization differ for zone +3 compared to the other zones.

6.7 Discussion

6.7.1 General Fluid Characteristics

Despite the described difficulties in quantification of data from microthermometry of fluid inclusions in sample Pa150, some qualitative information can be derived from it and the different zones can be grouped by microthermometric similarities. Zone -3 and -2, which represent the “milky core” of the quartz crystal, show very similar microthermometric results and can be correlated with zones F and E from sample Pa66 of Polya et al. (2000), respectively (c.f. Fig. 6.13 and Tab. 6.5).

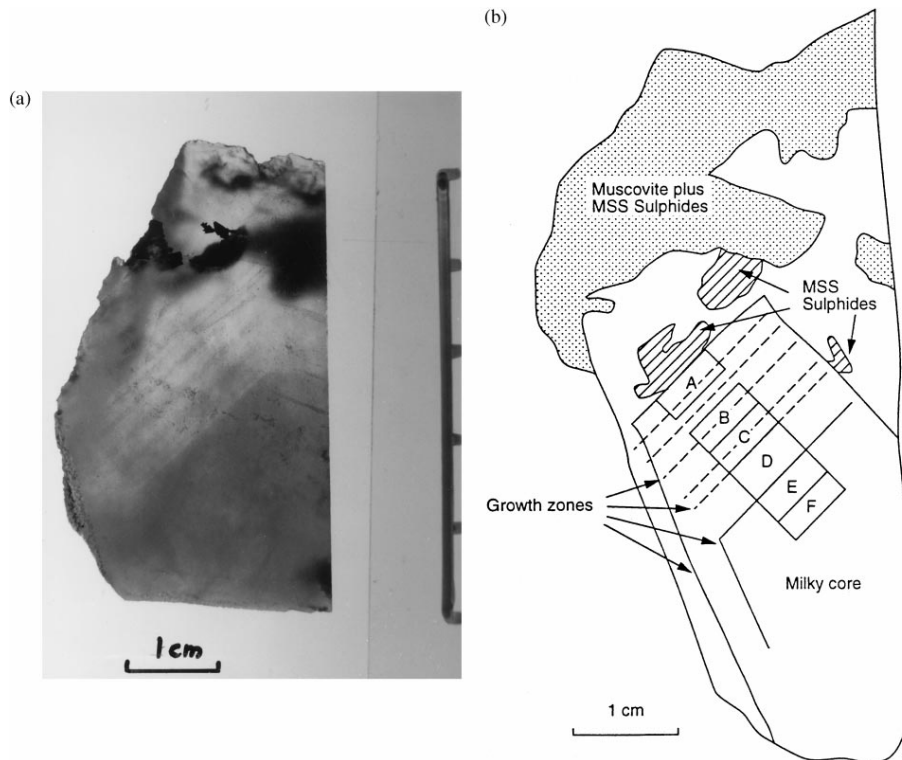


Fig. 6.13: (a) Photograph and (b) sketch from sample Pa66 of Polya et al. (2000). Similar to sample Pa150 it shows a “milky” core with numerous fluid inclusions, followed by primary growth zones along defined planes. The sketch was made from an adjacent slice of the quartz shown in (a).

Tab. 6.5: Comparison of zones from Pa150 (this study) and Pa66 (Polya et al., 2000) based on relative succession in the sample and comparison of mean salinities in wt% NaCl_{eq.} based on T_{m-ice} values. Note that these values lack a correction for C-species and concomitant clathrate formation and do not represent true salinities.

Chip	Zone from Pa150 (this study)	T _{m-ice} [°C]	Salinity based on T _{m-ice} [wt% NaCl _{eq.}]	Correlated zone from Pa66 after Polya et al. (2000)	Salinity based on T _{m-ice} [wt% NaCl _{eq.}]
H	-3	-4.5 ± 0.2	7.2 ± 0.3	F	no data
H	-2	-4.5 ± 0.3	7.2 ± 0.4	E	7.4 ± 0.1
E	-1	-5.4 ± 0.7	8.4 ± 0.9	D	8.3 ± 0.5
E	0	-4.7 ± 0.6	7.5 ± 0.6	C	8.0 ± 0.3
E	+1	-4.8 ± 0.4	7.6 ± 0.6	B	8.2 ± 0.2
D	+1	-5.5 ± 0.6	8.5 ± 0.8	A	8.7 ± 0.1
D	+2	-4.9 ± 0.1	7.7 ± 0.2	RIM1/RIM2	7.4 ± 0.1/7.2 ± 0.2
B	+3	-5.8 ± 0.1	8.9 ± 0.1	-	-

According to Polya et al. (2000) the milky zone represents either late MOSS or early MSS, which is supported by our observation that W concentrations do not vary significantly throughout Pa150 (Fig. 6.12) so that the majority of W precipitation must have happened prior to the formation of the quartz crystal. Fluid inclusions from subsequent zones in Pa66 are attributed to the MSS by Polya et al. (2000) and have been correlated to zones

of Pa150 from this study based on relative succession in the sample and comparison of mean salinities in wt% NaCl_{eq.} based on T_{m-ice} values (Tab. 6.5). It has to be noted that these values lack a correction for C-species and concomitant clathrate formation and do not represent true salinities. In general salinities from early studies (e.g., Bussink, 1984; Kelly and Rye, 1979; Noronha et al., 1992) lack a clathrate correction and probably overestimate true salinities, which should rather be in the range reported by Jaques and Pascal (2017) and Cathelineau et al. (2020), i.e., 3.6 to 5.8 wt% NaCl_{eq.}, who combined microthermometry with Raman spectroscopy on fluid inclusions. No zone in Pa66 was reported that could be correlated to zone +3 in Pa150. Based on microthermometric data, zone +3 shows considerable different characteristics, such as significantly lower mean T_{m-ice} and T_{eutec} , which implies both a higher total salinity (or volatile amount) and different salt composition of the fluid. It is therefore interpreted to represent a fluid from a later stage, which is not directly related to the fluids of the previous zones. Due to the large range between LA-ICP-MS data corrected with the upper and the lower estimate of NaCl_{eq.}, respectively, plus high standard deviations for most elements, major and trace element data for zone +3 are ambiguous and no definite conclusion can be drawn concerning the composition and origin of the fluids in this zone.

Zone 0, zone +1 (Chip E only) and possibly zone +2 show similar characteristics based on microthermometry and are similar to zones -3 and -2. Mean T_{m-ice} and T_{eutec} are slightly lower, which could be due to the increase in K, Ca and possibly Fe, suggested by LA-ICP-MS data. Microthermometric data from zone -1 and zone +1 shows a bimodal distribution. Whereas on one side of the distribution, the data is similar to that of zone -3, -2, 0 and +2, the other part deviates to considerably lower T_{m-ice} (and possibly T_{eutec}) and higher $T_{m-clath.}$ For zone +1 the “normal” side of the distribution correlates with fluid inclusion from Chip E and the “atypical” side with fluid inclusion from Chip D (unrelated to zone E and D from Polyá et al., 2000). A likely explanation is the ingress of and mixing with an additional fluid, rich in volatiles, in particular C-species. High values of $T_{m-clath.}$ argue for a considerable amount of reduced C-species, such as for example CH₄. This is in accordance with anomalously low hydrogen isotope values (δD) in fluids from the MSS observed by Polyá et al. (2000) in the different zones of Pa66, which get more depleted towards the rim of the crystal (Fig. 6.14).

Whereas δD and $\delta^{18}O$ isotope signatures of fluids from the MOSS determined by Kelly and Rye (1979) (blue dots in Fig. 6.14) can be explained by mixing and interaction of the

magmatic, supposedly ore-bearing fluid with another (possibly but not necessarily meteoric) source, signatures from fluids of the MSS analyzed by Polya et al. (2000) (orange dots in Fig. 6.14) were interpreted to be the result of interaction with carboniferous coals or coaly (meta)sediments (Launay, 2018; Polya et al., 2000). Such organic-rich material could be a likely source for the generally high C-content in fluids analyzed in Pa150 in this study, and also explain the source of the proposed ingress of a very reduced fluid particularly in zone -1 and +1 (Chip D). Interestingly, fluids from barren quartz veins analyzed by Noronha et al. (1992) are dominated by CH₄ and/or N₂ and possibly were derived from the same source as the inferred volatile-rich and reduced additional fluid added to the primary fluid in Pa150.

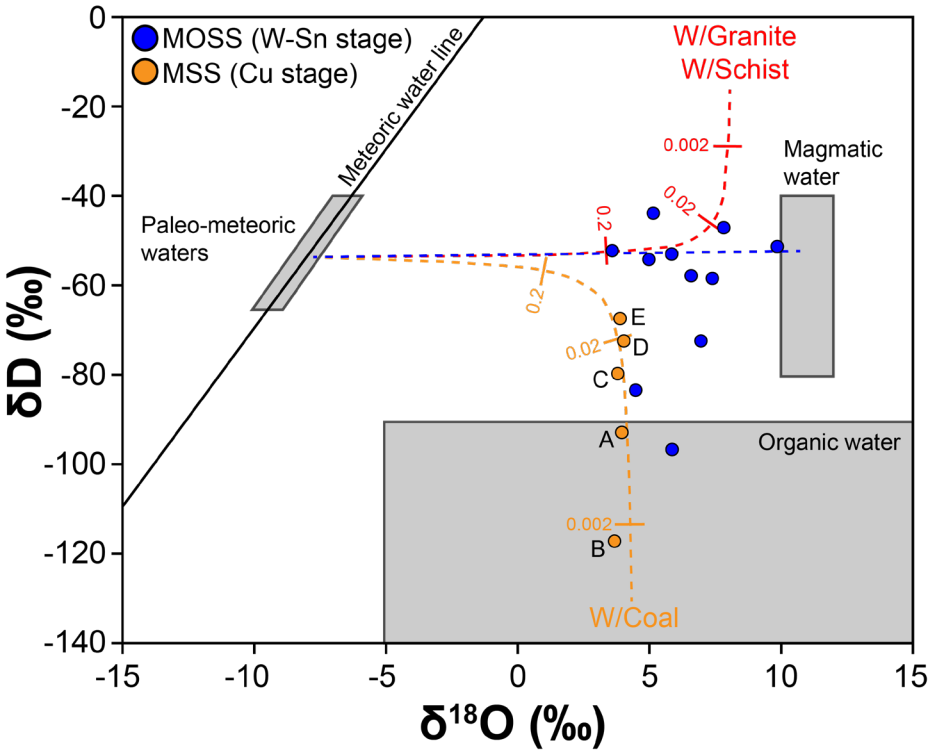


Fig. 6.14: Measured and modelled δD and $\delta^{18}\text{O}$ isotopic compositions from fluids of Panasqueira W-Sn-(Cu-) deposit. Blue dots represent data from fluids related to the MOSS by Kelly and Rye (1979), and orange dots represent data from Polya et al. (2000) related to the MSS. The dashed curves were calculated by Polya et al. (2000) after the method of Campbell et al. (1984) and modelled equilibrium isotopic compositions of a Paleo-meteoric water exchanged with granite or schist (red line) or coal-rich (meta-)sediments (orange line). Depicted numbers are water/rock exchange ratios. The Figure has been modified after Launay (2018) and Polya et al. (2000).

6.7.2 Chemical Evolution of the Fluid

Lithium, B, Rb and Cs are among the elements, whose concentrations could be measured above the detection limit in the majority of analyses, and which show low standard deviations (Fig. 6.11 and Fig. 6.12). The concentration of these elements in a fluid are considered to be representative of the magma, from which they exsolved. Their constant composition within error throughout zones -3 to +2 supports the idea that only one rather homogenous fluid, which was exsolved from the crystallizing magma was responsible for the formation of the MSS. If exchange with an external source (fluid or rock) had happened, the source would have to have similar concentrations of these elements. Alternatively, the exchange could have occurred prior to the formation of the MSS, e.g., as trigger for the deposition of the MOSS, as suggested by Lecumberri-Sanchez et al. (2017). This latter hypothesis is further supported by data from Codeço et al. (2017), who showed that the hydrothermally altered metasedimentary host rocks are enriched in, among other elements, Li, Rb and Cs compared to the unaltered host rocks, supporting the idea of element exchange between the magmatic fluid and adjacent metasediments of the Beira schist. The apparent increase in K and Cs concentrations from zone -3 to zone 0 is complicated by the high standard deviations for some of the zones and many analyses below the detection limits of the two elements (Fig. 6.11). Nevertheless, the increase is significant as the differences between the zones are beyond individual errors. This would imply that element exchange was still going on during the MSS and equilibration, at least with respect to some elements, was not attained at that point.

From our data it is not clear what lead to the precipitation of the ore minerals of the MSS, i.e., pyrite, chalcopyrite and arsenopyrite, with subordinate cassiterite, pyrrhotite and sphalerite (note: chalcopyrite is the only ore mineral of the MSS that was and is economically exploited). But the apparent sharp drop of Cu and As in zone +1 compared to previously formed zones seems to be concomitant to the precipitation of these elements in chalcopyrite and arsenopyrite, respectively. Iron does not follow this trend, but seems to rather increase slightly in zone +1, which lends further support to the theory of Lecumberri-Sanchez et al. (2017), who argue that Fe required for ore mineral precipitation is contributed by the host rock and not by the magmatic fluid itself. As mentioned before, fluid inclusions in zone +2 do not occur in a continuous growth zone but as three isolated clusters next to zone +1 in Chip D. Combined with the observation

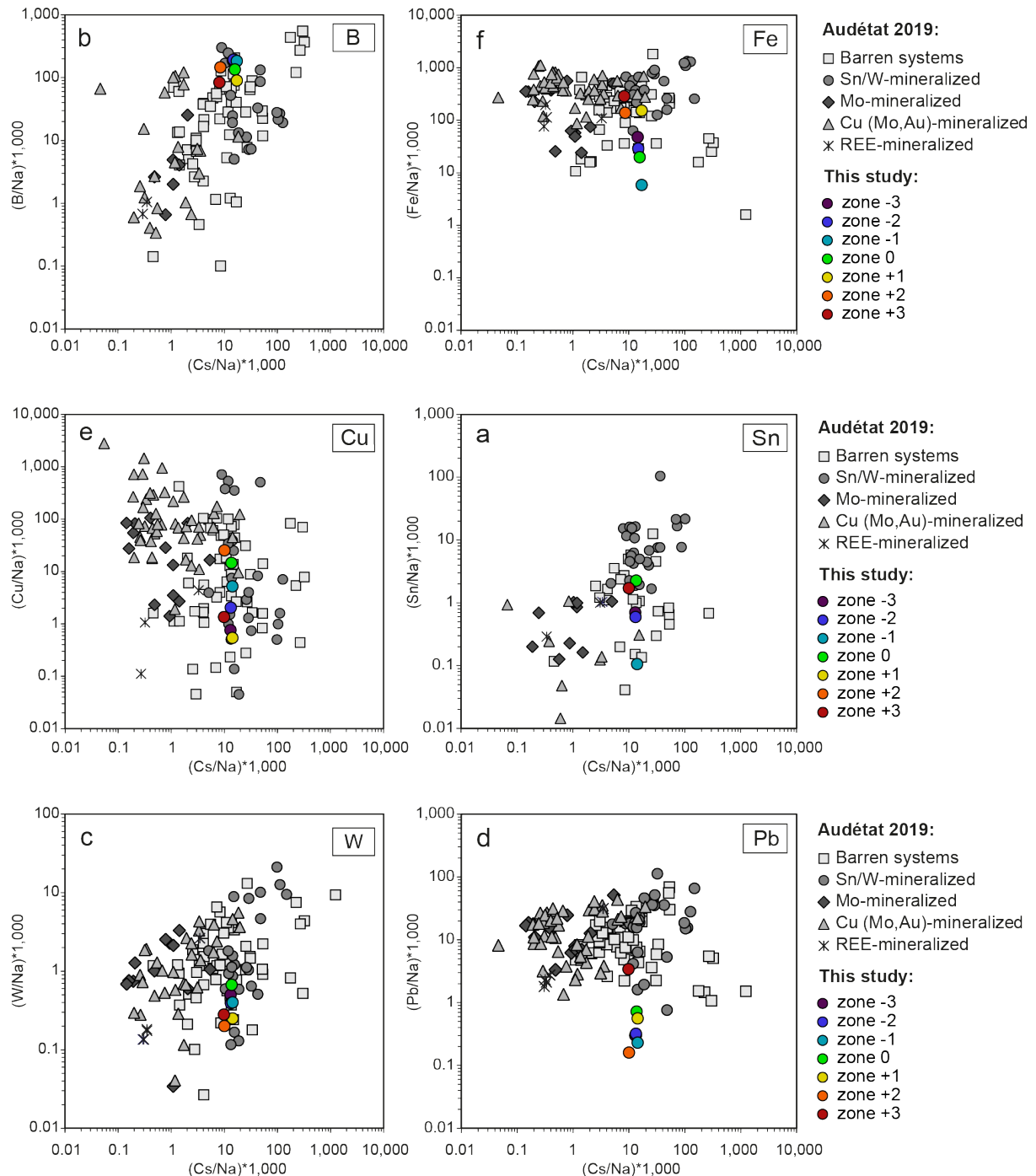
that Cu and As concentrations jump back up to their original concentrations from previous zones, zone +2 is of unknown genetic relation to the other zones in Pa150.

In a review of LA-ICP-MS data of high temperature fluid inclusions (temperature of homogenization (T_{hom}) > 450 °C) from magmatic-hydrothermal deposits by Audétat (2019), Na-normalized element ratios from different types of magmatic-hydrothermal ore deposits as well as barren magmatic-hydrothermal systems are compared to each other. The comparison of LA-ICP-MS data as element ratios is unaffected by uncertainties of internal standardization that arise especially for fluid inclusions that are dominated by other salts than NaCl or, as in the case of the present study, that contain significant amounts of gases (Audétat, 2019).

In Fig. 6.15 we compare sodium normalized ratios from selected elements of this study to the data collected by Audétat (2019), who specified the following criteria for the selection of fluid inclusion data: a) good preservation of the fluid inclusions, b) preferably inclusions of both intermediate density (ID-type) as well as brine inclusions, c) entrapment of the fluid at high temperatures (> 450 °C), d) data of a fluid inclusion assemblages rather than from single inclusions and e) a large range of Cs concentrations. The aim of this selection is to target pre-mineralization fluid inclusions. Of the above criteria only a) and d) are met without limitations in our study. We did not observe brine fluid inclusions, but only report ID-type inclusions. The entrapment temperature of the fluids at Panasqueira is still under debate, but recent studies point to a temperature of formation of 350 to 550 °C (Cathelineau et al., 2020; Jaques and Pascal, 2017; Launay et al., 2021). As mentioned before the reported Cs concentrations from our study do not vary much. Nevertheless, our data coincides very well with those of Sn/W-mineralized systems in the collection of Audétat (2019) (c.f., Fig. 6.15).

For elements, where only very few analyses are above the detection limit and relative errors are presumably high, the mean sodium normalized abundances of some zones deviate to lower values, i.e., for Fe/Na, Sn/Na and Pb/Na. Boron, Cu and W agree perfectly with the database of Audétat (2019). Whereas B/Na ratios are rather at the high end values of Sn/W-deposits, W/Na ratios are rather at the low end of this type of deposits. The latter supports the idea that sample Pa150 preserved fluids of the MSS (and possibly late MOSS) and the majority of W was already precipitated during the main stage of the MOSS. Likewise, Audétat (2019) suspected that W deposits are generally formed from W-rich fluids, but that due to the high formation temperature of many tungsten ores (e.g.,

Audétat et al., 2000; Hart, 2007) many of the analyzed fluid inclusions do not represent the transport stage, but rather the stage where fluids were already depleted in this element.



6.7.3 Implications for Ore Deposition and Required Fluid-Rock Ratios

Depending on the NaCl concentration (upper or lower limit) used for internal standardization and the in- or exclusion of 8 statistical outliers, mean W concentrations from fluids of the MSS in sample Pa150 are ca. 1 to 10 ppm (c.f., Tab. 6.4). In comparison, W concentrations from fluids of the MOSS determined by Lecumberri-Sanchez et al. (2017) range from 1-70 ppm. In Fig. 6.16, we compare the data from natural fluid inclusions from the Panasqueira W-Sn-(Cu-) deposit of Lecumberri-Sanchez et al. (2017) and this study to our experimental result of wolframite solubility in terms of equilibrium W-concentrations in the fluid. We feel confident to do so, as our experimental conditions (200 MPa, 8 wt% NaCl, FMQ buffered) are close to the inferred natural conditions of the Panasqueira deposit and temperature only has to be extrapolated to slightly lower values. Noronha et al. (1992) estimated redox conditions during the mineralizing episode at Panasqueira to lie between NNO and FMQ. Recent estimates of pressures at fluid entrapment at Panasqueira are ca. 250 to 300 MPa (Cathelineau et al., 2020; Jaques and Pascal, 2017), which is only slightly higher than our experimental conditions. Moreover, our experiments showed a negligible effect of pressure on ferberite solubility in the pressure range from 100 to 300 MPa (c.f., Fig. 5.8). A salinity of 8 wt% NaCl is in good accordance with estimates from early fluid inclusions studies at Panasqueira (e.g., Bussink, 1984; Kelly and Rye, 1979; Noronha et al., 1992), but is slightly too high when taking into account a correction for C-species and concomitant clathrate formation during microthermometry. Nevertheless, this should not influence wolframite solubility strongly. For comparison with data in Fig. 5.9, the estimated upper limit of 5.6 and lower limit of 3.8 wt% NaCl refer to a log NaCl [ppm] of 4.75 and 4.58, respectively. Based on this comparison of natural and experimental data, the following implications on the precipitation conditions of W at Panasqueira can be derived. A magmatic fluid with ca. 70 ppm W would be highly undersaturated with respect to ferberite at high temperatures (left star in Fig. 6.16). Upon cooling such a fluid would hit the solubility curve at ca. 480 °C (middle star in Fig. 6.16, based on Eq. 2 in Chapter 5.4.3). Upon further cooling more than 90 % of W from the fluid would be precipitated within a temperature interval of 100 °C. At ca. 380 °C the majority of W would have been precipitated and the residual (MSS) fluid would contain ca. 5 ppm W (right star in Fig. 6.16).

These considerations allow for an estimation of formation temperatures of the MOSS and MSS. They are in perfect accordance with estimates from arsenopyrite thermometry from

Jaques and Pascal (2017) (376-482 °C) and Ti-in quartz thermometry of vein quartz of Launay et al. (2021) (350-450 °C) and only slightly lower than estimates from Cathelineau et al. (2020) (500 ±20 °C) based on the intersection of isochores derived from microthermometry of fluid inclusions in topaz. This temperature range is considerably higher than measured homogenizations temperatures of fluid inclusions from the Panasqueira veins (c.f. Chapter 6.3), so that our data further supports the necessity of a pressure correction of homogenization temperatures derived from microthermometry as proposed by Jaques and Pascal (2017) and Cathelineau et al. (2020). It further supports the theory that fluids at Panasqueira were not boiling at least during the main ore-forming stages, but that few vapor-rich inclusions are due to tectonic stress and resulting stretching and necking-down of some previously homogenous fluid inclusions.

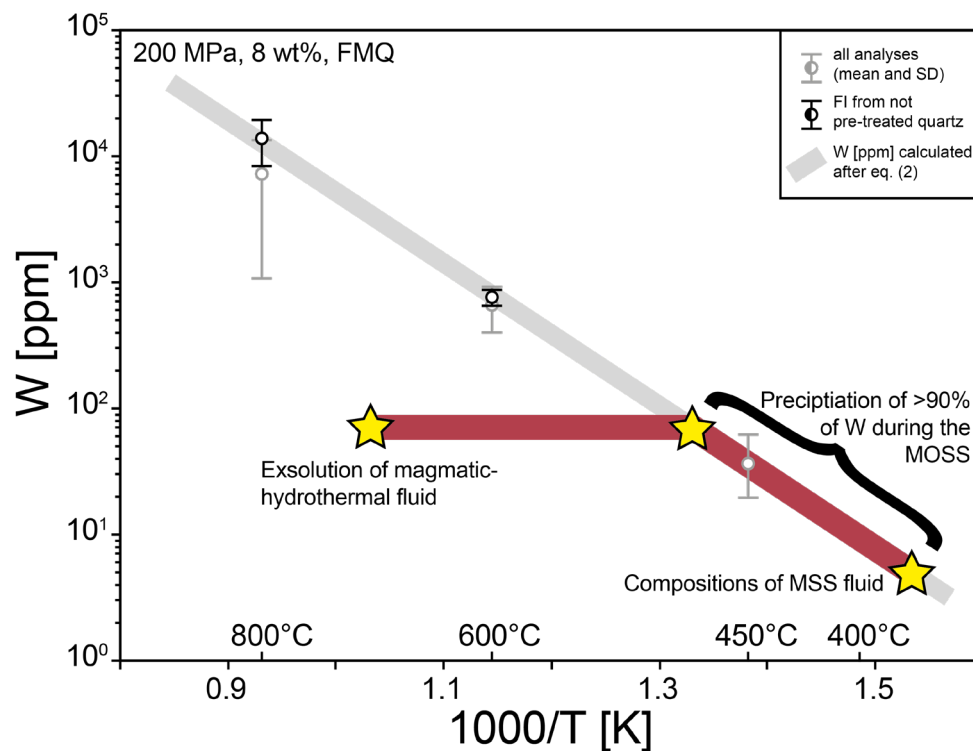


Fig. 6.16: Model of formation conditions during W deposition at the Panasqueira W-Sn-(Cu-)deposit, based on comparison of data from natural fluid inclusions from the Panasqueira W-Sn-(Cu-) deposit of the MOSS from Lecumberri-Sanchez et al. (2017) (up to 70 ppm) and the MSS from this study (ca. 5 ppm) to our experimental results of wolframite solubility in terms of equilibrium W-concentrations in the fluid (c.f., Fig. 5.7). The red curve depicts the postulated development of W concentration in the hydrothermal fluid with decreasing temperature.

Measured W concentrations of fluids from both MOSS and MSS from Lecumberri-Sanchez et al. (2017) and this study are one to two orders of magnitude higher than the calculated

estimate of 0.2 ppm W in the main stage fluids from Polyá (1989). Based on that value, Polyá (1989) had inferred that a total volume of ca. 1000 km³ of hydrothermal fluids must have passed through the vein system at Panasqueira solely during the MOSS and argued that such a large amount of fluid would make the dominance of a meteoric fluid during metal transport and deposition inevitable. Assuming a W-concentration of 10-70 ppm, which is representative of fluids during (c.f., Lecumberri-Sanchez et al., 2017) or after (this study) the mineralization stage, the required amount of hydrothermal fluid can be reduced to ca. 10 – 100 km³. This does not preclude the contribution of a meteoric fluid on metal transport and deposition, but it diminishes significantly the volume of fluids involved in the mineralization and gives room for other interpretations excluding the role of a meteoric fluid. Isotopic data from Polyá et al. (2000) of δD and $\delta^{18}O$ values of fluids from the MSS, which were discussed in chapter 6.7.1 (c.f., Fig. 6.14), might as well be explained by mixing between a magmatic water equilibrating with graphite or coal-bearing (meta-)sediments.

7 Conclusions

Several conclusions and implications can be inferred from the discussions in Chapters 5 and 6 regarding metal solubility in synthetic and metal concentrations in natural fluid inclusions.

- The solubility of Au in hydrothermal fluids determined in our experiments is reached at Au concentrations of tens to hundreds of parts per million and is in agreement with the calculated range of Pokrovski et al. (2015), who suggest that sulfur radical ions, such as S_3^- , are responsible for the formation of the majority of Au deposits on Earth. Our experiments seem to confirm the existence and important role of such species.
- Next to sulfur, temperature has an important effect on the solubility of gold. At high temperatures in experiments of this study (600 to 800 °C), maximum Au concentrations are considerably higher than Au concentrations observed in natural fluids. This supports the idea that hydrothermal fluids are Au-undersaturated at high temperatures, which is in agreement with the common lack of Au deposition at high temperatures, e.g., above 500 °C for Au in porphyry systems (Pokrovski et al., 2014).
- Temperature has the greatest effect on W transport and deposition, followed by salinity, oxygen and sulfur fugacity, whereas pressure does not show a significant effect in the investigated range at least as long as the fluids remain in the one phase field.
- The effect of temperature is more pronounced for ferberite than for scheelite solubility (Fig. 4.7), so that ferberite will precipitate more efficiently with cooling of the fluid than scheelite. This might explain the dominance of wolframite over scheelite in many W-deposits around the world (with the exemption of skarn deposits), where both minerals coexist. It further explains the observed decreasing wolframite/scheelite ratio with depth in some W-deposits, such as the Sannae deposit in Korea (Shelton et al., 1986).
- At salinities greater than ca. 10wt% NaCl, ferberite solubility is more dependent on salinity than scheelite solubility. This could be an explanation for the

observation noted by Wood and Samson (1998) that high salinity fluid inclusions (> 10 wt%) are restricted to deposits in which wolframite dominates, whereas at lower salinities both wolframite and scheelite can be the dominant or only W mineral. According to our experiments, at high salinities the ore-carrying capacity of a hydrothermal fluid will be much greater for ferberite than for scheelite and thus such a fluid will have a Fe/Ca ratio considerably greater than one and precipitate predominantly wolframite upon cooling.

- The model of Wood and Samson (2000), which predicts solubilities of scheelite and ferberite at 200 to 600 °C and 500 to 1000 bars, consistently underestimates W concentrations by a factor of 2 to 10, when comparing it to our and other experimental data. This implies that additional W species might have to be invoked, including Cl-bearing ones such as NaWO_3Cl or $\text{Na}_2\text{HWO}_4\text{Cl}_2$. So far, the underlying cause of the clear positive influence of salinity on W solubility remains unclear.
- The decrease of scheelite solubility at higher $\log f\text{O}_2$ observed experimentally is in agreement with W mineralizations usually occurring within the “oxide stage” of ore deposits typically associated with S-type granites. It further supports the observation that in contrast to porphyry Cu and porphyry Mo systems, porphyry Sn-W deposits are associated with reduced magmas (Burnham and Ohmoto, 1980), because W behaves as an incompatible element in granitic systems under reducing conditions, whereas Mo and Cu tend to be compatible (Candela, 1992). Therefore, W will preferentially partition into the exsolved fluid, which is then transported into shallower crustal levels, where upon oxidation (accompanied by other factors which favor deposition, e.g., cooling and dilution) W minerals will precipitate.
- The necessity of interaction of the ore forming fluids at Panasqueira with the country rocks is supported by combined microthermometric analyses of this study and isotopic compositions determined from Polya et al. (2000) from fluids of the MSS. The increase of reduced C-species as well as the decrease in δD of the fluids points to interaction of the supposedly magmatic-hydrothermal fluid with carboniferous coals or coaly (meta)sediments. The important role of geochemical interaction with the country rocks for the formation of W-deposits in general and at Panasqueira in particular was also pointed out by Lecumberri-Sanchez et al.

(2017) and Codeço et al. (2017). Low concentrations of Ca and Fe observed in natural fluids at Panasqueira and other W-deposits point to a necessary addition of these elements to precipitate either scheelite and/or wolframite. The commonly observed replacement of scheelite by ferberite stands in contrast to the reversal in solubility of ferberite and scheelite (Fig. 4.7) and also requires an external addition of Ca to the system.

- At Panasqueira, only one pulse of a magmatic-hydrothermal fluid seems to have been responsible for the formation of the MSS, as important indicators for magmatic fractionation, namely Li, B, Rb and Cs, do not change significantly throughout the investigated sequence. It is very likely that Cu in chalcopyrite and As in arsenopyrite from the MSS were derived directly from this fluid, as concentrations of these two elements drop sharply in the zone contemporary to sulfide formation.
- The combination of W-concentration from the MOSS from Lecumberri-Sanchez et al. (2017) of ca. 1-70 ppm and W-concentration from the MSS of this study of ca. 1-10 ppm with solubility data from this study derived from synthetic fluid inclusions, enables us to constrain a temperature interval during which the majority of W of the Panasqueira deposit precipitated, i.e., between ca. 480 and 380 °C.
- These W concentrations are one to two orders of magnitude higher than a previously calculated estimate of 0.2 ppm by Polyá (1989). This results in a reduction of the required amount of hydrothermal fluid to more realistic values of ca. 10 – 100 km³ to explain the amount of W precipitated during the MOSS and diminishes (but does not preclude) the necessity of the involvement of meteoric fluids.

8 References

- Akinfiyev, N.N., and Diamond, L.W. (2009) A simple predictive model of quartz solubility in water-salt-CO₂ systems at temperatures up to 1000 degrees C and pressures up to 1000 MPa. *Geochimica Et Cosmochimica Acta*, 73(6), 1597-1608.
- Albrecht, M. (2017) The role of the fluid composition in the formation of hydrothermal Sn-W ores: Insights from in situ analyses of fluid inclusions by UV-fs-LA-ICP-MS, Ph.D. thesis, p. 160. University of Hannover.
- Albrecht, M., Derrey, I.T., Horn, I., Schuth, S., and Weyer, S. (2014) Quantification of trace element contents in frozen fluid inclusions by UV-fs-LA-ICP-MS analysis. *Journal of Analytical Atomic Spectrometry*, 29(6), 1034-1041.
- Allan, M.M., Yardley, B.W., Forbes, L.J., Shmulovich, K.I., Banks, D.A., and Shepherd, T.J. (2005) Validation of LA-ICP-MS fluid inclusion analysis with synthetic fluid inclusions. *American Mineralogist*, 90(11-12), 1767-1775.
- Anderson, A.J., Clark, A.H., Ma, X.-P., Palmer, G.R., MacArthur, J.D., and Roedder, E. (1989) Proton-induced X-ray and gamma-ray emission analysis of unopened fluid inclusions. *Economic Geology*, 84(4), 924-939.
- Audétat, A. (2019) The metal content of magmatic-hydrothermal fluids and its relationship to mineralization potential. *Economic Geology*, 114(6), 1033-1056.
- Audétat, A., Günther, D., and Heinrich, C.A. (1998) Formation of a magmatic-hydrothermal ore deposit: Insights with LA-ICP-MS analysis of fluid inclusions. *Science*, 279(5359), 2091-2094.
- Audétat, A., Günther, D., and Heinrich, C.A. (2000) Magmatic-hydrothermal evolution in a fractionating granite: A microchemical study of the Sn-W-F mineralized Mole Granite (Australia). *Geochimica et Cosmochimica Acta*, 64(19), 3373-3393.
- Audétat, A., Pettke, T., Heinrich, C.A., and Bodnar, R.J. (2008) Special paper: the composition of magmatic-hydrothermal fluids in barren and mineralized intrusions. *Economic Geology*, 103(5), 877-908.
- Banks, D., and Yardley, B. (1992) Crush-leach analysis of fluid inclusions in small natural and synthetic samples. *Geochimica Et Cosmochimica Acta*, 56(1), 245-248.
- Barnes, H.L. (1997) *Geochemistry of hydrothermal ore deposits*. 972 p. Wiley, New York.
- Barré, G., Truche, L., Bazarkina, E.F., Michels, R., and Dubessy, J. (2017) First evidence of the trisulfur radical ion S₃⁻ and other sulfur polymers in natural fluid inclusions. *Chemical Geology*, 462, 1-14.
- Benning, L.G., and Seward, T.M. (1996) Hydrosulphide complexing of Au(I) in hydrothermal solutions from 150-400 degrees C and 500-1500bar. *Geochimica Et Cosmochimica Acta*, 60(11), 1849-1871.
- Berndt, J., Holtz, F., and Koepke, J. (2001) Experimental constraints on storage conditions in the chemically zoned phonolitic magma chamber of the Laacher See volcano. *Contributions to Mineralogy and Petrology*, 140(4), 469-486.

- Berry, A.J., Hack, A.C., Mavrogenes, J.A., Newville, M., and Sutton, S.R. (2006) A XANES study of Cu speciation in high-temperature brines using synthetic fluid inclusions. *American Mineralogist*, 91(11-12), 1773-1782.
- Bodnar, R. (1993) Revised equation and table for determining the freezing point depression of H₂O-NaCl solutions. *Geochimica Et Cosmochimica Acta*, 57(3), 683-684.
- Bodnar, R., Lecumberri-Sanchez, P., Moncada, D., and Steele-MacInnis, M. (2014) Fluid Inclusions in Hydrothermal Ore Deposits. In H. Holland, and K. Turekian, Eds. *Treatise on Geochemistry*, 13, p. 119-142. Elsevier, Oxford.
- Bodnar, R.J., Burnham, C.W., and Sterner, S.M. (1985) Synthetic Fluid Inclusions in Natural Quartz. III. Determination of Phase-Equilibrium Properties in the System H₂O-NaCl to 1000 °C and 1500 bars. *Geochimica et Cosmochimica Acta*, 49(9), 1861-1873.
- Borisova, A.Y., Thomas, R., Salvi, S., Candaudap, F., Lanzaova, A., and Chmeleff, J. (2012) Tin and associated metal and metalloid geochemistry by femtosecond LA-ICP-QMS microanalysis of pegmatite-leucogranite melt and fluid inclusions: new evidence for melt-melt-fluid immiscibility. *Mineralogical Magazine*, 76(1), 91-113.
- Burnard, P.G., and Poly, D.A. (2004) Importance of mantle derived fluids during granite associated hydrothermal circulation: He and Ar isotopes of ore minerals from Panasqueira. *Geochimica Et Cosmochimica Acta*, 68(7), 1607-1615.
- Burnham, C.W., and Ohmoto, H. (1980) Late-stage processes of felsic magmatism. *Mining Geology*, 8, 1-11.
- Bussink, R.W. (1984) Geochemistry of the Panasqueira tungsten-tin deposit, Portugal, PhD thesis, p. 169. Instituut voor Aardwetenschappen der Rijksuniversiteit te Utrecht.
- Campbell, A.R., Banks, D.A., Phillips, R.S., and Yardley, B.W. (1995) Geochemistry of Th-U-REE mineralizing magmatic fluids, Capitan mountains, New Mexico. *Economic Geology*, 90(5), 1271-1287.
- Campbell, A.R., Rye, D., and Petersen, U. (1984) A hydrogen and oxygen isotope study of the San Cristobal Mine, Peru; implications of the role of water to rock ratio for the genesis of wolframite deposits. *Economic Geology*, 79(8), 1818-1832.
- Candela, P.A. (1992) Controls on ore metal ratios in granite-related ore systems: an experimental and computational approach. *Earth and Environmental Science Transactions of The Royal Society of Edinburgh*, 83(1-2), 317-326.
- Carocci, E., Marignac, C., Cathelineau, M., Truche, L., Poujol, M., Boiron, M.C., and Pinto, F. (2021) Incipient wolframite deposition at Panasqueira (Portugal): W-rutile and tourmaline compositions as proxies for early fluid composition. *Economic Geology*, 16(1), 123-146.
- Cathelineau, M., Boiron, M.-C., Marignac, C., Dour, M., Dejean, M., Carocci, E., Truche, L., and Pinto, F. (2020) High pressure and temperatures during the early stages of tungsten deposition at Panasqueira revealed by fluid inclusions in topaz. *Ore Geology Reviews*, 126, 103741.

- Cattalani, S., and Williams-Jones, A.E. (1991) COHN fluid evolution at Saint-Robert, Quebec; implications for W-Bi-Ag mineral deposition. *The Canadian Mineralogist*, 29(3), 435-452.
- Chang, J., Li, J.-W., and Audétat, A. (2018) Formation and evolution of multistage magmatic-hydrothermal fluids at the Yulong porphyry Cu-Mo deposit, eastern Tibet: Insights from LA-ICP-MS analysis of fluid inclusions. *Geochimica Et Cosmochimica Acta*, 232, 181-205.
- Chen, H.-S. (1972) The thermodynamics and composition of carbon dioxide hydrate, M.Sc. thesis, p. 67. Syracuse University, Syracuse, New York.
- Chen, L.-L., Ni, P., Li, W.-S., Ding, J.-Y., Pan, J.-Y., Wang, G.-G., and Yang, Y.-L. (2018) The link between fluid evolution and vertical zonation at the Maoping tungsten deposit, Southern Jiangxi, China: Fluid inclusion and stable isotope evidence. *Journal of Geochemical Exploration*, 192, 18-32.
- Chen, P., Zeng, Q., Zhou, T., Wang, Y., Yu, B., and Chen, J. (2019) Evolution of fluids in the Dasuji porphyry Mo deposit on the northern margin of the North China Craton: Constraints from Microthermometric and LA-ICP-MS analyses of fluid inclusions. *Ore Geology Reviews*, 104, 26-45.
- Clark, A.H. (1970) Potassium-argon age and regional relationships of the Panasqueira tungsten mineralization. *Comun. Serv. Geol. Port.*, 54, 243-261.
- Codeço, M.S., Weis, P., Trumbull, R.B., Pinto, F., Lecumberri-Sanchez, P., and Wilke, F.D. (2017) Chemical and boron isotopic composition of hydrothermal tourmaline from the Panasqueira W-Sn-Cu deposit, Portugal. *Chemical Geology*, 468, 1-16.
- Collins, P.L. (1979) Gas hydrates in CO₂-bearing fluid inclusions and the use of freezing data for estimation of salinity. *Economic Geology*, 74(6), 1435-1444.
- Crerar, D., Wood, S., Brantley, S., and Bocarsly, A. (1985) Chemical controls on solubility of ore-forming minerals in hydrothermal solutions. *The Canadian Mineralogist*, 23(3), 333-352.
- Darling, R.S. (1991) An extended equation to calculate NaCl contents from final clathrate melting temperatures in H₂O-CO₂-NaCl fluid inclusions: Implications for PT isochore location. *Geochimica et Cosmochimica Acta*, 55(12), 3869-3871.
- Derrey, I.T., Albrecht, M., Dupliy, E., Botcharnikov, R.E., Horn, I., Junge, M., Weyer, S., and Holtz, F. (2017) Experimental tests on achieving equilibrium in synthetic fluid inclusions: results for scheelite, molybdenite and gold solubility at 800°C and 200 MPa. *American Mineralogist*, 102(2), 275-283.
- Diamond, L.W. (2001) Review of the systematics of CO₂-H₂O fluid inclusions. *Lithos*, 55(1-4), 69-99.
- Driesner, T. (2007) The system H₂O-NaCl. Part II: Correlations for molar volume, enthalpy, and isobaric heat capacity from 0 to 1000 degrees C, 1 to 5000 bar, and 0 to 1 X-NaCl. *Geochimica Et Cosmochimica Acta*, 71(20), 4902-4919.
- Driesner, T., and Heinrich, C.A. (2007) The system H₂O-NaCl. Part I: Correlation formulae for phase relations in temperature-pressure-composition space from 0 to 1000 degrees C, 0 to 5000 bar, and 0 to 1 X-NaCl. *Geochimica Et Cosmochimica Acta*, 71(20), 4880-4901.

- Duc-Tin, Q., Audétat, A., and Keppler, H. (2007) Solubility of tin in (Cl, F)-bearing aqueous fluids at 700 degrees C, 140 MPa: A LA-ICP-MS study on synthetic fluid inclusions. *Geochimica Et Cosmochimica Acta*, 71(13), 3323-3335.
- Eugster, H.P. (1957) Heterogeneous Reactions Involving Oxidation and Reduction at High Pressures and Temperatures. *Journal of Chemical Physics*, 26(6), 1760-1761.
- Fall, A., Tattitch, B., and Bodnar, R.J. (2011) Combined microthermometric and Raman spectroscopic technique to determine the salinity of H₂O-CO₂-NaCl fluid inclusions based on clathrate melting. *Geochimica Et Cosmochimica Acta*, 75(4), 951-964.
- Foster, R.P. (1977) Solubility of Scheelite in Hydrothermal Chloride Solutions. *Chemical Geology*, 20(1), 27-43.
- Foxford, K., Nicholson, R., and Polya, D. (1991) Textural evolution of W-Cu-Sn-bearing hydrothermal veins at Minas da Panasqueira, Portugal. *Mineralogical Magazine*, 55(380), 435-445.
- Foxford, K., Nicholson, R., Polya, D., and Hebblethwaite, R. (2000) Extensional failure and hydraulic valving at Minas da Panasqueira, Portugal: evidence from vein spatial distributions, displacements and geometries. *Journal of Structural Geology*, 22(8), 1065-1086.
- Foxford, K.A. (1992) Fluid flow patterns during ore formation: Controls on mineralogical zoning, Panasqueira, Portugal. Department of Geology, PhD Thesis, p. 463. University of Manchester.
- Frank, M.R., Simon, A.C., Pettke, T., Candela, P.A., and Piccoli, P.M. (2011) Gold and copper partitioning in magmatic-hydrothermal systems at 800 degrees C and 100 MPa. *Geochimica Et Cosmochimica Acta*, 75(9), 2470-2482.
- Frantz, J.D., Mao, H., Zhang, Y.-G., Wu, Y., Thompson, A., Underwood, J., Giauque, R., Jones, K., and Rivers, M. (1988) Analysis of fluid inclusions by X-ray fluorescence using synchrotron radiation. *Chemical Geology*, 69(3-4), 235-244.
- Gibert, F., Moine, B., Schott, J., and Dandurand, J.L. (1992) Modeling of the Transport and Deposition of Tungsten in the Scheelite-Bearing Calc-Silicate Gneisses of the Montagne Noire, France. *Contributions to Mineralogy and Petrology*, 112(2-3), 371-384.
- Gibert, F., Pascal, M.L., and Pichavant, M. (1998) Gold solubility and speciation in hydrothermal solutions: Experimental study of the stability of hydrosulphide complex of gold (AuHS degrees) at 350 to 450 degrees C and 500 bars. *Geochimica Et Cosmochimica Acta*, 62(17), 2931-2947.
- Giuliani, G. (1984) Les concentrations filoniennes à tungstène-étain du massif granitique des Zaër (Maroc Central): Minéralisations et phases fluides associées. *Mineralium Deposita*, 19(3), 193-201.
- Graupner, T., Brätz, H., and Klemd, R. (2005) LA-ICP-MS micro-analysis of fluid inclusions in quartz using a commercial Merchantek 266 nm Nd: YAG laser: a pilot study. *European journal of mineralogy*, 17(1), 93-102.
- Griffith, W.P., and Lesniak, P.J.B. (1969) Raman studies on species in aqueous solutions. Part III. Vanadates, molybdates, and tungstates. *Journal of the Chemical Society (A)*, 1066-1071.

- Guillong, M., and Heinrich, C.A. (2007) Sensitivity enhancement in laser ablation ICP-MS using small amounts of hydrogen in the carrier gas. *Journal of Analytical Atomic Spectrometry*, 22(12), 1488-1494.
- Guillong, M., Latkoczy, C., Seo, J.H., Gunther, D., and Heinrich, C.A. (2008a) Determination of sulfur in fluid inclusions by laser ablation ICP-MS. *Journal of Analytical Atomic Spectrometry*, 23(12), 1581-1589.
- Guillong, M., Meier, D., Allan, M., Heinrich, C., and Yardley, B. (2008b) SILLS: a MATLAB-based program for the reduction of laser ablation ICP-MS data of homogeneous materials and inclusions. *Mineralogical Association of Canada Short Course*, 40, 328-333.
- Günther, D., Audétat, A., Frischknecht, R., and Heinrich, C.A. (1998) Quantitative analysis of major, minor and trace elements in fluid inclusions using laser ablation inductively coupled plasma mass spectrometry. *Journal of Analytical Atomic Spectrometry*, 13(4), 263-270.
- Günther, D., Hattendorf, B., and Audétat, A. (2001) Multi-element analysis of melt and fluid inclusions with improved detection capabilities for Ca and Fe using laser ablation with a dynamic reaction cell ICP-MS Presented at the 2001 European Winter Conference on Plasma Spectrochemistry, Lillehammer, Norway, February 4-8, 2001. *Journal of Analytical Atomic Spectrometry*, 16(9), 1085-1090.
- Guo, H., Audétat, A., and Dolejš, D. (2018) Solubility of gold in oxidized, sulfur-bearing fluids at 500–850° C and 200–230 MPa: A synthetic fluid inclusion study. *Geochimica Et Cosmochimica Acta*, 222, 655-670.
- Hack, A.C., and Mavrogenes, J.A. (2006) A synthetic fluid inclusion study of copper solubility in hydrothermal brines from 525 to 725 degrees C and 0.3 to 1.7 GPa. *Geochimica Et Cosmochimica Acta*, 70(15), 3970-3985.
- Halter, W.E., Pettke, T., Heinrich, C.A., and Rothen-Rutishauser, B. (2002) Major to trace element analysis of melt inclusions by laser-ablation ICP-MS: methods of quantification. *Chemical Geology*, 183(1-4), 63-86.
- Hanley, J.J., Pettke, T., Mungall, J.E., and Spooner, E.T.C. (2005) The solubility of platinum and gold in NaCl brines at 1.5 kbar, 600 to 800 degrees C: A laser ablation ICP-MS pilot study of synthetic fluid inclusions (vol 10, pg 2593, 2005). *Geochimica Et Cosmochimica Acta*, 69(23), 5635-5637.
- Harlaux, M., Mercadier, J., Bonzi, W.M.-E., Kremer, V., Marignac, C., and Cuney, M. (2017) Geochemical signature of magmatic-hydrothermal fluids exsolved from the beauvoir rare-metal granite (Massif Central, France): insights from LA-ICPMS analysis of primary fluid inclusions. *Geofluids*, 2017, 25.
- Hart, C. (2007) Reduced intrusion-related gold systems. *Geological Association of Canada, Special Publication*, 5, 95-112.
- Heinrich, C., Günther, D., Audétat, A., Ulrich, T., and Frischknecht, R. (1999a) Metal fractionation between magmatic brine and vapor, determined by microanalysis of fluid inclusions. *Geology*, 27(8), 755-758.
- Heinrich, C.A. (1990) The chemistry of hydrothermal tin (-tungsten) ore deposition. *Economic Geology*, 85(3), 457-481.

- Heinrich, C.A., and Candela, P.A. (2014) Fluids and ore formation in the Earth's crust. *Treatise on Geochemistry* (Second Edition), 13, p. 1-28. Elsevier.
- Heinrich, C.A., Gunther, D., Audétat, A., Ulrich, T., and Frischknecht, R. (1999b) Metal fractionation between magmatic brine and vapor, determined by microanalysis of fluid inclusions. *Geology*, 27(8), 755-758.
- Heinrich, C.A., Pettke, T., Halter, W.E., Aigner-Torres, M., Audétat, A., Günther, D., Hattendorf, B., Bleiner, D., Guillong, M., and Horn, I. (2003) Quantitative multi-element analysis of minerals, fluid and melt inclusions by laser-ablation inductively-coupled-plasma mass-spectrometry. *Geochimica Et Cosmochimica Acta*, 67(18), 3473-3497.
- Heinrich, C.A., Ryan, C.G., Mernagh, T.P., and Eadington, P.J. (1992) Segregation of ore metals between magmatic brine and vapor; a fluid inclusion study using PIXE microanalysis. *Economic Geology*, 87(6), 1566-1583.
- Helgeson, H.C., and Garrels, R.M. (1968) Hydrothermal transport and deposition of gold. *Economic Geology*, 63(6), 622-635.
- Hergenröder, R. (2006) A model of non-congruent laser ablation as a source of fractionation effects in LA-ICP-MS. *Journal of Analytical Atomic Spectrometry*, 21(5), 505-516.
- Higgins, N., and Kerrich, R. (1982) Progressive 180 depletion during CO₂ separation from a carbon dioxide-rich hydrothermal fluid: evidence from the Grey River tungsten deposit, Newfoundland. *Canadian Journal of Earth Sciences*, 19(12), 2247-2257.
- Hirayama, Y., and Obara, M. (2005) Heat-affected zone and ablation rate of copper ablated with femtosecond laser. *Journal of Applied Physics*, 97(6), 064903.
- Horn, I., and von Blanckenburg, F. (2007) Investigation on elemental and isotopic fractionation during 196 nm femtosecond laser ablation multiple collector inductively coupled plasma mass spectrometry. *Spectrochimica Acta Part B: Atomic Spectroscopy*, 62(4), 410-422.
- Horn, I., von Blanckenburg, F., Schoenberg, R., Steinhoefel, G., and Markl, G. (2006) In situ iron isotope ratio determination using UV-femtosecond laser ablation with application to hydrothermal ore formation processes. *Geochimica Et Cosmochimica Acta*, 70(14), 3677-3688.
- Hsu, L.C. (1977) Effects of Oxygen and Sulfur Fugacities on Scheelite-Tungstenite and Powellite-Molybdenite Stability Relations. *Economic Geology*, 72(4), 664-670.
- Jaques, L., and Pascal, C. (2017) Full paleostress tensor reconstruction using quartz veins of Panasqueira Mine, central Portugal; part I: Paleopressure determination. *Journal of Structural Geology*, 102, 58-74.
- Jochum, K.P., Nohl, L., Herwig, K., Lammel, E., Toll, B., and Hofmann, A.W. (2005) GeoReM: A new geochemical database for reference materials and isotopic standards. *Geostandards and Geoanalytical Research*, 29(3), 333-338.
- Julivert, M., Fontboté, J.M., Ribeiro, A., and Conde, L. (1972) Mapa Tectónico de la Península Ibérica y Baleares E., 1:1.000.000. Inst. Geol. Min. España, Madrid.
- Kelly, W.C., and Rye, R.O. (1979) Geologic, fluid inclusion, and stable isotope studies of the tin-tungsten deposits of Panasqueira, Portugal. *Economic Geology*, 74(8), 1721-1822.

- Kesler, S.E. (2005) Ore-forming fluids. *Elements*, 1(1), 13-18.
- Kesler, S.E., and Simon, A.C. (2015) *Mineral resources, economics and the environment*. Cambridge University Press.
- Korges, M., Weis, P., Lüders, V., and Laurent, O. (2018) Depressurization and boiling of a single magmatic fluid as a mechanism for tin-tungsten deposit formation. *Geology*, 46(1), 75-78.
- Krauskopf, K.B. (1951) The solubility of gold. *Economic Geology*, 46(8), 858-870.
- Landis, G.P., and Rye, R.O. (1974) Geologic, fluid inclusion, and stable isotope studies of the Pasto Buena tungsten-base metal ore deposit, northern Peru. *Economic Geology*, 69(7), 1025-1059.
- Larson, S.D. (1955) Phase studies of the two-component carbon dioxide-water system involving the carbon dioxide hydrate, PhD thesis, p. 88. University of Illinois, Urbana, Illinois.
- Latunussa, C.E., Georgitzikis, K., Matos, C.T.d., Grohol, M., Eynard, U., Wittmer, D., Mancini, L., Unguru, M., Pavel, C., Carrara, S., Mathieux, F., Pennington, D., and Blengini, G.A. (2020) Study on the EU's list of Critical Raw Materials - Critical Raw Materials Factsheets (Final), p. 817. European Commission, Brussels.
- Launay, G. (2018) Hydrodynamique des systèmes minéralisés péri-granitiques : étude du gisement à W-Sn-(Cu) de Panasqueira (Portugal). Institut des Sciences de la Terre, PhD thesis, p. 523. Université d'Orléans.
- Launay, G., Sizaret, S., Guillou-Frottier, L., Gloaguen, E., and Pinto, F. (2018) Deciphering fluid flow at the magmatic-hydrothermal transition: A case study from the world-class Panasqueira W-Sn-(Cu) ore deposit (Portugal). *Earth and Planetary Science Letters*, 499, 1-12.
- Launay, G., Sizaret, S., Lach, P., Melleton, J., Gloaguen, É., and Poujol, M. (2021) Genetic relationship between greisenization and Sn-W mineralizations in vein and greisen deposits: Insights from the Panasqueira deposit (Portugal). *BSGF-Earth Sciences Bulletin*, 192(1), 2.
- Lecumberri-Sanchez, P., Vieira, R., Heinrich, C.A., Pinto, F., and Walle, M. (2017) Fluid-rock interaction is decisive for the formation of tungsten deposits. *Geology*, 45(7), 579-582.
- Legros, H., Richard, A., Tarantola, A., Kouzmanov, K., Mercadier, J., Vennemann, T., Marignac, C., Cuney, M., Wang, R.-C., and Charles, N. (2019) Multiple fluids involved in granite-related W-Sn deposits from the world-class Jiangxi province (China). *Chemical Geology*, 508, 92-115.
- Lerchbaumer, L., and Audétat, A. (2009) Partitioning of Cu between vapor and brine - An experimental study based on LA-ICP-MS analysis of synthetic fluid inclusions. *Geochimica Et Cosmochimica Acta*, 73(13), A744-A744.
- Li, Y., and Audétat, A. (2009) A method to synthesize large fluid inclusions in quartz at controlled times and under unfavorable growth conditions. *American Mineralogist*, 94(2-3), 367-371.
- Liu, X., and Xiao, C. (2020) Wolframite solubility and precipitation in hydrothermal fluids: insight from thermodynamic modeling. *Ore Geology Reviews*, 117(103289), 1-14.

- Longerich, H.P., Jackson, S.E., and Günther, D. (1996) Inter-laboratory note. Laser ablation inductively coupled plasma mass spectrometric transient signal data acquisition and analyte concentration calculation. *Journal of Analytical Atomic Spectrometry*, 11(9), 899-904.
- Loucks, R.R., and Mavrogenes, J.A. (1999) Gold solubility in supercritical hydrothermal brines measured in synthetic fluid inclusions. *Science*, 284(5423), 2159-2163.
- Malinin, S.D., and Kurovskaya, N.A. (1993) The Solubility of Scheelite in Aqueous NaCl, CaCl₂, and KCl Solutions at 600-800 °C and 2 kbar. *Geochemistry International*, 30, 76-88.
- . (1996) The Effect of Pressure on Mineral Solubility in Aqueous Chloride Solutions under Supercritical Conditions. *Geochemistry International*, 34, 45-52.
- Manning, D.A., and Henderson, P. (1984) The behaviour of tungsten in granitic melt-vapour systems. *Contributions to Mineralogy and Petrology*, 86(3), 286-293.
- Marignac, C. (1982) Geologic, fluid inclusions, and stable isotope studies of the tin-tungsten deposits of Panasqueira, Portugal; discussion. *Economic Geology*, 77(5), 1263-1266.
- Martínez Catalán, J., Arenas, R., García, F.D., Cuadra, P.G., Gómez-Barreiro, J., Abati, J., Castiñeiras, P., Fernández-Suárez, J., Martínez, S.S., and Andonaegui, P. (2007) Space and time in the tectonic evolution of the northwestern Iberian Massif: Implications for the Variscan belt. 4-D framework of continental crust, 200, p. 403-423. Geological Society of America Memoir Boulder, Colorado.
- Matthews, W., Linnen, R.L., and Guo, Q. (2003) A filler-rod technique for controlling redox conditions in cold-seal pressure vessels. *American Mineralogist*, 88(4), 701-707.
- Mavrogenes, J., Bodnar, R., Anderson, A., Bait, S., Sutton, S., and Rivers, M. (1995) Assessment of the uncertainties and limitations of quantitative elemental analysis of individual fluid inclusions using synchrotron X-ray fluorescence (SXRF). *Geochimica Et Cosmochimica Acta*, 59(19), 3987-3995.
- Neiva, A. (2008) Geochemistry of cassiterite and wolframite from tin and tungsten quartz veins in Portugal. *Ore Geology Reviews*, 33(3-4), 221-238.
- Newton, R.C., and Manning, C.E. (2000) Quartz solubility in H₂O-NaCl and H₂O-CO₂ solutions at deep crust-upper mantle pressures and temperatures: 2-15 kbar and 500-900 degrees C. *Geochimica Et Cosmochimica Acta*, 64(17), 2993-3005.
- Noronha, F., Doria, A., Dubessy, J., and Charoy, B. (1992) Characterization and timing of the different types of fluids present in the barren and ore-veins of the W-Sn deposit of Panasqueira, Central Portugal. *Mineralium Deposita*, 27(1), 72-79.
- O'Reilly, C., Gallagher, V., and Feely, M. (1997) Fluid inclusion study of the Ballinglen W-Sn-sulphide mineralization, SE Ireland. *Mineralium Deposita*, 32(6), 569-580.
- Pan, J.-Y., Ni, P., and Wang, R.-C. (2019) Comparison of fluid processes in coexisting wolframite and quartz from a giant vein-type tungsten deposit, South China: Insights from detailed petrography and LA-ICP-MS analysis of fluid inclusions. *American Mineralogist: Journal of Earth and Planetary Materials*, 104(8), 1092-1116.
- Pearson, R.G. (1963) Hard and soft acids and bases. *Journal of the American Chemical Society*, 85(22), 3533-3539.

- Pettke, T., Oberli, F., Audétat, A., Guillong, M., Simon, A.C., Hanley, J.J., and Klemm, L.M. (2012) Recent developments in element concentration and isotope ratio analysis of individual fluid inclusions by laser ablation single and multiple collector ICP-MS. *Ore Geology Reviews*, 44, 10-38.
- Pettke, T., Oberli, F., Audétat, A., Wiechert, U., Harris, C.R., and Heinrich, C.A. (2011) Quantification of transient signals in multiple collector inductively coupled plasma mass spectrometry: accurate lead isotope ratio determination by laser ablation of individual fluid inclusions. *Journal of Analytical Atomic Spectrometry*, 26(3), 475-492.
- Pitzer, K.S. (1983) Dielectric-Constant of Water at Very High-Temperature and Pressure. *Proceedings of the National Academy of Sciences of the United States of America-Physical Sciences*, 80(14), 4575-4576.
- Pokrovski, G.S., Akinfiyev, N.N., Borisova, A.Y., Zotov, A.V., and Kouzmanov, K. (2014) Gold speciation and transport in geological fluids: Insights from experiments and physical-chemical modelling. *Geological Society, London, Special Publications*, 402, 9-70.
- Pokrovski, G.S., Kokh, M.A., Guillaume, D., Borisova, A.Y., Gisquet, P., Hazemann, J.L., Lahera, E., Del Net, W., Proux, O., Testemale, D., Haigis, V., Jonchiere, R., Seitsonen, A.P., Ferlat, G., Vuilleumier, R., Saitta, A.M., Boiron, M.C., and Dubessy, J. (2015) Sulfur radical species form gold deposits on Earth. *Proceedings of the National Academy of Sciences of the United States of America*, 112(44), 13484-13489.
- Polya, D. (1989) Chemistry of the main-stage ore-forming fluids of the Panasqueira W-Cu (Ag)-Sn deposit, Portugal; implications for models of ore genesis. *Economic Geology*, 84(5), 1134-1152.
- Polya, D., Foxford, K., Stuart, F., Boyce, A., and Fallick, A. (2000) Evolution and paragenetic context of low δD hydrothermal fluids from the Panasqueira W-Sn deposit, Portugal: new evidence from microthermometric, stable isotope, noble gas and halogen analyses of primary fluid inclusions. *Geochimica Et Cosmochimica Acta*, 64(19), 3357-3371.
- Polya, D.A. (1988) Efficiency of hydrothermal ore formation and the Panasqueira W-Cu (Ag)-Sn vein deposit. *Nature*, 333(6176), 838-841.
- Polya, D.A. (1990) Pressure-Dependence of Wolframite Solubility for Hydrothermal Vein Formation. *Transactions of the Institution of Mining and Metallurgy Section B-Applied Earth Science*, 99, B120-B124.
- Pronko, P., Dutta, S., Du, D., and Singh, R. (1995) Thermophysical effects in laser processing of materials with picosecond and femtosecond pulses. *Journal of Applied Physics*, 78(10), 6233-6240.
- Ribeiro, A., Quesada, C., and Dallmeyer, R.D. (1990) Geodynamic Evolution of the Iberian Massif. In R.D. Dallmeyer, and E.M. Garcia, Eds. *Pre-Mesozoic Geology of Iberia*, p. 399-409. Springer Berlin Heidelberg, Berlin, Heidelberg.
- Robb, L. (2005) *Introduction to ore-forming processes*. 373 p. Blackwell publishing, Oxford.
- Roedder, E. (1972) Composition of fluid inclusions. In M. Fleischer, Ed. *Data of geochemistry*, p. 164. US Geological Survey, Washington.

- . (1984) *Fluid Inclusions*. 644 p. Mineralogical Society of America.
- Roedder, E., and Bodnar, R.J. (1997) Fluid inclusion studies of hydrothermal ore deposits. In H.L. Barnes, Ed. *Geochemistry of hydrothermal ore deposits*, p. 657-697. John Wiley, New York.
- Roedder, E., and Kopp, O.C. (1975) A check on the validity of the pressure correction in inclusion geothermometry, using hydrothermally grown quartz. *Fortschritte der Mineralogie*, 52, 431-446.
- Samson, I.M. (1990) Fluid evolution and mineralization in a subvolcanic granite stock; the Mount Pleasant W-Mo-Sn deposits, New Brunswick, Canada. *Economic Geology*, 85(1), 145-163.
- Schröcke, H., Trumm, A., and Hochleitner, R. (1984) Über den Transport von Wolfram und den Absatz von Wolfram-Doppel-Oxiden in fluiden wässrigen Lösungen. *Geochimica et Cosmochimica Acta*, 48(9), 1791-1805.
- Seal, R.R., Clark, A.H., and Morrissy, C.J. (1987) Stockwork tungsten (scheelite)-molybdenum mineralization, Lake George, southwestern New Brunswick. *Economic Geology*, 82(5), 1259-1282.
- Seo, J.H., Guillong, M., Aerts, M., Zajacz, Z., and Heinrich, C.A. (2011) Microanalysis of S, Cl, and Br in fluid inclusions by LA-ICP-MS. *Chemical Geology*, 284(1-2), 35-44.
- Seward, T.M. (1981) Metal complex formation in aqueous solutions at elevated temperatures and pressures. *Physics and Chemistry of the Earth*, 13, 113-132.
- Seyfried, W.E., Gordon, P.C., and Dickson, F.W. (1979) New Reaction Cell for Hydrothermal Solution Equipment. *American Mineralogist*, 64(5-6), 646-649.
- Shelton, K.L., and Orville, P.M. (1980) Formation of Synthetic Fluid Inclusions in Natural Quartz. *American Mineralogist*, 65(11-1), 1233-1236.
- Shelton, K.L., So, C.S., Rye, D.M., and Park, M.E. (1986) Geologic, Sulfur Isotope, and Fluid Inclusion Studies of the Sannae W-Mo Mine, Republic-of-Korea - Comparison of Sulfur Isotope Systematics in Korean W-Deposits. *Economic Geology*, 81(2), 430-446.
- Shepherd, T.J., Rankin, A.H., and Alderton, D.H. (1985) *A practical guide to fluid inclusion studies*. Blackie & Son, Glasgow and London.
- Simon, A.C., Frank, M.R., Pettke, T., Candela, P.A., Piccoli, P.M., Heinrich, C.A., and Glascock, M. (2007) An evaluation of synthetic fluid inclusions for the purpose of trapping equilibrated, coexisting, immiscible fluid phases at magmatic conditions. *American Mineralogist*, 92(1), 124-138.
- Simon, A.C., Pettke, T., Candela, P.A., Piccoli, P.M., and Heinrich, C.A. (2006) Copper partitioning in a melt-vapor-brine-magnetite-pyrrhotite assemblage. *Geochimica Et Cosmochimica Acta*, 70(22), 5583-5600.
- Snee, L.W., Sutter, J.F., and Kelly, W.C. (1988) Thermochronology of economic mineral deposits; dating the stages of mineralization at Panasqueira, Portugal, by high-precision $^{40}\text{Ar}/^{39}\text{Ar}$ age spectrum techniques on muscovite. *Economic Geology*, 83(2), 335-354.
- So, C.-S., and Yun, S.-T. (1994) Origin and evolution of W-Mo-producing fluids in a granitic hydrothermal system; geochemical studies of quartz vein deposits around the

- Susan Granite, Hwanggangri District, Republic of Korea. *Economic Geology*, 89(2), 246-267.
- Sorby, H.C. (1858) On the microscopical, structure of crystals, indicating the origin of minerals and rocks. *Quarterly Journal of the Geological Society*, 14(1-2), 453-500.
- Steinboeckel, G., Horn, I., and von Blanckenburg, F. (2009a) Matrix-independent Fe isotope ratio determination in silicates using UV femtosecond laser ablation. *Chemical Geology*, 268(1-2), 67-73.
- . (2009b) Micro-scale tracing of Fe and Si isotope signatures in banded iron formation using femtosecond laser ablation. *Geochimica Et Cosmochimica Acta*, 73(18), 5343-5360.
- Steinboeckel, G., von Blanckenburg, F., Horn, I., Konhauser, K.O., Beukes, N.J., and Gutzmer, J. (2010) Deciphering formation processes of banded iron formations from the Transvaal and the Hamersley successions by combined Si and Fe isotope analysis using UV femtosecond laser ablation. *Geochimica Et Cosmochimica Acta*, 74(9), 2677-2696.
- Sterner, S.M., and Bodnar, R.J. (1984) Synthetic Fluid Inclusions in Natural Quartz .1. Compositional Types Synthesized and Applications to Experimental Geochemistry. *Geochimica Et Cosmochimica Acta*, 48(12), 2659-2668.
- Sterner, S.M., Hall, D.L., and Bodnar, R.J. (1988) Synthetic Fluid Inclusions. V. Solubility Relations in the System NaCl-KCl-H₂O under Vapor-Saturated Conditions. *Geochimica Et Cosmochimica Acta*, 52(5), 989-1005.
- Thadeau, D. (1951) Geologia do couro mineiro da Panasqueira. *Comunicações dos Serviços Geológicos de Portugal*, 32, 5-64.
- Ulrich, T., Guenther, D., and Heinrich, C.A. (1999) Gold concentrations of magmatic brines and the metal budget of porphyry copper deposits. *Nature*, 399(6737), 676.
- Ulrich, T., Günther, D., and Heinrich, C.A. (2002) The evolution of a porphyry Cu-Au deposit, based on LA-ICP-MS analysis of fluid inclusions: Bajo de la Alumbrera, Argentina. *Economic Geology*, 97(8), 1889-1920.
- Ulrich, T., and Mavrogenes, J. (2008) An experimental study of the solubility of molybdenum in H₂O and KCl-H₂O solutions from 500 degrees C to 800 degrees C, and 150 to 300 MPa. *Geochimica Et Cosmochimica Acta*, 72(9), 2316-2330.
- Wang, X.-S., Williams-Jones, A., Hu, R.-Z., Shang, L.-B., and Bi, X.-W. (2021) The role of fluorine in granite-related hydrothermal tungsten ore genesis: Results of experiments and modeling. *Geochimica et Cosmochimica Acta*, 292, 170-187.
- Williams-Jones, A.E., and Heinrich, C.A. (2005) 100th Anniversary special paper: vapor transport of metals and the formation of magmatic-hydrothermal ore deposits. *Economic Geology*, 100(7), 1287-1312.
- Wood, S.A. (1992) Experimental determination of the solubility of WO₃ (s) and the thermodynamic properties of H₂WO₄ (aq) in the range 300–600 C at 1 kbar: calculation of scheelite solubility. *Geochimica Et Cosmochimica Acta*, 56(5), 1827-1836.
- Wood, S.A., and Samson, I.M. (1998) Solubility of ore minerals and complexation of ore metals in hydrothermal solutions. *Reviews in Economic Geology*, 10, 33-80.

- Wood, S.A., and Samson, I.M. (2000) The hydrothermal geochemistry of tungsten in granitoid environments: I. Relative solubilities of ferberite and scheelite as a function of T, P, pH, and m(NaCl). *Economic Geology and the Bulletin of the Society of Economic Geologists*, 95(1), 143-182.
- Wood, S.A., and Vlassopoulos, D. (1989) Experimental determination of the hydrothermal solubility and speciation of tungsten at 500° C and 1 kbar. *Geochimica Et Cosmochimica Acta*, 53(2), 303-312.
- Yastrebova, L., Borina, A., and Ravich, M. (1963) Solubility of calcium molybdate and tungstate in aqueous potassium and sodium chlorides at high temperatures. *Russian Journal of Inorganic Chemistry*, 8, 105-110.
- Zajacz, Z., Halter, W.E., Pettke, T., and Guillong, M. (2008) Determination of fluid/melt partition coefficients by LA-ICPMS analysis of co-existing fluid and silicate melt inclusions: Controls on element partitioning. *Geochimica Et Cosmochimica Acta*, 72(8), 2169-2197.
- Zajacz, Z., Seo, J.H., Candela, P.A., Piccoli, P.M., Heinrich, C.A., and Guillong, M. (2010) Alkali metals control the release of gold from volatile-rich magmas. *Earth and Planetary Science Letters*, 297(1-2), 50-56.
- Zhang, L., Audétat, A., and Dolejs, D. (2012) Solubility of molybdenite (MoS₂) in aqueous fluids at 600-800 degrees C, 200 MPa: A synthetic fluid inclusion study. *Geochimica Et Cosmochimica Acta*, 77, 175-185.

Appendix I

Supplements to Chapter 3 - Synthetic Fluid inclusions for the calibration of the analytical method

Suppl. Tab. 1: Compositions of the measured fluid inclusions from sample ID-188-Au. Accuracy relative to original composition of the experimental fluid. *Italic values were not used for calculation.*

Name	⁹ Be	¹¹ B	²³ Na	³⁹ K	⁵⁹ Co	⁶⁴ Zn	⁶⁹ Ga	⁸⁸ Sr	¹¹¹ Cd	¹²⁵ Te	¹³⁷ Ba	¹⁹⁵ Pt	¹⁹⁷ Au	²⁰³ Tl	²⁰⁸ Pb	²⁰⁹ Bi
	μg/g	μg/g	μg/g	μg/g	μg/g	μg/g	μg/g	μg/g	μg/g	μg/g	μg/g	μg/g	μg/g	μg/g	μg/g	μg/g
18nov03	45	34	38054	-	44	-	34	33	44	84	39	-	19873	45	45	49
18nov04	<i>51</i>	63	38054	-	46	-	<i>51</i>	43	<i>82</i>	56	48	-	24320	51	57	53
18nov05	45	33	38054	-	19	-	29	36	37	46	43	-	20044	42	43	34
18nov06	20	62	38054	-	19	-	39	36	43	60	34	-	20618	53	53	53
18nov08	19	54	38054	-	15	-	23	30	46	26	21	-	19967	51	31	32
18nov09	16	41	38054	-	43	-	25	33	42	53	32	-	13261	44	55	44
18nov10	8	55	38054	-	17	-	28	30	46	52	22	-	13812	46	47	49
18nov11	25	58	38054	-	32	-	34	38	47	70	30	-	20580	54	56	56
18nov13	28	53	38054	-	47	-	36	43	44	49	43	-	17481	55	56	57
18nov14	25	57	38054	-	54	-	33	42	45	81	41	-	17450	59	48	57
18nov15	19	47	38054	-	16	-	30	36	52	65	23	-	18352	55	51	59
18nov16	27	65	38054	-	37	-	27	41	58	62	39	-	17613	58	41	48
18nov20	51	63	38054	-	53	-	43	43	53	58	47	-	<i>3789</i>	38	52	47
18nov21	24	53	38054	-	20	-	28	25	45	73	28	-	19165	60	48	56
18nov23	9	51	38054	-	5	-	15	24	50	57	13	-	10121	50	38	44
18nov24	6	63	38054	-	13	-	26	29	45	<i>109</i>	10	-	18619	71	59	68
18nov25	26	53	38054	-	38	-	34	37	46	85	30	-	22838	53	54	61
18nov26	30	56	38054	-	56	-	25	53	45	71	53	-	14229	51	56	57
18nov28	20	47	38054	-	36	-	20	40	37	52	43	-	9976	50	43	44
18nov29	14	47	38054	-	5	-	17	28	38	44	18	-	13282	46	34	39
18nov30	4	53	38054	-	2	-	17	22	48	57	10	-	13886	54	38	48
18nov31	36	<i>30</i>	38054	-	39	-	16	26	26	7	31	-	5794	33	33	33
18nov33	36	58	38054	-	24	-	41	34	68	60	29	-	<i>27636</i>	65	52	69
18nov34	11	53	38054	-	1	-	19	23	49	53	9	-	13963	53	37	49
18nov35	18	54	38054	-	13	-	19	25	44	52	17	-	11946	53	42	47
18nov36	23	37	38054	-	24	-	31	23	41	33	19	-	8481	38	37	34
<i>18nov19</i>	<i>168</i>	<i>152</i>	<i>38054</i>	-	<i>40</i>	-	<i>3</i>	<i>6</i>	<i><2.1</i>	<i>26</i>	<i><1.1</i>	-	<i>11535</i>	<i>64</i>	<i><0.3</i>	<i>28</i>
Mean	23	52	-	-	28	-	28	33	46	58	30	-	16070	51	46	49
SD	12	9	-	-	17	-	8	7	7	14	13	-	4727	7	8	9
RSD	52%	17%	-	-	61%	-	29%	21%	14%	25%	43%	-	29%	13%	18%	19%
Accuracy*	44%	99%	-	-	52%	-	51%	62%	88%	108%	56%	-	-	97%	88%	91%
n	25	25	27	-	26	-	25	25	24	24	26	-	24	24	26	25

Suppl. Tab. 2: Compositions of the measured fluid inclusions from sample ID-189-Pt. *: Accuracy relative to original composition of the experimental fluid. *Italic values were not used for calculation*

Name	⁹ Be	¹¹ B	²³ Na	³⁹ K	⁵⁹ Co	⁶⁴ Zn	⁶⁹ Ga	⁸⁸ Sr	¹¹¹ Cd	¹²⁵ Te	¹³⁷ Ba	¹⁹⁵ Pt	¹⁹⁷ Au	²⁰³ Tl	²⁰⁸ Pb	²⁰⁹ Bi
	μg/g	μg/g	μg/g	μg/g	μg/g	μg/g	μg/g	μg/g	μg/g	μg/g	μg/g	μg/g	μg/g	μg/g	μg/g	μg/g
19nov03	16	64	38054	44	<i>80</i>	45	33	30	38	74	44	141	17	60	49	34
19nov04	36	54	38054	20	3	19	56	11	43	<i>< 6.7</i>	8	49	16	35	<i>18</i>	55
19nov05	79	122	38054	<i>146</i>	19	<i>< 4.3</i>	29	29	47	<i>107</i>	37	196	8	39	40	49
19nov06	18	64	38054	59	42	48	22	39	46	96	37	215	14	61	55	43
19nov08	<i>< 3.3</i>	<i>119</i>	38054	<i>110</i>	21	31	12	30	22	42	24	100	10	64	30	33
19nov09	17	74	38054	<i>< 6.4</i>	35	<i>74</i>	15	26	52	88	11	146	15	64	58	27
19nov10	32	57	38054	44	37	39	33	<i>54</i>	43	79	36	69	15	58	58	31
19nov11	16	30	38054	55	20	44	18	22	43	53	22	43	11	38	39	39
19nov14	24	74	38054	57	27	30	36	35	58	48	17	63	11	55	60	47
19nov15	33	56	38054	38	46	45	38	27	33	71	33	70	12	41	46	51
19nov16	16	45	38054	47	16	32	18	27	34	35	25	28	7	45	44	39
19nov17	23	59	38054	58	15	44	31	31	38	58	14	45	12	47	48	27
19nov19	15	53	38054	44	7	50	37	20	48	54	6	48	14	49	53	28
19nov20	7	61	38054	51	7	21	24	15	49	44	8	23	7	44	36	52
19nov21	12	48	38054	13	7	40	19	18	36	44	8	27	8	45	52	50
19nov22	35	57	38054	76	40	44	35	42	47	76	45	62	12	49	65	39
19nov24	11	58	38054	44	39	29	20	40	43	30	50	499	11	53	50	44
19nov25	22	53	38054	25	44	<i>< 11.8</i>	27	35	45	59	44	222	7	45	46	45
19nov26	40	55	38054	48	47	35	41	46	41	49	62	271	11	44	57	51
19nov27	28	63	38054	36	46	47	52	43	56	75	49	205	12	48	65	52
19nov29	12	52	38054	22	20	41	20	25	59	56	23	100	13	52	53	43
19nov30	9	64	38054	20	23	26	18	23	54	77	20	191	11	49	54	43
19nov31	15	55	38054	38	21	25	37	27	28	<i>< 14.1</i>	36	370	8	34	25	36
19nov32	36	55	38054	47	15	33	45	24	44	54	18	62	11	41	43	44
19nov34	29	16	38054	49	35	32	30	33	41	26	30	136	9	39	40	39
19nov35	19	29	38054	26	44	46	28	39	48	26	38	227	8	37	37	48
19nov37	<i>< 4.1</i>	57	38054	35	19	47	8	28	49	46	12	253	10	54	53	47
Mean	22	54	-	42	27	37	29	29	45	57	27	124	11	48	48	42
SD	10	13	-	15	14	9	11	9	8	19	14	93	3	9	10	8
RSD	45%	24%	-	37%	53%	25%	35%	30%	17%	34%	50%	73%	26%	18%	21%	19%
Accuracy*	41%	103%	-	79%	51%	70%	52%	55%	85%	105%	51%	-	-	90%	92%	79%
n	24	25	27	24	26	24	26	26	26	24	26	26	27	27	26	27

Appendix II

Supplements to Chapter 4 - Setup 2: Role of the intermediate quench

Suppl. Tab. 3: Homogenization temperatures from pre-cracked and etched quartz cylinders from setup 2. Experiments were run as described in the text at 200 MPa with three different salinities at 600 °C prior and 400 °C after the intermediate quench. Calculated temperatures were obtained from the SoWat model of Driesner and Heinrich (2007) and Driesner (2007).

Sample	#	Salinity [wt% NaCl]	T _{hom} [°C]	Sample	#	Salinity [wt% NaCl]	T _{hom} [°C]	Sample	#	Salinity [wt% NaCl]	T _{hom} [°C]
ID 145	1	2.5	266	ID 146	1	5	273	ID 147	1	10	281
	2	2.5	351		2	5	360		2	10	385
	3	2.5	351		3	5	359		3	10	382
	4	2.5	352		4	5	359		4	10	382
	5	2.5	354		5	5	360		5	10	275
	6	2.5	269		6	5	361		6	10	276
	7	2.5	352		7	5	360		7	10	382
	8	2.5	351		8	5	270		8	10	382
	9	2.5	352		9	5	276		9	10	282
	10	2.5	352		10	5	359		10	10	284
	11	2.5	352		11	5	268		11	10	n.d.
	12	2.5	351		12	5	359		12	10	n.d.
	13	2.5	351		13	5	269		13	10	283
	14	2.5	351		14	5	359		14	10	283
	15	2.5	354		15	5	359		15	10	284
	16	2.5	353		16	5	360		16	10	282
	17	2.5	353		17	5	255		17	10	357
	18	2.5	353		18	5	269		18	10	358
	19	2.5	353		19	5	n.d.		19	10	281
	20	2.5	353		20	5	357		20	10	280
	21	2.5	260		21	5	362		21	10	281
	22	2.5	261		22	5	361		22	10	286
	23	2.5	355		23	5	359		23	10	287
	24	2.5	353		24	5	270		24	10	285
	25	2.5	n.d.		25	5	360		25	10	284
	26	2.5	295		26	5	360		26	10	368
	27	2.5	353		27	5	360		27	10	380
	28	2.5	292		28	5	266		28	10	380
	29	2.5	n.d.		29	5	265		29	10	383
	30	2.5	353		30	5	264		30	10	381
calculated (400 °C, 200 MPa)		2.5	256	calculated (400 °C, 200 MPa)		5	258	calculated (400 °C, 200 MPa)		10	261
calculated (600 °C, 200 MPa)		2.5	356	Calculated (600 °C, 200 MPa)		5	364	Calculated (600 °C, 200 MPa)		10	378

Supplements to Chapter 4 - Setup 3: Time-dependent experiments

Suppl. Tab. 4: Results from the time dependent series from setup 3. All experiments were run at 800 °C, 200 MPa with an 8 wt% NaCl fluid and buffered with the PPM buffer. The sources for the metals were native gold of the capsule material and molybdenite or scheelite, respectively.

Duration [h]	Molybdenite Series			Scheelite Series		
	Sample	Mo [ppm]	Au [ppm]	Sample	W [ppm]	Au [ppm]
100	ID 191	1370	272	ID 192	5610	229
		1686	365		6175	220
		1419	347		5723	234
		1355	254		6377	221
		1317	262		6905	289
		754	6		7468	290
		1158	294		6620	300
		1652	377		10792	117
		1582	437		5758	176
		1231	193		8097	218
		1406	461		6061	229
		1157	223		6793	265
		1408	293		6382	136
		760	215			
		945	315			
31.6	ID 194	1527	464	ID 193	6282	63
		1749	340		3007	280
		1515	300		8687	105
		1612	365		6968	333
		575	174		7374	bdl
		816	161		8710	146
		1288	221		5920	257
		562	182		11239	206
		1773	374		5847	153
		1805	408		6849	265
		101	bdl		6961	300
		424	31		6039	34
		1516	250		10707	229
					7492	380
10	ID 195	1660	240	ID 197	6537	270
		939	144		14755	90
		1336	290		8311	373
		bdl	bdl		5764	201
		1350	144		5726	162
		1049	168		6918	139
		853	250		5935	214
		958	201		6647	242

		1160	193		6587	251
		1166	243		6810	242
		1277	213		11308	141
		1468	233		9661	303
3.17	ID 196	1285	240	ID 198	6335	212
		1238	288		247	22
		931	239		5672	bdl
		1267	260		6135	293
		1506	395		6655	258
		930	226		7105	248
1.78	ID 200	4340	302	ID 199	2221	323
		2567	528		130	53
		3067	332		2512	438
		2840	188		90	113
		481	89		72	bdl

*bdl: below detection limit

Appendix III

Supplements to Chapter 4 and 5 – LA-ICP-MS data of synthetic fluid inclusions

Suppl. Tab. 5: Normalized LA-ICP-MS data in ppm from individual, synthetic fluid inclusion. Values below the detection limit are marked with “< DL”. In the first column subsequent to the sample name, information is given on the experimental setup in the following order: ore mineral(s) in the capsule (Mol = molybdenite, Sch = scheelite, Pow = powellite, Fer = ferberite); experimental design as described in Chapter 4; salinity; used mineral buffer (PPM = pyrite : pyrrhotite : magnetite; FMQ = fayalite : magnetite : quartz; NNO = nickel : nickel oxide); experimental temperature; experimental pressure and used sample gas during LA-ICP-MS. Based on consistency of the internal standards (namely Na, Cs and Rb) as well as visual inspection of the signal and ablation site, each analysis was rated for its quality (- = poor, o = mediocre, + = good, ++ = very good).

Sample and exp. setup	Analysis	Quality	Na23	Rb85	Mo95	Mo97	Cs133	W182	Au197
ID 176 Mol + Sch, Chip 1 only, 8 wt% NaCl, PPM, 600 °C, 200 MPa, He + H	01apr08	++	32198	398	35	32	398	622	49
	01apr10	++	32663	398	9	10	406	368	14
	01apr11	++	33890	398	21	22	418	545	35
	01apr12	++	31674	398	20	18	400	526	33
	01apr13	+	37661	398	18	17	397	512	31
	01apr16	++	33249	398	59	29	374	819	28
	01apr19	+	26971	398	31	26	441	677	52
	02apr03	o	32028	398	< DL	< DL	296	9	< DL
	02apr04	o	30879	398	< DL	< DL	304	4	2
	02apr05	++	33525	398	< DL	< DL	419	< DL	4
	02apr06	-	218870	398	565	763	301	3561	785
	02apr08	++	34186	398	17	18	434	589	18
	02apr09	++	30541	398	20	15	407	556	39
	02apr10	++	33645	398	25	23	422	396	36
	02apr11	+	35586	398	< DL	< DL	413	258	< DL
	02apr14	o	31770	398	44	57	448	2741	66
	02apr15	+	29422	398	12	13	450	670	51
	02apr16	o	38791	398	29	31	402	808	41
	02apr17	+	35143	398	14	13	464	551	26
	02apr19	-	18348	398	4	< DL	479	368	5
02apr20	++	32171	398	20	20	437	556	36	
02apr21	+	29806	398	12	15	464	518	8	
02apr22	+	34924	398	24	21	413	777	32	
02apr24	++	28926	398	11	< DL	422	367	28	
02apr25	+	37111	398	13	13	406	332	31	
02apr26	o	38962	398	17	16	422	543	35	
02apr27	o	40515	398	21	18	435	482	27	
02apr28	+	32637	398	7	10	457	846	13	
ID 177 Mol + Sch, Chip 1 only, 8 wt% NaCl, PPM, 700 °C, 200 MPa, He + H	02aprB03	-	35041	398	642	675	851	5805	329
	02aprB04	-	39994	398	43	41	95	488	44
	02aprB05	++	32077	398	133	128	405	841	110
	02aprB06	o	37466	398	61	62	349	437	115
	02aprB08	+	35318	398	166	180	411	1531	66
	02aprB09	++	32485	398	264	261	434	3211	111
	02aprB10	+	33082	398	270	269	456	3189	129
	02aprB11	o	41784	398	296	282	404	2283	129
	02aprB13	++	32323	398	273	301	430	3084	126
	02aprB14	++	31958	398	273	260	410	3101	124
	02aprB15	+	37005	398	316	342	430	3343	173
	02aprB16	++	30464	398	267	264	439	1850	135
	02aprB18	o	39560	398	189	224	343	3225	85
	02aprB19	++	32949	398	245	236	418	2633	86
02aprB20	-	31992	398	403	396	579	4676	213	
02aprB21	++	29922	398	245	208	411	2653	102	

Sample and exp. setup	Analysis	Quality	Na23	Rb85	Mo95	Mo97	Cs133	W182	Au197
	02aprB23	+	30319	398	324	328	463	3918	259
	02aprB25	++	28514	398	220	233	416	2160	91
	02aprB26	++	31214	398	247	265	378	2541	107
	02aprB27	-	44979	398	146	135	241	1909	63
ID 178 Qtz, Chip 1 only, 20 wt% NaCl, PPM, 800 °C, 200 MPa, He + H	ID178_003	o	76565	398	25	29	502	11	71
	ID178_004	+	106985	398	61	51	362	15	257
	ID178_005	o	59318	398	53	54	368	13	264
	ID178_006	++	76152	398	40	45	408	13	297
	ID178_008	o	97773	398	86	91	393	16	441
	ID178_010	+	80444	398	70	61	330	13	182
	ID178_011	+	77561	398	62	56	455	13	136
	ID178_014	++	75979	398	50	53	393	14	384
	ID178_015	+	81020	398	45	47	349	11	84
	ID178_016	+	65348	398	66	58	378	12	339
	ID178_018	++	75366	398	58	60	429	13	339
	ID178_019	++	83946	398	19	19	398	10	103
	ID178_020	-	34535	398	4	5	375	4	2
ID178_021	+	92167	398	73	95	406	18	156	
ID178_022	+	98049	398	73	87	398	22	157	
ID 179 Qtz, Chip 1 only, 1 wt% NaCl, PPM, 800 °C, 200 MPa, He + H	ID179_03	+	4005	398	68	89	354	1	56
	ID179_04	o	5225	398	79	109	394	3	157
	ID179_05	+	4514	398	59	40	352	1	57
	ID179_06	+	4470	398	74	58	397	3	109
	ID179_08	+	4993	398	78	71	365	3	93
	ID179_09	o	5262	398	41	49	424	6	64
	ID179_10	+	4434	398	74	84	336	3	83
	ID179_11	+	4332	398	73	88	348	5	107
	ID179_13	-	6116	398	79	65	344	2	82
	ID179_14	+	4773	398	71	65	439	< DL	73
	ID179_15	-	6195	398	60	62	388	1	73
	ID179_16	o	5247	398	149	156	370	3	190
	ID179_18	+	4781	398	90	86	363	< DL	119
	ID179_19	o	2545	398	50	77	361	7	65
ID179_20	+	4692	398	66	66	390	< DL	83	
ID179_21	o	5107	398	85	77	350	3	82	
ID 180 Mol + Sch, HF only, 8 wt% NaCl, PPM, 800 °C, 200 MPa, He	20nov04	+	20680	398	1717	1724	433	7860	484
	20nov05	o	30078	398	87	92	190	255	4
	20nov07	++	33655	398	1188	1082	411	6776	315
	20nov09	++	32246	398	1248	1207	416	6584	306
	20nov10	+	34535	398	1095	1099	471	8763	183
	20nov11	-	44467	398	861	884	162	4434	288
	20nov12	+	29959	398	222	3324	337	4855	174
	20nov14	+	40891	398	2032	2006	361	11487	408
	20nov15	++	29530	398	1055	1048	408	5412	226
	20nov16	o	27682	398	1347	1287	481	6761	360
	20nov17	o	30878	398	1511	1552	546	7341	342
	20nov19	+	25774	398	1600	1553	398	7243	441
	20nov20	+	29673	398	1286	1286	449	6469	305
	20nov21	+	41961	398	1299	1197	411	5570	312
	20nov22	+	31871	398	1410	1262	475	6235	298
	20nov25	-	34389	398	873	963	1334	9850	208
	20nov26	+	30453	398	1446	1481	472	8106	378
	20nov27	++	28820	398	1284	1310	426	5953	350
	20nov29	+	35482	398	1517	1463	469	10240	297
20nov30	+	31610	398	1417	1202	454	6135	269	
20nov31	+	32051	398	710	715	464	6177	45	
20nov32	o	31732	398	1336	1436	523	7108	437	

Sample and exp. setup	Analysis	Quality	Na23	Rb85	Mo95	Mo97	Cs133	W182	Au197
ID 181 Pow HF only 8 wt% NaCl, PPM, 800 °C, 200 MPa, He	15jan03	++	38555	398	1656	1621	396	1002	260
	15jan04	o	36047	398	1081	1056	435	847	119
	15jan06	++	30742	398	1505	2600	431	955	275
	15jan09	++	31657	398	1588	1632	361	766	371
	15jan10	-	35440	398	1084	1132	481	1172	23
	15jan11	++	33188	398	1751	1751	434	996	253
	15jan12	++	33824	398	1624	1612	440	1003	269
	15jan14	++	33057	398	903	812	381	770	135
	15jan15	-	24529	398	2869	1937	471	1226	403
	15jan16	o	25841	398	243	233	386	667	73
	15jan17	o	27717	398	1998	2044	441	1181	320
	15jan19	o	28502	398	2040	1871	447	1156	343
	15jan20	++	31043	398	1495	1637	436	1102	235
	15jan21	++	29698	398	1580	1609	414	958	242
	15jan22	++	33224	398	1696	1639	427	929	245
	15jan24	-	31536	398	2025	2203	513	1228	317
	15jan25	++	29936	398	383	398	429	862	69
	15jan26	-	46774	398	2207	2043	430	976	331
	15jan27	++	32261	398	1359	1307	405	736	183
	15jan28	o	36184	398	1294	1361	455	1062	282
	16jan03	o	28129	398	2271	2233	445	1122	356
	16jan04	++	30159	398	1745	1739	387	940	190
	16jan05	-	31302	398	2072	2110	501	1297	427
	16jan06	++	30775	398	1776	2029	434	1152	294
	16jan08	-	24810	398	1059	1208	400	847	167
	16jan09	++	31392	398	1565	1617	409	880	188
16jan10	o	34977	398	1763	1837	461	1042	299	
16jan11	o	29865	398	528	652	449	1048	68	
ID 182_1 Mol + Sch, Chip 1, 8 wt% NaCl, PPM, 800 °C, 200 MPa, He	20novB03	+	27613	398	1301	809	463	4121	241
	20novB04	+	28364	398	572	550	447	2760	162
	20novB05	++	31306	398	1264	1232	401	5919	211
	20novB06	++	28104	398	1262	1170	416	6094	180
	20novB08	+	28128	398	1497	1488	473	7627	357
	20novB09	+	25323	398	1040	1094	409	7557	150
	20novB10	+	29833	398	1182	1070	449	3996	219
	20novB11	++	28754	398	1089	1268	410	4360	217
	20novB13	++	28372	398	1314	1289	418	5443	334
	20novB14	-	32858	398	1048	947	202	2978	321
	20novB15	+	31139	398	1176	1187	453	6794	394
	20novB16	-	26379	398	1259	1260	555	6544	313
	20novB21	+	34044	398	1218	1254	464	6805	338
	20novB22	o	32757	398	1265	1286	528	6417	268
	20novB23	-	52536	398	1759	1748	568	8216	382
	20novB24	o	26914	398	1388	1420	491	7120	372
	20novB27	o	29464	398	1691	2258	515	6428	351
	20novB28	o	33584	398	675	552	267	4591	71
20novB31	++	33774	398	226	219	381	4945	< DL	
20novB32	-	64203	398	1139	1114	279	16369	10	
20novB33	+	34776	398	1227	1260	466	6831	337	
20novB34	++	33217	398	1531	1523	401	5276	391	
ID 182_2 Mol + Sch, Chip 2, 8 wt% NaCl, PPM, 800 °C, 200 MPa,	21nov04	o	23624	398	1298	1299	343	6574	346
	21nov05	-	33958	398	1787	1874	571	8612	462
	21nov06	+	37835	398	1325	1291	399	6410	302
	21nov07	o	30819	398	920	2970	481	7143	162
	21nov10	++	30052	398	1556	1603	385	5860	344
	21nov11	++	34130	398	1161	1197	393	5958	340
	21nov12	-	29451	398	784	384	577	6225	49

Sample and exp. setup	Analysis	Quality	Na23	Rb85	Mo95	Mo97	Cs133	W182	Au197
He	21nov14	o	20177	398	1491	1549	440	7108	420
	21nov15	-	21258	398	2073	2034	749	9352	697
	21nov16	++	34494	398	1336	1446	432	6772	386
	21nov17	+	35082	398	1832	1845	415	6194	383
	21nov19	-	43204	398	830	868	158	4574	327
	21nov20	+	32613	398	1214	1184	454	5976	248
	21nov21	+	35130	398	1158	1129	381	5383	228
	21nov22	+	35193	398	905	876	368	6584	376
	21nov24	o	31767	398	1865	1672	486	7034	430
	21nov25	-	43935	398	< DL	< DL	128	4796	< DL
	21nov26	++	32679	398	904	780	381	5677	407
	21nov27	-	36604	398	2190	2203	725	8101	493
	21nov29	+	32370	398	460	639	448	6325	93
21nov30	-	39822	398	463	440	251	5849	76	
21nov31	+	36459	398	1387	1398	401	5386	318	
ID 183_1 Pow, Chip 1, 8 wt% NaCl, PPM, 800 °C, 200 MPa, He	27nov03	++	29659	398	1959	1848	427	626	430
	27nov04	++	28401	398	2219	2132	422	759	391
	27nov05	o	30108	398	3298	3165	493	1794	885
	27nov06	+	29914	398	1879	1962	460	1144	441
	27nov08	o	32992	398	433	380	300	425	58
	27nov09	+	30949	398	1021	1110	457	1439	246
	27nov10	++	29553	398	1532	1503	399	1019	239
	27nov11	+	32915	398	1595	1612	461	1369	409
	27nov13	-	22510	398	3475	3367	530	1040	873
	27nov14	+	35326	398	1843	1663	437	1183	254
	27nov15	+	36371	398	1535	1524	410	1087	251
	27nov16	+	34922	398	2005	1988	428	1293	339
	27nov18	+	33450	398	1034	986	460	1153	133
	27nov19	o	35660	398	1465	1452	502	1251	259
	27nov20	-	27735	398	3134	3440	614	2197	640
	27nov21	++	33779	398	1604	1628	392	1131	269
	27nov23	++	33111	398	1751	1799	434	1082	224
27nov24	-	44596	398	1079	1123	274	2016	65	
27nov25	+	49727	398	1882	1875	429	850	196	
27nov26	+	47281	398	1692	1656	374	622	241	
ID 183_2 Pow, Chip 2, 8 wt% NaCl, PPM, 800 °C, 200 MPa, He	27novB03	o	27615	398	2594	3067	509	1804	647
	27novB04	+	35369	398	1771	1798	444	1200	372
	27novB05	++	34632	398	1450	1527	413	1021	230
	27novB06	++	35387	398	1569	1501	406	1133	230
	27novB08	++	28667	398	2031	1920	425	1234	345
	27novB10	o	44138	398	1570	1450	455	1153	202
	27novB11	++	32258	398	1600	1555	430	1196	381
	27novB13	+	24345	398	< DL	< DL	426	776	< DL
	27novB14	++	35466	398	1878	2169	427	1234	156
	27novB16	-	31118	398	6645	5970	664	3204	845
	27novB18	o	29914	398	172	218	517	1168	< DL
	27novB19	+	37781	398	< DL	< DL	437	377	< DL
	27novB20	++	32531	398	398	463	363	732	< DL
	27novB24	++	35212	398	1701	1795	430	1263	309
	27novB25	++	30098	398	1533	1615	431	1023	247
	27novB26	+	28625	398	2036	2101	447	1298	510
	27novB28	++	32309	398	1378	1415	378	1017	218
27novB29	++	34239	398	1572	1451	429	1048	254	
27novB30	+	37814	398	976	1039	397	1021	71	
27novB31	++	32445	398	2103	2035	417	1189	307	
ID 184 Mol + Sch,	28nov03	o	48888	398	1181	1262	402	14875	77
	28nov06	-	30499	398	1590	1430	587	5260	447

Sample and exp. setup	Analysis	Quality	Na23	Rb85	Mo95	Mo97	Cs133	W182	Au197
P cycling, 8 wt% NaCl, PPM, 800 °C, 200 MPa, He	28nov08	+	35826	398	1602	1153	459	4700	279
	28nov09	-	19020	398	1521	1619	637	5791	432
	28nov10	o	38827	398	1141	1144	443	3570	225
	28nov11	+	34511	398	532	536	329	4462	66
	28nov14	-	23965	398	1554	1667	528	9166	281
	28nov15	+	37678	398	1362	1310	364	4556	462
	28nov16	+	35511	398	1325	1400	345	3898	502
	28nov18	+	32228	398	1473	1427	454	2040	466
	28nov19	++	35442	398	1124	1189	439	4590	355
	28nov20	+	37608	398	1262	1296	447	5039	272
	28nov21	++	29054	398	1354	1406	398	6409	304
	28nov23	o	46871	398	1238	1289	325	12409	38
	28nov24	-	15858	398	442	596	134	3650	101
	28nov25	o	70078	398	1328	1310	334	13444	95
	28nov26	o	41114	398	1284	1252	340	11440	122
	28nov28	+	38332	398	1453	1562	351	17561	49
28nov29	o	42282	398	1445	1440	450	14060	84	
28nov30	++	33395	398	1378	1368	391	9632	117	
28nov31	++	30820	398	1196	1217	370	7417	114	
28nov32	++	32338	398	963	927	367	6122	45	
ID 185 Pow, P cycling, 8 wt% NaCl, PPM, 800 °C, 200 MPa, He	28nov03	+	39335	398	2393	2413	425	380	302
	28nov04	-	18370	398	9006	8268	537	881	1010
	28nov06	o	44517	398	2288	2822	431	395	388
	28nov08	+	37626	398	1023	1019	401	303	63
	28nov09	-	49828	398	1840	1775	534	461	196
	28nov10	+	38129	398	882	954	364	488	36
	28nov13	o	51478	398	2677	2503	332	969	67
	28nov14	o	41177	398	2161	2174	358	927	48
	28nov15	o	47292	398	2234	2406	389	1131	117
	28nov16	o	40452	398	2005	1969	477	609	260
	28nov18	o	43626	398	544	520	327	403	54
	28nov19	-	84456	398	4390	4423	402	1715	528
	28nov20	o	42629	398	2712	2682	372	622	310
	28nov21	+	39028	398	2793	2702	472	771	263
	28nov23	++	35649	398	2327	2254	368	243	243
	28nov24	-	57311	398	2447	2638	524	398	478
28nov25	+	30929	398	2649	2575	464	375	451	
28nov26	o	63615	398	1970	1892	388	381	468	
28nov27	o	42378	398	1068	1018	398	339	19	
ID 191 Mol, Runtime 100 h, 8 wt% NaCl, PPM, 800 °C, 200 MPa, He	12dez03	+	36620	398	1370	1312	387	16	272
	12dez04	+	31260	398	1686	1653	449	10	365
	12dez05	++	31417	398	1419	1395	437	9	347
	12dez06	++	30659	398	1355	1361	375	6	254
	12dez08	o	24499	398	1668	1696	455	9	341
	12dez09	-	72345	398	1666	1707	355	11	254
	12dez10	o	23884	398	4607	1625	458	7	933
	12dez11	++	31243	398	1317	1427	417	6	262
	12dez14	-	62902	398	674	2282	385	13	98
	12dez16	o	30273	398	1856	1883	507	9	437
	12dez17	++	30635	398	1652	1629	397	7	377
	12dez19	+	25409	398	1582	1615	449	9	437
	12dez20	++	33931	398	1231	1295	431	10	193
	12dez21	++	33371	398	1406	1455	440	7	461
	12dez22	-	70296	398	1216	861	275	10	29
	12dez24	++	28402	398	1157	1195	380	6	223
12dez25	+	35338	398	1408	1387	411	7	293	
12dez26	+	30144	398	760	640	447	5	215	

Sample and exp. setup	Analysis	Quality	Na23	Rb85	Mo95	Mo97	Cs133	W182	Au197
	12dez27	o	25092	398	1210	1115	313	9	273
	12dez28	++	31502	398	945	1000	396	6	315
ID 192 Sch, Runtime 100 h, 8 wt% NaCl, PPM, 800 °C, 200 MPa, He	12dezB03	+	27118	398	12	< DL	420	5610	229
	12dezB04	o	46023	398	< DL	< DL	334	9719	293
	12dezB05	++	30740	398	6	7	408	6175	220
	12dezB06	++	34638	398	< DL	< DL	400	5723	234
	12dezB08	++	28688	398	< DL	< DL	429	6377	221
	12dezB09	+	33846	398	< DL	< DL	492	6905	289
	12dezB10	++	29823	398	8	< DL	393	7468	290
	12dezB11	+	35905	398	6	< DL	349	6620	300
	12dezB13	+	32204	398	4	7	481	10792	117
	12dezB14	++	32917	398	< DL	10	415	5758	176
	12dezB15	+	30603	398	< DL	8	447	8097	218
	12dezB16	++	33104	398	< DL	< DL	416	6061	229
	12dezB18	-	24301	398	< DL	< DL	551	8206	486
	12dezB19	o	31506	398	< DL	< DL	251	7012	239
	12dezB20	-	64754	398	6	7	278	22757	5
	12dezB21	o	44640	398	6	7	349	17760	32
	12dezB23	+	33722	398	16	22	465	6793	265
12dezB24	-	24306	398	< DL	< DL	566	8141	469	
12dezB25	+	35684	398	6	7	436	6382	136	
12dezB26	o	34716	398	< DL	< DL	120	6099	154	
ID 193 Sch, Runtime 31.6 h, 8 wt% NaCl, PPM, 800 °C, 200 MPa, He	13dez04	+	34777	398	6	< DL	472	6282	63
	13dez05	++	30819	398	< DL	< DL	387	3007	280
	13dez06	++	34048	398	< DL	< DL	421	8687	105
	13dez08	+	26551	398	< DL	< DL	384	6968	333
	13dez09	o	47805	398	< DL	< DL	359	1545	193
	13dez10	+	26927	398	< DL	< DL	440	7374	< DL
	13dez11	++	33598	398	< DL	< DL	361	8710	146
	13dez13	o	26260	398	< DL	< DL	526	6838	313
	13dez14	o	36341	398	< DL	< DL	295	8974	104
	13dez15	++	29089	398	< DL	< DL	418	5920	257
	13dez16	+	37703	398	< DL	< DL	430	11239	206
	13dez18	++	30855	398	5	6	375	5847	153
	13dez19	+	32932	398	10	10	477	6849	265
	13dez20	+	36882	398	8	5	434	6961	300
	13dez21	++	33955	398	< DL	10	402	6039	34
	13dez23	-	< DL	398	< DL	< DL	629	12929	839
	13dez24	+	27325	398	< DL	< DL	411	10707	229
13dez25	o	26447	398	< DL	25	502	8776	329	
13dez26	+	28303	398	< DL	< DL	348	7492	380	
13dez27	o	32672	398	< DL	10	285	6964	350	
ID 194 Mol, Runtime 31.6 h, 8 wt% NaCl, PPM, 800 °C, 200 MPa, He	13dezB03	o	44744	398	1907	925	392	23	76
	13dezB05	+	36076	398	1527	1564	424	10	464
	13dezB06	o	43529	398	1310	1302	410	11	190
	13dezB08	++	30675	398	1749	1808	433	12	340
	13dezB09	++	29669	398	1515	1450	394	12	300
	13dezB10	+	29721	398	1612	1749	444	17	365
	13dezB11	o	23422	398	1246	1179	322	9	242
	13dezB13	+	35828	398	575	510	439	10	174
	13dezB14	++	30887	398	816	929	375	11	161
	13dezB16	o	24203	398	66	65	295	8	4
	13dezB18	+	36692	398	1288	1713	395	10	221
	13dezB19	+	29277	398	562	525	481	12	182
	13dezB20	+	29359	398	1773	1708	446	14	374
	13dezB21	+	25295	398	16281	16198	475	43	4597
13dezB23	o	46711	398	1343	1450	400	17	140	

Sample and exp. setup	Analysis	Quality	Na23	Rb85	Mo95	Mo97	Cs133	W182	Au197
	13dezB24	+	27591	398	1805	1731	421	14	408
	13dezB25	++	31019	398	101	122	396	14	< DL
	13dezB26	++	34396	398	424	391	427	13	31
	13dezB28	-	122711	398	< DL	< DL	1175	782	21497
	13dezB29	+	35486	398	1516	1529	426	10	250
	13dezB30	o	44591	398	1631	1651	472	9	447
ID 195 Mol, Runtime 10 h, 8 wt% NaCl, PPM, 800 °C, 200 MPa, He	16jan14	+	35487	398	1660	1486	427	10	240
	16jan15	+	35642	398	939	1226	387	10	144
	16jan16	-	80997	398	141	121	358	14	< DL
	16jan17	+	36321	398	1336	1347	436	8	290
	16jan19	+	35712	398	< DL	< DL	459	11	< DL
	16jan20	+	37549	398	1350	1145	435	13	144
	16jan21	+	37489	398	1049	1213	372	10	168
	16jan22	++	34545	398	853	792	428	10	250
	16jan24	o	24720	398	1532	1543	404	10	421
	16jan25	+	36077	398	958	990	413	11	201
	16jan26	o	32044	398	639	577	514	15	273
	16jan27	+	37051	398	1160	1183	409	8	193
	16jan29	o	38208	398	1332	1289	427	10	297
	16jan30	o	25879	398	2272	2398	486	< DL	590
	16jan31	++	34440	398	1166	1115	423	9	243
16jan32	o	33489	398	1630	1719	540	7	238	
16jan33	++	31999	398	1277	1366	430	10	213	
16jan33b	++	30475	398	1468	1425	414	10	233	
ID 196 Mol, Runtime 3.17 h, 8 wt% NaCl, PPM, 800 °C, 200 MPa, He	16janB03	-	12836	398	3136	3520	524	< DL	547
	16janB04	+	36679	398	1285	1208	402	5	240
	16janB05	+	43099	398	1238	1189	428	< DL	288
	16janB06	-	56527	398	1890	1816	457	8	431
	16janB08	o	39087	398	1340	1353	466	9	281
	16janB09	+	44843	398	931	918	434	5	239
	16janB10	++	35128	398	1267	1307	412	9	260
	16janB11	o	44864	398	1315	1405	330	17	103
	16janB13	+	31957	398	1506	1482	478	10	395
	16janB14	+	27564	398	930	937	387	12	226
	16janB15	-	79471	398	1360	1764	376	11	176
	16janB16	o	31988	398	1704	1797	507	< DL	438
	16janB18	o	44757	398	731	769	462	8	136
	16janB19	o	39681	398	763	702	472	< DL	245
	16janB20	o	94459	398	648	604	335	7	66
16janB21	-	78323	398	1627	1979	446	< DL	1225	
16janB22	-	105217	398	2716	2967	424	< DL	1104	
ID 197 Sch, Runtime 10 h, 8 wt% NaCl, PPM, 800 °C, 200 MPa, He	23janB03	o	57637	398	< DL	< DL	365	181	< DL
	23janB04	+	27622	398	118	130	456	6537	270
	23janB05	o	48936	398	115	92	434	13989	190
	23janB06	+	36390	398	93	97	371	14755	90
	23janB08	o	20365	398	157	< DL	460	2550	270
	23janB09	-	13970	398	101	99	492	7413	284
	23janB10	o	57039	398	93	87	456	1639	177
	23janB11	+	33346	398	121	120	458	8311	373
	23janB13	++	29614	398	93	101	396	5764	201
	23janB14	+	27347	398	109	88	404	5726	162
	23janB15	o	28072	398	119	108	585	7937	364
	23janB16	++	30725	398	82	68	380	6918	139
	23janB18	-	31911	398	118	99	580	7866	345
	23janB19	++	30156	398	90	105	411	5935	214
	23janB20	o	38869	398	66	75	335	9061	106
23janB21	-	148517	398	< DL	< DL	512	73	< DL	

Sample and exp. setup	Analysis	Quality	Na23	Rb85	Mo95	Mo97	Cs133	W182	Au197
	23janB23	o	40823	398	100	111	378	10656	308
	23janB24	+	26015	398	97	109	460	6647	242
	23janB25	-	29099	398	4	< DL	654	2391	< DL
	23janB26	-	52059	398	153	176	603	15597	243
	23janB28	+	30347	398	97	90	455	6587	251
	23janB29	++	34320	398	95	91	428	6810	242
	23janB30	+	37554	398	76	69	502	11308	141
	23janB31	++	35120	398	105	111	441	9661	303
23janB32	o	24739	398	164	243	469	9759	1169	
ID 198 Sch, Runtime 3.17 h, 8 wt% NaCl, PPM, 800 °C, 200 MPa, He	22janB05	o	21934	398	< DL	< DL	480	6691	296
	22janB06	o	23400	398	< DL	< DL	449	788	< DL
	22janB08	+	25838	398	< DL	< DL	453	6335	212
	22janB09	++	36363	398	< DL	< DL	434	247	22
	22janB10	o	33544	398	< DL	< DL	514	7505	238
	22janB11	++	30213	398	< DL	< DL	412	5672	< DL
	22janB13	-	49280	398	< DL	< DL	22	7820	53
	22janB14	-	62696	398	< DL	< DL	544	15803	252
	22janB15	o	31252	398	< DL	< DL	495	7281	322
	22janB16	o	35033	398	< DL	< DL	488	7086	372
	22janB18	-	66559	398	< DL	< DL	501	13987	154
	22janB19	+	31386	398	28	< DL	536	6135	293
	22janB20	-	13192	398	< DL	< DL	342	4310	< DL
	22janB21	o	34182	398	< DL	< DL	519	7376	223
	22janB23	-	40046	398	< DL	< DL	270	3885	216
	22janB24	+	31611	398	17	< DL	487	6655	258
22janB25	o	63561	398	< DL	< DL	403	12627	148	
22janB26	+	35603	398	< DL	< DL	417	7105	248	
22janB27	o	35858	398	< DL	< DL	316	5687	236	
ID 199 Sch, Runtime 1.78 h, 8 wt% NaCl, PPM, 800 °C, 200 MPa, He	23jan03	o	< DL	398	< DL	< DL	475	48	< DL
	23jan04	+	25507	398	< DL	< DL	472	2221	323
	23jan05	+	26374	398	< DL	< DL	448	130	53
	23jan06	-	< DL	398	< DL	< DL	806	6642	937
	23jan08	o	26306	398	< DL	< DL	497	2672	746
	23jan09	-	< DL	398	< DL	< DL	631	2363	938
	23jan10	-	30732	398	< DL	< DL	565	3377	796
	23jan13	-	< DL	398	< DL	< DL	496	2897	157
	23jan14	++	28965	398	< DL	< DL	415	2512	438
	23jan15	+	26275	398	< DL	< DL	396	90	113
	23jan16	-	3641	398	< DL	< DL	471	68	< DL
23jan17	-	8272	398	< DL	< DL	439	49	< DL	
23jan18	++	33213	398	< DL	< DL	445	72	< DL	
ID 200 Mol, Runtime 1.78 h, 8 wt% NaCl, PPM, 800 °C, 200 MPa, He	22jan03	-	< DL	398	4310	4089	720	< DL	906
	22jan04	o	20870	398	2239	1962	393	< DL	419
	22jan06	-	119491	398	1931	2321	276	< DL	265
	22jan08	-	174329	398	2555	2862	362	< DL	414
	22jan09	o	86884	398	1654	2143	369	37	151
	22jan10	o	54478	398	2453	2548	451	32	401
	22jan11	o	95333	398	2714	2950	361	18	166
	22jan13	+	40922	398	4340	4010	454	33	302
	22jan14	o	91051	398	2591	2640	400	< DL	174
	22jan15	++	29495	398	2567	2530	432	< DL	528
	22jan18	-	52419	398	1675	1502	290	24	40
	22jan19	+	39129	398	3067	3249	472	18	332
	22jan20	+	38437	398	2840	2524	448	12	188
22jan21	+	23758	398	481	554	431	13	89	
ID 201 Sch,	23apr03	++	30105	398	6	< DL	419	195	15
	23apr04	+	35498	398	4	2	424	536	41

Sample and exp. setup	Analysis	Quality	Na23	Rb85	Mo95	Mo97	Cs133	W182	Au197
Chip 1, 8 wt% NaCl, PPM, 600 °C, 200 MPa, He + H	23apr05	+	31805	398	4	< DL	454	762	26
	23apr06	+	34993	398	2	< DL	411	191	26
	23apr08	o	34351	398	6	12	495	689	43
	23apr11	o	31497	398	14	6	495	1127	56
	23apr12	+	31122	398	22	7	465	729	19
	23apr14	-	44782	398	13	8	480	157	39
	23apr15	++	32072	398	1	6	413	345	36
	23apr16	+	34027	398	< DL	< DL	462	706	31
	23apr17	++	31522	398	< DL	< DL	415	525	29
	23apr19	+	32169	398	11	5	447	809	31
	23apr20	+	32694	398	29	7	482	777	26
23apr21	+	36999	398	3	4	437	255	26	
ID 201 Sch, Chip 2, 8 wt% NaCl, PPM, 600 °C, 200 MPa, He + H	23apr25	o	31485	398	< DL	< DL	406	36	18
	23apr26	o	31292	398	< DL	3	405	42	10
	23apr27	-	23126	398	40	59	474	13	17
	23apr28	-	26614	398	2	< DL	449	3	26
	23apr30	o	28513	398	1	3	392	2	< DL
	23apr31	o	21144	398	< DL	69	367	2	14
	23apr32	o	24757	398	5	< DL	480	3	< DL
23apr33	o	27031	398	< DL	36	501	26	41	
ID 202 Fer, Chip 1, 8 wt% NaCl, PPM, 600 °C, 200 MPa, He + H	23aprB03	o	39273	398	24	< DL	398	883	49
	23aprB04	++	31841	398	3	2	400	479	25
	23aprB05	+	32450	398	< DL	< DL	443	530	1
	23aprB06	++	32334	398	< DL	7	411	367	33
	23aprB08	++	33192	398	4	5	404	501	33
	23aprB09	+	31217	398	4	12	470	9	1
	23aprB10	o	26904	398	6	< DL	494	84	52
	23aprB11	+	33123	398	< DL	4	455	674	50
	23aprB13	+	25893	398	< DL	< DL	426	888	47
	23aprB14	o	26045	398	5	5	523	711	49
	23aprB15	+	26356	398	7	2	424	473	29
	23aprB16	++	31047	398	2	5	406	467	21
	23aprB18	-	89735	398	< DL	< DL	495	25	< DL
	23aprB20	-	47268	398	8	< DL	420	988	67
	23aprB21	-	44813	398	< DL	26	482	375	66
23aprB27	+	34387	398	< DL	1	468	470	8	
23aprB28	++	30458	398	3	7	434	15	7	
23aprB29	+	30519	398	0	2	442	513	35	
ID 202 Fer, Chip 2, 8 wt% NaCl, PPM, 600 °C, 200 MPa, He + H	23aprB31	o	29600	398	< DL	38	522	313	25
	23aprB32	+	26451	398	< DL	< DL	385	250	25
	23aprB33	++	31994	398	< DL	< DL	371	388	25
	23aprB34	o	32245	398	29	< DL	510	533	8
ID 203 Sch, Chip 1, 8 wt% NaCl, FMQ, 600 °C, 200 MPa, He + H	22apr04	o	27796	398	372	394	485	122	30
	22apr06	+	25836	398	< DL	< DL	446	328	< DL
	22apr08	+	30136	398	< DL	1	444	253	< DL
	22apr09	++	31077	398	< DL	2	422	288	2
	22apr10	++	32206	398	< DL	< DL	389	283	< DL
	22apr11	+	35433	398	4	< DL	415	305	0
	22apr14	++	32171	398	1	< DL	414	251	0
	22apr15	++	31340	398	16	< DL	417	276	1
	22apr16	+	28071	398	< DL	< DL	444	58	< DL
	22apr18	-	10602	398	< DL	< DL	421	0	< DL
	22apr19	+	33504	398	< DL	1	447	264	0
22apr20	+	35568	398	0	1	427	254	0	

Sample and exp. setup	Analysis	Quality	Na23	Rb85	Mo95	Mo97	Cs133	W182	Au197
	22apr23	++	30757	398	1	4	402	267	1
	22apr24	+	35276	398	1	2	422	284	0
	22apr25	++	31840	398	2	2	415	247	0
	22apr26	+	34835	398	< DL	1	409	294	0
ID 203 Sch, Chip 2, 8 wt% NaCl, FMQ, 600 °C, 200 MPa, He + H	22apr28	+	33849	398	< DL	4	454	276	< DL
	22apr29	++	32997	398	< DL	< DL	418	277	< DL
	22apr30	o	24812	398	< DL	< DL	491	453	3
	22apr31	o	23408	398	< DL	60	415	214	< DL
	22apr32	++	30790	398	< DL	< DL	432	257	< DL
ID 204 Fer, Chip 1, 8 wt% NaCl, FMQ, 600 °C, 200 MPa, He + H	08mai03	+	27674	398	< DL	< DL	404	45	< DL
	08mai04	+	30453	398	2	< DL	445	799	0
	08mai05	o	37868	398	< DL	< DL	488	782	0
	08mai06	+	33710	398	< DL	1	470	440	0
	08mai08	+	32924	398	2	1	445	773	< DL
	08mai10	-	11724	398	122	138	350	267	7
	08mai11	-	11698	398	< DL	3	325	29	1
	08mai13	++	30355	398	0	0	362	756	0
	08mai14	+	34587	398	< DL	< DL	470	843	0
	08mai15	++	31218	398	< DL	< DL	387	732	< DL
	08mai16	++	31399	398	< DL	< DL	416	1021	< DL
	08mai18	++	28683	398	< DL	< DL	427	480	< DL
	08mai19	++	31713	398	< DL	< DL	401	815	0
08mai20	++	33426	398	< DL	< DL	392	631	0	
08mai21	+	38735	398	6	< DL	340	224	< DL	
ID 204 Fer, Chip 2, 8 wt% NaCl, FMQ, 600 °C, 200 MPa, He + H	08mai23	+	26849	398	< DL	7	436	682	< DL
	08mai24	+	31324	398	1	1	447	878	0
	08mai25	+	32674	398	1	< DL	359	699	< DL
	08mai29	o	39207	398	38	37	431	973	8
ID 205 Sch, Chip 1, 1 wt% NaCl, FMQ, 600 °C, 200 MPa, He + H	07mai03	+	3415	398	< DL	< DL	363	30	0
	07mai04	++	3664	398	5	< DL	383	48	2
	07mai05	o	2769	398	< DL	3	325	11	< DL
	07mai06	o	2604	398	< DL	< DL	336	5	< DL
	07mai08	+	4173	398	1	1	339	39	< DL
	07mai09	++	3680	398	< DL	< DL	363	34	0
	07mai10	o	3393	398	< DL	< DL	319	10	< DL
	07mai11	++	4001	398	< DL	< DL	370	36	< DL
	07mai13	++	3509	398	4	< DL	382	27	< DL
	07mai14	+	3735	398	< DL	< DL	353	30	< DL
	07mai16	++	3743	398	< DL	8	376	28	0
	07mai20	++	3870	398	< DL	1	365	37	< DL
	07mai21	++	3901	398	0	1	378	30	< DL
	07mai22	+	3311	398	< DL	< DL	349	34	0
07mai24	+	3842	398	< DL	< DL	327	14	1	
07mai25	+	3308	398	< DL	< DL	362	30	< DL	
07mai26	+	3366	398	< DL	< DL	347	16	0	
ID 205 Sch, Chip 2, 1 wt% NaCl, FMQ, 600 °C, 200 MPa,	07mai29	o	2704	398	< DL	< DL	395	5	1
	07mai30	+	3471	398	< DL	< DL	344	34	< DL
	07mai31	o	3143	398	< DL	< DL	362	42	0
	07mai32	o	2923	398	4	< DL	381	26	29
	07mai34	++	3774	398	< DL	< DL	367	36	0
	07mai35	+	3453	398	< DL	< DL	361	28	< DL
07mai36	+	3509	398	< DL	< DL	356	37	< DL	

Sample and exp. setup	Analysis	Quality	Na23	Rb85	Mo95	Mo97	Cs133	W182	Au197
He + H	07mai37	o	2902	398	< DL	< DL	341	32	< DL
	07mai38	o	3071	398	0	1	360	35	< DL
ID 206 Sch, Chip 1, 20 wt% NaCl, FMQ, 600 °C, 200 MPa, He + H	07maiB03	+	63733	398	< DL	1	336	805	0
	07maiB04	++	74542	398	2	2	397	35	0
	07maiB05	+	69319	398	1	3	390	1027	0
	07maiB06	+	79393	398	1	1	357	2	< DL
	07maiB09	++	74713	398	< DL	< DL	386	688	< DL
	07maiB10	++	73271	398	0	0	378	698	< DL
	07maiB11	+	66243	398	2	1	373	767	0
	07maiB12	+	69026	398	< DL	< DL	331	579	< DL
	07maiB14	+	75606	398	1	0	389	802	0
	07maiB15	o	102300	398	0	< DL	359	48	< DL
	07maiB16	++	72752	398	1	1	378	1049	1
	07maiB17	++	85589	398	2	3	382	951	0
	07maiB19	+	90609	398	< DL	< DL	394	902	< DL
	07maiB20	+	74380	398	2	2	349	790	0
07maiB21	+	65161	398	0	< DL	341	25	< DL	
07maiB22	++	72745	398	2	1	375	803	0	
ID 206 Sch, Chip 2, 20 wt% NaCl, FMQ, 600 °C, 200 MPa, He + H	07maiB24	+	68561	398	0	< DL	371	1052	2
	07maiB25	++	74531	398	1	3	390	1043	< DL
	07maiB26	+	81978	398	1	< DL	445	1126	2
	07maiB27	++	73945	398	1	< DL	363	1037	0
	07maiB29	+	75053	398	1	< DL	355	965	< DL
	07maiB30	o	59217	398	4	< DL	392	1501	0
	07maiB31	++	77938	398	2	< DL	385	978	0
07maiB32	+	70200	398	< DL	2	348	1094	< DL	
ID 208 Sch, Chip 1, 8 wt% NaCl, NNO, 600 °C, 200 MPa, He + H	08maiB03	++	33837	398	4	1	392	78	< DL
	08maiB04	++	33968	398	< DL	1	396	71	< DL
	08maiB05	++	29582	398	1	< DL	418	76	< DL
	08maiB06	+	36219	398	20	5	439	59	< DL
	08maiB08	++	31307	398	1	1	417	64	< DL
	08maiB09	++	31368	398	< DL	< DL	413	36	< DL
	08maiB10	+	35608	398	1	2	423	85	0
	08maiB11	+	36678	398	< DL	< DL	438	94	< DL
	08maiB13	o	42977	398	2	2	452	99	0
	08maiB14	o	29977	398	2	6	485	120	0
	08maiB15	++	31740	398	1	2	409	93	< DL
	08maiB16	o	38298	398	< DL	< DL	450	77	< DL
	08maiB19	++	32805	398	< DL	< DL	416	83	< DL
	08maiB20	+	35446	398	< DL	< DL	439	85	< DL
	08maiB21	++	32835	398	< DL	1	412	85	< DL
	08maiB23	++	33937	398	1	3	422	79	< DL
	08maiB24	++	30511	398	2	0	437	30	< DL
08maiB25	++	32160	398	1	< DL	439	24	0	
08maiB26	+	34344	398	< DL	1	442	83	< DL	
08maiB27	++	34339	398	< DL	< DL	403	96	< DL	
08maiB28	+	36231	398	14	< DL	423	78	0	
ID 208 Sch, Chip 2, 8 wt% NaCl, NNO, 600 °C, 200 MPa, He + H	08maiB31	++	32950	398	5	3	428	94	< DL
	08maiB32	++	29876	398	< DL	< DL	381	81	1
	08maiB33	+	36871	398	< DL	< DL	410	90	0
	08maiB34	o	36515	398	< DL	< DL	478	54	0
ID 210 Sch, Chip 1,	22mai03	+	34638	398	1	< DL	414	305	< DL
	22mai04	++	34551	398	1	1	432	351	< DL
	22mai05	+	42478	398	0	0	346	174	< DL

Sample and exp. setup	Analysis	Quality	Na23	Rb85	Mo95	Mo97	Cs133	W182	Au197
8 wt% NaCl, FMQ, 600 °C, 300 MPa, He + H	22mai06	+	34170	398	1	0	449	215	< DL
	22mai08	o	38557	398	1	1	386	204	0
	22mai09	o	38961	398	0	0	397	164	0
	22mai10	+	36844	398	2	5	409	219	< DL
	22mai11	o	43588	398	1	< DL	348	145	0
	22mai13	+	35260	398	0	1	388	276	< DL
	22mai14	+	36463	398	< DL	1	391	184	0
	22mai15	+	35529	398	< DL	0	422	203	0
	22mai16	+	37144	398	1	< DL	404	209	< DL
	22mai18	+	36381	398	1	0	392	195	< DL
	22mai19	+	36521	398	2	< DL	360	165	< DL
22mai20	++	31220	398	< DL	0	398	181	0	
22mai21	o	40303	398	1	< DL	416	230	0	
ID 210 Sch, Chip 2, 8 wt% NaCl, FMQ, 600 °C, 300 MPa, He + H	22mai23	++	31751	398	4	< DL	425	231	0
	22mai24	++	31684	398	< DL	< DL	439	< DL	< DL
ID 211 Sch, Chip 1, 8 wt% NaCl, FMQ, 600 °C, 100 MPa, He + H	22maiB03	+	33465	398	< DL	9	357	125	< DL
	22maiB04	++	28991	398	2	3	385	133	1
	22maiB05	++	34214	398	< DL	< DL	404	152	< DL
	22maiB06	++	31920	398	2	< DL	413	127	0
	22maiB08	++	30365	398	< DL	< DL	389	141	< DL
	22maiB09	++	34316	398	1	1	385	137	< DL
	22maiB10	+	41143	398	3	< DL	402	162	0
	22maiB11	++	33581	398	1	< DL	400	138	0
	22maiB13	++	33246	398	1	3	384	144	< DL
	22maiB14	+	32906	398	0	< DL	341	124	0
	22maiB15	++	30194	398	< DL	1	404	153	0
	22maiB16	-	58056	398	3	3	381	236	< DL
	22maiB18	-	48364	398	2	1	400	183	1
	22maiB19	-	1314	398	< DL	< DL	217	< DL	< DL
	22maiB20	++	31834	398	4	5	383	120	< DL
	22maiB21	+	36337	398	< DL	1	376	154	< DL
22maiB23	+	26535	398	< DL	< DL	418	158	2	
22maiB24	++	28433	398	< DL	< DL	404	139	0	
22maiB25	++	29803	398	1	< DL	382	158	< DL	
22maiB26	+	30171	398	182	179	354	134	1	
ID 211 Sch, Chip 2, 8 wt% NaCl, FMQ, 600 °C, 100 MPa, He + H	22maiB28	-	905453	398	5676	6060	379	710	< DL
	22maiB29	++	31743	398	59	< DL	413	230	< DL
	22maiB30	o	34498	398	< DL	< DL	562	370	1
	22maiB31	+	26755	398	7	< DL	456	319	< DL
	22maiB32	-	5134	398	< DL	< DL	121	< DL	129
ID 212 Fer, Chip 1, 8 wt% NaCl, FMQ, 600 °C, 300 MPa, He + H	23mai03	+	35365	398	1	0	442	1152	0
	23mai04	+	37953	398	1	< DL	402	690	< DL
	23mai05	++	29120	398	1	< DL	440	1176	1
	23mai06	++	29415	398	1	2	427	1101	0
	23mai08	++	30624	398	1	< DL	389	940	< DL
	23mai09	o	39908	398	1	1	559	964	0
	23mai10	++	30232	398	1	3	401	906	17
	23mai11	++	32302	398	0	1	399	1059	0
	23mai13	++	34404	398	3	3	405	998	< DL
23mai14	+	35447	398	1	< DL	428	1007	0	

Sample and exp. setup	Analysis	Quality	Na23	Rb85	Mo95	Mo97	Cs133	W182	Au197
	23mai15	+	35340	398	0	< DL	404	971	11
	23mai16	o	38556	398	2	< DL	436	1195	< DL
	23mai18	o	24535	398	1	< DL	291	718	< DL
	23mai20	+	31202	398	< DL	2	456	1267	1
	23mai21	++	32701	398	< DL	2	405	1061	0
	23mai23	+	35854	398	< DL	< DL	417	1225	< DL
	23mai24	++	34480	398	1	< DL	393	1085	< DL
ID 212 Fer, Chip 2, 8 wt% NaCl, FMQ, 600 °C, 300 MPa, He + H	23mai25	+	34612	398	0	1	390	1321	1
	23mai26	+	24130	398	10	2	426	1314	1
	23mai27	+	35431	398	< DL	< DL	392	1241	< DL
ID 213 Fer, Chip 1, 8 wt% NaCl, FMQ, 600 °C, 100 MPa, He + H	23maiB03	+	35425	398	< DL	1	429	165	1
	23maiB04	+	30704	398	< DL	1	449	385	< DL
	23maiB05	+	32286	398	5	0	447	778	0
	23maiB06	+	28878	398	2	< DL	354	132	2
	23maiB08	++	32705	398	1	2	422	774	< DL
	23maiB09	++	32712	398	< DL	1	420	294	< DL
	23maiB10	++	33309	398	37	37	421	621	< DL
	23maiB11	++	30565	398	2	2	420	764	< DL
	23maiB13	++	32457	398	2	< DL	427	812	< DL
	23maiB14	++	28884	398	1	2	428	927	< DL
	23maiB15	-	73508	398	2242	2147	254	1.8·10 ⁷	< DL
ID 213 Fer, Chip 2, 8 wt% NaCl, FMQ, 600 °C, 100 MPa, He + H	23maiB18	-	49373	398	1473	650	< DL	3368	65
ID 215 Fer, Chip 1, 8 wt% NaCl, FMQ, 800 °C, 200 MPa, He + H	21nov03	++	30614	398	< DL	< DL	411	4039	2
	21nov04	++	30606	398	< DL	3	395	3669	4
	21nov05	+	31991	398	3	< DL	446	4931	1
	21nov06	++	32558	398	1	5	410	3001	3
	21nov08	++	33144	398	< DL	< DL	430	867	3
	21nov09	++	28899	398	< DL	1	375	1965	2
	21nov10	+	36041	398	3	2	464	4860	3
	21nov11	++	33698	398	< DL	< DL	385	3002	3
	21nov13	++	32790	398	< DL	< DL	416	4476	2
	21nov14	++	29910	398	< DL	3	411	4924	4
	21nov15	++	32198	398	1	1	425	2514	2
	21nov16	o	40623	398	4	< DL	413	14628	17
	21nov18	+	27591	398	< DL	< DL	431	6900	2
	21nov19	++	28634	398	1	0	425	7881	3
	21nov20	++	32869	398	< DL	< DL	380	800	2
	21nov21	++	30239	398	3	3	389	96	1
21nov23	+	26637	398	1	< DL	446	19547	8	
21nov24	o	26993	398	< DL	10	498	7402	21	
21nov25	++	31358	398	< DL	2	377	9219	2	
	21nov26	o	27543	398	16	51	297	4191	< DL
ID 215 Fer, Chip 2, 8 wt% NaCl, FMQ,	21novB03	o	24812	398	4	< DL	286	9080	8
	21novB04	o	31116	398	0	1	488	16575	13
	21novB05	o	27149	398	1	< DL	500	13189	19
	21novB06	+	30260	398	2	< DL	463	14913	12
	21novB08	o	32443	398	5	1	301	8253	16

Sample and exp. setup	Analysis	Quality	Na23	Rb85	Mo95	Mo97	Cs133	W182	Au197
800 °C, 200 MPa, He + H	21novB09	o	34872	398	2	4	324	3700	13
	21novB10	o	25414	398	1	< DL	487	16096	< DL
	21novB11	+	26026	398	6	< DL	355	13346	8
	21novB13	+	27508	398	1	26	428	3203	17
	21novB14	o	22516	398	6	12	356	8446	14
	21novB15	o	35735	398	< DL	< DL	266	5883	11
	21novB16	o	33006	398	1	3	311	7032	12
	21novB18	o	41333	398	2	< DL	299	4975	11
	21novB19	+	32899	398	5	< DL	453	17715	16
	21novB20	-	11867	398	22	< DL	886	19228	< DL
	21novB21	-	42149	398	< DL	< DL	42	1270	32
	21novB23	o	29317	398	< DL	9	490	18015	5
	21novB24	-	42687	398	0	< DL	272	3791	29
	21novB25	++	31829	398	< DL	2	425	14978	13
21novB26	-	116776	398	214	441	562	4972	1740	
21novB27	-	41337	398	< DL	< DL	73	1032	< DL	
ID 221 Fer, Chip 1, 1 wt% NaCl, FMQ, 600 °C, 200 MPa, He + H	ID221_I_004	-	5029	398	< DL	24	567	191	10
	ID221_I_005	-	630	398	2	2	401	0	< DL
	ID221_I_006	++	3660	398	< DL	8	371	265	2
	ID221_I_008	-	8535	398	< DL	3	501	329	9
	ID221_I_009	o	3766	398	< DL	< DL	310	151	< DL
	ID221_I_010	-	8530	398	< DL	61	746	422	30
	ID221_I_011	+	3442	398	< DL	< DL	353	242	< DL
	ID221_I_013	++	4014	398	12	3	390	221	< DL
	ID221_I_014	+	3567	398	< DL	< DL	331	249	< DL
	ID221_I_015	-	30325	398	1196	1237	280	97	8419
	ID221_I_016	+	3227	398	3	5	401	308	< DL
	ID221_I_018	-	7327	398	0	3	455	466	7
ID221_I_019	-	5587	398	< DL	8	485	377	7	
ID221_I_020	o	2885	398	5	< DL	407	343	< DL	
ID221_I_021	+	4639	398	< DL	11	436	352	6	
ID 222 Fer, Chip 1, 20 wt% NaCl, FMQ, 600 °C, 200 MPa, He + H	ID222_I_03	++	71485	398	1	< DL	369	3651	< DL
	ID222_I_04	++	73174	398	1	< DL	403	4012	< DL
	ID222_I_05	++	73053	398	2	< DL	377	3398	< DL
	ID222_I_06	++	71719	398	1	< DL	394	3886	< DL
	ID222_I_08	++	77148	398	< DL	1	375	445	< DL
	ID222_I_09	+	77925	398	< DL	0	349	3060	< DL
	ID222_I_10	+	80591	398	< DL	10	468	4127	< DL
	ID222_I_11	+	72625	398	0	< DL	355	3128	< DL
	ID222_I_13	++	77527	398	< DL	< DL	413	3451	1
	ID222_I_14	+	92212	398	1	< DL	373	3383	< DL
	ID222_I_15	+	74080	398	1	< DL	408	3199	< DL
	ID222_I_16	o	62415	398	< DL	5	452	4689	< DL
	ID222_I_18	+	83262	398	< DL	< DL	474	3594	< DL
ID222_I_20	+	72667	398	1	6	373	3052	0	
ID222_I_21	++	75364	398	1	< DL	390	3322	< DL	
ID 222 Fer, Chip 2, 20 wt% NaCl, FMQ, 600 °C, 200 MPa, He + H	ID222_II_02	++	79770	398	< DL	< DL	390	4188	< DL
	ID222_II_03	+	72284	398	< DL	< DL	346	3570	2
ID 223 Sch, Chip 2, 8 wt% NaCl,	ID223_I_003	++	33107	398	0	< DL	428	4389	3
	ID223_I_004	+	33354	398	< DL	< DL	325	4174	2
	ID223_I_005	++	32051	398	1	1	424	3525	3
	ID223_I_006	+	36497	398	1	1	412	1487	1

Sample and exp. setup	Analysis	Quality	Na23	Rb85	Mo95	Mo97	Cs133	W182	Au197
FMQ, 800 °C, 200 MPa, He + H	ID223_I_008	+	31736	398	3	3	444	3351	3
	ID223_I_009	+	29831	398	< DL	5	473	3598	< DL
	ID223_I_010	+	29124	398	2	< DL	441	3201	4
	ID223_I_011	+	28150	398	< DL	2	405	3661	1
	ID223_I_013	+	31191	398	6	< DL	449	3892	5
	ID223_I_014	++	30608	398	4	< DL	425	4171	5
	ID223_I_015	+	29897	398	6	< DL	462	3073	< DL
	ID223_I_016	++	33876	398	1	1	417	2122	2
	ID223_I_018	+	32706	398	1	2	452	3388	3
	ID223_I_019	++	32421	398	3	< DL	422	993	2
ID223_I_021	++	31610	398	1	< DL	411	3802	5	
ID 223 Sch, Chip 1, 8 wt% NaCl, FMQ, 800 °C, 200 MPa, He + H	ID223_II_002	+	32895	398	< DL	2	457	1552	< DL
	ID223_II_003	+	32022	398	3	3	447	1388	2
	ID223_II_004	+	37192	398	2	1	452	3038	2
	ID223_II_005	+	34160	398	2	2	443	3631	0
	ID223_II_006	o	44074	398	2	3	419	4697	4
	ID223_II_007	++	31375	398	2	2	438	1314	3
	ID223_II_008	++	32659	398	< DL	< DL	438	3968	2
	ID223_II_009	+	28123	398	1	17	445	120	0
	ID223_II_010	+	32694	398	< DL	< DL	458	125	7
	ID223_II_012	+	31565	398	2	< DL	464	2506	3
	ID223_II_013	+	31540	398	2	< DL	447	1255	3
	ID223_II_014	+	32487	398	< DL	2	470	1709	0
	ID223_II_015	+	27976	398	1	4	418	< DL	5
	ID223_II_017	o	31477	398	2	2	503	2974	2
ID223_II_018	++	32925	398	< DL	3	401	3523	1	
ID223_II_019	++	32192	398	3	1	411	3600	2	
ID223_II_020	+	37345	398	4	4	417	3474	3	
ID 224 Sch, Chip 1, 8 wt% NaCl, FMQ, 450 °C, 200 MPa, He + H	ID_224_003	++	33543	398	1	< DL	386	23	0
	ID_224_005	++	34396	398	3	< DL	438	28	< DL
	ID_224_006	++	33877	398	0	< DL	427	56	0
	ID_224_007	+	35273	398	< DL	4	422	29	1
	ID_224_010	+	34923	398	1	< DL	399	20	< DL
	ID_224_011	++	29229	398	< DL	< DL	431	52	< DL
	ID_224_012	++	29586	398	< DL	7	411	32	< DL
	ID_224_013	+	31984	398	< DL	< DL	450	86	< DL
	ID_224_014	+	37074	398	< DL	0	391	37	< DL
	ID_224_016	-	48023	398	3	3	358	21	1
	ID_224_017	-	68660	398	1	< DL	374	24	< DL
	ID_224_018	o	40173	398	< DL	< DL	371	24	2
	ID_224_019	o	39556	398	< DL	< DL	398	27	28
	ID_224_020	-	43726	398	1	< DL	437	22	3
	ID_224_023	o	38773	398	1	< DL	385	23	< DL
ID_224_024	o	40303	398	< DL	< DL	335	32	< DL	
ID_224_025	o	38713	398	1	< DL	362	21	< DL	
ID_224_026	-	44467	398	1	1	381	20	2	
ID 225 Fer, Chip 1, 8 wt% NaCl, FMQ, 450 °C, 200 MPa, He + H	ID224_031	-	94217	398	< DL	< DL	910	687	4092
	ID224_032	-	60136	398	< DL	< DL	417	45	0
	ID224_033	-	76000	398	< DL	< DL	471	52	6
	ID224_034	++	28806	398	< DL	< DL	398	33	5
	ID224_036	++	34157	398	2	1	423	33	37
	ID224_037	++	34573	398	< DL	6	425	40	< DL
	ID224_038	+	37122	398	< DL	3	437	36	3
	ID224_039	-	28671	398	< DL	< DL	574	35	26
	ID224_040	-	58751	398	< DL	< DL	550	44	< DL
	ID224_042	o	37242	398	3	< DL	482	35	< DL
ID224_043	++	30286	398	< DL	2	407	34	3	

Sample and exp. setup	Analysis	Quality	Na23	Rb85	Mo95	Mo97	Cs133	W182	Au197
	ID224_044	++	34189	398	< DL	17	411	47	< DL
	ID224_045	o	37677	398	2	< DL	481	40	< DL
	ID224_048	+	38005	398	< DL	2	406	37	< DL
	ID224_049	++	34555	398	< DL	< DL	404	44	1
	ID224_050	++	29170	398	< DL	10	397	35	19
	ID224_051	+	32105	398	4	< DL	464	57	1
	ID224_052	++	33702	398	< DL	< DL	440	38	< DL
	ID224_055	+	35519	398	0	< DL	413	42	< DL
	ID224_056	+	35863	398	< DL	< DL	393	17	< DL
	ID224_057	+	37145	398	< DL	< DL	418	13	< DL
	ID224_058	o	41061	398	< DL	< DL	366	14	0
	ID224_060	-	28560	398	< DL	< DL	590	80	< DL

Appendix IV

Supplements to Chapter 6 - Microthermometry results of natural fluid inclusions from the Panasqueira W-Sn-(Cu-)deposit

Suppl. Tab. 6: Results from microthermometry of fluid inclusion from Pa150 from the Panasqueira W-Sn-(Cu-) deposit. Final ice melting temperatures (T_{m-ice}), eutectic temperatures (T_{eutec}) and final melting of clathrate ($T_{m-clath}$) from zones -3 to +4 in chips A, B, D, E and H from sample Pa150. Values for T_{eutec} and $T_{m-clath}$ were only determined roughly due to visibility and metastability problems during analyses.

Chip	Zone	FI #	T_{m-CO2}	T_{eutec}	T_{m-ice}	$T_{m-clath}$
A	+4	1a		-40	-2.7	
A	+4	1b		-38	-2.7	
A	+4	1d		-30	-2.7	
A	+4	1e		-33	-2.7	
A	+4	3a			-4.5	10.2
A	+4	3b		-25	-2.5	
A	+4	5a		-27	-2.7	
A	+4	7a		-34	-2.7	
A	+4	7b		-35	-2.5	
A	+4	7c		-32	-2.7	
A	+4	9a		-34	-2.5	
A	+4	9b		-35	-2.5	
A	+4	13a		-39	-6.2	11
A	+4	13b		-41	-2.7	
A	+4	17a		-35	-5.8	
A	+4	17b		-36	-5.3	
A	+4	17c		-35	-5.7	10
A	+4	17d			-6.0	11
A	+4	17e			-5.9	11
A	+4	18e			-5.9	11
A	+4	23a			-6.0	
A	+4	25a		-30	-2.8	
A	+4	25b			-5.4	
A	+4	33a		-35	-3.5	
A	+4	33b			-3.3	
B	+3	1a		-22	-6	8
B	+3	1b		-22	-6	7
B	+3	1c		-25	-6	8
B	+3	4a		-28	-5.9	8
B	+3	4a		-27	-5.8	8
B	+3	6a		-25	-5.8	8
B	+3	6a		-25	-5.8	8
B	+3	6b=a		-21	-5.8	10
B	+3	6c		-26	-6.0	9
B	+3	8a		-27	-5.7	7
B	+3	11a		-27	-5.8	7
B	+3	11b		-24	-5.7	7.3
B	+3	11c		-24	-5.9	10
B	+3	11d		-28	-6	11
B	+3	11e		-27	-5.9	12
B	+3	12e		-26	-5.9	14
B	+3	14a		-24	-5.7	7
B	+3	14b		-25	-5.8	9
B	+3	16a		-28	-5.7	9
B	+3	18a		-23	-5.7	10
B	+3	18b		-27	-5.7	10
B	+3	18c=b		-27	-5.7	10
B	+3	18d		-23	-5.7	9
B	+3	20a			-5.8	
B	+3	23a		-26	-5.7	9
B	+3	23b		-26	-5.7	10
B	+3	23c		-23	-5.9	
B	+3	25a		-27	-5.8	10
B	+3	25b		-23	-5.8	10
B	+3	29a		-26	-5.8	12
B	+3	31a		-24	-5.8	
B	+3	31b		-26	-5.8	11
B	+3	36a		-24	-5.9	9
B	+3	40a		-26	-5.8	12
B	+3	44a		-26	-5.8	10
B	+3	44b		-25	-6	
B	+3	44c		-26	-5.8	10
B	+3	48a		-26	-5.7	9
B	+3	54a		-27	-5.9	9
B	+3	54b			-6.1	
B	+3	54c		-25	-5.9	11
B	+3	58a			-6	
B	+3	58b		-27	-5.9	9
B	+3	58c		-28	-6	9
B	+3	58d		-24	-5.9	9
D	+1	1a	-60.0	-19	-5	12
D	+1	1b=a	-60.0	-19	-5	12
D	+1	3a	-60.6	-25	-6.2	12
D	+1	5a	-60.1	-25	-5.2	18
D	+1	5b	-59.5	-24	-6.1	11
D	+1	5c	-58.6	-22	-4.5	12
D	+1	5d	-59.5	-21	-5.8	12
D	+1	7b	-59.4	-20	-5.1	14
D	+1	9a	-59.6	-24	-4.9	11
D	+1	9b	-58.8		-6	12
D	+1	9c	-59.0			10
D	+1	11a	-59.9	-40	-6	12
D	+1	13a	-58.5	-25	-5.7	10
D	+1	13b	-59.4	-30	-5.2	12
D	+1	13c	-59.1	-25	-5.1	11
D	+1	13d=c	-59.2	-25	-5.1	11
D	+1	15a	-58.9	-30	-7	13
D	+1	17a	-60.5	-25	-5.6	12
D	+1	17b=a	-60.5	-22	-5.3	11
D	+1	17c=a	-60.5	-22	-5.6	11
D	+1	19a	-59.2	-35	-6.1	11
D	+1	19b	-59.5	-38	-5.7	11
D	+1	19c=b	-59.5	-38	-5.7	11
D	+1	19d	-60.6	-20	-5	11
D	+1	19d	-60.9	-23	-5.1	11
D	+1	21a	-60.1	-25	-6.3	11
D	+2	25a		-22	-5.3	7
D	+2	27a		-23	-4.8	10

Chip	Zone	FI #	T _{m-CO2}	T _{eutec}	T _{m-ice}	T _{m-clath}
D	+2	27b		-22	-4.9	8
D	+2	27c		-22	-5	8
D	+2	27d=c		-22	-4.9	12
D	+2	27e		-22	-4.9	8
D	+2	27f		-21	-4.8	13
D	+2	29a		-21	-4.8	12
D	+2	29b=a		-21	-4.8	12
D	+2	33a		-22	-4.9	
D	+2	39a		-22	-4.7	
D	+2	39b		-21	-4.8	12
D	+2	39c		-23	-4.9	9
D	+2	41a		-22	-4.8	7
D	+2	41b		-22	-4.7	
E	+1	1a		-26	-4.6	7
E	+1	1b		-24	-4.5	
E	+1	1c		-23	-4.5	9
E	+1	1d		-22	-5.1	
E	+1	3a		-22	-4.5	
E	+1	5a		-21	-4.6	
E	+1	5b		-22	-4.5	
E	+1	5c		-20	-4.7	4
E	+1	5d=c		-20	-4.7	4
E	+1	5e		-21	-4.5	
E	+1	11a		-22	-4.3	6
E	+1	11b=a		-22	-4.3	6
E	+1	11c		-23	-4.7	4
E	+1	13a		-24	-4.5	3
E	+1	13b		-23	-4.4	2
E	0	17a	-61.2	-17	-2.4	12
E	0	17b	-60.5	-18	-6.6	12
E	+1	24a		-20	-4.4	4
E	+1	24b		-20	-4.5	
E	0	26a		-22	-4.6	
E	0	26b = a		-23	-4.6	
E	0	26c		-22	-4.6	6.0
E	0	26d		-23	-4.8	9
E	0	28b	-60.9	-16	-5.5	12
E	0	28c=b	-60.9	-16	-5.5	12
E	0	32a			-4.5	2
E	0	32b			-4.4	
E	0	34a		-27	-4.7	8
E	0	34b		-25	-4.7	
E	0	36a		-23	-4.7	
E	0	36b		-25	-4.9	
E	0	40a		-23	-4.9	6.0
E	0	40b		-25	-4.8	5
E	0	42a		-22	-4.7	6.0
E	0	44a		-24	-4.6	5
E	0	48a		-24	-4.8	6
E	0	50a		-25	-4.7	7
E	0	52a			-5.2	6
E	0	52b			-5.3	6
E	0	54a			-5.7	6
E	0	54b			-5.8	
E	0	57a			-5.1	
E	0	59a		-25	-4.7	
E	0	61a		-27	-4.6	
E	-1	65a			-5.6	10
E	-1	65b			-6.4	
E	-1	65c			-6.1	4
E	-1	65d			-5.4	

Chip	Zone	FI #	T _{m-CO2}	T _{eutec}	T _{m-ice}	T _{m-clath}
E	-1	65e			-5.4	
E	-1	67a			-5.5	
E	-1	67b				12
E	-1	67c	-62.2		-6.3	12
E	-1	67d	-62.0		-6.2	12
E	-1	67e				12
E	-1	67f=e				12
E	-1	67g			-5.2	
E	-1	67h			-4.7	4
E	-1	69a			-4.6	
E	-1	69b	-59.6	-23	-6.4	12
E	-1	69c=b	-59.6	-23	-6.4	12
E	-1	69d			-4.5	
E	-1	72a			-4.5	6
E	-1	72b			-4.7	2
E	-1	74a			-5	4
E	-1	74b	-60.0		-5.8	12
E	-1	74c			-4.7	
E	-1	74d	-59.1			12
E	-1	74e=d	-59.1			12
E	-1	74f			-4.8	
E	-1	76a	-59.7		-6.2	
E	-1	76b=a	-59.7		-6.2	
E	-1	76c		-30	-4.7	5
E	-1	76d			-4.7	4
E	-1	80a	-59.9		-6	12
E	-1	80b			-4.8	2
E	0	83a		-24	-3.8	4
E	0	83b		-27	-3.9	3
E	0	83c		-27	-4.1	3
E	0	83d			-3.9	
E	0	89a		-24	-4.0	5
E	0	89b		-25	-3.7	3
E	0	89c		-23	-4	6
E	0	91a		-21	-4.5	2
E	0	91b		-20	-4.4	6
E	0	93a		-21	-3.8	
E	0	93b		-24	-4.2	4
E	0	93c		-22	-4	
E	0	95a		-22	-5.3	6
E	0	95b		-22	-4.8	
E	0	97a		-22	-5.2	6
E	0	97b		-22	-4.8	
E	0	99a		-23	-4.8	6
E	0	99b			-5.2	5
E	0	99c			-5.3	4
E	0	101a		-26	-5.0	6
E	0	101b		-26	-4.9	4
E	0	103a			-5.0	
E	0	103b			-4.8	7
E	0	103c			-5.0	
E	0	103d			-5.1	
E	0	107a		-20	-5.2	6
E	0	109a		-22	-5.0	
E	0	109b		-20	-4.9	
E	0	111a		-22	-4.9	8
E	0	111b		-20	-5.3	
E	0	111c			-4.9	7
E	0	113a		-21	-5.1	8
E	0	113b			-4.8	
E	0	117a		-20	-4.9	6

Chip	Zone	FI #	T _{m-CO2}	T _{eutec}	T _{m-ice}	T _{m-clath}
E	0	117b		-22	-4.9	5
E	0	117c		-21	-4.8	9
E	0	117d		-21	-5.2	
E	0	119a			-5.1	7
E	0	119b			-4.9	6
E	0	119c			-4.9	
E	0	121a		-24	-4.4	6
E	0	121b		-25	-4.5	9
E	0	121c		-22	-3.2	10
E	0	121d		-23	-4.1	6
E	0	121e		-20	-4.4	6
E	0	121f		-20	-4.5	6
E	0	123a		-23	-4.6	8
E	0	123b		-20	-5.1	
E	0	123c		-21	-4.8	7
E	0	123d		-21	-4.2	7
E	0	125a		-22	-4.5	3
E	0	125b		-21	-4.7	8
E	0	125c		-21	-4.8	4
E	0	127a		-21	-5.1	6
E	0	127b		-20	-5.1	10
E	0	129a		-21	-4.8	
E	0	129b		-20	-4.6	6
E	0	131a		-22	-4.4	3
E	0	135a		-20	-4.2	10
E	0	135b		-21	-4.4	10
E	0	136a		-20	-4.6	11
E	0	138a		-21	-4.9	4
E	+1	140a			-4.9	
E	+1	140b		-21	-4.9	6
E	+1	142a			-4.7	7
E	+1	144a		-22	-4.9	7
E	+1	146a		-22	-5.1	5
E	+1	148a		-22	-5.5	6
E	+1	148b		-20	-5.9	6
E	+1	150a			-6.0	8
E	+1	152a			-5.1	12
H	-2	1a		-25	-4.8	
H	-2	3a		-23	-4.7	
H	-2	3b=a		-23	-4.7	
H	-2	3c		-27	-4.8	
H	-2	5a		-25	-4.4	8
H	-2	5b		-24	-4.2	8
H	-2	7a		-23	-4.4	
H	-2	7b=a		-23	-4.4	
H	-2	7c		-24	-4.4	10
H	-2	9a		-24	-4.1	
H	-2	11a		-23	-4.3	
H	-2	11b		-24	-4.3	6
H	-2	21a		-24	-4.7	5
H	-2	21b		-26	-4.6	6
H	-2	23a		-24	-4.4	
H	-2	25a		-24	-4.6	
H	-2	31a		-25	-4.7	
H	-2	31b		-22	-4.6	6
H	-2	33a		-23	-4.8	6
H	-2	35a		-21	-4.6	5
H	-2	37a		-20	-4.7	
H	-2	39a		-23	-4.7	12
H	-2	39b=a		-21	-4.7	12
H	-2	41a		-22	-5.1	9

Chip	Zone	FI #	T _{m-CO2}	T _{eutec}	T _{m-ice}	T _{m-clath}
H	-2	43a		-24	-5	5
H	-2	43b=a		-24	-5	5
H	-2	43c		-24	-4.6	
H	-2	49a		-20	-4.6	4
H	-2	51a		-22	-4.8	
H	-2	53a		-21	-4.8	
H	-2	53b		-23	-4.7	
H	-3	55a		-22	-4.6	
H	-3	55b		-22	-4.7	5
H	-3	57a		-20	-4.6	6
H	-3	57b=a		-20	-4.6	6
H	-3	59a		-21	-4.5	6
H	-3	61a		-20	-4.5	
H	-3	63a		-19	-4.5	8
H	-3	65a		-21	-4.6	8
H	-3	65b		-21	-4.5	6
H	-3	67a		-20	-4.5	13
H	-3	67b=a		-20	-4.5	13
H	-3	69a		-20	-4.4	
H	-3	69b=a		-20	-4.4	
H	-3	69c		-21	-4.4	
H	-3	69d=c		-21	-4.4	
H	-3	71a		-23	-4.5	
H	-3	71b=a		-23	-4.5	
H	-3	73a		-18	-4.6	7
H	-3	73b=a		-18	-4.6	7
H	-3	75a		-19	-4.4	
H	-3	75b		-22	-4.6	6
H	-3	77a		-20	-4.5	5
H	-2	79a		-20	-4.6	10
H	-2	79b		-21	-4.3	6
H	-2	81a		-23	-4.2	8
H	-2	81b		-20	-4.2	4
H	-2	81c=b		-20	-4.2	4
H	-2	83a		-21	-4.2	7
H	-2	85a		-23	-3.7	10
H	-2	87a		-21	-4.2	5
H	-2	89a		-20	-4.3	7
H	-2	89b=a		-20	-4.3	7
H	-2	91a		-20	-4.1	5
H	-2	91b=a		-20	-4.1	5
H	-2	91c		-20	-4.3	5
H	-2	91d=c		-20	-4.3	5
H	-2	91e=c		-20	-4.3	5
H	-2	93a		-20	-4	5
H	-2	95a		-19	-4.3	8
H	-2	95b			-4.1	
H	-3	97a		-22	-4.4	
H	-3	97b		-20	-4.3	5
H	-3	97c=b		-20	-4.3	5
H	-3	99a		-21	-4.2	
H	-3	101a		-19	-4.2	5
H	-3	101b		-20	-4.2	12
H	-3	103a		-19	-4.2	
H	-3	103b		-20	-4.1	8
H	-3	105a		-22	-4.2	10
H	-3	105b=a		-20	-4.2	10
H	-3	107a		-20	-4	4
H	-3	107b		-20	-4.2	6
H	-3	107c=b		-20	-4.2	6
H	-3	107d=b		-20	-4.2	6

Chip	Zone	FI #	T _{m-CO2}	T _{eutec}	T _{m-ice}	T _{m-clath}
H	-3	107e=b		-20	-4.2	6
H	-3	109a		-20	-4.1	
H	-3	111a			-4.5	
H	-3	113a		-19	-4.6	6
H	-3	113b=a		-19	-4.6	6
H	-3	115a		-20	-4.6	8
H	-3	117a		-21	-4.5	8
H	-3	117b=a		-21	-4.3	8
H	-3	119a		-20	-4.6	8
H	-3	121a		-20	-4.4	10
H	-3	123a		-19	-4.5	9
H	-2	126a		-19	-4.7	4
H	-2	128a		-19	-4.5	10
H	-2	130a		-19	-4.5	8
H	-2	132a		-20	-4.5	
H	-2	136a		-19	-4.3	9
H	-2	136b=a		-19	-4.3	9
H	-2	138a		-20	-4.5	4
H	-3	140a		-20	-4.4	
H	-3	142a		-20	-4.3	10
H	-3	144a		-19	-4.3	
H	-3	146a		-21	-4.6	
H	-3	146b		-22	-4.5	8
H	-3	146c		-20	-4	7
H	-3	148a		-21	-4.6	10
H	-3	148b		-20	-4.6	
H	-3	148c=b		-20	-4.7	
H	-3	148b		-22	-4.6	5
H	-3	150a		-21	-4.6	
H	-3	150b		-21	-4.6	
H	-3	152a		-19	-4.6	
H	-3	152b=a		-19	-4.4	
H	-3	154a		-20	-4.7	5
H	-3	154b=a		-20	-4.6	5
H	-3	154c		-20	-4.7	10
H	-3	156a		-19	-4.6	5
H	-3	156b=a		-19	-4.6	6
H	-3	156c		-20	-4.8	
H	-3	158a		-19	-4.5	
H	-3	158b		-18	-4.7	7
H	-3	158c		-18	-4.6	
H	-3	158d=c		-18	-4.6	
H	-3	158e=c		-18	-4.6	
H	-3	160a		-19	-4.2	5
H	-3	160b=a		-19	-4.2	5
H	-3	160c		-19	-4.1	5
H	-3	160d=c		-19	-4.1	5
H	-3	160e		-18	-4.2	5
H	-3	160f		-20	-4.2	6
H	-3	162a		-20	-4.2	
H	-3	162b		-20	-4.2	5
H	-3	162c		-20	-4	
H	-3	165a		-20	-3.9	
H	-3	165b		-21	-4.2	6
H	-3	165c		-20	-4.2	
H	-3	167a		-20	-4.1	
H	-3	167b		-21	-4.2	
H	-3	169a		-20	-4.5	
H	-3	169b		-20	-3.9	
H	-3	169c		-19	-4.1	4
H	-3	169d		-19	-4.2	6

Chip	Zone	FI #	T _{m-CO2}	T _{eutec}	T _{m-ice}	T _{m-clath}
H	-3	171a		-20	-4.5	5
H	-2	173a		-19	-4.4	8
H	-2	173b=a		-19	-4.4	8
H	-2	173c		-20	-4.5	6
H	-2	175a		-22	-4.5	8
H	-2	175b		-20	-4.6	5
H	-2	177a		-21	-4.8	
H	-2	179a		-20	-4.4	7
H	-2	179b=a		-20	-4.3	7
H	-2	179c		-20	-4.6	
H	-2	179d		-21	-4.6	
H	-2	179e		-22	-4.6	
H	-3	181a		-21	-4.4	8
H	-3	183a		-21	-4.5	6
H	-3	183b=a		-21	-4.5	6
H	-3	183c=a		-21	-4.5	6
H	-3	183d		-21	-4.4	4
H	-3	185a		-19	-4.4	5
H	-3	185a		-21	-4.4	5
H	-3	185b=a		-21	-4.4	5
H	-3	185c		-20	-4.5	6
H	-3	185d		-19	-4.4	
H	-3	187a		-19	-4.5	4
H	-3	187b		-20	-4.4	
H	-3	189a		-20	-4.5	6
H	-3	189b		-20	-4.4	
H	-3	191a		-20	-4.5	
H	-3	191b		-19	-4.5	
H	-3	191c		-20	-4.5	5
H	-3	193a		-21	-4.6	6
H	-3	193b		-19	-4.4	6
H	-3	193c		-20	-4.5	7
H	-3	193d =		-20	-4.5	
H	-3	195a		-20	-4.8	
H	-3	195b		-21	-4.5	
H	-3	197a		-20	-4.7	
H	-3	199a		-20	-4.7	5
H	-3	199b		-20	-4.7	
H	-3	199c=b		-20	-4.6	
H	-3	201a		-21	-4.7	
H	-3	201b		-20	-4.5	
H	-3	201c=b		-20	-4.5	
H	-3	203a		-20	-4.6	8
H	-3	203b		-20	-4.6	
H	-3	205a		-20	-4.5	7
H	-3	205b		-19	-4.7	
H	-3	207a		-22	-4.6	4
H	-3	207b		-20	-4.8	
H	-3	207c=b		-20	-4.8	
H	-3	209a		-20	-4.5	8
H	-3	209b		-19	-4.6	9
H	-3	211a		-20	-4.5	5
H	-3	211b		-20	-4.4	
H	-3	213a		-19	-4.3	8
H	-3	213b		-19	-4.5	
H	-3	217a		-19	-4.2	
H	-3	219a		-19	-4.4	5
H	-3	221a		-21	-4.2	6
H	-3	221b=a		-21	-4.2	6
H	-3	221c		-22	-4.3	6
H	-3	221d		-21	-4.2	7

Chip	Zone	FI #	T _{m-CO2}	T _{eutec}	T _{m-ice}	T _{m-clath}
H	-3	221e=d		-21	-4.2	7
H	-3	223a		-21	-4.3	
H	-3	223b		-20	-4.3	
H	-3	225a		-20	-4.4	6
H	-3	225b		-19	-4.3	
H	-3	225c=b		-19	-4.3	
H	-3	227a		-20	-4.6	6
H	-3	227b		-20	-4.5	7
H	-3	229a		-20	-4.5	5
H	-3	229b		-21	-4.8	
H	-3	231a		-19	-4.5	
H	-3	231b=a		-20	-4.5	
H	-3	231c		-22	-4.8	
H	-3	233a		-21	-4.8	
H	-3	233b		-22	-4.8	5
H	-3	235a		-21	-4.6	6
H	-3	235b		-21	-4.6	
H	-3	237a		-20	-4.5	
H	-3	237b=a		-20	-4.5	
H	-3	237c		-19	-4.7	
H	-3	239a		-19	-4.5	5
H	-3	239b		-20	-4.7	
H	-3	241a		-20	-4.6	
H	-3	241b		-19	-4.6	
H	-3	241c		-20	-4.6	
H	-3	243a		-21	-4.6	
H	-3	243b		-19	-4.6	
H	-3	245a		-19	-4.4	
H	-3	245a			-4.7	
H	-3	247a		-21	-4.6	
H	-3	247a		-20	-4.6	
H	-3	247a		-22	-4.6	
H	-3	247a			-4.6	
H	-3	249a		-19	-4.6	8
H	-3	249b		-21	-4.6	8
H	-3	251a		-20	-4.6	
H	-3	253a			-4.8	
H	-3	253b		-19	-4.7	
H	-3	253c		-20	-4.8	
H	-3	255a			-4.9	
H	-3	255b			-4.9	
H	-3	255c			-4.8	
H	-3	257a		-19	-4.8	
H	-3	257b		-19	-4.8	
H	-3	257c		-20	-4.8	
H	-3	259a		-21	-5.2	
H	-3	259b		-20	-4.9	
H	-3	261a		-20	-4.8	
H	-3	261b		-21	-4.8	
H	-3	263a		-21	-4.7	
H	-3	263b		-19	-4.8	
H	-3	265a		-21	-4.8	
H	-3	265b			-4.9	
H	-3	265c		-20	-4.9	
H	-3	267a		-21	-4.9	
H	-3	267b		-19	-4.8	
H	-3	273a		-20	-5	
H	-3	275a		-20	-5.1	
H	-3	275b		-19	-5	
H	-3	275c=b		-19	-5	
H	-3	277a			-5.1	

Chip	Zone	FI #	T _{m-CO2}	T _{eutec}	T _{m-ice}	T _{m-clath}
H	-3	279a		-21	-5.2	
H	-3	281a		-20	-5.1	
H	-3	281b		-20	-5.1	
H	-2	285a			-5.5	
H	-2	287a		-21	-5.1	
H	-2	289a		-21	-5	
H	-2	289b		-20	-4.7	
H	-2	291a		-20	-4.6	
H	-2	295c		-21	-4.7	
H	-2	297a		-21	-4.6	
H	-2	297b		-21	-4.6	
H	-2	299a		-21	-4.8	6
H	-2	301a		-20	-4.4	
H	-2	291b		-21	-4.5	
H	-2	293a		-22	-4.7	
H	-2	293b		-21	-4.6	
H	-2	295a		-21	-4.8	
H	-2	295b		-21	-4.6	
H	-2	303a		-21	-4.5	
H	-2	305a		-21	-4.3	
H	-2	307a		-19	-4.5	
H	-2	309a		-19	-4.3	
H	-2	309b=a		-19	-4.3	
H	-2	311a		-20	-4.5	
H	-2	315a		-21	-4.7	
H	-2	317a		-21	-4.2	8
H	-2	319a		-21	-4.3	
H	-2	321a		-21	-4.6	
H	-3	323a		-21	-4.5	
H	-3	323b=a		-21	-4.5	
H	-2	325a		-22	-4.4	
H	-2	327a		-21	-4.5	
H	-2	329a		-21	-4.4	
H	-2	331a		-20	-4.5	
H	-2	333a		-21	-4.6	
H	-2	335a		-20	-4.6	
H	-2	337a		-20	-4.5	
H	-2	339a		-21	-4.6	
H	-2	341a		-20	-4.2	
H	-2	343a		-21	-4.6	8
H	-2	345a			-4.8	
H	-2	347a		-23	-4.6	6
H	-2	347b=a		-23	-4.6	6
H	-2	349a		-21	-4.7	5
H	-2	349b=a		-21	-4.7	5
H	-2	351a		-19	-4.7	5

Supplements to Chapter 6 – LA-ICP-MS data of natural fluid inclusions from the Panasqueira W-Sn-(Cu-)deposit

Suppl. Tab. 7: Normalized LA-ICP-MS data in ppm from individual fluid inclusion from sample Pa150 of the Panasqueira W-Sn-(Cu-)deposit. Values below the detection limit are marked with “< DL”. Upper and lower limit refer to the upper and lower limits of internal standardization as discussed in Chapter 6.5.2. Based on visual inspection of the signal and ablation site, each analysis was rated for its quality (- = very poor, o = poor, +o = mediocre, + = good, ++ = very good).

Chip	Zone	Sample Filename	Carrier gas	Anal ysis	Qual ity	Limit	Li	B	Na	Mg	K	Ca	Mn	Fe	Zn	Cu	As	Rb	Sn	Sb	Cs	Ba	W	Au	Pb
B	+3	19jan29	He + H	Spot	++	Upper	< DL	2585	34974	< DL		< DL	< DL	< DL	< DL	< DL	88	253	< DL	20	249	< DL	< DL	< DL	< DL
B	+3	19jan04	He + H	Spot	+	Upper	227	2745	30510	< DL		5849	< DL	2950	< DL	< DL	31	48	< DL	< DL	271	< DL	< DL	< DL	< DL
B	+3	19jan05	He + H	Spot	+	Upper	60	1841	11132	219		43536	< DL	< DL	217	< DL	80	1024	< DL	39	134	56	< DL	< DL	< DL
B	+3	19jan06	He + H	Spot	+	Upper	249	4344	34655	< DL		< DL	< DL	< DL	< DL	< DL	66	182	< DL	12	388	< DL	1.4	< DL	< DL
B	+3	19jan08	He + H	Spot	+	Upper	< DL	2117	29629	< DL		7646	< DL	2718	80	< DL	56	1209	< DL	13	267	< DL	< DL	< DL	< DL
B	+3	19jan09	He + H	Spot	+	Upper	359	4314	33655	< DL		< DL	86	3041	< DL	< DL	32	163	< DL	< DL	403	< DL	3	< DL	< DL
B	+3	19jan11	He + H	Spot	+	Upper	862	3007	35012	< DL		< DL	253	< DL	< DL	< DL	87	143	< DL	19	354	< DL	3	< DL	16
B	+3	19jan13	He + H	Spot	o	Upper	< DL	3515	27570	< DL		4474	4088	11168	562	< DL	64	2633	141	< DL	276	583	263	< DL	19
B	+3	19jan14	He + H	Spot	+	Upper	159	4102	31085	< DL		< DL	1208	8691	412	< DL	67	1432	56	< DL	347	221	10	< DL	< DL
B	+3	19jan15	He + H	Spot	+	Upper	280	3275	34850	< DL		< DL	65	< DL	< DL	< DL	29	110	< DL	< DL	326	< DL	< DL	< DL	< DL
B	+3	19jan16	He + H	Spot	++	Upper	354	3180	34819	< DL		< DL	< DL	< DL	< DL	< DL	39	38	< DL	< DL	469	< DL	4	< DL	< DL
B	+3	19jan19	He + H	Spot	+	Upper	202	3094	31871	< DL		< DL	< DL	5122	105	< DL	135	180	< DL	32	343	< DL	11	< DL	363
B	+3	19jan20	He + H	Spot	-	Upper	144	5230	31917	< DL		< DL	< DL	< DL	< DL	< DL	151	1684	< DL	< DL	491	< DL	12	< DL	< DL
B	+3	19jan21	He + H	Spot	o-	Upper	692	2508	34487	< DL		< DL	< DL	< DL	< DL	< DL	< DL	160	< DL	< DL	551	< DL	< DL	< DL	< DL
B	+3	19jan22	He + H	Spot	+	Upper	726	4741	34319	< DL		< DL	< DL	< DL	< DL	< DL	42	496	< DL	< DL	417	< DL	46	< DL	< DL
B	+3	19jan24	He + H	Spot	+	Upper	278	3042	34558	< DL		< DL	42	< DL	< DL	< DL	109	47	< DL	30	286	< DL	< DL	< DL	< DL
B	+3	19jan25	He + H	Spot	+	Upper	277	3254	33958	< DL		< DL	62	2351	101	16	89	194	< DL	19	385	< DL	11	< DL	19
B	+3	19jan26	He + H	Spot	-	Upper	< DL	2927	26050	< DL		< DL	< DL	< DL	< DL	< DL	< DL	< DL	< DL	< DL	329	< DL	< DL	< DL	< DL
B	+3	19jan27	He + H	Spot	++	Upper	< DL	4838	32523	< DL		< DL	< DL	< DL	89	< DL	< DL	1142	< DL	< DL	375	< DL	< DL	< DL	< DL
B	+3	19jan28	He + H	Spot	+	Upper	< DL	2635	33749	< DL		< DL	56	2821	48	69	38	49	< DL	< DL	271	< DL	< DL	< DL	< DL
B	+3	19jan29	He + H	Spot	++	Lower	< DL	552	7466	< DL		< DL	< DL	< DL	< DL	< DL	19	54	< DL	4	53	< DL	< DL	< DL	< DL
B	+3	19jan04	He + H	Spot	+	Lower	48	586	6513	< DL		1249	< DL	630	< DL	< DL	7	10	< DL	< DL	58	< DL	< DL	< DL	< DL
B	+3	19jan05	He + H	Spot	+	Lower	13	393	2376	47		9294	< DL	< DL	46	< DL	17	219	< DL	8	29	12	< DL	< DL	< DL
B	+3	19jan06	He + H	Spot	+	Lower	53	927	7398	< DL		< DL	< DL	< DL	< DL	< DL	14	39	< DL	2	83	< DL	0.3	< DL	< DL
B	+3	19jan08	He + H	Spot	+	Lower	< DL	452	6325	< DL		1632	< DL	580	17	< DL	12	258	< DL	3	57	< DL	< DL	< DL	< DL
B	+3	19jan09	He + H	Spot	+	Lower	77	921	7185	< DL		< DL	18	649	< DL	< DL	7	35	< DL	< DL	86	< DL	0.6	< DL	< DL
B	+3	19jan11	He + H	Spot	+	Lower	184	642	7475	< DL		< DL	54	< DL	< DL	< DL	19	31	< DL	4	76	< DL	0.7	< DL	3
B	+3	19jan13	He + H	Spot	o	Lower	< DL	750	5886	< DL		955	873	2384	120	< DL	14	562	30	< DL	59	125	56	< DL	4
B	+3	19jan14	He + H	Spot	+	Lower	34	876	6636	< DL		< DL	258	1855	88	< DL	14	306	12	< DL	74	47	2	< DL	< DL
B	+3	19jan15	He + H	Spot	+	Lower	60	699	7440	< DL		< DL	14	< DL	< DL	< DL	6	23	< DL	< DL	70	< DL	< DL	< DL	< DL
B	+3	19jan16	He + H	Spot	++	Lower	76	679	7433	< DL		< DL	< DL	< DL	< DL	< DL	8	8	< DL	< DL	100	< DL	0.9	< DL	< DL
B	+3	19jan19	He + H	Spot	+	Lower	43	660	6804	< DL		< DL	< DL	1094	22	< DL	29	38	< DL	7	73	< DL	2	< DL	77
B	+3	19jan20	He + H	Spot	-	Lower	31	1117	6814	< DL		< DL	< DL	< DL	< DL	< DL	32	359	< DL	< DL	105	< DL	2	< DL	< DL
B	+3	19jan21	He + H	Spot	o-	Lower	148	535	7362	< DL		< DL	< DL	< DL	< DL	< DL	< DL	34	< DL	< DL	118	< DL	< DL	< DL	< DL
B	+3	19jan22	He + H	Spot	+	Lower	155	1012	7326	< DL		< DL	< DL	< DL	< DL	< DL	9	106	< DL	< DL	89	< DL	10	< DL	< DL
B	+3	19jan24	He + H	Spot	+	Lower	59	649	7378	< DL		< DL	9	< DL	< DL	< DL	23	10	< DL	6	61	< DL	< DL	< DL	< DL
B	+3	19jan25	He + H	Spot	+	Lower	59	695	7249	< DL		< DL	13	502	22	3	19	41	< DL	4	82	< DL	2	< DL	4
B	+3	19jan26	He + H	Spot	-	Lower	< DL	625	5561	< DL		< DL	< DL	< DL	< DL	< DL	< DL	< DL	< DL	< DL	70	< DL	< DL	< DL	< DL
B	+3	19jan27	He + H	Spot	++	Lower	< DL	1033	6943	< DL		< DL	< DL	< DL	19	< DL	< DL	244	< DL	< DL	80	< DL	< DL	< DL	< DL
B	+3	19jan28	He + H	Spot	+	Lower	< DL	562	7205	< DL		< DL	12	602	10	15	8	10	< DL	< DL	58	< DL	< DL	< DL	< DL
B	+3	20jan12	He + H	Spot	+	Upper	293	2634	34509	< DL		< DL	< DL	< DL	48	< DL	79	92	< DL	38	274	< DL	15	< DL	35

Chip	Zone	Sample Filename	Carrier gas	Anal ysis	Qual ity	Limit	Li	B	Na	Mg	K	Ca	Mn	Fe	Zn	Cu	As	Rb	Sn	Sb	Cs	Ba	W	Au	Pb
B	+3	20jan03	He + H	Spot	+	Upper	187	2502	34701	< DL		< DL	< DL	< DL	< DL	< DL	58	17	< DL	< DL	158	< DL	< DL	< DL	< DL
B	+3	20jan05	He + H	Spot	+	Upper	301	3445	33620	< DL		< DL	75	1417	< DL	< DL	60	141	< DL	< DL	305	< DL	2	< DL	< DL
B	+3	20jan06	He + H	Spot	+	Upper	611	4843	32962	< DL		< DL	< DL	< DL	< DL	< DL	78	353	< DL	< DL	343	< DL	< DL	< DL	< DL
B	+3	20jan07	He + H	Spot	++	Upper	179	2766	34966	< DL		< DL	37	< DL	< DL	< DL	59	126	< DL	2	288	< DL	1.8	< DL	< DL
B	+3	20jan09	He + H	Spot	+	Upper	512	4056	35012	< DL		< DL	< DL	< DL	< DL	< DL	36	130	< DL	20	383	< DL	5	< DL	< DL
B	+3	20jan10	He + H	Spot	+	Upper	328	2995	34924	< DL		< DL	82	< DL	< DL	< DL	35	137	< DL	< DL	309	< DL	< DL	< DL	< DL
B	+3	20jan11	He + H	Spot	+	Upper	305	3439	34048	< DL		< DL	< DL	< DL	< DL	< DL	42	106	< DL	< DL	309	< DL	< DL	< DL	< DL
B	+3	20jan12	He + H	Spot	+	Lower	63	562	7367	< DL		< DL	< DL	< DL	10	< DL	17	20	< DL	8	58	< DL	3	< DL	8
B	+3	20jan03	He + H	Spot	+	Lower	40	534	7408	< DL		< DL	< DL	< DL	< DL	< DL	12	4	< DL	< DL	34	< DL	< DL	< DL	< DL
B	+3	20jan05	He + H	Spot	+	Lower	64	735	7177	< DL		< DL	16	303	< DL	< DL	13	30	< DL	< DL	65	< DL	0.5	< DL	< DL
B	+3	20jan06	He + H	Spot	+	Lower	130	1034	7037	< DL		< DL	< DL	< DL	< DL	< DL	17	75	< DL	< DL	73	< DL	< DL	< DL	< DL
B	+3	20jan07	He + H	Spot	++	Lower	38	590	7465	< DL		< DL	8	< DL	< DL	< DL	13	27	< DL	0.5	61	< DL	0.4	< DL	< DL
B	+3	20jan09	He + H	Spot	+	Lower	109	866	7475	< DL		< DL	< DL	< DL	< DL	< DL	8	28	< DL	4	82	< DL	1.1	< DL	< DL
B	+3	20jan10	He + H	Spot	+	Lower	70	639	7456	< DL		< DL	17	< DL	< DL	< DL	8	29	< DL	< DL	66	< DL	< DL	< DL	< DL
B	+3	20jan11	He + H	Spot	+	Lower	65	734	7269	< DL		< DL	< DL	< DL	< DL	< DL	9	23	< DL	< DL	66	< DL	< DL	< DL	< DL
D	+2	16jan52	He + H	Spot	o	Upper	986	4207	22111	< DL		< DL	1885	< DL	< DL	< DL	< DL	< DL	< DL	< DL	313	< DL	< DL	< DL	< DL
D	+2	16jan26	He + H	Spot	++	Upper	177	2944	18762	< DL		6911	162	< DL	< DL	< DL	< DL	70	< DL	< DL	290	< DL	< DL	< DL	< DL
D	+2	16jan27	He + H	Spot		Upper	176	3564	22111	< DL		< DL	113	< DL	< DL	< DL	120	69	< DL	< DL	159	< DL	3	< DL	1.9
D	+2	16jan28	He + H	Spot	++	Upper	150	2771	22111	< DL		< DL	< DL	< DL	< DL	< DL	15	48	< DL	< DL	252	< DL	1.3	< DL	< DL
D	+2	16jan29	He + H	Spot	+	Upper	190	3840	20125	< DL		4098	< DL	< DL	< DL	< DL	18	82	< DL	< DL	133	< DL	< DL	< DL	< DL
D	+2	16jan31	He + H	Spot	+	Upper	124	2731	19402	< DL		5591	< DL	< DL	< DL	< DL	280	< DL	< DL	< DL	44	< DL	< DL	< DL	< DL
D	+2	16jan32	He + H	Spot	+	Upper	91	2553	22111	< DL		< DL	< DL	< DL	< DL	< DL	367	68	< DL	< DL	87	< DL	< DL	< DL	< DL
D	+2	16jan33	He + H	Spot	++	Upper	224	2740	22111	< DL		< DL	< DL	< DL	< DL	< DL	558	46	< DL	< DL	208	< DL	11	< DL	2
D	+2	16jan34	He + H	Spot	+	Upper	249	3011	18525	< DL		7402	429	< DL	< DL	< DL	< DL	703	< DL	< DL	249	< DL	< DL	< DL	< DL
D	+2	16jan36	He + H	Spot	++	Upper	90	2308	20970	< DL		< DL	260	2355	29	< DL	218	94	< DL	17	198	< DL	5	< DL	< DL
D	+2	16jan37	He + H	Spot	+	Upper	167	3085	22111	< DL		< DL	< DL	< DL	< DL	< DL	273	47	< DL	< DL	277	< DL	< DL	< DL	< DL
D	+2	16jan38	He + H	Spot	++	Upper	149	3311	22111	< DL		< DL	44	< DL	< DL	< DL	81	49	< DL	< DL	300	< DL	0.7	< DL	< DL
D	+2	16jan39	He + H	Spot	++	Upper	69	2708	21490	< DL		< DL	104	1281	14	< DL	121	38	< DL	3	250	< DL	1.3	< DL	< DL
D	+2	16jan41	He + H	Spot	o	Upper	207	1766	13972	< DL		16798	< DL	< DL	< DL	336	330	128	< DL	< DL	101	< DL	18	< DL	< DL
D	+2	16jan42	He + H	Spot	+	Upper	175	2633	22111	< DL		< DL	2176	< DL	< DL	< DL	349	74	< DL	< DL	117	< DL	< DL	< DL	< DL
D	+2	16jan43	He + H	Spot	++	Upper	90	2629	21254	< DL		< DL	119	1770	23	< DL	247	44	< DL	4	243	< DL	< DL	< DL	< DL
D	+2	16jan44	He + H	Spot	++	Upper	179	2692	22111	< DL		< DL	< DL	< DL	< DL	< DL	109	16	< DL	< DL	228	< DL	1.6	< DL	< DL
D	+2	16jan46	He + H	Spot	-	Upper	162	2682	20456	< DL		3416	< DL	< DL	< DL	< DL	208	36	< DL	< DL	264	< DL	< DL	< DL	< DL
D	+2	16jan47	He + H	Spot	+	Upper	272	2461	16675	< DL		11220	< DL	< DL	< DL	< DL	329	29	< DL	< DL	236	< DL	< DL	< DL	< DL
D	+2	16jan48	He + H	Spot	++	Upper	187	2325	21529	< DL		< DL	62	1202	10	< DL	52	26	< DL	3	232	< DL	< DL	< DL	< DL
D	+2	16jan49	He + H	Spot	++	Upper	245	2965	22111	< DL		< DL	< DL	< DL	< DL	611	644	219	< DL	12	252	< DL	11	< DL	7
D	+2	16jan50	He + H	Spot	o	Upper	1582	11745	22111	< DL		< DL	< DL	< DL	< DL	< DL	< DL	< DL	< DL	< DL	386	< DL	< DL	< DL	< DL
D	+2	16jan51	He + H	Spot	o	Upper	271	1571	16976	< DL		10597	< DL	< DL	91	671	434	520	< DL	99	160	< DL	< DL	< DL	41
D	+2	16jan52	He + H	Spot	o	Lower	612	2611	13724	< DL		< DL	1170	< DL	< DL	< DL	< DL	< DL	< DL	< DL	194	< DL	< DL	< DL	< DL
D	+2	16jan26	He + H	Spot	++	Lower	110	1828	11646	< DL		4290	101	< DL	< DL	< DL	< DL	44	< DL	< DL	180	< DL	< DL	< DL	< DL
D	+2	16jan27	He + H	Spot		Lower	109	2212	13724	< DL		< DL	70	< DL	< DL	< DL	74	43	< DL	< DL	98	< DL	2	< DL	1.2
D	+2	16jan28	He + H	Spot	++	Lower	93	1720	13724	< DL		< DL	< DL	< DL	< DL	< DL	10	30	< DL	< DL	156	< DL	0.8	< DL	< DL
D	+2	16jan29	He + H	Spot	+	Lower	118	2383	12492	< DL		2544	< DL	< DL	< DL	< DL	11	51	< DL	< DL	82	< DL	< DL	< DL	< DL
D	+2	16jan31	He + H	Spot	+	Lower	77	1695	12043	< DL		3470	< DL	< DL	< DL	< DL	174	< DL	< DL	27	< DL	< DL	< DL	< DL	< DL
D	+2	16jan32	He + H	Spot	+	Lower	57	1585	13724	< DL		< DL	< DL	< DL	< DL	< DL	228	42	< DL	< DL	54	< DL	< DL	< DL	< DL
D	+2	16jan33	He + H	Spot	++	Lower	139	1701	13724	< DL		< DL	< DL	< DL	< DL	< DL	347	28	< DL	< DL	129	< DL	7	< DL	1.3
D	+2	16jan34	He + H	Spot	+	Lower	154	1869	11498	< DL		4594	266	< DL	< DL	< DL	< DL	437	< DL	< DL	155	< DL	< DL	< DL	< DL
D	+2	16jan36	He + H	Spot	++	Lower	56	1433	13016	< DL		< DL	161	1462	18	< DL	135	58	< DL	11	123	< DL	3	< DL	< DL

Chip	Zone	Sample Filename	Carrier gas	Anal ysis	Qual ity	Limit	Li	B	Na	Mg	K	Ca	Mn	Fe	Zn	Cu	As	Rb	Sn	Sb	Cs	Ba	W	Au	Pb
D	+2	16jan37	He + H	Spot	+	Lower	104	1915	13724	< DL		< DL	< DL	< DL	< DL	< DL	170	29	< DL	< DL	172	< DL	< DL	< DL	< DL
D	+2	16jan38	He + H	Spot	++	Lower	93	2055	13724	< DL		< DL	27	< DL	< DL	< DL	50	31	< DL	< DL	186	< DL	0.5	< DL	< DL
D	+2	16jan39	He + H	Spot	++	Lower	43	1681	13339	< DL		< DL	65	795	9	< DL	75	24	< DL	2.0	155	< DL	0.8	< DL	< DL
D	+2	16jan41	He + H	Spot	o	Lower	129	1096	8672	< DL		10426	< DL	< DL	< DL	209	205	79	< DL	< DL	63	< DL	11	< DL	< DL
D	+2	16jan42	He + H	Spot	+	Lower	109	1634	13724	< DL		< DL	1350	< DL	< DL	< DL	217	46	< DL	< DL	72	< DL	< DL	< DL	< DL
D	+2	16jan43	He + H	Spot	++	Lower	56	1632	13192	< DL		< DL	74	1098	14	< DL	154	28	< DL	3	151	< DL	< DL	< DL	< DL
D	+2	16jan44	He + H	Spot	++	Lower	111	1671	13724	< DL		< DL	< DL	< DL	< DL	< DL	68	10	< DL	< DL	141	< DL	1.0	< DL	< DL
D	+2	16jan46	He + H	Spot	-	Lower	100	1665	12697	< DL		2120	< DL	< DL	< DL	< DL	129	22	< DL	< DL	164	< DL	< DL	< DL	< DL
D	+2	16jan47	He + H	Spot	+	Lower	169	1527	10350	< DL		6964	< DL	< DL	< DL	< DL	204	18	< DL	< DL	147	< DL	< DL	< DL	< DL
D	+2	16jan48	He + H	Spot	++	Lower	116	1443	13363	< DL		< DL	38	746	6	< DL	32	16	< DL	1.8	144	< DL	< DL	< DL	< DL
D	+2	16jan49	He + H	Spot	++	Lower	152	1840	13724	< DL		< DL	< DL	< DL	< DL	379	400	136	< DL	7	157	< DL	7	< DL	4
D	+2	16jan50	He + H	Spot	o-	Lower	982	7290	13724	< DL		< DL	< DL	< DL	< DL	< DL	< DL	< DL	< DL	< DL	240	< DL	< DL	< DL	< DL
D	+2	16jan51	He + H	Spot	o	Lower	168	975	10537	< DL		6578	< DL	< DL	56	416	270	323	< DL	61	99	< DL	< DL	< DL	26
D	+1	16jan03	He + H	Spot	+	Upper	269	1752	16507	< DL		11566	< DL	< DL	49	< DL	< DL	54	< DL	< DL	208	22	< DL	< DL	< DL
D	+1	16jan04	He + H	Spot	o+	Upper	231	2182	20410	< DL		3512	< DL	< DL	20	< DL	12	6	< DL	< DL	147	< DL	< DL	< DL	< DL
D	+1	16jan05	He + H	Spot	++	Upper	213	1102	14675	< DL		13328	100	2019	90	< DL	13	78	< DL	15	316	12	8	2	3
D	+1	16jan06	He + H	Spot	+	Upper	213	1345	17605	< DL		7693	< DL	1607	49	< DL	< DL	62	< DL	< DL	232	< DL	3	< DL	3
D	+1	16jan09	He + H	Spot	o	Upper	174	740	22111	< DL		< DL	< DL	< DL	< DL	< DL	< DL	< DL	< DL	< DL	49	< DL	< DL	< DL	< DL
D	+1	16jan10	He + H	Spot	-	Upper	120	< DL	291	< DL		41348	63	3684	158	9	< DL	< DL	< DL	< DL	1	21	1.3	3	5
D	+1	16jan11	He + H	Spot	-	Upper	90	< DL	421	< DL		40441	103	4323	236	32	< DL	< DL	< DL	< DL	1.3	21	1.9	4	6
D	+1	16jan12	He + H	Spot	o+	Upper	340	1573	17730	< DL		9041	< DL	< DL	< DL	< DL	< DL	54	< DL	< DL	221	< DL	< DL	< DL	< DL
D	+1	16jan14	He + H	Spot	+	Upper	212	1238	13875	< DL		16998	< DL	< DL	< DL	< DL	< DL	54	< DL	< DL	219	17	< DL	< DL	< DL
D	+1	16jan15	He + H	Spot	+	Upper	156	804	19505	< DL		5379	< DL	< DL	< DL	< DL	< DL	84	< DL	< DL	226	< DL	< DL	< DL	< DL
D	+1	16jan16	He + H	Spot	+	Upper	197	5424	22111	< DL		< DL	< DL	< DL	< DL	< DL	< DL	83	< DL	< DL	303	< DL	< DL	< DL	< DL
D	+1	16jan17	He + H	Spot	o+	Upper	385	2324	22111	< DL		< DL	< DL	< DL	< DL	< DL	< DL	136	< DL	< DL	457	< DL	< DL	< DL	< DL
D	+1	16jan19	He + H	Spot	-	Upper	157	< DL	53	< DL		44038	< DL	1486	271	< DL	< DL	< DL	< DL	< DL	11	1.3	2	4	
D	+1	16jan20	He + H	Spot	+	Upper	196	5379	18683	< DL		7075	< DL	< DL	< DL	< DL	< DL	64	< DL	30	295	< DL	12	< DL	< DL
D	+1	16jan21	He + H	Spot	+	Upper	158	1580	15192	< DL		14279	152	< DL	< DL	< DL	< DL	58	< DL	< DL	228	< DL	< DL	< DL	< DL
D	+1	16jan22	He + H	Spot	+	Upper	144	3076	22111	< DL		< DL	< DL	< DL	< DL	< DL	< DL	71	< DL	< DL	321	< DL	< DL	< DL	< DL
D	+1	16jan23	He + H	Spot	o+	Upper	155	886	6895	< DL		28926	< DL	2477	47	< DL	< DL	9	< DL	< DL	67	10	< DL	2	1.7
D	+1	16jan03	He + H	Spot	+	Lower	167	1087	10246	< DL		7179	< DL	< DL	31	< DL	< DL	34	< DL	< DL	129	14	< DL	< DL	< DL
D	+1	16jan04	He + H	Spot	o+	Lower	143	1354	12668	< DL		2180	< DL	< DL	12	< DL	7	4	< DL	< DL	91	< DL	< DL	< DL	< DL
D	+1	16jan05	He + H	Spot	++	Lower	132	684	9109	< DL		8273	62	1253	56	< DL	8	48	< DL	< DL	196	7	5	1.5	2
D	+1	16jan06	He + H	Spot	+	Lower	132	835	10927	< DL		4775	< DL	998	30	< DL	< DL	39	< DL	< DL	144	< DL	1.9	< DL	1.6
D	+1	16jan09	He + H	Spot	o	Lower	108	460	13724	< DL		< DL	< DL	< DL	< DL	< DL	< DL	< DL	< DL	< DL	30	< DL	< DL	< DL	< DL
D	+1	16jan10	He + H	Spot	-	Lower	75	< DL	181	< DL		25664	39	2287	98	5	< DL	< DL	< DL	< DL	0.6	13	0.8	1.8	3
D	+1	16jan11	He + H	Spot	-	Lower	56	< DL	261	< DL		25101	64	2683	146	20	< DL	< DL	< DL	< DL	0.8	13	1.2	2	4
D	+1	16jan12	He + H	Spot	o+	Lower	211	976	11005	< DL		5612	< DL	< DL	< DL	< DL	< DL	34	< DL	< DL	137	< DL	< DL	< DL	< DL
D	+1	16jan14	He + H	Spot	+	Lower	131	768	8612	< DL		10550	< DL	< DL	< DL	< DL	< DL	33	< DL	< DL	136	10	< DL	< DL	< DL
D	+1	16jan15	He + H	Spot	+	Lower	97	499	12107	< DL		3339	< DL	< DL	< DL	< DL	< DL	52	< DL	< DL	140	< DL	< DL	< DL	< DL
D	+1	16jan16	He + H	Spot	+	Lower	123	3367	13724	< DL		< DL	< DL	< DL	< DL	< DL	< DL	52	< DL	< DL	188	< DL	< DL	< DL	< DL
D	+1	16jan17	He + H	Spot	o+	Lower	239	1443	13724	< DL		< DL	< DL	< DL	< DL	< DL	< DL	84	< DL	< DL	283	< DL	< DL	< DL	< DL
D	+1	16jan19	He + H	Spot	-	Lower	98	< DL	33	< DL		27334	< DL	923	168	< DL	< DL	< DL	< DL	< DL	7	0.8	1.3	3	
D	+1	16jan20	He + H	Spot	+	Lower	122	3339	11597	< DL		4391	< DL	< DL	< DL	< DL	< DL	40	< DL	19	183	< DL	8	< DL	< DL
D	+1	16jan21	He + H	Spot	+	Lower	98	981	9430	< DL		8863	94	< DL	< DL	< DL	< DL	36	< DL	< DL	142	< DL	< DL	< DL	< DL
D	+1	16jan22	He + H	Spot	+	Lower	89	1909	13724	< DL		< DL	< DL	< DL	< DL	< DL	< DL	44	< DL	< DL	199	< DL	< DL	< DL	< DL
D	+1	16jan23	He + H	Spot	o+	Lower	97	550	4280	< DL		17954	< DL	1537	29	< DL	< DL	5	< DL	< DL	41	6	< DL	1.4	1.0
D	+1	ChipD_He_on ly_021	He only	Spot	o+	Upper	310	1887	22437	< DL	967	< DL	< DL	< DL	< DL	< DL	< DL	42	< DL	13	295	< DL	4	< DL	3

Chip	Zone	Sample Filename	Carrier gas	Analysis	Quality	Limit	Li	B	Na	Mg	K	Ca	Mn	Fe	Zn	Cu	As	Rb	Sn	Sb	Cs	Ba	W	Au	Pb
D	+1	ChipD_He_only_003	He only	Spot	o	Upper	161	61	11318	1418	7297	11647	51	2970	2447	422	15	6	29	7	< DL	161	38	19	147
D	+1	ChipD_He_only_004	He only	Spot	+o	Upper	176	94	9473	1071	6375	13958	157	5659	3067	247	20	7	26	5	< DL	63	11	< DL	354
D	+1	ChipD_He_only_005	He only	Spot	-	Upper	< DL	628	7667	< DL	27305	9014	124	< DL	224	< DL	< DL	1091	< DL	< DL	154	< DL	< DL	< DL	4
D	+1	ChipD_He_only_006	He only	Spot	-	Upper	< DL	1344	16331	< DL	1201	< DL	538	< DL	< DL	< DL	< DL	< DL	< DL	< DL	144	< DL	< DL	< DL	< DL
D	+1	ChipD_He_only_007	He only	Spot	-	Upper	< DL	770	18168	< DL	458	8221	< DL	< DL	< DL	< DL	< DL	9	< DL	< DL	165	< DL	< DL	< DL	< DL
D	+1	ChipD_He_only_009	He only	Spot	+o	Upper	133	1016	17497	< DL	1525	8280	224	531	118	< DL	9	47	< DL	8	174	7	3	< DL	3
D	+1	ChipD_He_only_010	He only	Spot	+	Upper	118	1485	18313	< DL	4162	5098	111	< DL	< DL	< DL	9	101	< DL	9	200	< DL	4	< DL	< DL
D	+1	ChipD_He_only_011	He only	Spot	o	Upper	163	81	7763	1793	6874	16665	290	4520	1685	492	< DL	4	331	12	< DL	274	9	< DL	310
D	+1	ChipD_He_only_012	He only	Spot	+	Upper	179	1804	20376	< DL	2332	2579	63	342	42	< DL	9	64	< DL	8	236	3	4	< DL	2
D	+1	ChipD_He_only_013	He only	Spot	o	Upper	294	1651	21145	< DL	1389	< DL	77	< DL	23	< DL	57	55	< DL	11	260	< DL	5	< DL	3
D	+1	ChipD_He_only_015	He only	Spot	o	Upper	< DL	96	12463	1234	5577	7077	253	7745	1001	134	19	9	48	< DL	< DL	44	12	< DL	109
D	+1	ChipD_He_only_017	He only	Spot	+	Upper	135	2266	21412	< DL	1468	< DL	117	< DL	< DL	< DL	< DL	86	< DL	14	338	< DL	5	< DL	< DL
D	+1	ChipD_He_only_018	He only	Spot	+o	Upper	162	1973	22387	< DL	1099	< DL	< DL	< DL	< DL	< DL	9	51	< DL	24	242	< DL	5	< DL	< DL
D	+1	ChipD_He_only_019	He only	Spot	o	Upper	131	1858	22335	< DL	1286	< DL	< DL	< DL	< DL	< DL	< DL	51	< DL	9	236	< DL	< DL	< DL	< DL
D	+1	ChipD_He_only_020	He only	Spot	+	Upper	374	1824	22440	< DL	859	< DL	< DL	< DL	< DL	< DL	10	48	< DL	15	227	< DL	4	< DL	< DL
D	+1	ChipD_He_only_021	He only	Spot	+o	Lower	193	1171	13927	< DL	600	< DL	< DL	< DL	< DL	< DL	< DL	26	< DL	8	183	< DL	3	< DL	1.7
D	+1	ChipD_He_only_003	He only	Spot	o	Lower	100	38	7025	880	4529	7229	32	1843	1519	262	9	4	18	4	< DL	100	24	12	91
D	+1	ChipD_He_only_004	He only	Spot	+o	Lower	109	58	5880	665	3957	8663	98	3512	1904	153	12	4	16	3	< DL	39	7	< DL	220
D	+1	ChipD_He_only_005	He only	Spot	-	Lower	< DL	390	4759	< DL	16948	5595	77	< DL	139	< DL	< DL	677	< DL	< DL	96	< DL	< DL	< DL	2
D	+1	ChipD_He_only_006	He only	Spot	-	Lower	< DL	834	10137	< DL	746	< DL	334	< DL	< DL	< DL	< DL	< DL	< DL	< DL	89	< DL	< DL	< DL	< DL
D	+1	ChipD_He_only_007	He only	Spot	-	Lower	< DL	478	11276	< DL	284	5103	< DL	< DL	< DL	< DL	< DL	5	< DL	< DL	102	< DL	< DL	< DL	< DL
D	+1	ChipD_He_only_009	He only	Spot	+o	Lower	82	631	10860	< DL	947	5139	139	329	73	< DL	5	29	< DL	5	108	4	1.6	< DL	1.6
D	+1	ChipD_He_only_010	He only	Spot	+	Lower	73	922	11367	< DL	2583	3164	69	< DL	< DL	< DL	6	62	< DL	5	124	< DL	2	< DL	< DL
D	+1	ChipD_He_only_011	He only	Spot	o	Lower	101	50	4818	1113	4267	10344	180	2806	1046	306	< DL	2	205	7	< DL	170	6	< DL	192
D	+1	ChipD_He_only_012	He only	Spot	+	Lower	111	1120	12647	< DL	1448	1601	39	212	26	< DL	5	40	< DL	5	146	2	2	< DL	1.3
D	+1	ChipD_He_only_013	He only	Spot	o	Lower	182	1025	13124	< DL	862	< DL	48	< DL	15	< DL	35	34	< DL	7	161	< DL	3	< DL	1.9
D	+1	ChipD_He_only_015	He only	Spot	o	Lower	< DL	60	7736	766	3462	4393	157	4807	621	83	12	5	30	< DL	< DL	27	8	< DL	68
D	+1	ChipD_He_only_017	He only	Spot	+	Lower	84	1406	13290	< DL	911	< DL	73	< DL	< DL	< DL	< DL	53	< DL	8	210	< DL	3	< DL	< DL
D	+1	ChipD_He_only_018	He only	Spot	+o	Lower	100	1224	13895	< DL	682	< DL	< DL	< DL	< DL	< DL	5	31	< DL	15	150	< DL	3	< DL	< DL
D	+1	ChipD_He_only_019	He only	Spot	o	Lower	81	1154	13863	< DL	798	< DL	< DL	< DL	< DL	< DL	< DL	32	< DL	6	147	< DL	< DL	< DL	< DL

Chip	Zone	Sample Filename	Carrier gas	Analysis	Quality	Limit	Li	B	Na	Mg	K	Ca	Mn	Fe	Zn	Cu	As	Rb	Sn	Sb	Cs	Ba	W	Au	Pb
D	+1	ChipD_He_only_020	He only	Spot	+	Lower	232	1132	13928	< DL	533	< DL	< DL	< DL	< DL	< DL	6	30	< DL	9	141	< DL	3	< DL	< DL
D	+1	ChipD_He_only_B_014	He only	Spiral	+	Upper	81	2172	21884	< DL	2487	< DL	< DL	< DL	< DL	< DL	12	93	< DL	10	348	1	5	< DL	< DL
D	+1	ChipD_He_only_B_004	He only	Spiral	+	Upper	< DL	1949	22134	< DL	1820	< DL	< DL	< DL	153	10	18	103	< DL	20	339	< DL	6	< DL	25
D	+1	ChipD_He_only_B_005	He only	Spiral	+o	Upper	< DL	2335	22350	76	1076	< DL	< DL	< DL	119	21	16	25	< DL	15	326	2	0.7	< DL	15
D	+1	ChipD_He_only_B_006	He only	Spiral	+	Upper	< DL	1521	22364	< DL	1208	< DL	< DL	< DL	222	21	14	61	< DL	13	271	< DL	4	< DL	49
D	+1	ChipD_He_only_B_007	He only	Spiral	+	Upper	< DL	2039	22177	< DL	1704	< DL	< DL	< DL	31	4	10	66	< DL	12	298	< DL	5	< DL	9
D	+1	ChipD_He_only_B_010	He only	Spiral	+	Upper	31	2046	22178	< DL	1705	< DL	< DL	< DL	10	< DL	11	69	< DL	5	333	< DL	1.8	< DL	2
D	+1	ChipD_He_only_B_011	He only	Spiral	+	Upper	< DL	2737	21591	< DL	2118	793	< DL	< DL	62	< DL	13	97	< DL	22	444	1	7	< DL	3
D	+1	ChipD_He_only_B_012	He only	Spiral	+	Upper	181	1679	22296	< DL	1390	< DL	< DL	< DL	< DL	< DL	7	55	< DL	7	259	< DL	3	< DL	< DL
D	+1	ChipD_He_only_B_013	He only	Spiral	+	Upper	232	1953	22272	< DL	1454	< DL	< DL	< DL	< DL	< DL	7	77	< DL	< DL	313	< DL	3	< DL	< DL
D	+1	ChipD_He_only_B_014	He only	Spiral	+	Lower	51	1348	13583	< DL	1544	< DL	< DL	< DL	< DL	< DL	7	58	< DL	6	216	1	3	< DL	< DL
D	+1	ChipD_He_only_B_004	He only	Spiral	+	Lower	< DL	1209	13739	< DL	1130	< DL	< DL	< DL	95	6	11	64	< DL	13	210	< DL	4	< DL	15
D	+1	ChipD_He_only_B_005	He only	Spiral	+o	Lower	< DL	1449	13872	47	668	< DL	< DL	< DL	74	13	10	16	< DL	9	202	1	0.4	< DL	9
D	+1	ChipD_He_only_B_006	He only	Spiral	+	Lower	< DL	944	13881	< DL	750	< DL	< DL	< DL	138	13	9	38	< DL	8	168	< DL	3	< DL	30
D	+1	ChipD_He_only_B_007	He only	Spiral	+	Lower	< DL	1266	13765	< DL	1058	< DL	< DL	< DL	19	2	6	41	< DL	7	185	< DL	3	< DL	6
D	+1	ChipD_He_only_B_010	He only	Spiral	+	Lower	19	1270	13765	< DL	1058	< DL	< DL	< DL	6	< DL	7	43	< DL	3	207	< DL	1.1	< DL	1.3
D	+1	ChipD_He_only_B_011	He only	Spiral	+	Lower	< DL	1699	13401	< DL	1314	492	< DL	< DL	39	< DL	8	60	< DL	14	276	1	4	< DL	2
D	+1	ChipD_He_only_B_012	He only	Spiral	+	Lower	112	1042	13839	< DL	863	< DL	< DL	< DL	< DL	< DL	4	34	< DL	5	161	< DL	1.6	< DL	< DL
D	+1	ChipD_He_only_B_013	He only	Spiral	+	Lower	144	1212	13824	< DL	902	< DL	< DL	< DL	< DL	< DL	4	48	< DL	< DL	194	< DL	1.9	< DL	< DL
E	-1	Panasqueira_ChipE_22	He + H	Spiral	+	Upper	< DL	1248	12459	< DL	< DL	19017	< DL	< DL	< DL	111	255	53	< DL	< DL	149	< DL	1.3	< DL	4
E	-1	Panasqueira_ChipE_03	He + H	Spot	+	Upper	226	1932	21906	< DL	< DL	1039	38	< DL	1879	< DL	31	31	< DL	50	227	< DL	< DL	< DL	< DL
E	-1	Panasqueira_ChipE_04	He + H	Spiral	-	Upper	333	1796	21563	234	2025	< DL	70	703	< DL	< DL	26	65	12	78	170	< DL	1.6	< DL	< DL
E	-1	Panasqueira_ChipE_05	He + H	Spiral	+	Upper	262	3139	19006	< DL	2446	4894	22	510	76	49	109	43	4	17	343	2	0.2	< DL	1.6
E	-1	Panasqueira_ChipE_06	He + H	Spiral	-	Upper	< DL	1607	18946	< DL	3383	4224	37	675	< DL	< DL	7	35	6	31	161	< DL	1.1	< DL	1.1
E	-1	Panasqueira_ChipE_07	He + H	Spiral	-	Upper	< DL	1825	22636	< DL	329	< DL	8	< DL	< DL	< DL	15	58	< DL	25	226	< DL	1.5	< DL	0.6
E	-1	Panasqueira_ChipE_09	He + H	Spiral	+	Upper	< DL	3543	21093	< DL	1110	2252	18	< DL	< DL	16	147	57	< DL	< DL	351	< DL	0.2	< DL	< DL
E	-1	Panasqueira_ChipE_10	He + H	Spot	+	Upper	181	5237	22230	< DL	1565	< DL	< DL	< DL	< DL	< DL	268	29	< DL	< DL	376	< DL	9	< DL	< DL
E	-1	Panasqueira_ChipE_11	He + H	Spot	++	Upper	177	3485	22658	< DL	424	< DL	27	< DL	52	427	337	88	< DL	68	279	< DL	0.5	< DL	16
E	-1	Panasqueira_ChipE_12	He + H	Spot	+	Upper	158	3455	22257	< DL	1183	< DL	< DL	< DL	< DL	< DL	168	44	< DL	< DL	254	< DL	3	< DL	< DL
E	-1	Panasqueira_ChipE_13	He + H	Spiral	-	Upper	441	1585	21247	386	3393	< DL	< DL	< DL	< DL	< DL	17	199	< DL	39	196	< DL	< DL	< DL	< DL

Chip	Zone	Sample Filename	Carrier gas	Analysis	Quality	Limit	Li	B	Na	Mg	K	Ca	Mn	Fe	Zn	Cu	As	Rb	Sr	Sb	Cs	Ba	W	Au	Pb
E	-1	Panasqueira_ChipE_15	He + H	Spot	+	Upper	122	4470	22729	< DL	231	< DL	< DL	< DL	< DL	< DL	188	186	< DL	< DL	382	< DL	67	< DL	< DL
E	-1	Panasqueira_ChipE_16	He + H	Spot	+	Upper	200	3604	22778	< DL	< DL	< DL	< DL	< DL	15	72	191	55	< DL	10	362	< DL	2	< DL	< DL
E	-1	Panasqueira_ChipE_17	He + H	Spiral	++	Upper	< DL	2873	20413	< DL	< DL	4412	< DL	< DL	42	46	116	46	< DL	< DL	296	< DL	0.1	< DL	0.7
E	-1	Panasqueira_ChipE_18	He + H	Spiral	+	Upper	167	3242	22506	404	< DL	< DL	22	< DL	< DL	< DL	156	32	< DL	9	385	< DL	< DL	< DL	< DL
E	-1	Panasqueira_ChipE_19	He + H	Spiral	-	Upper	< DL	1518	19515	624	< DL	5179	< DL	< DL	< DL	84	136	22	< DL	< DL	130	< DL	< DL	< DL	< DL
E	-1	Panasqueira_ChipE_20	He + H	Spot	+	Upper	202	3670	22817	< DL	< DL	< DL	< DL	< DL	< DL	< DL	454	34	< DL	< DL	367	< DL	2	< DL	< DL
E	-1	Panasqueira_ChipE_22	He + H	Spiral	+	Lower	< DL	775	7733	< DL	< DL	11804	< DL	< DL	< DL	69	158	33	< DL	< DL	92	< DL	0.8	< DL	3
E	-1	Panasqueira_ChipE_03	He + H	Spot	+	Lower	140	1199	13597	< DL	< DL	645	24	< DL	1166	< DL	19	20	< DL	31	141	< DL	< DL	< DL	< DL
E	-1	Panasqueira_ChipE_04	He + H	Spiral	-	Lower	207	1115	13384	145	1257	< DL	43	436	< DL	< DL	16	40	7	49	105	< DL	1.0	< DL	< DL
E	-1	Panasqueira_ChipE_05	He + H	Spiral	+	Lower	163	1948	11797	< DL	1518	3037	13	317	47	31	68	27	2	11	213	1.0	0.1	< DL	1.0
E	-1	Panasqueira_ChipE_06	He + H	Spiral	-	Lower	< DL	998	11760	< DL	2100	2622	23	419	< DL	< DL	4	22	4	19	100	< DL	0.7	< DL	0.7
E	-1	Panasqueira_ChipE_07	He + H	Spiral	-	Lower	< DL	1133	14050	< DL	204	< DL	5	< DL	< DL	< DL	9	36	< DL	15	140	< DL	0.9	< DL	0.4
E	-1	Panasqueira_ChipE_09	He + H	Spiral	+	Lower	< DL	2199	13092	< DL	689	1398	11	< DL	< DL	10	91	35	< DL	< DL	218	< DL	0.1	< DL	< DL
E	-1	Panasqueira_ChipE_10	He + H	Spot	+	Lower	113	3251	13798	< DL	972	< DL	< DL	< DL	< DL	< DL	167	18	< DL	< DL	233	< DL	5	< DL	< DL
E	-1	Panasqueira_ChipE_11	He + H	Spot	++	Lower	110	2163	14064	< DL	263	< DL	17	< DL	33	265	209	54	< DL	42	173	< DL	0.3	< DL	10
E	-1	Panasqueira_ChipE_12	He + H	Spot	+	Lower	98	2145	13815	< DL	734	< DL	< DL	< DL	< DL	< DL	104	27	< DL	< DL	158	< DL	1.9	< DL	< DL
E	-1	Panasqueira_ChipE_13	He + H	Spiral	-	Lower	274	984	13188	239	2106	< DL	< DL	< DL	< DL	< DL	10	124	< DL	24	122	< DL	< DL	< DL	< DL
E	-1	Panasqueira_ChipE_15	He + H	Spot	+	Lower	76	2774	14108	< DL	143	< DL	< DL	< DL	< DL	< DL	117	115	< DL	< DL	237	< DL	42	< DL	< DL
E	-1	Panasqueira_ChipE_16	He + H	Spot	+	Lower	124	2237	14138	< DL	< DL	< DL	< DL	< DL	10	45	118	34	< DL	6	224	< DL	1.4	< DL	< DL
E	-1	Panasqueira_ChipE_17	He + H	Spiral	++	Lower	< DL	1783	12670	< DL	< DL	2738	< DL	< DL	26	29	72	29	< DL	< DL	184	< DL	0.1	< DL	0.4
E	-1	Panasqueira_ChipE_18	He + H	Spiral	+	Lower	104	2012	13969	251	< DL	< DL	13	< DL	< DL	< DL	97	20	< DL	5	239	< DL	< DL	< DL	< DL
E	-1	Panasqueira_ChipE_19	He + H	Spiral	-	Lower	< DL	942	12113	388	< DL	3215	< DL	< DL	< DL	52	84	14	< DL	< DL	81	< DL	< DL	< DL	< DL
E	-1	Panasqueira_ChipE_20	He + H	Spot	+	Lower	125	2278	14162	< DL	< DL	< DL	< DL	< DL	< DL	< DL	282	21	< DL	< DL	228	< DL	1.0	< DL	< DL
E	-1	Panasqueira_ChipE_II_03	He + H	Spot	-	Upper	358	1768	22817	< DL	< DL	< DL	< DL	< DL	126	< DL	42	78	< DL	< DL	57	< DL	< DL	< DL	< DL
E	-1	Panasqueira_ChipE_II_04	He + H	Spiral	++	Upper	279	2234	22817	194	< DL	< DL	15	< DL	< DL	< DL	21	31	< DL	< DL	209	< DL	3	< DL	< DL
E	-1	Panasqueira_ChipE_II_05	He + H	Spiral	++	Upper	416	3506	22352	< DL	< DL	804	29	59	30	8	449	75	1.0	7	368	< DL	3	< DL	0.5
E	-1	Panasqueira_ChipE_II_06	He + H	Spot	+	Upper	276	3133	22778	< DL	< DL	< DL	< DL	< DL	< DL	< DL	412	73	< DL	< DL	223	< DL	< DL	< DL	< DL
E	-1	Panasqueira_ChipE_II_07	He + H	Spot	++	Upper	285	4415	22817	< DL	< DL	< DL	< DL	< DL	< DL	< DL	185	78	< DL	< DL	370	< DL	31	< DL	< DL
E	0	Panasqueira_ChipE_II_11	He + H	Spiral	+o	Upper	30	1163	22817	174	< DL	< DL	10	< DL	< DL	< DL	10	45	2	23	168	3	0.5	< DL	0.6
E	0	Panasqueira_ChipE_II_12	He + H	Spiral	+	Upper	692	2624	22782	105	93	< DL	< DL	< DL	58	1.7	78	132	1.8	4	279	< DL	5	< DL	0.4

Chip	Zone	Sample Filename	Carrier gas	Analysis	Quality	Limit	Li	B	Na	Mg	K	Ca	Mn	Fe	Zn	Cu	As	Rb	Sn	Sb	Cs	Ba	W	Au	Pb
E	0	Panasqueira_ChipE_II_13	He + H	Spiral	+	Upper	282	2971	22487	31	874	< DL	25	< DL	7	0.9	102	99	1.9	6	288	4	4	< DL	< DL
E	0	Panasqueira_ChipE_II_14	He + H	Spiral	+	Upper	< DL	1500	13150	< DL	4878	14268	< DL	< DL	7	3	51	37	< DL	< DL	173	< DL	3	< DL	< DL
E	0	Panasqueira_ChipE_II_16	He + H	Spot	+	Upper	330	3837	22738	< DL	< DL	< DL	3630	< DL	235	739	395	100	28	14	279	< DL	38	< DL	25
E	0	Panasqueira_ChipE_II_17	He + H	Spiral	+o	Upper	1011	1737	22036	121	1988	< DL	36	< DL	203	< DL	198	58	< DL	< DL	181	< DL	3	< DL	1.6
E	0	Panasqueira_ChipE_II_18	He + H	Spiral	++	Upper	43	2272	17522	< DL	3354	7141	9	332	11	1.7	80	46	< DL	5	217	2	38	< DL	0.5
E	0	Panasqueira_ChipE_II_19	He + H	Spiral	+	Upper	395	2980	22811	34	17	< DL	4	< DL	6	< DL	107	49	< DL	< DL	289	< DL	0.5	< DL	0.2
E	0	Panasqueira_ChipE_II_20	He + H	Spot	+	Upper	335	2622	22817	< DL	< DL	< DL	< DL	< DL	128	70	174	112	< DL	< DL	243	< DL	49	< DL	18
E	0	Panasqueira_ChipE_II_22	He + H	Spiral	+	Upper	88	2112	22081	69	1931	< DL	45	27	11	10	55	132	0.9	15	245	3	7	< DL	28
E	0	Panasqueira_ChipE_II_23	He + H	Spiral	+	Upper	2297	2990	22817	447	< DL	< DL	< DL	< DL	< DL	318	314	23	< DL	< DL	359	< DL	0.7	< DL	< DL
E	0	Panasqueira_ChipE_II_26	He + H	Spiral	+	Upper	863	3117	21870	124 9	872	< DL	18	1389	242 1	194	362	80	22	< DL	313	34	23	< DL	13
E	0	Panasqueira_ChipE_II_27	He + H	Spot	++	Upper	235	2860	21723	< DL	2916	< DL	< DL	< DL	595	2643	142 1	90	257	56	304	< DL	35	< DL	59
E	0	Panasqueira_ChipE_II_28	He + H	Spiral	+	Upper	1875	3222	22817	698	< DL	< DL	< DL	< DL	10	< DL	16	56	< DL	< DL	380	< DL	0.9	< DL	< DL
E	0	Panasqueira_ChipE_II_29	He + H	Spot	+	Upper	474	3135	22298	< DL	1259	< DL	35	< DL	< DL	< DL	152	168	< DL	< DL	349	< DL	2	< DL	< DL
E	0	Panasqueira_ChipE_II_30	He + H	Spiral	+	Upper	2663	3023	22817	837	< DL	< DL	< DL	< DL	17	48	141	41	< DL	< DL	357	< DL	3	< DL	< DL
E	0	Panasqueira_ChipE_II_34	He + H	Spiral	+	Upper	379	3395	22817	377	< DL	< DL	< DL	< DL	< DL	69	333	26	< DL	< DL	382	< DL	3	< DL	0.2
E	0	Panasqueira_ChipE_II_35	He + H	Spot	+	Upper	430	2931	22428	< DL	904	< DL	< DL	< DL	12	< DL	431	22	< DL	5	283	< DL	< DL	< DL	< DL
E	0	Panasqueira_ChipE_II_36	He + H	Spiral	o	Upper	195	2680	22817	113 9	< DL	< DL	< DL	< DL	< DL	97	755	58	< DL	< DL	264	< DL	4	< DL	< DL
E	0	Panasqueira_ChipE_II_37	He + H	?	-	Upper	212	3520	21608	< DL	3152	< DL	< DL	< DL	< DL	< DL	320	97	< DL	< DL	310	< DL	15	< DL	< DL
E	-1	Panasqueira_ChipE_II_03	He + H	Spot	-	Lower	222	1097	14162	< DL	< DL	< DL	< DL	< DL	78	< DL	26	48	< DL	< DL	35	< DL	< DL	< DL	< DL
E	-1	Panasqueira_ChipE_II_04	He + H	Spiral	++	Lower	173	1387	14162	121	< DL	< DL	9	< DL	< DL	< DL	13	19	< DL	< DL	130	< DL	2	< DL	< DL
E	-1	Panasqueira_ChipE_II_05	He + H	Spiral	++	Lower	258	2176	13874	< DL	< DL	499	18	37	19	5	279	46	0.6	4	228	< DL	2	< DL	0.3
E	-1	Panasqueira_ChipE_II_06	He + H	Spot	+	Lower	171	1945	14138	< DL	< DL	< DL	< DL	< DL	< DL	< DL	256	45	< DL	< DL	138	< DL	< DL	< DL	< DL
E	-1	Panasqueira_ChipE_II_07	He + H	Spot	++	Lower	177	2740	14162	< DL	< DL	< DL	< DL	< DL	< DL	< DL	115	48	< DL	< DL	230	< DL	19	< DL	< DL
E	0	Panasqueira_ChipE_II_11	He + H	Spiral	+o	Lower	19	722	14162	108	< DL	< DL	6	< DL	< DL	< DL	6	28	1.3	14	104	1.6	0.3	< DL	0.4
E	0	Panasqueira_ChipE_II_12	He + H	Spiral	+	Lower	429	1628	14140	65	58	< DL	< DL	< DL	36	1.1	49	82	1.1	3	173	< DL	3	< DL	0.3
E	0	Panasqueira_ChipE_II_13	He + H	Spiral	+	Lower	175	1844	13957	19	543	< DL	16	< DL	4	0.6	63	61	1.2	4	179	3	2	< DL	< DL
E	0	Panasqueira_ChipE_II_14	He + H	Spiral	+	Lower	< DL	931	8162	< DL	3028	8856	< DL	< DL	4	1.6	31	23	< DL	< DL	107	< DL	1.7	< DL	< DL
E	0	Panasqueira_ChipE_II_16	He + H	Spot	+	Lower	205	2382	14113	< DL	< DL	< DL	2253	< DL	146	459	245	62	18	9	173	< DL	24	< DL	16
E	0	Panasqueira_ChipE_II_17	He + H	Spiral	+o	Lower	628	1078	13677	75	1234	< DL	23	< DL	126	< DL	123	36	< DL	< DL	112	< DL	2	< DL	1.0
E	0	Panasqueira_ChipE_II_18	He + H	Spiral	++	Lower	27	1410	10876	< DL	2082	4432	6	206	7	1.1	49	29	< DL	3	135	1.1	23	< DL	0.3

Chip	Zone	Sample Filename	Carrier gas	Anal ysis	Qual ity	Limit	Li	B	Na	Mg	K	Ca	Mn	Fe	Zn	Cu	As	Rb	Sn	Sb	Cs	Ba	W	Au	Pb
E	0	Panasqueira_ChipE_II_19	He + H	Spiral	+	Lower	245	1850	14158	21	10	< DL	2	< DL	3	< DL	66	30	< DL	< DL	180	< DL	0.3	< DL	0.1
E	0	Panasqueira_ChipE_II_20	He + H	Spot	+	Lower	208	1627	14162	< DL	< DL	< DL	< DL	< DL	79	44	108	69	< DL	< DL	151	< DL	30	< DL	11
E	0	Panasqueira_ChipE_II_22	He + H	Spiral	+	Lower	54	1311	13705	43	1199	< DL	28	17	7	6	34	82	0.6	9	152	1.8	4	< DL	17
E	0	Panasqueira_ChipE_II_23	He + H	Spiral	+	Lower	1426	1856	14162	277	< DL	< DL	< DL	< DL	< DL	197	195	14	< DL	< DL	223	< DL	0.4	< DL	< DL
E	0	Panasqueira_ChipE_II_26	He + H	Spiral	+	Lower	535	1934	13574	775	541	< DL	11	862	1503	120	224	50	13	< DL	194	21	14	< DL	8
E	0	Panasqueira_ChipE_II_27	He + H	Spot	++	Lower	146	1775	13483	< DL	1810	< DL	< DL	< DL	369	1641	882	56	160	35	189	< DL	22	< DL	37
E	0	Panasqueira_ChipE_II_28	He + H	Spiral	+	Lower	1164	2000	14162	434	< DL	< DL	< DL	< DL	6	< DL	10	35	< DL	< DL	236	< DL	0.6	< DL	< DL
E	0	Panasqueira_ChipE_II_29	He + H	Spot	+	Lower	294	1946	13840	< DL	781	< DL	22	< DL	< DL	< DL	95	104	< DL	< DL	216	< DL	1.5	< DL	< DL
E	0	Panasqueira_ChipE_II_30	He + H	Spiral	+	Lower	1653	1876	14162	519	< DL	< DL	< DL	< DL	10	30	87	25	< DL	< DL	221	< DL	2	< DL	< DL
E	0	Panasqueira_ChipE_II_34	He + H	Spiral	+	Lower	235	2107	14162	234	< DL	< DL	< DL	< DL	< DL	43	207	16	< DL	< DL	237	< DL	2	< DL	0.1
E	0	Panasqueira_ChipE_II_35	He + H	Spot	+	Lower	267	1819	13921	< DL	561	< DL	< DL	< DL	8	< DL	268	14	< DL	3	175	< DL	< DL	< DL	< DL
E	0	Panasqueira_ChipE_II_36	He + H	Spiral	o	Lower	121	1663	14162	707	< DL	< DL	< DL	< DL	< DL	60	469	36	< DL	< DL	164	< DL	2	< DL	< DL
E	0	Panasqueira_ChipE_II_37	He + H	?	-	Lower	131	2185	13412	< DL	1956	< DL	< DL	< DL	< DL	< DL	199	60	< DL	< DL	193	< DL	9	< DL	< DL
H	-2	13feb04	He only	Spot	+	Upper	< DL	3446	22445	< DL	324	< DL	207	< DL	< DL	< DL	416	82	< DL	6	311	< DL	30	< DL	< DL
H	-2	13feb05	He only	Spot	+	Upper	< DL	2476	22049	< DL	1434	< DL	180	< DL	< DL	< DL	276	74	< DL	6	215	< DL	5	< DL	5
H	-2	13feb06	He only	Spot	+	Upper	82	2598	20221	< DL	554	4289	327	< DL	< DL	< DL	346	63	< DL	6	248	< DL	3	< DL	< DL
H	-2	13feb07	He only	Spot	+o	Upper	179	3365	21969	< DL	245	1383	13	< DL	21	2	431	45	< DL	3	293	1.2	7	< DL	0.2
H	-2	13feb09	He only	Spot	+	Upper	< DL	2388	20627	< DL	894	3395	< DL	< DL	33	50	387	84	< DL	7	217	< DL	18	< DL	9
H	-2	13feb10	He only	Spot	+	Upper	93	3524	22693	< DL	313	< DL	< DL	< DL	92	< DL	531	60	< DL	10	317	< DL	13	< DL	< DL
H	-2	13feb11	He only	Spot	+	Upper	< DL	2315	19875	< DL	4671	2185	< DL	< DL	< DL	< DL	364	210	7	6	219	< DL	18	< DL	21
H	-2	13feb12	He only	Spot	++	Upper	254	4060	22251	< DL	174	< DL	< DL	< DL	< DL	< DL	556	50	< DL	4	306	< DL	< DL	< DL	< DL
H	-2	13feb14	He only	Spot	+	Upper	263	4079	22682	< DL	344	< DL	< DL	< DL	< DL	< DL	640	61	< DL	11	358	< DL	< DL	< DL	< DL
H	-2	13feb15	He only	Spot	+	Upper	164	4120	22725	< DL	246	< DL	< DL	< DL	< DL	7	599	38	< DL	18	323	< DL	4	< DL	< DL
H	-3	13feb16	He only	Spot	+	Upper	220	4358	22726	< DL	242	< DL	< DL	< DL	< DL	< DL	682	66	< DL	7	341	< DL	< DL	< DL	< DL
H	-3	13feb17	He only	Spot	+o	Upper	< DL	2769	22618	< DL	507	< DL	< DL	< DL	< DL	< DL	294	63	< DL	< DL	199	< DL	< DL	< DL	< DL
H	-3	13feb19	He only	Spot	+	Upper	256	3921	22726	< DL	232	< DL	< DL	< DL	< DL	< DL	541	87	< DL	8	331	< DL	< DL	< DL	< DL
H	-3	13feb20	He only	Spot	+	Upper	305	2975	22600	< DL	290	< DL	< DL	< DL	< DL	< DL	464	37	< DL	< DL	261	< DL	< DL	< DL	< DL
H	-3	13feb21	He only	Spot	+	Upper	236	3778	22730	< DL	232	< DL	< DL	< DL	< DL	< DL	560	56	< DL	10	319	< DL	< DL	< DL	< DL
H	-3	13feb22	He only	Spot	+	Upper	274	3606	22747	< DL	186	< DL	< DL	< DL	< DL	< DL	412	43	< DL	< DL	298	< DL	< DL	< DL	< DL
H	-3	13feb24	He only	Spot	+	Upper	< DL	3389	22273	< DL	1442	< DL	< DL	< DL	23	3	555	241	< DL	10	316	2	13	< DL	9
H	-3	13feb25	He only	Spot	++	Upper	259	3817	22717	< DL	267	< DL	< DL	< DL	< DL	12	592	32	< DL	10	307	< DL	1.7	< DL	< DL
H	-3	13feb26	He only	Spot	+	Upper	205	3975	22575	< DL	275	< DL	< DL	< DL	< DL	< DL	561	35	< DL	16	308	< DL	< DL	< DL	< DL
H	-3	13feb27	He only	Spot	+	Upper	516	4062	22660	< DL	371	< DL	< DL	< DL	< DL	< DL	598	57	< DL	< DL	229	< DL	< DL	< DL	1.7
H	-3	13feb29	He only	Spot	+o	Upper	68	3163	22694	< DL	281	< DL	< DL	< DL	< DL	13	468	52	< DL	9	244	< DL	1.8	< DL	< DL
H	-3	13feb30	He only	Spot	+	Upper	159	3300	22705	< DL	258	< DL	< DL	< DL	22	8	526	51	< DL	13	360	< DL	7	< DL	< DL
H	-3	13feb31	He only	Spot	+	Upper	203	4682	22529	< DL	339	< DL	67	< DL	< DL	< DL	618	58	< DL	5	283	< DL	5	< DL	< DL
H	-3	13feb32	He only	Spot	+	Upper	314	3642	22760	< DL	137	< DL	< DL	< DL	< DL	< DL	512	72	< DL	< DL	295	< DL	1.7	< DL	< DL
H	-3	13feb34	He only	Spot	-	Upper	160	1554	21206	< DL	3929	< DL	179	< DL	175	63	301	83	1428	13	114	< DL	304	< DL	17
H	-3	13feb35	He only	Spot	-	Upper	325	3994	22521	< DL	246	< DL	< DL	< DL	< DL	< DL	596	45	< DL	< DL	284	< DL	20	< DL	< DL
H	-3	13feb36	He only	Spot	+	Upper	304	3858	22630	< DL	499	< DL	< DL	< DL	< DL	< DL	615	67	< DL	5	349	< DL	12	< DL	< DL

Chip	Zone	Sample Filename	Carrier gas	Anal ysis	Qual ity	Limit	Li	B	Na	Mg	K	Ca	Mn	Fe	Zn	Cu	As	Rb	Sn	Sb	Cs	Ba	W	Au	Pb
H	-3	13feb37	He only	Spot	+	Upper	< DL	3988	22751	< DL	176	< DL	< DL	< DL	< DL	< DL	583	56	< DL	11	339	< DL	7	< DL	< DL
H	-2	13feb04	He only	Spot	+	Lower	< DL	2139	13931	< DL	201	< DL	129	< DL	< DL	< DL	258	51	< DL	4	193	< DL	18	< DL	< DL
H	-2	13feb05	He only	Spot	+	Lower	< DL	1537	13685	< DL	890	< DL	112	< DL	< DL	< DL	171	46	< DL	4	133	< DL	3	< DL	3
H	-2	13feb06	He only	Spot	+	Lower	51	1612	12551	< DL	344	2662	203	< DL	< DL	< DL	215	39	< DL	4	154	< DL	1.9	< DL	< DL
H	-2	13feb07	He only	Spot	+o	Lower	111	2088	13636	< DL	152	858	8	< DL	13	1.4	267	28	< DL	1.7	182	0.8	4	< DL	0.1
H	-2	13feb09	He only	Spot	+	Lower	< DL	1482	12803	< DL	555	2107	< DL	< DL	20	31	240	52	< DL	4	135	< DL	11	< DL	6
H	-2	13feb10	He only	Spot	+	Lower	58	2187	14085	< DL	194	< DL	< DL	< DL	57	< DL	330	37	< DL	6	196	< DL	8	< DL	< DL
H	-2	13feb11	He only	Spot	+	Lower	< DL	1437	12336	< DL	2899	1356	< DL	< DL	< DL	< DL	226	130	5	4	136	< DL	11	< DL	13
H	-2	13feb12	He only	Spot	++	Lower	157	2520	13811	< DL	108	< DL	< DL	< DL	< DL	< DL	345	31	< DL	3	190	< DL	< DL	< DL	< DL
H	-2	13feb14	He only	Spot	+	Lower	163	2532	14079	< DL	213	< DL	< DL	< DL	< DL	< DL	398	38	< DL	7	222	< DL	< DL	< DL	< DL
H	-2	13feb15	He only	Spot	+	Lower	102	2557	14105	< DL	153	< DL	< DL	< DL	< DL	4	372	24	< DL	11	201	< DL	3	< DL	< DL
H	-3	13feb16	He only	Spot	+	Lower	136	2705	14106	< DL	150	< DL	< DL	< DL	< DL	< DL	423	41	< DL	5	212	< DL	< DL	< DL	< DL
H	-3	13feb17	He only	Spot	+o	Lower	< DL	1718	14039	< DL	314	< DL	< DL	< DL	< DL	< DL	182	39	< DL	< DL	123	< DL	< DL	< DL	< DL
H	-3	13feb19	He only	Spot	+	Lower	159	2434	14106	< DL	144	< DL	< DL	< DL	< DL	< DL	336	54	< DL	5	206	< DL	< DL	< DL	< DL
H	-3	13feb20	He only	Spot	+	Lower	189	1847	14027	< DL	180	< DL	< DL	< DL	< DL	< DL	288	23	< DL	< DL	162	< DL	< DL	< DL	< DL
H	-3	13feb21	He only	Spot	+	Lower	147	2345	14108	< DL	144	< DL	< DL	< DL	< DL	< DL	348	35	< DL	6	198	< DL	< DL	< DL	< DL
H	-3	13feb22	He only	Spot	+	Lower	170	2238	14119	< DL	115	< DL	< DL	< DL	< DL	< DL	256	27	< DL	< DL	185	< DL	< DL	< DL	< DL
H	-3	13feb24	He only	Spot	+	Lower	< DL	2104	13825	< DL	895	< DL	< DL	< DL	14	1.9	345	150	< DL	6	196	1.3	8	< DL	6
H	-3	13feb25	He only	Spot	++	Lower	161	2369	14100	< DL	166	< DL	< DL	< DL	< DL	7	367	20	< DL	6	191	< DL	1.1	< DL	< DL
H	-3	13feb26	He only	Spot	+	Lower	127	2468	14012	< DL	171	< DL	< DL	< DL	< DL	< DL	348	22	< DL	10	191	< DL	< DL	< DL	< DL
H	-3	13feb27	He only	Spot	+	Lower	321	2521	14065	< DL	230	< DL	< DL	< DL	< DL	< DL	371	35	< DL	< DL	142	< DL	< DL	< DL	1.1
H	-3	13feb29	He only	Spot	+o	Lower	42	1963	14086	< DL	174	< DL	< DL	< DL	< DL	8	290	33	< DL	6	152	< DL	1.1	< DL	< DL
H	-3	13feb30	He only	Spot	+	Lower	99	2048	14093	< DL	160	< DL	< DL	< DL	14	5	326	32	< DL	8	223	< DL	4	< DL	< DL
H	-3	13feb31	He only	Spot	+	Lower	126	2906	13983	< DL	210	< DL	42	< DL	< DL	< DL	383	36	< DL	3	176	< DL	3	< DL	< DL
H	-3	13feb32	He only	Spot	+	Lower	195	2260	14127	< DL	85	< DL	< DL	< DL	< DL	< DL	318	45	< DL	< DL	183	< DL	1.1	< DL	< DL
H	-3	13feb34	He only	Spot	-	Lower	100	964	13162	< DL	2439	< DL	111	< DL	109	39	187	51	886	8	70	< DL	189	< DL	11
H	-3	13feb35	He only	Spot	-	Lower	202	2479	13979	< DL	153	< DL	< DL	< DL	< DL	< DL	370	28	< DL	< DL	176	< DL	12	< DL	< DL
H	-3	13feb36	He only	Spot	+	Lower	189	2395	14046	< DL	310	< DL	< DL	< DL	< DL	< DL	382	41	< DL	3	217	< DL	7	< DL	< DL
H	-3	13feb37	He only	Spot	+	Lower	< DL	2475	14121	< DL	109	< DL	< DL	< DL	< DL	< DL	362	35	< DL	7	210	< DL	4	< DL	< DL
H	-2	20jan47	He + H	Spot	+	Upper	215	3691	22672	< DL		< DL	25	< DL	< DL	< DL	393	62	< DL	3	314	< DL	14	< DL	< DL
H	-2	20jan17	He + H	Spot	++	Upper	235	3089	22672	< DL		< DL	< DL	< DL	< DL	25	477	40	< DL	2	249	< DL	14	< DL	< DL
H	-2	20jan18	He + H	Spot	+	Upper	116	3201	22379	< DL		< DL	58	590	10	< DL	490	55	< DL	5	326	< DL	19	< DL	1.2
H	-2	20jan19	He + H	Spot	+	Upper	282	3667	22672	< DL		< DL	< DL	< DL	< DL	< DL	521	43	< DL	8	336	< DL	4	< DL	< DL
H	-2	20jan20	He + H	Spot	+	Upper	139	2626	22672	< DL		< DL	< DL	< DL	41	27	380	36	< DL	6	221	< DL	1.5	< DL	< DL
H	-2	20jan22	He + H	Spot	++	Upper	186	3401	22672	< DL		< DL	37	< DL	< DL	< DL	420	53	< DL	< DL	320	< DL	3	< DL	< DL
H	-2	20jan23	He + H	Spot	++	Upper	183	3300	22672	< DL		< DL	32	< DL	< DL	3	514	92	< DL	< DL	341	< DL	4	< DL	< DL
H	-2	20jan24	He + H	Spot	+	Upper	62	3790	22672	< DL		< DL	< DL	< DL	< DL	< DL	622	42	< DL	< DL	295	< DL	3	< DL	< DL
H	-2	20jan25	He + H	Spot	+	Upper	138	2981	21945	< DL		< DL	126	1462	18	< DL	400	70	< DL	4	256	< DL	2.0	< DL	< DL
H	-2	20jan27	He + H	Spot	+	Upper	243	3447	22333	< DL		< DL	101	682	32	< DL	408	43	< DL	< DL	298	< DL	4	< DL	< DL
H	-2	20jan28	He + H	Spot	+	Upper	177	2740	22672	< DL		< DL	< DL	< DL	19	187	504	144	17	10	213	< DL	6	< DL	13
H	-2	20jan29	He + H	Spot	+	Upper	297	5918	22672	< DL		< DL	133	< DL	< DL	< DL	666	64	< DL	< DL	331	< DL	< DL	< DL	< DL
H	-2	20jan30	He + H	Spot	+	Upper	251	3110	22412	< DL		< DL	31	523	22	< DL	514	52	< DL	4	315	< DL	< DL	< DL	< DL
H	-2	20jan32	He + H	Spot	++	Upper	303	3682	22672	< DL		< DL	< DL	< DL	< DL	21	601	62	< DL	< DL	345	< DL	20	< DL	< DL
H	-2	20jan33	He + H	Spot	+	Upper	207	4114	22672	< DL		< DL	< DL	< DL	< DL	< DL	693	78	< DL	< DL	307	< DL	6	< DL	< DL
H	-2	20jan34	He + H	Spot	++	Upper	141	2775	22406	< DL		< DL	42	535	26	< DL	416	105	< DL	5	270	< DL	7	< DL	0.8
H	-2	20jan35	He + H	Spot	+	Upper	< DL	4685	22672	< DL		< DL	502	< DL	< DL	< DL	884	91	< DL	< DL	308	< DL	< DL	< DL	< DL
H	-2	20jan38	He + H	Spot	+	Upper	223	5038	22672	< DL		< DL	52	< DL	19	< DL	559	63	< DL	< DL	347	< DL	5	< DL	< DL
H	-2	20jan40	He + H	Spot	+	Upper	180	3412	22672	< DL		< DL	< DL	< DL	< DL	< DL	517	48	< DL	4	334	< DL	3	< DL	< DL

Chip	Zone	Sample Filename	Carrier gas	Anal ysis	Qual ity	Limit	Li	B	Na	Mg	K	Ca	Mn	Fe	Zn	Cu	As	Rb	Sn	Sb	Cs	Ba	W	Au	Pb
H	-2	20jan41	He + H	Spot	+	Upper	272	3789	22672	< DL		< DL	38	< DL	< DL	< DL	381	64	< DL	< DL	338	< DL	0.8	< DL	< DL
H	-2	20jan43	He + H	Spot	+	Upper	91	2980	21078	< DL		3208	< DL	< DL	< DL	< DL	454	88	< DL	< DL	265	< DL	7	< DL	5
H	-2	20jan44	He + H	Spot	+	Upper	239	3344	22672	< DL		< DL	26	< DL	6	< DL	550	80	< DL	16	352	< DL	7	< DL	0.5
H	-2	20jan45	He + H	Spot	+	Upper	221	4811	22672	< DL		< DL	< DL	< DL	< DL	< DL	402	55	< DL	< DL	357	< DL	10	< DL	< DL
H	-2	20jan46	He + H	Spot	+	Upper	246	3302	22672	< DL		< DL	< DL	< DL	< DL	< DL	459	44	< DL	< DL	293	< DL	9	< DL	< DL
H	-2	20jan47	He + H	Spot	+	Lower	133	2291	14072	< DL		< DL	16	< DL	< DL	< DL	244	38	< DL	2	195	< DL	9	< DL	< DL
H	-2	20jan17	He + H	Spot	++	Lower	146	1917	14072	< DL		< DL	< DL	< DL	< DL	16	296	25	< DL	1.4	155	< DL	9	< DL	< DL
H	-2	20jan18	He + H	Spot	+	Lower	72	1987	13890	< DL		< DL	36	366	6	< DL	304	34	< DL	3	202	< DL	12	< DL	0.7
H	-2	20jan19	He + H	Spot	+	Lower	175	2276	14072	< DL		< DL	< DL	< DL	< DL	< DL	324	27	< DL	5	208	< DL	3	< DL	< DL
H	-2	20jan20	He + H	Spot	+	Lower	86	1630	14072	< DL		< DL	< DL	< DL	25	16	236	23	< DL	3	137	< DL	0.9	< DL	< DL
H	-2	20jan22	He + H	Spot	++	Lower	115	2111	14072	< DL		< DL	23	< DL	< DL	< DL	261	33	< DL	< DL	199	< DL	2.0	< DL	< DL
H	-2	20jan23	He + H	Spot	++	Lower	113	2048	14072	< DL		< DL	20	< DL	< DL	2.0	319	57	< DL	< DL	212	< DL	3	< DL	< DL
H	-2	20jan24	He + H	Spot	+	Lower	38	2352	14072	< DL		< DL	< DL	< DL	< DL	< DL	386	26	< DL	< DL	183	< DL	2	< DL	< DL
H	-2	20jan25	He + H	Spot	+	Lower	85	1850	13621	< DL		< DL	78	908	11	< DL	248	43	< DL	3	159	< DL	1.2	< DL	< DL
H	-2	20jan27	He + H	Spot	+	Lower	151	2140	13862	< DL		< DL	63	424	20	< DL	253	27	< DL	< DL	185	< DL	2	< DL	< DL
H	-2	20jan28	He + H	Spot	+	Lower	110	1701	14072	< DL		< DL	< DL	< DL	12	116	313	90	10	6	132	< DL	4	< DL	8
H	-2	20jan29	He + H	Spot	+	Lower	184	3673	14072	< DL		< DL	82	< DL	< DL	< DL	414	39	< DL	< DL	205	< DL	< DL	< DL	< DL
H	-2	20jan30	He + H	Spot	+	Lower	156	1930	13911	< DL		< DL	19	325	14	< DL	319	32	< DL	3	196	< DL	< DL	< DL	< DL
H	-2	20jan32	He + H	Spot	++	Lower	188	2285	14072	< DL		< DL	< DL	< DL	< DL	13	373	39	< DL	< DL	214	< DL	12	< DL	< DL
H	-2	20jan33	He + H	Spot	+	Lower	129	2554	14072	< DL		< DL	< DL	< DL	< DL	< DL	430	48	< DL	< DL	190	< DL	4	< DL	< DL
H	-2	20jan34	He + H	Spot	++	Lower	87	1722	13907	< DL		< DL	26	332	16	< DL	258	65	< DL	3	168	< DL	4	< DL	0.5
H	-2	20jan35	He + H	Spot	+	Lower	< DL	2908	14072	< DL		< DL	312	< DL	< DL	< DL	549	57	< DL	< DL	191	< DL	< DL	< DL	< DL
H	-2	20jan38	He + H	Spot	+	Lower	139	3127	14072	< DL		< DL	33	< DL	12	< DL	347	39	< DL	< DL	215	< DL	3	< DL	< DL
H	-2	20jan40	He + H	Spot	+	Lower	112	2118	14072	< DL		< DL	< DL	< DL	< DL	< DL	321	29	< DL	2	207	< DL	1.9	< DL	< DL
H	-2	20jan41	He + H	Spot	+	Lower	169	2352	14072	< DL		< DL	24	< DL	< DL	< DL	236	40	< DL	< DL	210	< DL	0.5	< DL	< DL
H	-2	20jan43	He + H	Spot	+	Lower	57	1849	13083	< DL		1992	< DL	< DL	< DL	< DL	282	55	< DL	< DL	165	< DL	4	< DL	3
H	-2	20jan44	He + H	Spot	+	Lower	148	2076	14072	< DL		< DL	16	< DL	4	< DL	341	50	< DL	10	218	< DL	5	< DL	0.3
H	-2	20jan45	He + H	Spot	+	Lower	137	2986	14072	< DL		< DL	< DL	< DL	< DL	< DL	249	34	< DL	< DL	222	< DL	6	< DL	< DL
H	-2	20jan46	He + H	Spot	+	Lower	152	2049	14072	< DL		< DL	< DL	< DL	< DL	< DL	285	28	< DL	< DL	182	< DL	6	< DL	< DL
H	-3	21jan32	He + H	Spot	+	Upper	160	3054	22207	< DL		< DL	< DL	936	< DL	< DL	514	80	< DL	11	281	< DL	< DL	< DL	< DL
H	-3	21jan14	He + H	Spot	-	Upper	212	3140	22672	< DL		< DL	33	< DL	< DL	< DL	546	40	< DL	14	311	< DL	2	< DL	< DL
H	-3	21jan03	He + H	Spot	+	Upper	152	3423	22672	< DL		< DL	58	< DL	< DL	< DL	456	62	< DL	4	323	< DL	3	< DL	0.5
H	-3	21jan04	He + H	Spot	+	Upper	43	3515	22155	< DL		1040	24	< DL	< DL	12	460	57	< DL	7	304	< DL	9	< DL	0.6
H	-3	21jan05	He + H	Spot	+	Upper	< DL	3294	22351	< DL		647	73	< DL	15	3	567	60	< DL	16	334	< DL	7	< DL	< DL
H	-3	21jan06	He + H	Spot	+	Upper	< DL	3031	21797	< DL		1760	28	< DL	< DL	< DL	470	45	< DL	10	299	< DL	8	< DL	< DL
H	-3	21jan08	He + H	Spot	+	Upper	19	2956	21918	< DL		1517	< DL	< DL	< DL	9	478	40	< DL	12	305	< DL	5	< DL	< DL
H	-3	21jan09	He + H	Spot	+	Upper	< DL	2551	22190	< DL		488	< DL	482	27	< DL	443	47	< DL	< DL	244	< DL	8	< DL	< DL
H	-3	21jan10	He + H	Spot	+	Upper	165	3219	22672	< DL		< DL	27	< DL	< DL	< DL	514	56	< DL	< DL	301	< DL	< DL	< DL	< DL
H	-3	21jan11	He + H	Spot	+	Upper	241	3158	21346	< DL		1186	78	1482	< DL	< DL	195	41	< DL	< DL	268	< DL	1.9	< DL	< DL
H	-3	21jan13	He + H	Spot	o	Upper	67	3049	19577	< DL		2800	478	3429	41	1372	467	1122	175	18	321	< DL	137	< DL	29
H	-3	21jan15	He + H	Spot	+o	Upper	151	3288	22672	< DL		< DL	< DL	< DL	< DL	< DL	416	46	< DL	< DL	341	< DL	< DL	< DL	< DL
H	-3	21jan16	He + H	Spot	+	Upper	118	3019	22672	< DL		< DL	< DL	< DL	< DL	< DL	503	35	< DL	18	284	< DL	4	< DL	< DL
H	-3	21jan18	He + H	Spot	+	Upper	131	3367	22672	< DL		< DL	< DL	< DL	< DL	3	631	58	< DL	17	335	< DL	< DL	< DL	< DL
H	-3	21jan19	He + H	Spot	+o	Upper	< DL	4367	17669	< DL		4654	< DL	5415	< DL	< DL	489	63	< DL	< DL	265	< DL	< DL	< DL	< DL
H	-3	21jan20	He + H	Spot	+	Upper	136	3069	22672	< DL		< DL	16	< DL	< DL	4	505	64	< DL	13	288	138	0.4	< DL	< DL
H	-3	21jan21	He + H	Spot	+	Upper	226	3017	22672	< DL		< DL	< DL	< DL	< DL	< DL	448	48	< DL	< DL	237	< DL	5	< DL	< DL
H	-3	21jan23	He + H	Spot	+	Upper	223	2788	22672	< DL		< DL	< DL	< DL	< DL	< DL	507	100	< DL	< DL	239	< DL	< DL	< DL	3
H	-3	21jan24	He + H	Spot	o	Upper	382	4025	22672	< DL		< DL	< DL	< DL	< DL	< DL	718	54	< DL	< DL	331	< DL	< DL	< DL	< DL

Chip	Zone	Sample Filename	Carrier gas	Anal ysis	Qual ity	Limit	Li	B	Na	Mg	K	Ca	Mn	Fe	Zn	Cu	As	Rb	Sn	Sb	Cs	Ba	W	Au	Pb
H	-3	21jan25	He + H	Spot	++	Upper	240	3867	22672	< DL		< DL	< DL	< DL	< DL	< DL	460	51	< DL	< DL	290	< DL	52	< DL	< DL
H	-3	21jan26	He + H	Spot	+	Upper	96	3300	22672	< DL		< DL	177	< DL	< DL	< DL	580	31	< DL	18	297	< DL	9	< DL	39
H	-3	21jan28	He + H	Spot	+	Upper	180	3199	22672	< DL		< DL	< DL	< DL	< DL	< DL	566	52	< DL	15	344	< DL	< DL	< DL	< DL
H	-3	21jan29	He + H	Spot	+	Upper	84	3310	22672	< DL		< DL	< DL	< DL	11	< DL	465	44	< DL	3	288	< DL	< DL	< DL	< DL
H	-3	21jan30	He + H	Spot	+	Upper	191	3206	22672	< DL		< DL	< DL	< DL	34	11	453	53	26	4	259	< DL	21	< DL	6
H	-3	21jan31	He + H	Spot	+	Upper	267	2662	22672	< DL		< DL	< DL	< DL	< DL	< DL	376	50	< DL	< DL	229	< DL	14	< DL	5
H	-3	21jan32	He + H	Spot	+	Lower	99	1895	13784	< DL		< DL	< DL	581	< DL	< DL	319	49	< DL	7	174	< DL	< DL	< DL	< DL
H	-3	21jan14	He + H	Spot	-	Lower	132	1949	14072	< DL		< DL	20	< DL	< DL	< DL	339	25	< DL	9	193	< DL	1.4	< DL	< DL
H	-3	21jan03	He + H	Spot	+	Lower	94	2125	14072	< DL		< DL	36	< DL	< DL	< DL	283	38	< DL	3	200	< DL	1.6	< DL	0.3
H	-3	21jan04	He + H	Spot	+	Lower	27	2182	13752	< DL		645	15	< DL	< DL	7	286	36	< DL	4	189	< DL	6	< DL	0.4
H	-3	21jan05	He + H	Spot	+	Lower	< DL	2045	13873	< DL		401	45	< DL	9	1.9	352	37	< DL	10	208	< DL	4	< DL	< DL
H	-3	21jan06	He + H	Spot	+	Lower	< DL	1881	13529	< DL		1092	17	< DL	< DL	< DL	292	28	< DL	6	186	< DL	5	< DL	< DL
H	-3	21jan08	He + H	Spot	+	Lower	12	1835	13604	< DL		942	< DL	< DL	< DL	5	297	25	< DL	8	189	< DL	3	< DL	< DL
H	-3	21jan09	He + H	Spot	+	Lower	< DL	1583	13773	< DL		303	< DL	299	17	< DL	275	29	< DL	< DL	151	< DL	5	< DL	< DL
H	-3	21jan10	He + H	Spot	+	Lower	103	1998	14072	< DL		< DL	16	< DL	< DL	< DL	319	35	< DL	< DL	187	< DL	< DL	< DL	< DL
H	-3	21jan11	He + H	Spot	+	Lower	150	1960	13249	< DL		736	49	920	< DL	< DL	121	25	< DL	< DL	167	< DL	1.2	< DL	< DL
H	-3	21jan13	He + H	Spot	o	Lower	41	1893	12151	< DL		1738	297	2128	26	851	290	697	108	11	200	< DL	85	< DL	18
H	-3	21jan15	He + H	Spot	+o	Lower	94	2041	14072	< DL		< DL	< DL	< DL	< DL	< DL	258	28	< DL	< DL	212	< DL	< DL	< DL	< DL
H	-3	21jan16	He + H	Spot	+	Lower	73	1874	14072	< DL		< DL	< DL	< DL	< DL	< DL	312	22	< DL	11	176	< DL	3	< DL	< DL
H	-3	21jan18	He + H	Spot	+	Lower	82	2090	14072	< DL		< DL	< DL	< DL	< DL	1.8	392	36	< DL	10	208	< DL	< DL	< DL	< DL
H	-3	21jan19	He + H	Spot	+o	Lower	< DL	2711	10967	< DL		2889	< DL	3361	< DL	< DL	304	39	< DL	< DL	164	< DL	< DL	< DL	< DL
H	-3	21jan20	He + H	Spot	+	Lower	85	1905	14072	< DL		< DL	10	< DL	< DL	3	314	40	< DL	8	178	85	0.3	< DL	< DL
H	-3	21jan21	He + H	Spot	+	Lower	140	1873	14072	< DL		< DL	< DL	< DL	< DL	< DL	278	30	< DL	< DL	147	< DL	3	< DL	< DL
H	-3	21jan23	He + H	Spot	+	Lower	138	1731	14072	< DL		< DL	< DL	< DL	< DL	< DL	314	62	< DL	< DL	148	< DL	< DL	< DL	1.9
H	-3	21jan24	He + H	Spot	o	Lower	237	2498	14072	< DL		< DL	< DL	< DL	< DL	< DL	446	33	< DL	< DL	206	< DL	< DL	< DL	< DL
H	-3	21jan25	He + H	Spot	++	Lower	149	2400	14072	< DL		< DL	< DL	< DL	< DL	< DL	286	32	< DL	< DL	180	< DL	32	< DL	< DL
H	-3	21jan26	He + H	Spot	+	Lower	59	2048	14072	< DL		< DL	110	< DL	< DL	< DL	360	19	< DL	11	185	< DL	5	< DL	24
H	-3	21jan28	He + H	Spot	+	Lower	112	1986	14072	< DL		< DL	< DL	< DL	< DL	< DL	351	32	< DL	9	214	< DL	< DL	< DL	< DL
H	-3	21jan29	He + H	Spot	+	Lower	52	2054	14072	< DL		< DL	< DL	< DL	7	< DL	289	27	< DL	1.9	179	< DL	< DL	< DL	< DL
H	-3	21jan30	He + H	Spot	+	Lower	118	1990	14072	< DL		< DL	< DL	< DL	21	7	281	33	16	2	160	< DL	13	< DL	4
H	-3	21jan31	He + H	Spot	+	Lower	166	1652	14072	< DL		< DL	< DL	< DL	< DL	< DL	233	31	< DL	< DL	142	< DL	9	< DL	3
H	-3	22jan33	He + H	Spot	+	Upper	186	3218	22672	< DL		< DL	19	< DL	< DL	< DL	546	62	< DL	20	296	< DL	< DL	< DL	< DL
H	-3	22jan14	He + H	Spot	+	Upper	82	3783	22672	< DL		< DL	< DL	< DL	< DL	< DL	554	62	< DL	< DL	335	< DL	3	< DL	< DL
H	-3	22jan03	He + H	Spot	+o	Upper	276	3211	22672	< DL		< DL	< DL	< DL	< DL	< DL	495	70	< DL	< DL	266	< DL	< DL	< DL	< DL
H	-3	22jan04	He + H	Spot	+	Upper	207	3659	22672	< DL		< DL	< DL	< DL	8	< DL	528	58	< DL	< DL	339	< DL	0.8	< DL	< DL
H	-3	22jan05	He + H	Spot	+	Upper	170	3384	22672	< DL		< DL	29	< DL	< DL	< DL	554	52	< DL	13	328	< DL	4	< DL	< DL
H	-3	22jan06	He + H	Spot	++	Upper	207	3724	22672	< DL		< DL	< DL	< DL	< DL	< DL	601	50	< DL	10	316	< DL	6	< DL	< DL
H	-3	22jan08	He + H	Spot	++	Upper	198	3941	22672	< DL		< DL	41	< DL	< DL	< DL	472	52	< DL	< DL	353	< DL	6	< DL	< DL
H	-3	22jan09	He + H	Spot	+	Upper	218	3541	22672	< DL		< DL	< DL	< DL	< DL	< DL	552	55	< DL	< DL	321	< DL	7	< DL	< DL
H	-3	22jan10	He + H	Spot	+	Upper	< DL	3953	22672	< DL		< DL	< DL	< DL	< DL	< DL	641	52	< DL	8	317	< DL	11	< DL	< DL
H	-3	22jan11	He + H	Spot	+	Upper	208	3533	22672	< DL		< DL	< DL	< DL	< DL	< DL	488	44	< DL	< DL	277	< DL	7	< DL	< DL
H	-3	22jan15	He + H	Spot	+	Upper	86	4034	22672	< DL		< DL	< DL	< DL	< DL	< DL	576	73	< DL	< DL	330	< DL	0.8	< DL	< DL
H	-3	22jan16	He + H	Spot	+	Upper	96	3188	22672	< DL		< DL	< DL	< DL	< DL	< DL	480	49	< DL	1.7	267	< DL	1.7	< DL	< DL
H	-3	22jan17	He + H	Spot	+	Upper	415	2909	22672	< DL		< DL	< DL	< DL	< DL	< DL	381	81	< DL	< DL	174	< DL	< DL	< DL	2
H	-3	22jan19	He + H	Spot	+	Upper	< DL	3862	22672	< DL		< DL	< DL	< DL	< DL	< DL	612	55	< DL	6	345	< DL	< DL	< DL	< DL
H	-3	22jan20	He + H	Spot	+	Upper	222	3229	22672	< DL		< DL	< DL	< DL	< DL	< DL	531	45	< DL	6	264	< DL	< DL	< DL	< DL
H	-3	22jan21	He + H	Spot	+	Upper	274	3158	22672	< DL		< DL	< DL	< DL	< DL	< DL	497	35	< DL	< DL	232	< DL	5	< DL	< DL
H	-3	22jan22	He + H	Spot	+	Upper	< DL	3247	22672	< DL		< DL	< DL	< DL	< DL	91	466	61	6	7	266	< DL	132	< DL	2

Chip	Zone	Sample Filename	Carrier gas	Analysis	Quality	Limit	Li	B	Na	Mg	K	Ca	Mn	Fe	Zn	Cu	As	Rb	Sn	Sb	Cs	Ba	W	Au	Pb
H	-3	22jan24	He + H	Spot	+	Upper	180	4714	22672	< DL		< DL	< DL	< DL	< DL	< DL	595	63	< DL	< DL	339	< DL	< DL	< DL	< DL
H	-3	22jan25	He + H	Spot	+	Upper	201	3774	22672	< DL		< DL	< DL	< DL	< DL	< DL	553	96	< DL	20	291	< DL	8	< DL	5
H	-3	22jan26	He + H	Spot	+o	Upper	295	3726	22672	< DL		< DL	< DL	< DL	< DL	< DL	484	83	< DL	< DL	307	< DL	6	< DL	< DL
H	-3	22jan27	He + H	Spot	+	Upper	309	3844	22672	< DL		< DL	< DL	< DL	< DL	< DL	461	38	< DL	< DL	238	< DL	< DL	< DL	< DL
H	-3	22jan29	He + H	Spot	+o	Upper	68	3742	22672	< DL		< DL	153	< DL	< DL	< DL	601	38	< DL	< DL	284	< DL	< DL	< DL	< DL
H	-3	22jan30	He + H	Spot	+	Upper	405	3612	22672	< DL		< DL	< DL	< DL	< DL	< DL	624	36	< DL	< DL	328	< DL	< DL	< DL	< DL
H	-3	22jan31	He + H	Spot	+	Upper	435	3298	22672	< DL		< DL	< DL	< DL	< DL	< DL	403	78	< DL	< DL	281	< DL	6	< DL	< DL
H	-3	22jan32	He + H	Spot	+	Upper	213	3246	22672	< DL		< DL	< DL	< DL	< DL	< DL	201	62	< DL	< DL	292	< DL	< DL	< DL	< DL
H	-3	22jan33	He + H	Spot	+	Lower	115	1998	14072	< DL		< DL	12	< DL	< DL	< DL	339	38	< DL	13	184	< DL	< DL	< DL	< DL
H	-3	22jan14	He + H	Spot	+	Lower	51	2348	14072	< DL		< DL	< DL	< DL	< DL	< DL	344	39	< DL	< DL	208	< DL	2	< DL	< DL
H	-3	22jan03	He + H	Spot	+o	Lower	171	1993	14072	< DL		< DL	< DL	< DL	< DL	< DL	307	44	< DL	< DL	165	< DL	< DL	< DL	< DL
H	-3	22jan04	He + H	Spot	+	Lower	129	2271	14072	< DL		< DL	< DL	< DL	5	< DL	327	36	< DL	< DL	210	< DL	0.5	< DL	< DL
H	-3	22jan05	He + H	Spot	+	Lower	106	2100	14072	< DL		< DL	18	< DL	< DL	< DL	344	33	< DL	8	203	< DL	2	< DL	< DL
H	-3	22jan06	He + H	Spot	++	Lower	129	2312	14072	< DL		< DL	< DL	< DL	< DL	< DL	373	31	< DL	6	196	< DL	4	< DL	< DL
H	-3	22jan08	He + H	Spot	++	Lower	123	2446	14072	< DL		< DL	25	< DL	< DL	< DL	293	32	< DL	< DL	219	< DL	4	< DL	< DL
H	-3	22jan09	He + H	Spot	+	Lower	135	2198	14072	< DL		< DL	< DL	< DL	< DL	< DL	343	34	< DL	< DL	199	< DL	5	< DL	< DL
H	-3	22jan10	He + H	Spot	+	Lower	< DL	2454	14072	< DL		< DL	< DL	< DL	< DL	< DL	398	32	< DL	5	197	< DL	7	< DL	< DL
H	-3	22jan11	He + H	Spot	+	Lower	129	2193	14072	< DL		< DL	< DL	< DL	< DL	< DL	303	27	< DL	< DL	172	< DL	5	< DL	< DL
H	-3	22jan15	He + H	Spot	+	Lower	53	2504	14072	< DL		< DL	< DL	< DL	< DL	< DL	358	45	< DL	< DL	205	< DL	0.5	< DL	< DL
H	-3	22jan16	He + H	Spot	+	Lower	60	1979	14072	< DL		< DL	< DL	< DL	< DL	< DL	298	30	< DL	1.1	166	< DL	1.0	< DL	< DL
H	-3	22jan17	He + H	Spot	+	Lower	258	1806	14072	< DL		< DL	< DL	< DL	< DL	< DL	237	50	< DL	< DL	108	< DL	< DL	< DL	1.4
H	-3	22jan19	He + H	Spot	+	Lower	< DL	2397	14072	< DL		< DL	< DL	< DL	< DL	< DL	380	34	< DL	4	214	< DL	< DL	< DL	< DL
H	-3	22jan20	He + H	Spot	+	Lower	137	2004	14072	< DL		< DL	< DL	< DL	< DL	< DL	330	28	< DL	4	164	< DL	< DL	< DL	< DL
H	-3	22jan21	He + H	Spot	+	Lower	170	1960	14072	< DL		< DL	< DL	< DL	< DL	< DL	308	22	< DL	< DL	144	< DL	3	< DL	< DL
H	-3	22jan22	He + H	Spot	+	Lower	< DL	2015	14072	< DL		< DL	< DL	< DL	< DL	57	289	38	4	4	165	< DL	82	< DL	1.4
H	-3	22jan24	He + H	Spot	+	Lower	112	2926	14072	< DL		< DL	< DL	< DL	< DL	< DL	369	39	< DL	< DL	210	< DL	< DL	< DL	< DL
H	-3	22jan25	He + H	Spot	+	Lower	125	2343	14072	< DL		< DL	< DL	< DL	< DL	< DL	343	60	< DL	12	181	< DL	5	< DL	3
H	-3	22jan26	He + H	Spot	+o	Lower	183	2313	14072	< DL		< DL	< DL	< DL	< DL	< DL	300	52	< DL	< DL	190	< DL	4	< DL	< DL
H	-3	22jan27	He + H	Spot	+	Lower	192	2386	14072	< DL		< DL	< DL	< DL	< DL	< DL	286	24	< DL	< DL	148	< DL	< DL	< DL	< DL
H	-3	22jan29	He + H	Spot	+o	Lower	42	2323	14072	< DL		< DL	95	< DL	< DL	< DL	373	24	< DL	< DL	176	< DL	< DL	< DL	< DL
H	-3	22jan30	He + H	Spot	+	Lower	251	2242	14072	< DL		< DL	< DL	< DL	< DL	< DL	387	23	< DL	< DL	203	< DL	< DL	< DL	< DL
H	-3	22jan31	He + H	Spot	+	Lower	270	2047	14072	< DL		< DL	< DL	< DL	< DL	< DL	250	49	< DL	< DL	175	< DL	4	< DL	< DL
H	-3	22jan32	He + H	Spot	+	Lower	132	2015	14072	< DL		< DL	< DL	< DL	< DL	< DL	125	39	< DL	< DL	181	< DL	< DL	< DL	< DL

Curriculum Vitae

Personal details

Insa Theresa Cassens (née Derrey)

Date of birth: 12/25/1984

Place of birth: Lüneburg (Germany)

Family status: married, two children (*2015 and *2019)

Parental leave: 03/2015 - 02/2016, 04/2019 - 03/2020

Work experience

Since 06/2021	Research Coordinator at Leibniz Institute for Applied Geophysics (LIAG), Hannover, Germany
11/2016 – 05/2021	Research Coordinator of Leibniz Research Center FZ:GEO (formerly FI:GEO) at Leibniz University of Hannover, Germany
05/2012 – 10/2016	Research Assistant at Institute of Mineralogy, Leibniz University of Hannover, Germany
10/2006 – 07/2011	Student Assistant at Institute of Mineralogy, Eberhard Karls University of Tübingen, Germany
10/2007 – 01/2011	Student Assistant at Institute of Geology, Eberhard Karls University of Tübingen, Germany
01/2006 – 07/2006	Student Assistant at Institute of Physical Geography, Eberhard Karls University of Tübingen, Germany

Education

Since 05/2012	PhD student at Institute of Mineralogy, Leibniz University of Hannover, Germany
10/2006 – 04/2012	Graduate Studies (M.Sc. equivalent) of Mineralogy at Eberhard Karls University of Tübingen, Germany (Grade 1.1)

08/2008 – 05/2009	Graduate Student at Department of Geology & Geophysics, Yale University, New Haven, CT, USA
10/2006 – 07/2008	Undergraduate Studies (Vordiplom) of Geosciences at Eberhard Karls University of Tübingen, Germany (Grade 1.2)
10/2004 – 09/2006	Undergraduate Studies (Vordiplom) of Geography at Eberhard Karls University of Tübingen, Germany (Grade 1.0)
06/2004	German secondary school graduation (Abitur) at Wilhelm-Raabe Gymnasium Lüneburg (Grade 1.2)

Awards

2009 – 2012	Fellowship of the German Academic Scholarship Foundation (Studienstiftung des deutschen Volkes)
2008 – 2009	Fellowship of the German Academic Exchange Service (DAAD), including tuition fees as a Graduate Student at Yale University, New Haven, CT, USA

Memberships

Since 01/2019	Member of the Science Management Network (Netzwerk Wissenschaftsmanagement e.V.)
Since 01/2018	Elected member of the advisory board of the Alumni Club of Geosciences Hannover (Freunde der Geowissenschaften Hannover e.V.)
Since 01/2011	Member of the German Mineralogical Society (DMG e.V.); elected member of the advisory board from 01/2015 – 12/2016

List of Publications (Peer-reviewed)

Remark: Please note that I am publishing under my birth name, i.e., Insa Theresa Derrey.

Li, N., **Derrey, I.T.**, Holtz, F., Horn, I., Weyer, S., and Xi, W. (2021) Molybdenum solubility and partitioning in H₂O-CO₂-NaCl fluids at 600° C and 200 MPa. *Chemical Geology*, 120438.

Qi, D., Behrens, H., Botcharnikov, R., **Derrey, I.T.**, Holtz, F., Zhang, C., Li, X., and Horn, I. (2020) Reaction between Cu-bearing minerals and hydrothermal fluids at 800 °C and 200 MPa: Constraints from synthetic fluid inclusions. *American Mineralogist*, 105(8), 1126-1139.

Junge, M., Oberthür, T., Kraemer, D., Melcher, F., Piña, R., **Derrey, I.T.**, Manyeruke, T., and Strauss, H. (2019) Distribution of platinum-group elements in pristine and near-surface oxidized Platreef ore and the variation along strike, northern Bushveld Complex, South Africa. *Mineralium Deposita*, 54(6), 885-912.

Wang, M., Deng, J., Hou, T., **Derrey, I.T.**, Botcharnikov, R.E., Liu, X., Zhang, C., Qi, D.-M., Zhang, Z., and Holtz, F. (2019) Experimental evidence for a protracted enrichment of tungsten in evolving granitic melts: implications for scheelite mineralization. *Mineralium Deposita*, 1-8.

Derrey, I.T., Albrecht, M., Dupliy, E., Botcharnikov, R.E., Horn, I., Junge, M., Weyer, S., and Holtz, F. (2017) Experimental tests on achieving equilibrium in synthetic fluid inclusions: results for scheelite, molybdenite and gold solubility at 800°C and 200 MPa. *American Mineralogist*, 102(2), 275-283.

Albrecht, M., **Derrey, I.T.**, Horn, I., Schuth, S., and Weyer, S. (2014) Quantification of trace element contents in frozen fluid inclusions by UV-fs-LA-ICP-MS analysis. *Journal of Analytical Atomic Spectrometry*, 29(6), 1034-1041.

Markl, G., Marks, M.A., **Derrey, I.**, and Gühling, J.-E. (2014) Weathering of cobalt arsenides: Natural assemblages and calculated stability relations among secondary Ca-Mg-Co arsenates and carbonates. *American Mineralogist*, 99(1), 44-56.